



The Alliance of Laboratories in Europe for  
Education, Research and Technology

## **ALERT Doctoral School 2016**

### *Modelling of instabilities and bifurcation in Geomechanics*

Editors:

Jean Sulem

Ioannis Stefanou

Euripides Papamichos

Manolis Veveakis



---

## Editorial

---

The ALERT Doctoral School 2016 entitled *Modelling of instabilities and bifurcation in Geomechanics* is organized by Jean Sulem and Ioannis Stefanou (both from Ecole des Ponts ParisTech), Euripides Papamichos (Aristotle University of Thessaloniki) and Manolis Veveakis (University of New South Wales). I sincerely thank the Organizers and all the authors of the contributions to this book for their effort: thank you!

Instability and bifurcation are of course among the core topics in the research and educational activities of our community; nevertheless, they are still considered rather impervious and difficult chapters for students in Geomechanics. The ALERT Doctoral School 2016, and the present book, are exactly aimed at filling this gap. Starting from the experimental evidence both at laboratory and real scale, and going through the introduction of the basis of the theoretical and numerical modelling of such phenomena, the Authors built a rigorous and comprehensive didactical tool.

I am convinced that the book will be useful not only to students attending the Doctoral School, but even to anybody interested in such classic (but fundamental) themes of the modern Geomechanics.

As usual, the pdf file of the book can be downloaded for free from the website of ALERT Geomaterials – <http://alertgeomaterials.eu>.

On behalf of the ALERT Board of Directors I wish all participants a successful ALERT Doctoral School 2016!

Andrea Galli  
Director of ALERT Geomaterials  
Politecnico di Milano



## Contents

Foreword J. Sulem, I. Stefanou, E. Papamichos, M. Veveakis .....	1
Instability Phenomena in Geomechanics- A Review from a Multi-Physics Point of View T. Hueckel .....	3
Fundamentals of bifurcation theory and stability analysis I. Stefanou, S. Alevizos .....	29
Material instability and strain localization analysis J. Sulem .....	69
Experimental investigation of the emergence of strain localization in geomaterials P. Bésuelle, P. Lanatà .....	87
Numerical modelling of strain localization P. Papanastasiou, A. Zervos .....	133
Numerical modeling of bifurcation: Applications to borehole stability, multilayer buckling, and rock bursting E. Papamichos .....	166
Multiphysics couplings and strain localization in geomaterials J. Sulem, I. Stefanou .....	188
Thermo-poro-mechanics of chemically active faults M. Veveakis .....	215
Numerical modelling of multiphysics couplings and strain localization F. Collin, P. Kotronis, B. Pardoen .....	247



---

## Modelling of instabilities and bifurcation in Geomechanics: Foreword

---

*Nuclear waste disposal, petroleum engineering, CO<sub>2</sub> sequestration, geothermal energy, tunneling, slope stability, geotechnics, borehole stability, drying cracking, earthquake nucleation are important applications of geomechanics with short and long term environmental and societal impacts. Geomechanical systems involve various multiphysical and non-linear processes at several length and time scales. These complex mechanisms are described by non-linear differential equations that express the evolution of the various state variables of a system (e.g. displacements, temperature, pore pressure etc.). In order to study the evolution of the system and the possible occurrence of instabilities, it is necessary to explore the mathematical properties of the governing equations. Therefore questions of existence, uniqueness, and stability of solutions arise naturally. Bifurcation theory and stability analysis are robust and rigorous tools for investigating qualitatively and quantitatively various instabilities such as strain localization, thermal runaway, unstable pressure increase, without determining explicitly the solutions of the governing non-linear equations of a geomechanical system.*

*The purpose of this volume is to present the basic ideas of bifurcation theory and its application to classical problems of geomechanics. The volume is organized in nine chapters.*

*The first chapter “Overview of instability phenomena in Geomechanics” provides in situ and laboratory evidence of instabilities in geomechanical applications, mostly induced by multiphysical phenomena at various scales, such as heat generated during precursor creep, geochemical reactions, thermal pressurization and induced suction and air entry during drying and subsequent cracking of soils.*

*The second chapter “Fundamentals of bifurcation and stability analysis” aims at providing the basic ideas of bifurcation theory and stability analysis. It focuses on giving the necessary vocabulary for the classification of common bifurcations that are often met in applications and, finally, it presents the application of the theory for studying strain localization in solids. Some aspects related to shear band thickness, mesh dependency and higher order continua are also briefly discussed.*

*The following chapter “Material instability and strain localization analysis” covers the principles of strain localization analysis as applied to geomaterials. The conditions for the formation of different types of deformation bands are given and an extension of the analysis to fluid saturated porous media is presented.*

## 2 Foreword

*The fourth chapter “Experimental investigation of strain localization” focuses on strain field measurements of strain localization. Full field methods, imaging tools and experimental loading apparatus have evolved considerably over past 15 years. This chapter presents recent developments on the characterization of the strain localization process and introduces the methods frequently used.*

*The chapter “Numerical modelling of strain localization” gives the basic concepts of numerical modeling of the post-localization regime of strain softening geomaterials. For this purpose two higher order continua with microstructure are presented. This type of continua is used to regularize the ill-posed mathematical problem of strain-softening materials and enable the modelling of progressive localization of deformation in zones of intense shearing that eventually leads to failure.*

*The fifth chapter “Numerical modeling of bifurcation: Applications to borehole stability, multilayer buckling, and rock bursting” presents typical boundary value problems of bifurcation theory in applications related to petroleum industry, mining, and structural geology. The formulation of the bifurcation problem is described and the governing equations are numerically integrated using higher order continua with microstructure such as the Cosserat continuum.*

*The next two chapters “Multiphysics couplings and instabilities I & II” provide a review of recent research regarding the effects of temperature, pore-pressure, chemical reactions and microstructure on strain localization in geomaterials. Examples have been taken in relation with seismic slip in outcrops and core drillings on active faults and with compaction banding.*

*The last chapter “Numerical modelling of Multiphysics couplings and strain localization” focuses on the numerical modeling of localized phenomena induced by multiphysical couplings. To deal with interactions occurring between the different phases of porous media, a regularization technique based on the second gradient model is used.*

*We would like to thank all the contributors to this volume and we hope that the chapters provide a valuable introduction to bifurcation theory and stability in geomechanics covering the state of the art of theoretical, experimental and numerical developments in the field.*

*Finally, we would like to acknowledge the pioneering work of late Professor Ioannis Vardoulakis (1949-2009) who published major contributions on the topic and introduced innovative research in Geomechanics covering large fields of theoretical and computational modelling as well as advanced experimental achievements.*

J. Sulem  
I. Stefanou  
E. Papamichos  
M. Veveakis

---

# Instability Phenomena in Geomechanics- A Review from a Multi-Physics Point of View

**Tomasz Hueckel**

*Duke University, Durham, NC, USA*

---

*In situ and laboratory evidence of instabilities, strain localization, bifurcation in landslides, borehole instability in nuclear waste disposal, drying cracking are discussed considering the multi-physical nature of the complex phenomena involved. The multi-physics include: the effect of heat generated during pre-cursor creep in development of landslides, as well as the effect of geo-chemical reactions, the effect of heat on inducing possible failure through pressurization of pore water, the effect of evaporation induced suction and air entry during drying and subsequent cracking of soils. The phenomena illustrated with specific natural or engineered events are interpreted as scenarios of processes either simultaneous or sequential, that are either coupled, or rely on accumulation of dissipative variables. As pointed out by Terzaghi, the causes of the instabilities are often long-term phenomena rather than single events, such as major rainfalls, which are contributing factors. The need for a proper description of these long-term phenomena and their coupling to variable mechanical properties of soil and rock is emphasized.*

## **1 Introduction**

The engineering practice in all branches of geomechanics is now at an interesting stage of development, when the customary tools of evaluation of margin of safety, which are “admissible stress” and “factors of safety” are felt to lead to an oversimplification, of what we are capable to say about a sample, or soil/rock mass, or structure. This is mainly because of the developed computational capabilities of contemporary engineering, as well as experimentally supported modeling capabilities, including coupled fields, through which soil and rock behavior is mathematically described. In the above statement I have adapted the words of Giulio Maier, with which he opens the Foreword to a fascinating book by Davide Bigoni on bifurcation

## 4 Instability Phenomena in Geomechanics

and material instabilities, [Big12]. While the book refers to bifurcations in a larger class of materials than just geomaterials, the above pronouncement catches exactly the situation: we can predict much more in detail than a few years ago, the stress field evolution, together with strain and/or damage progress along a process of loading following multiple scenarios of coupling with temperature or concentration or reaction progress field. That potentially includes patterns related to failure/instability and their precursors. However, how this information could/should be utilized to quantify “the distance from failure” or “factor of safety”, remains often an open question.

The purpose of this paper is to provide an overview of a series of phenomena in geomechanics, which qualify as instabilities/failure of various kinds. The use of this less than strictly defined term is intentional, as we want to encompass a widest possible class of phenomena for which the criteria are not necessarily within a single type of definition, but in loose terms correspond to Lyapunov’s definition: an unlimited response to a limited solicitation. Solicitation is meant as a trigger of any sort: mechanical, hydraulic, thermal or chemical. We shall start with classical phenomena associated with purely mechanical loading induced instabilities and their criteria and implications, to expand into an array of non-classical multi-physics instability phenomena. Current observations and understanding of geomechanical processes indicate a critical role of non-mechanical variables, whereas the conceptual base is lagging behind. Material instabilities (local) and field instabilities (global) based on the actual instability events leading to failure are both discussed.

## 2 General remarks

As we started with a promise of being wide open and inclusive we have to issue several warnings in order to try to wave off an inevitable confusion that the subject brings, despite an appearance of a strictly rigorous approach.

To start with, in geo-engineering/geophysics context, instability, or better, loss of stability, may mean instability of a material per se (at a point), or instability of a soil/rock mass, or mathematically speaking of a boundary value problem. In other terms, we speak of a local or global stability. A local loss of stability at at least a single point of the continuum is considered a necessary (but by far not sufficient) condition for global instability. Similarly, a local instability in a volume around a tunnel opening may be critical for a highway authority, but of no relevance to the stability of the mountain in which it is built. On the other end of the spectrum, local fault instability *may* induce global slope instability, or trigger an earthquake. It does depend on the geometrical constraints that the considered boundary value problem implies.

The local stability is usually tested in materials laboratory on a uniform specimen, or in a mathematical model, for a single material point. Global stability can rarely be tested in a large scale, but there were attempts made to monitor known landslide sites, or earthquake source sites, or in large liquefaction experiments.

Physically, instability may mean many things depending on the type of material and on the geometrical scale of consideration. In the plainest case, a macroscopically homogeneous material element in laboratory at a sufficiently low stress deforms in a homogeneous manner when a uniform traction is applied at its boundary. However, for unspecified physical reasons, at a certain stress level it responds with an unconstrained strain in response to say, a small stress perturbation. Often, the homogeneous strain is associated with a diffuse dilatancy (increased volume). This is a classical representation of instability. The key point is the homogeneity of the response maintained during the instable phase.

Alternatively, always with a homogeneous response, we perceive as critical a loss of uniqueness of response, which means that such a response in a repetition of the theoretically the same experiment would yield a different response. An additional option is to treat as unstable a response in which the increase in internal energy over a virtual displacement is less than work of the external forces. Each of the above critical conditions, in principle leads to a different criterion, both locally and globally.

In addition, when in a homogeneous sample the straining becomes more advanced, this strain homogeneity may be spontaneously lost. It is inevitable that, due to the actual irregularities in the distribution of minerals with a different stiffness, interface properties, pre-existence of structural defects, etc., concentrations of high stress and/or strain occur. Such concentrations may result in various forms of local damage, like mineral decohesion, micro-fissures, nucleation of pores, inter-mineral, or inter-grain slips, depending much on the structure, mineralogy and the history of the material. The interaction of such local singularities gives rise to a variety of mechanisms of failure. Despite differences, their common feature is a possibility of a development of micro-defects into large-scale mechanisms of failure, such as slip-surface, or fault, compaction band, leading to landslide, sinkhole, faulting, subsidence etc... Such mechanisms are often characterized as macroscopic strain localization, when certain features of continuity abruptly cease to persist, like intergranular or inter-mineral phase contact. Commonly, more than one mechanism occur simultaneously, as in figure. 1 obtained for a sample of sand, in which two separate slip surfaces and a substantial volume of diffuse dilatancy are observed after a triaxial compression test.

A mathematical representation of the above physics is equally complex. Often, Lyapunov type of instability (defined as an unconstrained response to a limited perturbation) is implied resulting from a solution of a system of differential equations describing the non-linear material behavior. The instability consists of bifurcation of the solution of the system of such equations, which clearly implies non-uniqueness of the solution.

## 6 Instability Phenomena in Geomechanics



Figure 1: Multiple shear bands and a volume increase due to diffuse dilatancy

The criteria for exclusion of instability may be local (or for uniformly deformed systems) or global for a piece of continuum. There are several different criteria, expressing very similar, but not identical conditions.

The first type of criteria refers to certain characteristics of material energy or work required to deform in a unique manner (meaning one uniform solution) under the conditions of equilibrium, for a specific stress-strain relationship, and geometrical strain-displacement relationship. The second type allows for strain localization, with a particular geometrical form of deformed configuration that satisfies conditions of equilibrium allowing certain forms of discontinuity, that is admits certain type of discontinuities (shear, or compaction bands). Global criteria consist in the same requirements but integrated over the entire volume of the considered body. The very definition of bifurcation point varies from author to author, although in any specific situation there is usually no doubt about what should be called a bifurcation point. The above types of instabilities and their implications have been studied in the context of geomaterials for nearly 50 years, and an example of their implications and their relationships is reproduced here from an old paper in figure 2 [Big91a]. The most interesting (to this writer) recent developments concern geomaterials in their multi-physics context.

### 3. Solid phase material criteria

To start with we will limit ourselves to considering exclusively incipient elastoplastic straining at small strains. At the moment we will not deal with materials that exhibit strong viscous effects.

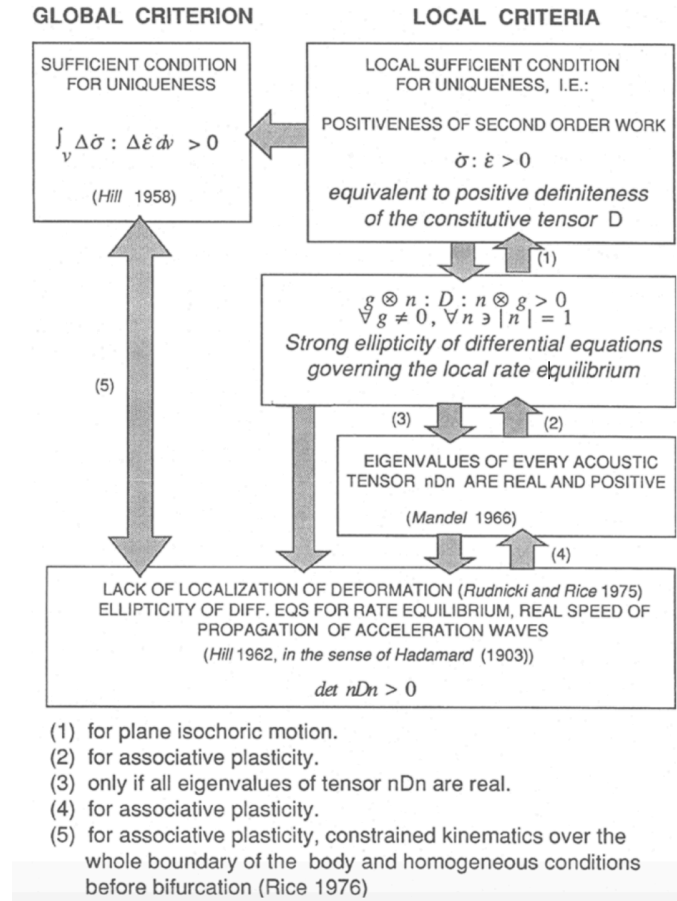


Figure 2: Relationships between criteria for uniqueness, second order work, strong ellipticity, Mandel's stability and localization.

In what follows we will outline the basic formulae of elasto-plasticity (equation 1) at small strains, to introduce basic concepts that will be referred to [Ros68]. The given set of equations implies the existence a yield limit,  $f = f(p', q, r, p_c')$  in the effective stress invariant space, which if  $f = 0$ , means yielding, otherwise  $f < 0$  it means an elastic unloading state. The case of  $f > 0$  is deemed as statically inadmissible. The core of the multi-physical aspects of soil/sediment/rock behavior is embedded in the last of the equations, which describes the evolution of the principal mechanical property of the material, which is the size of the yield locus  $p_c' = p_c'(\epsilon^{pl}, \mu(\Delta T, \xi, c...))$  with changes in a series of the environmental (non-mechanical) variables (see e.g. [Hue92], [Hue02]).

## 8 Instability Phenomena in Geomechanics

$$\begin{aligned}
 f &= f(p', q, r, p_c') \leq 0 \\
 p' &= \frac{1}{3} \sigma_{kk}'; \quad q = \sqrt{3} \sqrt{J_2''}; \quad J_2'' = \frac{1}{2} s_{ij} s_{ij}; \\
 f &= \left( \frac{2p'}{p_c'} - 1 \right)^2 + \left( \frac{2q}{gMp_c'} \right)^2 - 1 \\
 M &= \text{const.} \\
 g &= 2k / \left[ 1 + k + \frac{2k}{2} (1-k) \left( \frac{r}{q} \right)^3 \right]; \quad k = \frac{-3}{3+M} \\
 r &= \sqrt[3]{J_3'}; \quad J_3' = J_3'' = \frac{1}{3} s_{ik} s_{ij} s_{kj}; \\
 p_c' &= p_c' (\varepsilon^{pl}, \mu(\Delta T, \xi, c...))
 \end{aligned} \tag{1}$$

That implies that variables such as temperature, chemical mass removal (accretion), ion concentration of pore fluid affect in an essential way the geomaterial strength and apparent preconsolidation pressure, and elasto-plastic stiffness.

As customary in inelasticity theories the deformation can only be uniquely determined for the incremental deformation, rather than total strain, as in elasticity. Therefore the plastic strain rate is defined as

$$d\varepsilon_{ij}^{pl} = d\lambda P_{ij}; \text{ under condition that } d\lambda df \leq 0, \text{ while } d\lambda \geq 0 \text{ and } df \leq 0 \tag{2}$$

where  $P_{ij}$  is the gradient of the plastic potential, or a resultant direction tensor of all inelastic strain components of various origins, including the irreversible change in elasticity due to plastic straining or damage [Hue75, 76], [Mai79], [Big91, 12]. Most of physical evidence suggests that  $P_{ij} \neq Q_{ij}$ , where  $Q_{ij} = \frac{\partial f}{\partial \sigma'_{ij}}$  is the yield locus gradient, but for a number of reasons it is often seen as convenient to ignore the difference.

Non-associativity, i.e.  $P_{ij} \neq Q_{ij}$ , for instance via an elasto-plastic coupling, or any other forms of irreversible (not necessarily mechanical) straining leading to a non-symmetrical stress-strain incremental relationship are notorious for inducing a premature loss of stability and/or strain localization.

Among several criteria for (local) material stability the most commonly accepted is an energetic one: stating the positiveness of the increment of internal energy, or in other terms, of second order work, in the sense of Hill [Hil58], or Drucker [Dru64]. Following Dru [64], the continuum considered will be said to be stable in a given equilibrium configuration, if and only if an external agency imposing a kinematically admissible (compatible) infinitesimal geometric disturbance, by preserving equilibrium, performs nonnegative (second-order) work whatever the disturbance may be, i.e.

$$\delta\sigma'_{ij} \delta\varepsilon_{ij} \geq 0 \quad (2)$$

Considering the set of constitutive equations (1) and expressing the incremental effective stress as a function of an incremental strain [Mai79] and properties of the material behavior: elasticity tensor,  $E_{ijkl}$ , plastic hardening modulus,  $H$  (positive during plastic strain-hardening and negative during strain-softening) and its critical value,  $H_c$ , which may depend on stress and plastic strain

$$H = -\frac{\partial f}{\partial \varepsilon_{ij}^p} P_{ij}; H_c = -P_{ij} E_{ijkl} Q_{kl}, \text{ where } Q_{ij} \text{ and } P_{ij} \text{ are respectively yield locus gradient}$$

and a second order tensor defining the mode of incremental irreversible strain, one arrives at the following stress-strain incremental relationship characterized by elasto-plastic stiffness tensor  $D_{ijkl}$ , as follows

$$\delta\sigma'_{ij} = D_{ijkl} \delta\varepsilon_{kl}; \text{ with } D_{ijkl} = E_{ijkl} - \frac{1}{H - H_c} U_{ij} M_{kl} \quad (3)$$

and  $U_{ij} = E_{ijkl} Q_{kl}$  and  $M_{ij} = E_{ijkl} P_{kl}$

Employing the above introduced material properties in a local condition of stability (2) we conclude that the criterion is articulated through the hardening modulus  $H$  which if larger than the first value or lower than the second one [Mai79][Big91a]

$$H > H_1 = \frac{1}{2} \left( H_c + \sqrt{P_{ij} E_{ijkl} P_{kl} Q_{mn} E_{mnpq} Q_{rs}} \right) \quad (4)$$

$$H < H_2 = \frac{1}{2} \left( H_c - \sqrt{P_{ij} E_{ijkl} P_{kl} Q_{mn} E_{mnpq} Q_{rs}} \right)$$

ensures stability.

For the associative flow rules ( $P_{ij} = Q_{ij}$ ) the hardening modulus at loss of stability  $H=H_1=0$ , while for materials with so called-subcritical softening, the hardening modulus at the point of re-gaining stability  $H=H_2=H_c$ . Hence, the stability range coincides with that of hardening, and the post-critical range, while the softening range is all unstable. Fig.2. The most important departure from this rule is for all sorts of non-associative flow rules, for which it can be seen that  $H_1 > 0$  [Big91a,b]. Notably, an earlier, particular version of such conditions for a non-associated flow rule for a Mohr-Coulomb material was published by Mróz [Mro63].

A separate issue is the uniqueness of material response. It appears that in certain situations, certain type of incremental solicitation is not admissible, in the sense that the response is not unique, which means that two possible, or infinite possible responses can be expected. The classical result is that in the softening range, i.e.  $H \leq 0$ ,

## 10 Instability Phenomena in Geomechanics

$d\sigma_{ij}$  such that  $d\sigma_{ij}Q_{ij} \geq 0$  is statically not admissible, as it violates the flow rules of equation (2b). In addition  $d\sigma_{ij}$  such that  $d\sigma_{ij}Q_{ij} < 0$  is admissible, but generates two possible types of response: an elastic unloading and an elasto-plastic softening. In other terms, the range of  $H \leq 0$  is not stress controllable. Analogous ranges of static admissibility may be established for  $d\epsilon_{ij}$ , with a range of the hardening modulus at  $H \leq H_c$  is not strain controllable. Consequently, the range  $0 \leq H \leq H_c$  is strain controllable. The issues of controllability are relevant in experimental studies of material behavior.

Nova and Buscarnera [Bus08] have generalized the question of controllability to experiments with a mixed stress-strain control of loading programs. These are of relevance for instance in undrained tests in which (under the assumption of incompressibility of solids and water) volumetric strain rate is imposed as zero.

An alternative form of instability is the one with strain localization. Originally identified in the seminal paper by Rudnicki and Rice [Rud75], the condition is less restrictive than (4), nevertheless it does admit strain localization of a particular form of strain tensor in inequality (2), which is a product of a unit vector  $n_i$  normal to the planar band and a vector  $g_j$  defining the jump in the velocity derivative. This condition is equivalent to positive definiteness of all possible acoustic tensors  $n_i D_{ijkl} n_l$ . A special case of the strain localization into a planar band takes place when the differential equations describing the behavior of the material in equilibrium ceases to be elliptic. Two modes of strain rate discontinuity are possible depending on directions of vectors  $n_i$  and  $g_i$  which are normal modes of split and compaction [Cas09], when the two vectors are coaxial, and a shear band mode, when they are not.

The criterium for localization at a particular direction specified by versor  $n_i$  orthogonal to the discontinuity shear band is given in the form of a hardening modulus

$$H^{sb}(n_j) = 2G \left[ 2n_j P_{ij} Q_{jk} n_k - (n_j P_{ij} n_j) (n_m Q_{mn} n_n) - P_{ij} Q_{ij} - \frac{\nu}{1-\nu} \left( (n_j P_{ij} n_j) - P_{rr} \right) \left( (n_s Q_{st} n_t) - Q_{nn} \right) \right] \quad (5)$$

with  $G$  and  $\nu$  being elastic shear modulus and Poisson coefficient. To determine a critical modulus at a given point, constrained maximization of equation (2) needs to be performed over all possible directions of  $n_i$ .

A global condition of stability is guaranteed in the medium for the entire boundary value problem if

$$2W \doteq \int_S \dot{T}_i \dot{u}_i dS + \int_V \dot{X}_i \dot{u}_i dV = \int_V \dot{\sigma}'_{ij} (\dot{\epsilon}_{kl}) \dot{\epsilon}_{ij} (\dot{u}_r) dV \geq, \text{ for any } \dot{u}_r \quad (6)$$

which is again stated as non-negativeness of the second order work of tractions integrated over the whole boundary (plus that of body forces, over volume).

Through a standard consideration the condition is brought to the requirement of positiveness of the second order work integrated over the entire volume of the body, under the assumptions that both the constitutive laws and geometric conditions are fulfilled. That condition clearly is much much less restrictive than the local condition (4), which requires the same, but at every point of the body. Thus (6) admits large areas of a negative second order work, as long that there are areas that can overweight the negative areas.

One other way to guarantee the stability of the solution of the boundary value problem in geomechanics is to ensure that the solution is unique, or in other terms, there are no alternative solutions for the obtained one to snap through to. The solution uniqueness is guaranteed only under sufficient conditions of local or overall nature, the overall condition being much less stringent than the above sufficient conditions for stability [Hue79].

In geoenineering practice analyses, the assessment of stability is often made on the basis on the finite element result, through either detection of failure as a loss of global equilibrium seen as a lack of convergence of the solution identified by the lack of convergence within a certain iteration number [Gri 99] [Zie05]. Alternatively, loss of stability for instance of a slope is identified as an onset of a kinematically admissible “sliding” mechanism through monitoring as the solution evolves of the selected nodes to detect a sudden increase of displacements [Hic10][San15].

### 4 Material sample stability: experimental

To provide an experimental illustration of a local instability, under the assumption of the absence of localization (diffuse plastic strain) is almost impossible. Fig. 3a shows a series of triaxial test results with increasing confining stress values, after Paterson [Pat, 58] for Wombeyan marble. All of them except for those with the highest confining stress, exhibit eventually an unstable behavior, but for pressure values lower than 35 MPa the material exhibits localized instability, either as a vertical spalling(1), single (2), or conjugate (3) shear bands, whereas for larger confining stress the behavior is qualified as ductile, (4,5) for 70 and 100MPa, (3,4), Fig.3b.

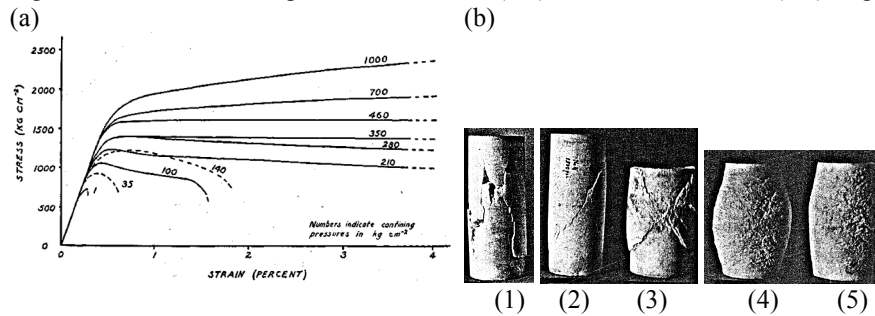


Figure 3: Triaxial compression of Wombeyan marble. (a) axial stress – strain curves; (b) localization and diffused damage modes, after Patterson [PAT58].

Notably, for higher level of confining stress in these tests (70 and 100 MPa) the deformation pattern, with a substantial inelastic component, can be viewed as uniform, or non-localized. The stress – strain curves do not suggest an unstable, or non-unique behavior. Nevertheless, the pattern formation of micro-cracks brings some concerns about homogeneity of the strain and stress distribution across the sample, which in reality homogeneous is not. However, rigorous, or at least somewhat codified measure and understanding what is “sufficiently homogeneous” are conspicuously missing.

In contrast, for all tests below 35 MPa of confining stress, one or more of stability criteria are failed, but the deformation is invariably a localized at certain point.

Acoustic emission recording techniques allow to monitor sound emitting microfracturing, which initiates long before the loss of stress-strain curve linearity, even before noticeable dilatancy onset, and far before approaching the peak stress in triaxial conditions for marble, figure 4 [Hal73]. Indeed, what could qualify as an onset of non-uniqueness and instability coincide rather with the coalescence of micro-cracks into a shear band or macro-crack. Notably, the crack pattern evolution is a gradual process and does not suggest any threshold behavior or values. However, that is not always the case as seen in a figure where comparison for uniaxial failure is reported for salt-rock, granite and marble [Zha15].

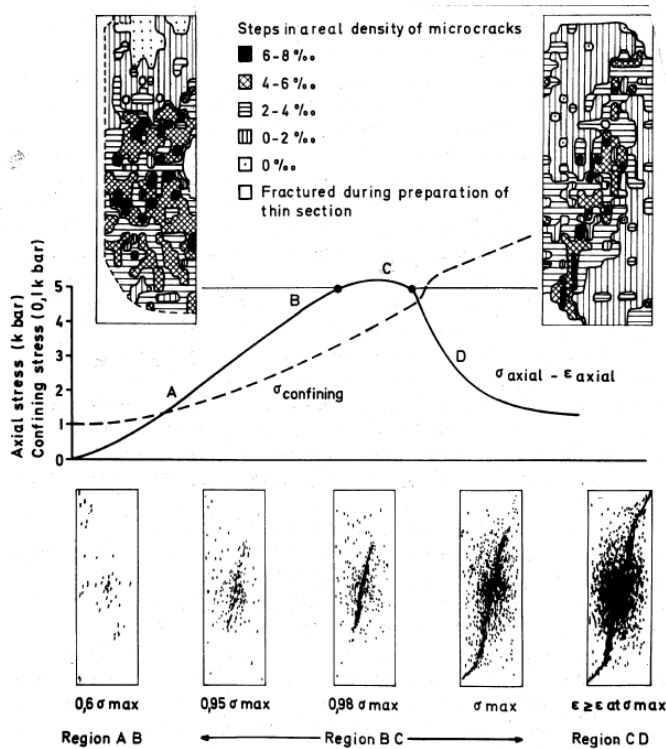


Figure 4: Axial and lateral stress measured on a set of argillaceous quartzite with the corresponding evolution of the distribution of microcracking [Hal73]

For sand the situation is quite similar. Unstable and non-unique behavior is seen in triaxial tests at low confining stress, and invariably associated with a localized deformation into a shear band, figure 5, (VAR78].

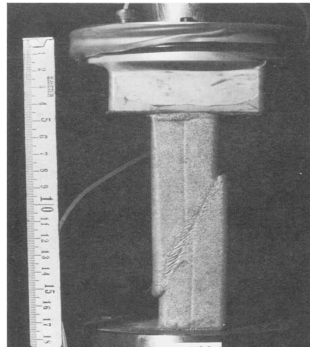


Figure: 5 Biaxial compression of sand with visible localized shear band [Var78]

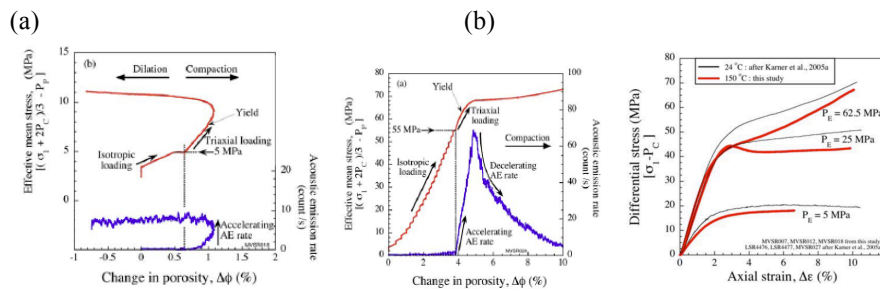


Figure 6: Low (a) and high (b) confining stress compression of a quartz sand: isotropic effective stress vs porosity and acoustic emission decreasing after yielding at high confinement; (c) deviatoric stress-strain curves showing stable behavior at 24°C at high confining pressure [Kar05]

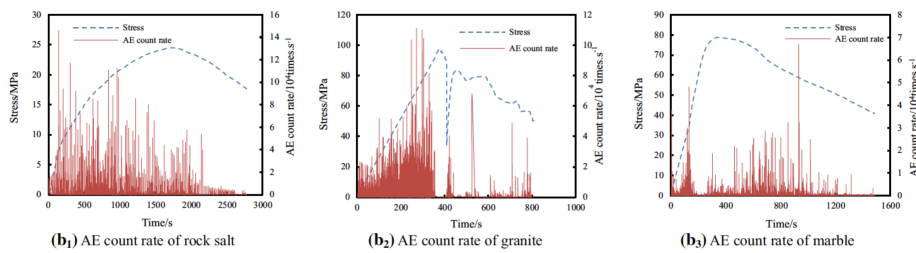


Figure 7: Comparison of uniaxial compression of rock salt, granite and marble, with different intensity of acoustic emission at different stages of loading [Zha15]

A homogeneous behavior at higher confining stress is rarely seen in triaxial strain, and usually is associated with material stability and uniqueness of response to drained tests. There is no established-data base to support the claim that there may

be an unstable sand behavior with a uniform strain across the sample, at least in drained triaxial tests [DRE16]. Karner et al., [KAR08] report sound emission attributed to intense intergranular friction at low mean stress, but at higher stress (and sometimes elevated temperature) if little is said about the location of the sound source, it does not mention strain-localization, while post-test observations indicate grain breaking and comminution. The associated stress-strain curve does imply stable behavior at high confinement (figure 6.).

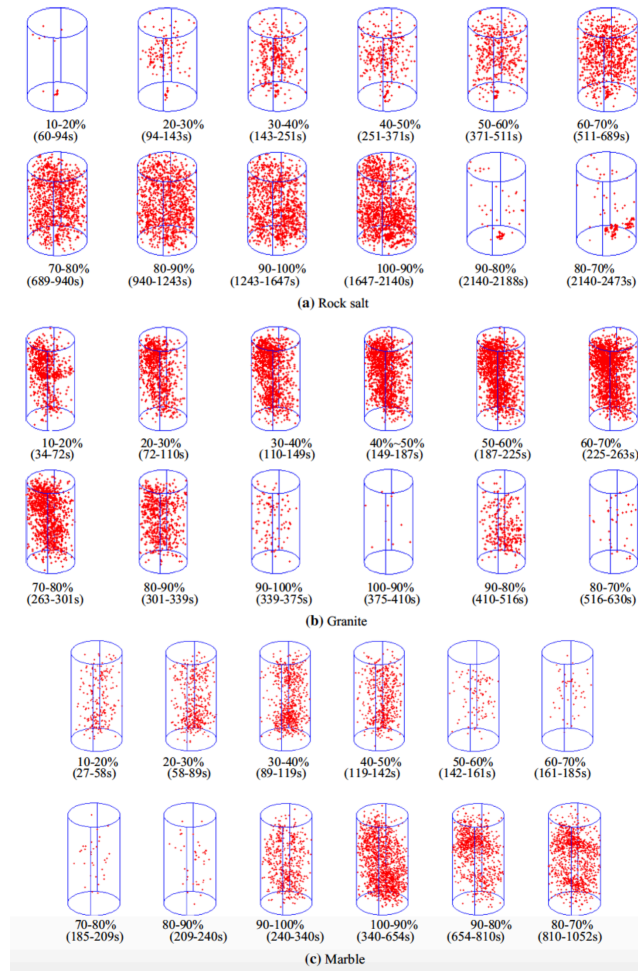


Figure 8: Evolution of distribution of acoustic emission during uniaxial compression of a salt rock, granite and marble

A separate issue arises in undrained tests on sands, during which the volumetric strain is imposed to be constant. In such tests the material exhibit an unstable behav-

ior, however, there is no indication of localization, or in other words the deformation appears to be homogeneous, or diffuse. The term diffuse failure has been adopted for this type of behavior [Dau10]. Figure 9 shows the corresponding stress-strain curve and the effective stress path for such test on Hostun sand. Rightfully, [Dau10] indicate a restriction of the undrained, or constant volume conditions, clearly imposing peculiar deformation pattern.

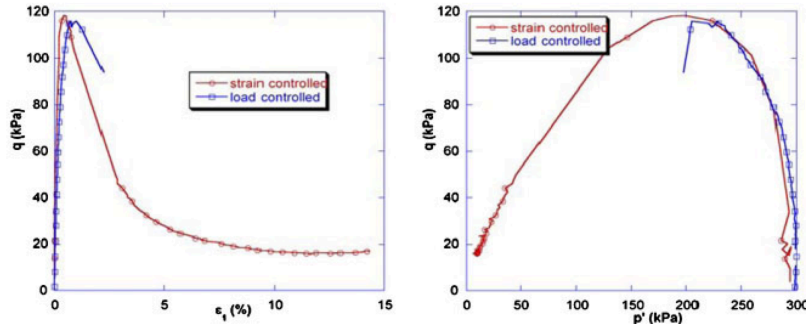


Figure 9: Unstable behavior during undrained test of Hostun sand [Dau10].

Also interesting is the instability developing in sand during constant deviatoric stress drained tests. In these tests failure occurs in coincidence with the changing sign of the volumetric strain (or at a maximum of attained dilatancy) see figure 10. However, in such tests the condition of static admissibility of the local stress rate at the softening regime may be violated. As will be seen later in the paper, experiment with thermal pressurization of clay at constant stress deviator undrained heating test leads to a similar response [Hue91]. However, in that test both localized and diffuse strains were developing at failure.

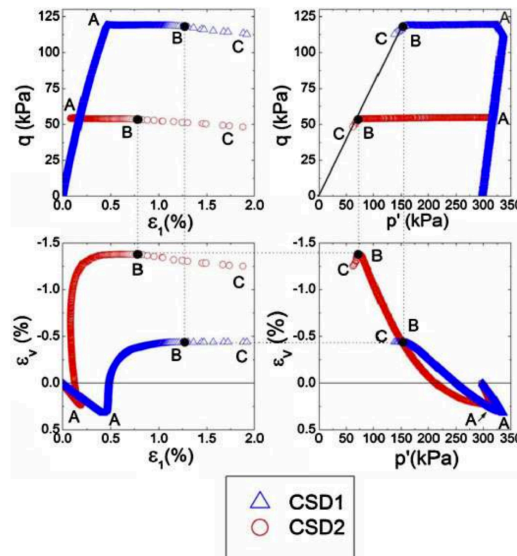


Figure 10: Stress–strain curves in  $q = \text{const.}$  drained test with a instability [Dau10]

There are several observations to be made concerning laboratory experiments on small triaxial samples. The underlining assumption for such experiments is that all the fields: stress, strain, plastic strain (and possibly micro-cracking) are uniform across the sample until a possible appearance of localization. This unfortunately is not necessarily true, as for instance visible in Figure 4 [Hal73]. Similarly, the evolution of local porosity monitored via CAT in sand suggests an early loss of uniformity prior to shear-banding [Des96]. Stress is obviously not measurable directly in such experiments. It is usually considered as an average resulting from the measured force assumed as uniformly distributed across the area. A number of reasons of the non-uniformity are quoted, such as axial symmetry of specimens and a development of roughly planar shear bands, stress concentration at a piston boundaries, with different intensity in sand, clay or rock. Remedies to the experimental techniques have been sought, by introducing Truly-Triaxial – Testers [Woo73], biaxial strain tester (e.g. [Var 1978]) etc. De Josselin de Yong and Drescher [DeJ76] conducted a series of tests in which they subjected a 2-D photo-sensitive granular medium to shear under constant vertical load between two rigid smooth arms rotating around a pin with a controlled rate, causing a displacement of the medium between the arms with a globally unstable or stable force response, depending on the direction of the medium displacement, and dilative or contractile volumetric strain. These, and many other subsequent similar experiments have shown, that contact stresses lead to formation of chains of compressed columns forces within the medium separated by lightly, or completely un – loaded grains. In addition, the said compressed columns undergo periodic unstable buckling and rebuilding of such columns, so that the entire process while apparently monotonic at the force-displacement level is unstable, non-homogeneous and non-monotonic at the level of grain structures, which form vortices and other patterns [Koz16]. Similar conclusions were derived from much later studies of discrete element methods [Iwa98]. This prompted to investigate even small-scale experiments as BVPs and treating their stability and uniqueness through global criteria. Finally, there is a question of validity beyond the point of loss of stability or uniqueness of the stress-strain curves obtained in a single experiment. Indeed each such curve in a non-uniqueness range is just one of an infinity of possible responses, as they go through a singularity point of  $H=0$ . Some additional insight may be expected from multi-scale analyses using DEM computations, together with a progress in a rigorous approach to inter-scale data interpretation.

## 5. Boundary value problems: uniqueness, stability at the field level

### *Landslides*

Landslides are the most common consequences of soil and rock instabilities at the field-scale. In addition, they more common than earthquakes, and may claim many victims per occurrence in populated areas. Classically, shallow sliding is considered separately from deep rotational slope failures. The latter ones are considered here

only. The traditional factor of safety (FOS), understood as a ratio of resisting resultant moment to the driving resultant moment, approaching unity is considered as a condition of failure in classical geotechnics. However, as will be seen in what follows, in several historical landslides, failure occurred at a FOS substantially higher than 1, 2, or even 3. Incorrect evaluation of several variables, material properties or contributing processes led to misleading assessment of FOS.

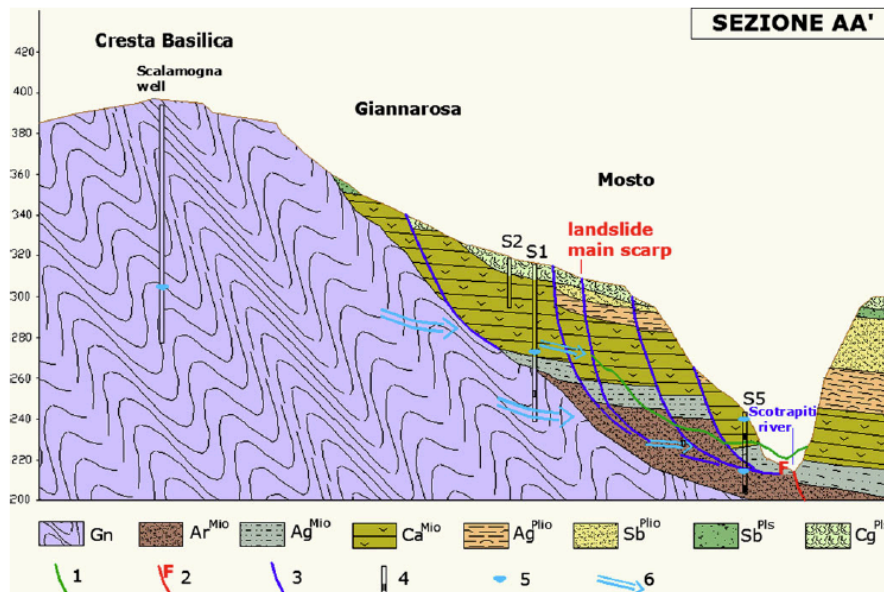
A recent (Feb. 2010) well-documented landslide is that of Maierato (Vibo Valentia), Calabria, which occurred at a site of paleo-landslides of 1783 and 1932. A rare, dramatic, but very instructive video by Patrizia Venturino [Ven10] has documented [http://www.youreporter.it/video\\_Frana\\_Maierato\\_il\\_video\\_integrale\\_in\\_presa\\_diretta\\_1](http://www.youreporter.it/video_Frana_Maierato_il_video_integrale_in_presa_diretta_1) the event in detail. The most important in this video is to note a succession of localized rotational collapses of individual scarps, intercalated with a mass flow. The general trigger of the landslide was a protracted period of rainfalls. As in so many similar cases there were numerous pre-cursors of the final event, in this case a day, to several hours of minor local slides, one of them toppling a high voltage power-line. Because of that warning signs no fatalities occurred. The area affected was 0.3 km<sup>2</sup>, with a front of ab. 800m, depth of 60-70 m and involving ab. 10 Mm<sup>3</sup>, figure 11. The geological structure, shown in a cross-section in figure 12, points out to two particularities of relevance: the presence of two particularly weak permeable rocks: evaporitic limestone and Miocene sandstone, intercalated by two, ab. 10 m thick layers of clay. Prior to the main collapse a substantial swelling was observed suggesting a rotational collapse of a part of mass. It is believed [Gat12], and confirmed by lab experiments that evaporitic limestone transformed from plastic to semi-fluid behavior. Such transformation is suggested to explain rapid change from a mode of sliding to flowing debris mass, observed in the videos.



Figure 11: General view of the Maierato landslide site [Bor14]

The most surprising finding from preliminary FE calculations [Gat12] is that when dry the slope has FOS equal to 3.36, with slip surface within the evaporitic limestone, while with water table up by max 10-15 m there is a reduction of FOS by 40%, but still to ab. 2. Thus, the conventional understanding of slope stability highly overestimates FOS. Among the causes of failure not given a proper consideration, the [Gat12] list penetration and pressurization of pore water along the contact be-

tween Miocene sandstone and Miocene clay, as well as presence (and evolution upon inundation) of evaporitic limestone and Miocenic sandstone, as well as autobrecciation processes induced by dissolution of halite and gypsum during... weathering and dissolution diagenesis [Gat12] [Bor14].



**Fig. 8** Geological cross-section of the study area before the landslide. *Gn* crystalline metamorphic bedrock (Paleozoic), *ArMio* sandstone and sandy days (Middle–Late Miocene), *AgMio* days (Late Miocene), *CaMio* evaporitic limestone (Upper Miocene), *AgPlio* days (Middle Pliocene), *SbPlio* clayey sands (Middle Pliocene), *SbPls* continental sands (Pleistocene), *CgPls* continental conglomerates (Pleistocene). 1 Actual topographic surface, 2 Faults, 3 Sliding surfaces, 4 Piezometers and their filters, 5 Post-landslide water table, 6 Groundwater flow direction. The vertical scale is 5 times more exaggerated than the horizontal

Figure12: A geological profile across the area prior to landslide. Green line denotes post event topography (from [Gat12]).

The most surprising finding from preliminary FE calculations [Gat12] is that when dry the slope has FOS equal to 3.36, with slip surface within the evaporitic limestone, while with water table up by max 10-15 m there is a reduction by 40%, but still to ab. 2. Thus, the conventional understanding of slope stability highly overestimates FOS. Among the causes of failure not given a proper consideration, the authors list penetration and pressurization of pore water along the contact between-Miocene sandstone and Miocene clay, as well as presence (and evolution upon inundation) of evaporitic limestone and Miocenic sandstone, as well as autobrecciation processes induced by dissolution of halite and gypsum during... weathering and dissolution diagenesis [Gat12] [Bor14].

These findings from the preliminary analyses of Maierato landslide by [Gat12] [Bor14] interestingly connect to observations made about instability of slopes made by Terzaghi in his 1950 paper on “Mechanism of Landslides” [Ter50]. Analyzing “landslide producing processes” he emphasizes the difference between the “causes”

and the “contributing factors” of landslides. He defines the latter via an example as follows: “if a slope is old, heavy rainstorms (...) can hardly be the sole cause of a slope failure, because it is most unlikely that they are without any precedent in the history of the slope. They can only be considered contributing factors”. In the same paper, in Table 1, Terzaghi introduces causes or “acting agents”, among which there is water from heavy rainstorm or snow melt. Among several “modes of action of agent” linked to water, he lists at #9 the chemical weathering, which “weakens intergranular bonds” which leads to decrease of cohesion. For an “old slope” slide of Mount Turtle in Alberta, 1903, he then shows after McConnell and Brock [McC04] a progressive decrease in Factor of Safety, over 15 years, with some variations corresponding to dry and wet spells, reaching eventually 1, in conjunction with “a contributing factor” of high pore water pressure, figure 13. He returns to this mechanism in the case of loess, where water from external reservoirs is listed as removing soluble binders destroying intergranular bond(s), with the same macroscopic effect of a decreasing cohesion.

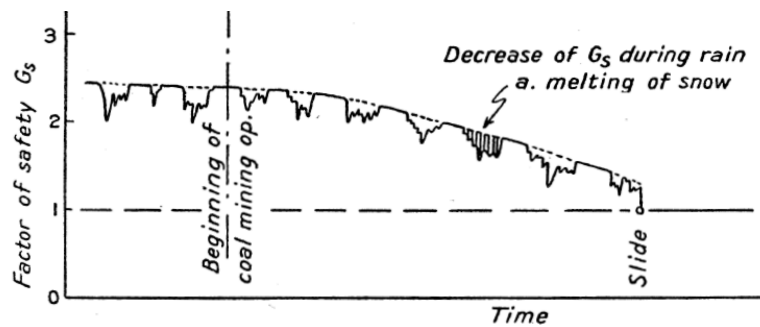


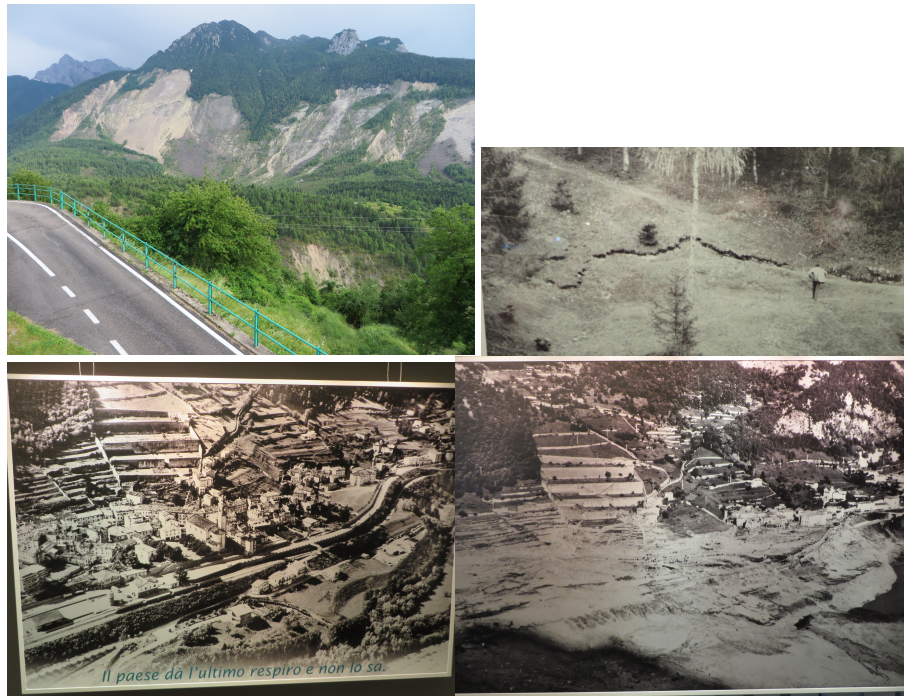
Figure 13: Evolution of Factor of Safety of the slope at Mount Turtle along the process of soil weathering (from Terzaghi [Ter50])

Sensitivity of basic mechanical soil properties to chemical processes in the environment has been seen to become a critical factor of stability of slopes and coastal structures for a variety of reasons, from periodic changes in salinity of pore water affecting clay behavior of coastal slopes, to heat effect at the slip surface during a creep phase of the process, to oxidation and dissolution of sandstone, to dissolution of calcite, dissolution of silica in aging sediments, dissolution of gypsum in abandoned mines, to mention just a few examples.

The conclusion from the above considerations, in a bit more modern terms, is that a proper approach to a realistic evaluation of FOS would be to view the stability as a scenario composed of several processes coupled between them. These processes would be solid- and fluid- mechanical as well as geo-chemical, coupled through both balance equations including exchanges, as well as through constitutive (phenomenological) coupling, i.e. reactions vs porosity (permeability) vs elasticity or softening. The processes may be either simultaneous, or sequential. Hence, the evaluation of the instability of such processes, or differential equations describing them

should be approached accordingly, either as instability of the whole process, or of any of the element of the sequence.

An example of such an approach proposed by Veveakis et al. [Vev07] is an analysis of Vajont dam landslide of 1963 in Northern Italy, Figs.14-16. This was one of the largest disasters of this sort in the previous century, killing nearly 2000 people in a town below the dam (which survived). In their analysis Veveakis et al. postulated that 2-3 year prior to the collapse, creep of the rock mass localized in a clay-rich layer was self-alkiminated by shear generated heat pressurizing and possibly vaporizing water within the layer, and thus leading to thermal softening of clay and accelerating the creep leading eventually to the massive landslide.



Figures 14-16: View of the landslide scarp (2014)-top left; a crack (50-100cm across, -2 km long developed parallel to the reservoir shore a few months before the collapse-top right; The town of Longarone 2km below the dam, before and after the tragedy

They calibrated their model against the data from the site obtaining 35°C temperature and 2.5 MPa of pore pressure increases, which were sufficient to produce velocity of creep of 20cm/day, prior to the failure (Fig. 17).

The model has been subsequently generalized to a thermo-plasticity simulation by Cecinato et al. [Cec11].

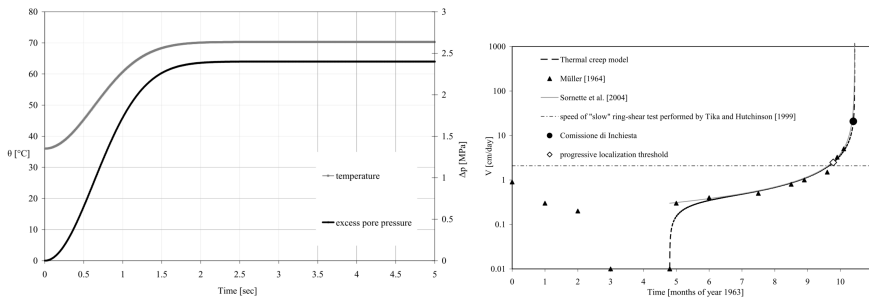


Figure 17: (left) Predicted temperature and excess pore pressure arising in the shear band during sliding vs time (sec.); (right) Calculated velocity of creep vs time in months, compared to other assessments (from [Vev07].)

In a similar spirit, a case study of two landslide slip surfaces at Diao Jiao Zui and Qian Jiang Ping sites in the Three Gorges area, China, has been undertaken using a multi-physics approach. Geochemical testing revealed that due to acid rain (with pH between 5.4 and 3.45) potassium ions at the slide surface were released, the cementation was reduced, and the ratio of interlayer clay minerals evolved. Accordingly, illite or montmorillonite–illite mixtures were transformed first into kaolinite and subsequently into montmorillonite associated with a complex chemical softening evolution, including a 30% drop in shear strength at the slide surface, but not at a close vicinity [Zha01]. Interestingly, both effective internal friction angle and cohesion appear for remolded smectite samples to be non-monotonic functions of time, figure 18.

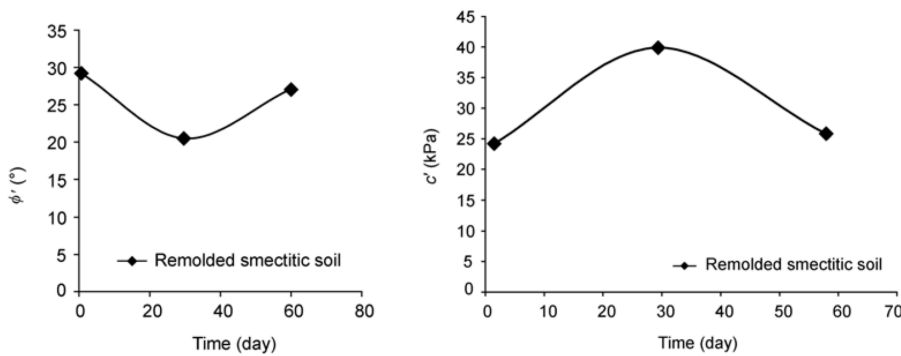


Figure 18: Evolution with time of the effective internal friction angle and cohesion during laboratory simulated chemical transformation due to increase of pore water pH of a model smectite soil corresponding to the slip surface at Diao Jiao Zui and Qian Jiang Ping sites in the Three Gorges area, China (from [Zha11].)

In a similar direction of chemo-mechanical coupling at the slide surface, an interesting extension of their thermal run away creep instability developed for Vajont simulation, was proposed by Veveakis et al. [Vev10]. They postulated that the aforementioned frictional motion is not only affected by the generated heat, but also the strain rate. It appears that steady state heat diffusion across the shear band may be unstable and lead to localization of heat dissipation (and hence thermal softening) at the center of the band. Hence, the Authors consider the effect of localized dissipation on endothermic chemical reaction, leading to a variety of possibilities depending on the nature of specific chemical reaction.

In an analogous spirit Stefanou and Sulem [Ste15] investigated conditions of chemically induced compaction band instability via chemo-plasticity model.

**Thermal pressurization problem**

One of concerns in the technology of nuclear waste disposal in clays is the effect of heat of nuclear decay on mechanical behavior of clay as a supporting medium surrounding the heat source. One of the multi-physics effects results from a huge difference between thermal expansion of pore water and thermal expansion (or thermal contraction of clay, depending if it is in elastic or plastic range). Laboratory experiments have shown that undrained heating at constant total stress loading conditions of relevance to the technology leads to instability, at temperatures between 70 – 90°C, as can be seen from the effective stress path in figure 19a [Hue91].

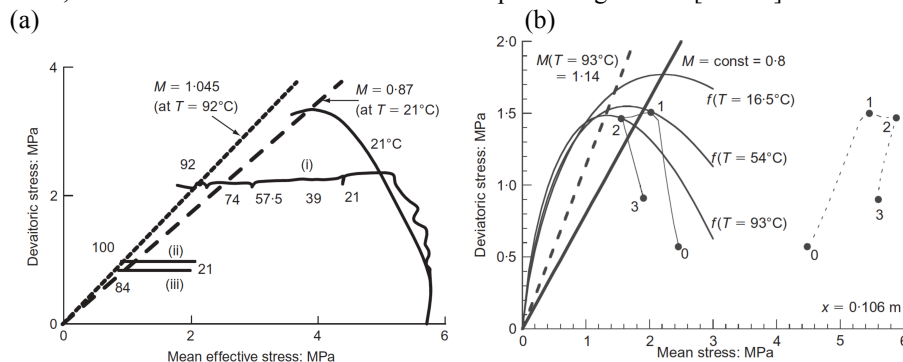


Figure 19: (a) Effective stress paths during undrained heating of Boom clay [Hue91]. Notably the thermally generated pore pressure caused the effective stress to reach values where their further decrement is statically inadmissible, see Sect. 3. Compare to figure 10.

In a borehole bvp, the problem is exacerbated by a very low permeability of clay, compared to thermal conductivity. Indeed, the effective stress path up to the 0.5 m vicinity of the waste canister approaches the critical states, in both considered cases of constant and variable friction angle, figure19b [Hue11]. As the thermo-elasto-plastic deformation is coupled with heat flow and hydraulic flow, its stability and uniqueness should result from consideration of all three fields.

### *Localization during drying of geomaterials*

Cracking of geomaterials during drying is a purely mechanical problem, but highly coupled with the pore fluid flow. Per definition, drying is a multi-phase phenomenon, with a quite complex multi-physics, including phase change, capillarity, flow, deformability, and (perhaps) water cavitation during the phenomenon of air entry, which per se is a fluid - gas interface instability. In addition, it requires considerations to be made at three scales: macroscale continuum, meso-scale of grain and pore clusters, and micro-scale of individual pore structure or grains with liquid bridges. Hueckel et al. [Hue14] postulate that drying cracking consists of a series of processes, starting with evaporation of water at the external surface, inducing a negative liquid pressure and flow out from the deformable soil undergoing shrinkage in response. The air invasion according to Terzaghi takes place when the menisci at the saturated external soil surface reach the size of the biggest pores, but when the soil pores are deformable, that affects air entry. As for the drying-cracking, it is postulated that air finger entering the soil as an instability of the water surface (figure 20) constitutes a defect in the soil body, around which a stress concentration arises, when there are external constraints to shrinkage. An amplification of total tensile stress induces local tensile effective stress despite a high suction value, resulting in a tensile failure, i.e. crack. Hence, a local value of air entry suction controls local stress amplification at the defect. The meso-scale linear fracture mechanics analysis yields the stress values in the plausible range of tensile strength. In this scenario, the cracking needs to be considered at a continuum scale, while the air entry is a micro-scale phenomenon. In addition, the air entry requires certain threshold suction to develop, which in turn changes the size of the pores. Hence, certain processes are sequential.

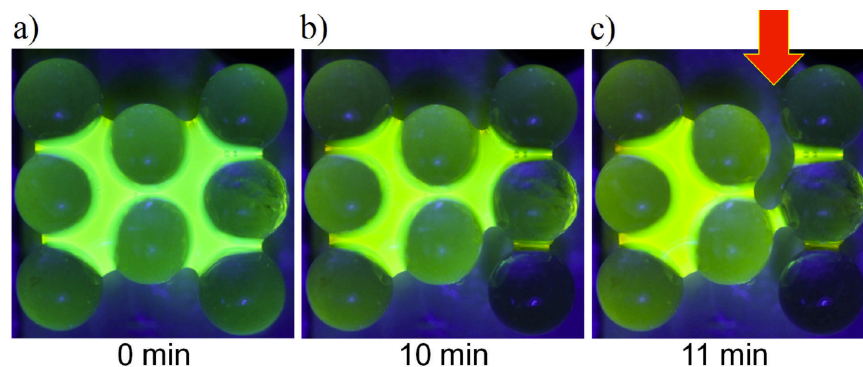


Figure 20: Evolution of the water body between 8 glass spheres subjected to evaporation at a constant temperature and constant ambient vapor pressure. The arrow indicates a localized non-symmetric unstable mode of the interface evolution (air entry finger).

There is a host of other similar problems in which multi-physical behavior leads to instabilities, which were addressed here due to limited space. They include, e.g. liquefaction, instability of rock faults, and mine pillars related to earthquakes, break-through flow due to dissolution of minerals affecting permeability, sinkholes, mine collapses.

## 5 Conclusions

A wide range of failure, instability, non-uniqueness and strain localization phenomena developing in geomaterials were reviewed. It was concluded that in many real life problems such occurrences result from complex multi-physical fields, including flow of pore water, differential thermal expansion of soil constituents, generation of heat through friction, geochemical reactions, evaporation, air invasion, etc. Mechanical instabilities of the solid skeleton, while no doubt an important part of the overall behavior of geomaterials, do not exhaust the complexity of the overall behavior of such materials. A call for a comprehensive approach to multi-physics instability is more than due. The phenomena involved can be modeled as scenarios of processes that occur either simultaneously or sequentially, that are either coupled, or depend on accumulation of dissipative variables. Hence, the stability of such processes should be investigated as those of coupled mechanical, hydraulic, thermal and chemical processes, or as of single processes of a sequence. In the latter case, an instability of one step-process likely affects the formulation of the successor process model. As pointed out by Terzaghi, the causes of the instabilities are often long-term phenomena rather than single events, such as major rainfalls, which are contributing factors. The need for a proper description of these long-term phenomena and their coupling to variable mechanical properties of soil and rock is emphasized.

## References

- [Big91a] Bigoni, D. and Hueckel T., Uniqueness and Localization I. Associative and Non-Associative Elastoplasticity. *Int. J. of Solids Structures*, 28, 2, 197 -213, 1991
- [Big91b] Bigoni, D. and Hueckel T., Uniqueness and Localization II. Coupled Elastoplasticity. *Int. J. of Solids Structures*, 28, 2, 215-224, 1991
- [Big12] Bigoni, D. *Nonlinear Solid Mechanics – Bifurcation Theory and Material Instability*, Cambridge 2012

- [Bor14] Borrelli L., Antronico, L., Gullà, G., and Sorriso-Valvo, GM, Geology, geomorphology and dynamics of the 15 February 2010 Maierato landslide (Calabria, Italy), *Geomorphology*, 208 50–73, 2014
- [Bus08] Buscarnera, G. and Nova, R. Loss of Controllability in Partially Saturated Soils, *8th International Workshop on bifurcation and Degradations in Geomaterials Location: Lake Louise, CANADA*, Edited by: Wan, R; Alsaleh, M; Labuz, J; MAY 28-31, 2008, in: *Bifurcations, Instabilities And Degradations In Geomaterials* Book Series: Springer Series in Geomechanics and Geoengineering Pages: 53-68, 2011
- [Cas09] Castellanza, R.; Gerolymatou, E.; Nova, R. Experimental Observations and Modelling of Compaction Bands in Oedometric Tests on High Porosity Rocks, *Strain*, 45, 5, 410-423, 2009
- [Cec11] Cecinato, F., Zervos, A., Veveakis, E, A thermo-mechanical model for the catastrophic collapse of large landslides, *International Journal for Numerical and Analytical Methods in Geomechanics*, 35, 14, 1507-1535, 2011
- [Dao12] Daouadji, A., Darve, F., Al Gali, H., Hicher P. Y, Laouafa, F., Lignon, S., F. Nicot, R. Nova, M. Pinheiro, F. Prunier, L. Sibille and R. Wan, Diffuse failure in geomaterials: Experiments, theory and modelling, *Int. J. Numer. Anal. Meth. Geomech.* 35:1731–1773, 2011;
- [Des96] Desrues, J., Chambon, R., Mokni, M., Mazerolle, F., Void ratio evolution inside shear bands in triaxial sand specimens studied by computed tomography, *Geotechnique*, 46, 3, 529-546, 1996
- [Dre16] Drescher A. Private communication, 2016
- [Dru64] Drucker D.C., On the postulate of stability of material in mechanics of continua, *J. Mécanique*, 3 pp. 235–249, 1964
- [Gat12] Gattinoni P., Scesi L., Arieni, L., Marco Canavesi, M., The February 2010 large landslide at Maierato, Vibo Valentia, Southern Italy,
- [Gri99] Griffiths, D.V., and Lane, P.A.. Slope stability analysis by finite element *Geotechnique*, 49(3): 387–403. 1999
- [Hal73] Hallbauer, DK, Wagner, H. and Cook, NGW, Some Observations Concerning the Microscopic and Mechanical Behaviour of Quartzite Specimens in Stiff, Triaxial Compression Tests, *Int. J. of Rock Mechanics and Mining Sciences & Geomechanics Abstracts*, 10,6, 713-726, 1973

- [Hic10] Hicks, M.A., and Spencer, W.A. 2010. Influence of heterogeneity on the reliability and failure of a long 3D slope. *Computer and Geotechnics*, 37(7–8): 948–955.
- [Hil58] Hill R., A general theory of uniqueness and stability in elastic-plastic solids *J. Mech. Phys. Solids*, 6, 236,1958
- [Hil62] Hill, R., Acceleration waves in solids, *J. Mech. Phys. Solids*, 10, 1–16, 1962
- [Hue75] Hueckel, T. On Plastic Flow of Granular and Rocklike Materials with Variable Elasticity Moduli, *Bulletin of the Polish Academy of Science, Engineering Sciences Series*, 23, 8, 405-414, 1975
- [Hue76] Hueckel, T. Coupling of Elastic and Plastic Deformations of Bulk Solids, *Meccanica*, 4, 11, 227-235, 1976
- [Hue77] Hueckel T. and G. Maier, Incremental Boundary Value Problems in the Presence of Coupling of Elastic and Plastic Deformations: A Rock Mechanics Oriented Theory, *International Journal of Solids and Structures*, 1, 1-15, 1977,
- [Hue91] Hueckel, T. and Pellegrini, R. Thermoplastic modeling of undrained failure of saturated clay due to heating. *Soils & Foundations* 31, 3, 1–16. 1991
- [Hue92] Hueckel, T. A., Water - Mineral Interaction in Hygro-Mechanics of Clays Exposed to Environmental Loads: a Mixture Theory Approach, *Canadian Geotechnical Journal*, 29, 1071-1086, 1992
- [Hue02] Hueckel, T., Reactive Plasticity for Clays during Dehydration and Rehydration. Part I: Concepts and Options, *International Journal of Plasticity*, 18, 3, 281 – 312, 2002,
- [Hue11] Hueckel T., B. Francois, L. Laloui, Temperature dependent internal friction of clay in a heat source problem, *Geotechnique*, 61, 14, 831–844, 2011,
- [Hue09] Hueckel, T., Francois, B. & Laloui, L. (2009). Explaining thermal failure in saturated clays. *Geotechnique* 59, 3, 197–212,
- [Hue14] Hueckel, T., Mielniczuk, B., El Youssefi, M.S. Hu, L.B. and Laloui, L., A Three-Scale Cracking Criterion For Drying Soils, *Acta Geophysica*, 62, 5, 1049-1059, 2014

- [Iwa98] Iwashita, K; Oda, M, Rolling resistance at contacts in simulation of shear band development by DEM, *Journal of Engineering Mechanics-ASCE*, 124, 3, 285-292, 1998
- [Jae71] Jaeger, J.C. and N.G.W. Cook, *Fundamentals of Rock Mechanics*, Chapman and Hall, Science Paperbacks, New York (1971)
- [Kar08] Karner, S. L., A. K. Kronenberg, F. M. Chester, J. S. Chester, and A. Hajash Jr., Hydrothermal deformation of granular quartz sand, *J. Geophys. Res.*, 113, B05404, (2008) doi:10.1029/2006JB004710.
- [Koz16] Kozicki J. and J. Tejchman, DEM investigations of two-dimensional granular vortex- and anti-vortex-structures during plane strain compression, *Granular Matter*, March 2016, 10.1007/s10035-016-0627-z
- [Le15] Le, T.M.H, Gallipoli, D., Sanchez M., Wheeler S. Stability and failure mass of unsaturated heterogeneous slopes, *Canadian Geotechnical J.*, 52,11,1747-1761
- [Mai79] Maier G. and T. Hueckel, Non-associated and Coupled Flow Rules of Elastoplasticity for Rock-like Materials, *International Journal Rock Mechanics and Mining Science*, 16, 77-92, 1979
- [McC04] McConnell R.G. and Brock R.W., Report on the great landslide at Frank, Alberta, Canada, Dept. Interior Ann. Reports, 1902-1908, pt.8, 17 pages
- [Man66] Mandel, J. Conditions de stabilité et postulat de Drucker, *Rheology and Soil Mechanics*, J. Kravtchenko, P.M. Sirieys (Eds.), Springer, Berlin (1966), p. 58
- [Mro63] Mroz, Z., Non-associated Flow Laws in Plasticity, *J. de Mécanique*, 2, 21-42, 1963
- [Pat58] Paterson, M.S., Experimental Deformation and Faulting in Wombeyan Marble, *Bull. Geol. Soc. of Amer.* 60, 465-476, 1958
- [Ric76] Rice, J.R., The localization of plastic deformation, *Theoretical and Applied Mechanics*, W.T. Koiter (Ed.), North-Holland, Amsterdam (1976), p. 207
- [Ros68] Roscoe, K.H. and J.B. Burland, The generalized stress-strain behaviour of soft clays, in *Engineering Plasticity*, J. Heyman, F. Leckie (Eds.), Cambridge Univ. Press pp. 535–610 (1968),

- [Rud75] Rudnicki, J.W., J.R. Rice, Conditions for localization of deformation in pre-sure -sensitive dilatant materials, *J. Mech. Ph. Solids*, 25, 371–94, 1975
- [Ste15] Stefanou, I., Sulem, J., Chemically induced compaction bands: Triggering conditions and band thickness' *Journal of Geophysical Research-Solid Earth*, 119, 2, 880-899
- [Ter50] Terzaghi, K. Mechanism of Landslides. Cambridge, Ma: Harvard University, Department of Engineering;1950.
- [Var78] Vardoulakis, I., Goldscheider, M. Gudehus, G, Formation of Shear Bands in Sand Bodies as a Bifurcation Problem, *International Journal For Numerical And Analytical Methods In Geomechanics*, 2, 2 , 99-128
- [Ven10] Venturino, P.:
- [http://www.youreporter.it/video\\_Frana\\_Maierato\\_il\\_video\\_integrale\\_in\\_presa\\_diretta\\_1](http://www.youreporter.it/video_Frana_Maierato_il_video_integrale_in_presa_diretta_1)
- [Vev07] Veveakis, E., Vardoulakis, I.; Di Toro, G., Thermoporoelasticity of creeping landslides: The 1963 Vaiont slide, northern Italy, *Journal of Geophysical Research-Earth Surface*, 112, F3, Art #F03026, 2007
- [Vev10] Veveakis, E.; Alevizos, S.; Vardoulakis, I, Chemical reaction capping of thermal instabilities during shear of frictional faults, *Journal of the Mechanics and Physics of Solids*, 58, 9, 1175-1194, 2010
- [Woo73] Muir Wood, D. Truly Triaxial Stress-Strain Behaviour of Kaolin, in *Proceedings of the Symposium on the Role of Plasticity in Soil Mechanics*, September 13-15, 1973, Cambridge, Cambridge University Press
- [Zha15] Zhang, Z., Zhang, R., Xie, H., Liu, J., Were, P. Differences in the acoustic emission characteristics of rock salt compared with granite and marble during the damage evolution process, *Environmental Earth Sciences* 73,11 6987-6999 2015
- [Zha11] Zhao Y., Cui P., Hu, L.B., Hueckel, T., Multi-scale chemo-mechanical analysis of the slip surface of landslides in the Three Gorges, China, *Science China-Technological Sciences* , 54, 7, 1757-1765, 2011
- [Zie05] Zienkiewicz, O.C., Taylor, R.L., and Zhu, J.L. 2005. *The finite element method: its basis and fundamentals*. 5th ed. McGraw-Hill, Oxford.

---

# Fundamentals of bifurcation theory and stability analysis

Ioannis Stefanou<sup>1</sup> and Sotiris Alevizos<sup>2</sup>

<sup>1</sup>Université Paris-Est, Laboratoire Navier, ENPC, IFSTTAR, CNRS, Marne-la-Vallée, France

<sup>2</sup>University of New South Wales, Sydney, New South Wales, Australia

---

*Geomechanical systems are of particular interest as they involve various multiphysical, non-linear processes at several length and time scales. These complex mechanisms are described by non-linear differential equations that express the evolution of the various state variables of a system (e.g. displacements, temperature, pore pressure etc.). The solution of the governing equations, if it is possible to find, can provide complete information of the system and its behavior in time, but for specific initial and boundary conditions. Bifurcation theory and stability analysis are very useful tools for investigating qualitatively and quantitatively the behavior of complex systems without determining explicitly the solutions of its governing equations for various initial and boundary conditions. This chapter is an introduction to the corresponding mathematical theories. It aims at providing the basic ideas of bifurcation theory and stability analysis, it focuses on giving the necessary vocabulary for the classification of equilibria and of common bifurcations that are often met in applications and, finally, it presents the application of the theory for studying strain localization in solids. Some aspects related to shear band thickness, mesh dependency and generalized continua are also briefly discussed.*

## 1 Introduction

Geomechanical systems are of particular interest as they involve various multiphysical, non-linear processes that are characterized by several length and time scales. The inherent complex geomechanical procedures span from the terrestrial kilometeric scale to the nanoscale of rock porosity, grain comminution and physicochemical activity, as well as from the geological time scale to the sudden formation of shear bands related to earthquake nucleation, landslides or failure of geotechnical sites.

These complex mechanisms are described by non-linear differential equations that express the evolution of the state variables of a system in time (e.g. the evolution of displacements, temperature, pore fluid pressure, internal energy etc.). The solution of the differential equations can provide complete information of the system and its behavior in time.

Ideally we would like to compute directly and in analytical form all the solutions of a differential equation. Unfortunately, this is not possible except in the case of linear equations with constant coefficients or in the case of some special types of non-linear differential equations. Numerical methods can help us go further and by using fast computers to approximate the solutions of specific initial and boundary value problems. Nevertheless, these are unique solutions, bound to the specific choice of numerical values for the initial and boundary conditions and no further information can be deduced for the spatio-temporal evolution of the system even for small perturbations of these conditions. Moreover, a universal numerical method that can solve any problem (any system of non-linear differential equations) does not exist yet. Numerical problems such as non-convergence of the numerical algorithm and inaccurate numerical results are common in practice. Finally, in most of the cases we are not interested in the exact evolution of the complete system, but just in the evolution of some critical state variables or of its equilibrium.

It is natural therefore to ask if we can investigate the qualitative and quantitative properties of the solutions of a complex system without solving its governing equations analytically or numerically. Stability analysis and bifurcation analyses are the main tools for that.

A complete list of references on bifurcation and stability analysis exceeds the scope of the present chapter. Here, we refer only to some that we find fundamental from a pedagogical point of view. For an introduction to bifurcation theory and stability analysis of general dynamical systems we refer to [Bra69, Cro91, Str94]. Of course the pioneering work of Lyapunov [Lya66, Lya92a, Lya92b] is very interesting for deepening into dynamical systems and their stability. Concerning the application of bifurcation theory in solid mechanics and plasticity we refer, among others, to [Big91a, Big91b, Lem09, Ric76]. Focusing on geomechanics and multiphysical couplings for classical and generalized continua such as Cosserat, we suggest the following references [Ben00, Ben03, Vev13, Bes00, Bés01, Iss00, Per93, Ste14, Sul11, Var95, Vev12].

Despite the various theoretical and mathematical complications related to constitutive modeling, one has to bear in mind that once the equations for the (dynamical) system are established, bifurcation (and stability) analysis is a standard methodology. One needs to identify and solve for certain types of solutions that act as attractors (or repellers) of the system of equations, i.e. "special" types of solutions that irrespective of the initial data all other solutions will tend towards to (or move away from). These might be time independent *equilibria* or periodic motions, for instance. In Figure 1 we attempt to illustrate this concept. The solid lines (constant solutions)

depict the time independent solutions and the dashed lines are the time dependent ones. We observe that the latter can hover around (top), deviate (middle) or approach (bottom) the equilibria as time elapses. In this way, one might know where all the solutions will tend to in time without the need of computing them. Furthermore, the bifurcation theory can help us determine whether a particular attractor of a system, which we might not even know explicitly, is the only one, under which conditions (due to parameter variations) it might lose stability and become a repeller or whether other possible solutions can exist.

For instance, consider a homogeneously deformed solid under loading. Bifurcation analysis can indicate the existence of other solutions under a given a load and their stability (for example a localized zone inside the solid, such as a shear band, can develop). In other words bifurcation theory can help us determine under which conditions a small perturbation of the reference solution (in this example the homogeneous deformation of the solid) will grow in time (unstable solution leading to strain localization) or not (see Figure 1).

It is worth emphasizing that the notion of stability, well established and defined by the original work of Lyapunov [Lya92a] in the end of 19<sup>th</sup> century, is related with the time evolution of a system. Even if in common practice time is neglected (quasi-static conditions), the transition from a state (e.g. the homogeneous deformation state) to another one (e.g. the formation of shear bands) happens in a certain time scale, which might be very short (sudden failure of brittle materials) or very slow (geological phenomena). This is why time is central in stability theory as it will be seen in the following sections.

The current chapter follows the following structure. In the beginning of section 2 we present a simple example of a dynamic mechanical system in order to introduce some basic notions of stability and bifurcation theory. Then, the necessary definitions of stable and unstable equilibria are given. The stability of general linear and non-linear systems is investigated next. In section 3 the dynamics and stability of two dimensional systems is described. A classification of the various equilibrium points is made. The dynamics can be surprisingly rich allowing even to represent Romeo's and Juliet's affair (see Love mechanics, paragraph 3.2). In section 4 we present the most common bifurcations and their classification. The notion of limit cycles is also introduced. All these sections focus on Ordinary Differential Equation's (ODE's), which is the key block for studying bifurcation and stability. The study of Partial Differential Equations (PDE's), which is of main importance in geomechanics, is based on the same principles and techniques with ODE's. In section 5 we discuss how the study of ODE's is generalized in the case of PDE's. The condition for deformation band formation (such compaction, shear, dilation bands and their combinations) is retrieved (acoustic tensor) with two different approaches and their stability is discussed. Finally, some aspects related to shear band thickness, mesh dependency and generalized continua are also briefly discussed.

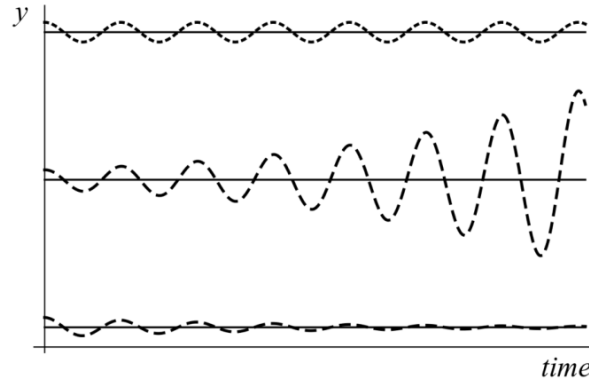


Figure 1. Different types of stability. Solid lines depict the fixed points and dashed lines depict the time evolution of solutions starting from initial conditions near them. From bottom to top the fixed points are asymptotically stable, unstable and (neutrally) stable.

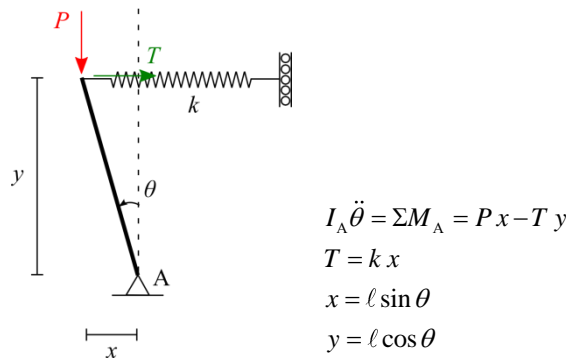


Figure 2: Spring - rigid beam system.

## 2 Bifurcation and stability of dynamical systems

Let's start with the simple example of the mechanical system of Figure 2, which is subjected to a vertical force  $P$ . The spring coefficient is  $k$ , the length of the rigid beam  $\ell$  and its moment of inertia with respect to the out-of-plane axis passing through point A is  $I_A$ . The dynamic behavior of the system is described by the following non-linear differential equation:

$$I_A \ddot{\theta} = k \ell^2 \sin \theta \left( \frac{P}{k \ell} - \cos \theta \right) \quad (1)$$

where  $\theta$  is the rotation angle around A, as shown in Figure 2. The double dot represents the second derivative in time. By setting  $\dot{\theta} = \omega$  the above equation can be written in the following equivalent form:

$$\begin{cases} \dot{\theta} = \omega \\ I_A \dot{\omega} = k \ell^2 \sin \theta \left( \frac{P}{k \ell} - \cos \theta \right) \end{cases} \quad (2)$$

The system is in equilibrium when  $\ddot{\theta} = 0$  or equivalently when  $\dot{\theta} = 0$  and  $\dot{\omega} = 0$ . Therefore, in order to be in equilibrium either  $\cos \theta_0 = P/k\ell$  or  $\theta_0 = n\pi$ , where  $n \in \mathbb{Z}$ . Figure 3 shows all the possible values of the angle  $\theta$  for which equilibrium is possible for given  $P^* = P/k\ell$ . Points  $B_i$  are called bifurcation points of the (equilibrium) solutions. The diagram of Figure 3 is called *bifurcation diagram* and  $P^*$  bifurcation parameter. Depending on the problem at hand various bifurcation parameters can be selected. The bifurcation diagram is a very useful tool for presenting the possible equilibria or steady states of a system (mechanical, chemical, geomechanical etc.). More details about bifurcation types and bifurcation diagrams are given in section 4. It is worth mentioning that for a given value of  $P^*$  we may have several equilibrium solutions. However, some equilibria might be stable and some other unstable, in the sense that, if we are in a certain equilibrium and a tiny perturbation takes place (a fly that sits on the beam!) the system will stay close to its initial equilibrium (stable equilibrium) or it will diverge away of it (unstable equilibrium, see Figure 1). But how stability is rigorously defined and how we can assess it for a given system?

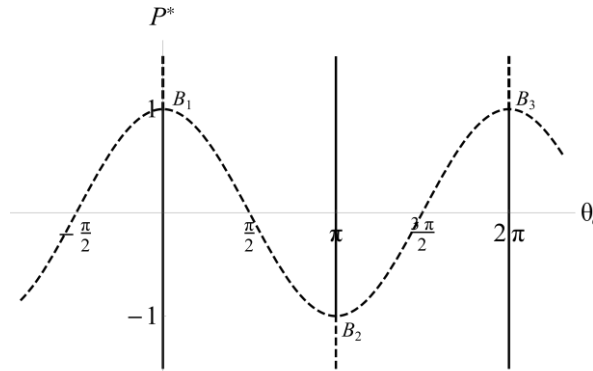


Figure 3: Bifurcation diagram. Dashed lines represent unstable branches and solid stable.

## 2.1 Definition of stability

Let us consider a physical system which is described by the following ODE's (set of first order ordinary differential equations):

$$\dot{\underline{y}} = \underline{f}(\underline{y}) \quad (3)$$

$\underline{y}$  is a vector of  $n$  components that contains the various quantities that determine the evolution of the physical system. The dot represents again the time derivative and  $\underline{f}$  is a vector function that does not depend explicitly on the independent variable which is the time  $t$  (autonomous system).  $\underline{f}$  belongs to  $C^1(D)$  ( $\underline{f} \in C^1(D)$ ), which assures existence and uniqueness of the initial value problem defined by Eq.(3).  $D$  is the  $n$ -dimensional real Euclidean space over which  $\underline{f}$  is defined and  $C^1$  denotes that  $\underline{f}$  and its derivatives, in terms of the components of  $\underline{y}$ , are continuous. The existence and uniqueness of solutions of the initial value problem does not mean that the system has only one equilibrium point. It means that for given initial conditions the system follows a unique trajectory. In other words it can be proven that the response of the initial value problem, even if it is very sensitive to initial conditions (chaotic behavior), has a unique evolution in time as long as  $\underline{f} \in C^1(D)$ . Though, various equilibria points (or steady states) might exist, as shown in the previous example (Figure 2, Figure 3). In practice, when we use the term loss of uniqueness (see [Cha04] for a discussion) of solutions we refer to the existence of several different equilibrium solutions that satisfy  $\underline{f}(\underline{y}_0) = 0$ .  $\underline{y}_0$  are called *fixed points*.

The important question, as far as applications are concerned, is if a certain equilibrium is stable or not. In other words, if at time  $t_0$  we are in equilibrium ( $\dot{\underline{y}}_0 = \underline{f}(\underline{y}_0) = 0$ ) and a tiny perturbation  $\tilde{\underline{y}}$  takes place such as  $\underline{y} = \underline{y}_0 + \tilde{\underline{y}}$ , do we return to the initial equilibrium,  $\underline{y}_0$ , or the system diverges to another state? Lyapunov [Lya66, Lya92b, Lya92a] introduced the following definitions of stability:

*Definition 1:* The equilibrium solution  $\underline{y}_0$  is said to be stable if for each number  $\varepsilon > 0$  we can find a number  $\delta > 0$  (depending on  $\varepsilon$ ) such that if  $\underline{y}(t)$  is any solution of Eq.(3) having  $\|\underline{y}(t_0) - \underline{y}_0\| < \delta$  then the solution  $\underline{y}(t)$  exists for all  $t \geq t_0$  and  $\|\underline{y}(t) - \underline{y}_0\| < \varepsilon$  for  $t \geq t_0$  (see Figure 1, top).

$\|\cdot\|$  denotes here the Euclidian norm ( $\|\underline{a}\| = \sqrt{a_1^2 + a_2^2 + \dots + a_n^2}$ ).

*Definition 2:* The equilibrium solution  $\underline{y}_0$  is said to be asymptotically stable if it is stable and if there exists a number  $\delta_0 > 0$  such that if  $\underline{\psi}(t)$  is any solution of Eq.(3) having  $\|\underline{\psi}(t_0) - \underline{y}_0\| < \delta_0$  then  $\lim_{t \rightarrow +\infty} \underline{\psi}(t) = \underline{y}_0$  (see Figure 1, bottom).

*Definition 3:* The equilibrium solution  $\underline{y}_0$  is said to be unstable if it is not stable (see Figure 1, middle).

## 2.2 Linear systems of ODEs's

The simplest dynamical system for which stability questions can be easily addressed is the following first order linear system of ODE's:

$$\dot{\underline{y}} = \underline{A} \underline{y} \quad (4)$$

where  $\underline{A}$  is a real constant  $n \times n$  matrix.  $\underline{y}_0 = 0$  is the equilibrium solution.

We would like to determine its evolution in time. In other words, if initially the system was in equilibrium, how a small, tiny perturbation would evolve over time? To answer this question, we can determine the general solution of the system, a task that is possible because of its linearity.

A particular solution of the above system is  $\underline{\psi}(t) = \underline{\eta} e^{st}$ , where  $\underline{\eta}$  is a vector of constants with  $\underline{\eta} \neq 0$ . Injecting this form into Eq.(4) we obtain:

$$(\underline{A} - s\underline{I})\underline{\eta} = 0 \quad (5)$$

As  $\underline{\eta}$  is not the zero vector, the above equation is satisfied for  $s$  such that the determinant  $\det(\underline{A} - s\underline{I}) = 0$ . Equation (5) defines an eigenvalue problem, which has  $n$  eigenvalues,  $s^{(i)}$ , and  $n$  associated eigenvectors  $\underline{\eta}^{(i)}$ . The calculation of the determinant results to a polynomial of  $n$  degree in terms of  $s$ , which is called *characteristic polynomial* and whose roots are called *eigenvalues*  $s^{(i)}$ . If the eigenvalues of the system are distinct (no repeated eigenvalues, called *simple eigenvalues*) the general solution of this ODE system is:

$$\underline{\psi}(t) = \sum_{i=1}^n c_i \underline{\eta}^{(i)} e^{s^{(i)}t} \quad (6)$$

where  $c_i$  are constants that are determined by the initial conditions of the problem. The eigenvalues of the system can be real or imaginary. The imaginary part is responsible of an oscillatory behavior of the system while the real part is related to stability. If one of the eigenvalues is positive, then Eq.(6) indicates that the solution of the system will increase exponentially in time (monotonously increasing term).

If the characteristic polynomial has  $p$  distinct eigenvalues (roots)  $s^{(i)}$  ( $1 \leq i \leq p$ ) with multiplicity  $m^{(i)}$  each one (if the eigenvalue  $k$  is simple, then  $m^{(k)} = 1$ ) and associated eigenvectors  $\underline{\eta}^{(i)}$ , then it can be shown that the general solution of the ODE system is:

$$\underline{\psi}(t) = \sum_{i=1}^p \sum_{j=1}^{m^{(i)}} c_{i,j} \underline{\eta}^{(i)} t^{j-1} e^{s^{(i)}t} \quad (7)$$

where again  $c_{i,j}$  are  $n$ , in total, constants that are determined by the initial conditions of the problem. For example, if the system consists of  $n=3$  ODE's and it has only two distinct eigenvalues (one of the eigenvalues has multiplicity 2) then its general solution is:  $\underline{y} = c_{1,1} \underline{\eta}^{(1)} e^{s^{(1)}t} + c_{2,1} \underline{\eta}^{(2)} e^{s^{(2)}t} + c_{2,2} \underline{\eta}^{(2)} t e^{s^{(2)}t}$ . Notice, the term  $t e^{s^{(2)}t}$ , which is strictly increasing in a region close to  $t=0, 0 \leq t \leq \varepsilon$ , even if  $s^{(2)} \leq 0$ .

By combining the aforementioned definitions of stability and the behavior of the solutions of Eq.(4) the following theorem can be proven [Bra69]:

*Theorem 1:*

- If all eigenvalues of  $\underline{A}$  have non-positive real parts and all those eigenvalues with zero real parts are simple, then the zero solution  $\underline{y}_0 = 0$  of Eq.(4) is stable.
- If (and only if) all eigenvalues of  $\underline{A}$  have negative real parts, the zero solution of Eq.(4) is asymptotically stable.
- If one or more eigenvalues of  $\underline{A}$  have a positive real part, the zero solution of Eq.(4) is unstable.

In other words the stability of the equilibrium state of a linear system is investigated by simply studying the eigenvalues of the matrix  $\underline{A}$ .

Can this theorem be extended for non-linear systems as the one presented in the beginning of this section?

### 2.3 Non-linear systems of ODE's

The system described by Eq.(3),  $\dot{\underline{y}} = \underline{f}(\underline{y})$ , is non-linear in the sense that  $\underline{f}(\underline{y})$  is a non-linear function of  $\underline{y}$ . Expressing its solution  $\underline{\psi}(t)$  in the form:

$$\underline{\psi}(t) = \underline{y}_0 + \underline{\tilde{\psi}}(t) \quad (8)$$

where  $\underline{y}_0$  is one of the equilibrium solutions (fixed point), we obtain:

$$\dot{\underline{\tilde{\psi}}}(t) = \underline{f}(\underline{y}_0 + \underline{\tilde{\psi}}(t)) = \underline{f}(\underline{y}_0 + \underline{\tilde{\psi}}(t)) - \underline{f}(\underline{y}_0) \quad (9)$$

If the difference at the right hand side can be written in the following almost-linear form:

$$\dot{\underline{\tilde{\psi}}}(t) = \underline{A} \underline{\tilde{\psi}} + \underline{p}(\underline{\tilde{\psi}}) \quad (10)$$

where  $\underline{A} = \underline{J}(\underline{y}_0) = \left\{ \left. \begin{array}{c} \frac{\partial f_i}{\partial y_j} \\ \hline \end{array} \right|_{\underline{y}=\underline{y}_0} \right\}$  the Jacobian of  $\underline{f}(\underline{y})$  at point  $\underline{y}_0$  ( $\underline{A}$  is a real constant  $n \times n$  matrix),  $\underline{p}$  a continuous function with  $\underline{p}(0) = 0$  and  $\lim_{\|\underline{\tilde{\psi}}\| \rightarrow 0} \frac{\|\underline{p}(\underline{\tilde{\psi}})\|}{\|\underline{\tilde{\psi}}\|} = 0$ , then the following theorem can be proven [Bra69]:

*Theorem 2:* Suppose that  $\underline{p}$  is continuous,  $\|\underline{\tilde{\psi}}\| < k$ , where  $k > 0$  is a constant, and  $\underline{g}$  is small in the sense that  $\lim_{\|\underline{\tilde{\psi}}\| \rightarrow 0} \frac{\|\underline{p}(\underline{\tilde{\psi}})\|}{\|\underline{\tilde{\psi}}\|} = 0$ , then:

- If all eigenvalues of  $\underline{A}$  have negative real parts, the solution  $\underline{\tilde{\psi}} = 0$  of Eq.(10) is asymptotically stable.
- If one or more eigenvalues of  $\underline{A}$  have a positive real part, the solution  $\underline{\tilde{\psi}} = 0$  of Eq.(10) is unstable.

Notice that if the second derivative of  $\underline{f}$  with respect to  $\underline{y}$  exists, then the term  $\underline{p}(\underline{\tilde{\psi}})$  is the remainder of a Taylor expansion of  $\underline{f}$ , which satisfies  $\underline{p}(0) = 0$  and

$\lim_{\|\tilde{\psi}\| \rightarrow 0} \frac{\|p(\tilde{\psi})\|}{\|\tilde{\psi}\|} = 0$ . If all eigenvalues of  $\underline{\underline{A}}$  have non-positive real parts and there exists

at least one eigenvalue with zero real part then the dynamics of the linearized system do not represent the dynamics of the non-linear system and no conclusion can be safely derived for the stability of the non-linear system. However, in the special case of conservative (systems where a conserved quantity exists, e.g. the total energy) or reversible systems (systems with time reversal symmetry) it can be proven that when all the eigenvalues of  $\underline{\underline{A}}$  have non-positive real parts and there exists at least one eigenvalue with zero real part, then all orbits close to a fixed point are closed (see [Str94]). In this case the (isolated) fixed point is called non-linear center and is stable in the Lyapunov sense (but not asymptotically stable).

The above theorem gives the conditions for which any perturbation  $\tilde{\psi}$  is bounded, decays or grows exponentially with time. According to the definitions of stability, the system will be respectively (*asymptotically stable*) or *unstable*. Therefore, the eigenvalues of the matrix  $\underline{\underline{A}}$  can provide useful information about the stability of an equilibrium solution, even in the case of non-linear ODE's. The investigation of stability by using the above theorem is called Linear Stability Analysis (LSA), as it is based on the linearization of  $\underline{f}(\underline{y})$ .

#### 2.4 An example of Linear Stability Analysis

The system presented in the beginning of this section (Eq.(2)) is expressed in the form of Eq.(3) as follows:

$$\underline{y} = \begin{bmatrix} \theta \\ \omega \end{bmatrix} \text{ and } \underline{f} = \begin{bmatrix} \omega \\ \frac{k\ell^2}{I_A} \sin \theta \left( \frac{P}{k\ell} - \cos \theta \right) \end{bmatrix} \quad (11)$$

At equilibrium  $\dot{\underline{y}} = 0$  and  $\underline{y} = \underline{y}_0$ . Perturbing the equilibrium solution we replace  $\underline{y}(t)$  by  $\underline{\psi}(t) = \underline{y}_0 + \tilde{\psi}(t)$  (Eq.(8)). Performing a Taylor expansion of  $\underline{f}$  up to the first order around the point  $\underline{y} = \underline{y}_0$  we retrieve a linear equation of the form of (10)

$$\text{where: } \underline{\underline{A}} = \underline{\underline{J}}(\underline{y}_0) = \left. \frac{\partial f_i}{\partial y_j} \right|_{\underline{y}=\underline{y}_0} = \begin{bmatrix} 0 & 1 \\ \frac{k\ell^2}{I_A} \left( \frac{P}{k\ell} - \cos \theta_0 \right) \cos \theta_0 + \frac{k\ell^2}{I_A} \sin^2 \theta_0 & 0 \end{bmatrix}.$$

The characteristic polynomial of the eigenvalue problem is:

$$s^2 - \frac{k\ell^2}{I_A} \left( \frac{P}{k\ell} - \cos\theta_0 \right) \cos\theta_0 - \frac{k\ell^2}{I_A} \sin^2\theta_0 = 0 \quad (12)$$

which leads to two eigenvalues:

$$s_{1,2} = \pm \sqrt{\frac{k\ell^2}{I_A} \left( \frac{P}{k\ell} - \cos\theta_0 \right) \cos\theta_0 + \frac{k\ell^2}{I_A} \sin^2\theta_0} \quad (13)$$

Now we can investigate the stability of the various branches of the bifurcation diagram (Figure 3). When we are on the sinusoidal branch  $\frac{P}{k\ell} - \cos\theta_0 = 0$ , and there-

fore  $s_{1,2} = \pm |\sin\theta_0| \sqrt{\frac{k\ell^2}{I_A}}$ , which means that there is always a positive eigenvalue (imaginary part is zero). When we are on the vertical branches  $\sin\theta_0 = 0$  and

$$s_{1,2} = \pm \sqrt{\frac{k\ell^2}{I_A} \left( \frac{P}{k\ell} - 1 \right)} \text{ for } \theta_0 = 2n\pi \text{ or } s_{1,2} = \pm \sqrt{-\frac{k\ell^2}{I_A} \left( \frac{P}{k\ell} + 1 \right)} \text{ for } \theta_0 = (2n+1)\pi.$$

In the first case, i.e. for  $\theta_0 = 2n\pi$ , if  $P > k\ell$  then one of the eigenvalues is positive (the imaginary part is zero), which means that the system is unstable. If  $P < k\ell$  then

$$s_{1,2} = \pm \mathbf{i} \sqrt{\frac{k\ell^2}{I_A} \left| \frac{P}{k\ell} - 1 \right|}, \text{ which are two distinct imaginary eigenvalues } (\mathbf{i} = \sqrt{-1}) \text{ and}$$

consequently, according to paragraph 2.3, the equilibrium is (neutrally) stable (conservative and reversible system). In the second case, i.e. for  $\theta_0 = (2n+1)\pi$ , if  $P < -k\ell$  then one of the eigenvalues is positive (the imaginary part is zero), which

means that the system is unstable. If  $P > -k\ell$  then  $s_{1,2} = \pm \mathbf{i} \sqrt{\frac{k\ell^2}{I_A} \left| \frac{P}{k\ell} + 1 \right|}$  which are

two distinct imaginary eigenvalues and consequently, according to paragraph 2.3, the equilibrium is (neutrally) stable. Figure 3 summarizes these results in the bifurcation diagram. If  $P = \pm k\ell$  and  $\theta_0 = n\pi$ , then  $s_{1,2} = 0$  and no conclusion can be drawn about the stability of these points.

### 3 Stability of two dimensional linear dynamical systems

The general form of a two dimensional linear system is:

$$\begin{aligned}\dot{y}_1 &= a y_1 + b y_2 \\ \dot{y}_2 &= c y_1 + d y_2\end{aligned}\quad (14)$$

The equilibrium solution of this system (fixed point) is obviously  $\underline{y}_0 = 0$ . The constants matrix is  $\underline{\underline{A}} = \begin{bmatrix} a & b \\ c & d \end{bmatrix}$  and the characteristic polynomial:

$$s^2 - \tau s + \Delta = 0 \quad (15)$$

where  $\tau = a + d$  and  $\Delta = ad - bc$ . Let  $s_1$  and  $s_2$  be the roots of the characteristic polynomial (eigenvalues of  $\underline{\underline{A}}$ ):

$$s_1 = \frac{\tau + \sqrt{\tau^2 - 4\Delta}}{2}, \quad s_2 = \frac{\tau - \sqrt{\tau^2 - 4\Delta}}{2}, \quad (16)$$

#### 3.1 Classification of fixed points

Take for instance the following case for  $\underline{\underline{A}} = \begin{bmatrix} a & 0 \\ 0 & -1 \end{bmatrix}$ . The eigenvalues are  $s_1 = a$  and  $s_2 = -1$ . Let also  $a$  real. The solution of this linear system is  $y_1 = c_1 e^{at}$ ,  $y_2 = c_2 e^{-t}$  (see paragraph 2.2). The initial conditions determine the constants  $c_1$  and  $c_2$ . Plotting this solution in the (phase) space  $(y_1, y_2)$  we obtain the trajectories presented in Figure 4 for various initial conditions. Such a diagram is called phase diagram and it depicts the dynamics or the so-called mathematical flow of the system. From the solution of this system we get  $\frac{dy_1}{dy_2} = -a \frac{c_1}{c_2} e^{(a-1)t}$ , which illustrates that the dynamic behavior of the system evolves (is concentrated) in the direction with the slowest in absolute value eigenvalue (slow eigen-direction of the linearized system). In other words, for  $a < -1$ ,  $y_2$  reduces faster than  $y_1$  and the solution approaches the equilibrium point having as an asymptote the axis  $y_2$  (see Figure 4a). The direction of the slowest evolution of the system is called *slow manifold* (slow manifold of an equilibrium point of a dynamical system). The contrary holds for  $-1 < a < 0$  (see Figure 4b). In both cases the equilibrium point is an *attractor* (

$y_1$  and  $y_2$  are stable manifolds) and the fixed point is called *stable node*. If both eigenvalues are real and positive then the fixed point is called *unstable node*. If  $a=0$  then  $y_2$  is constant ( $y_1 = c_1$ ) and the system evolves as shown in Figure 4c. In the case that  $a > 0$  the system is unstable and the equilibrium point is a *saddle node* (Figure 4d). For initial conditions such that  $c_1 = 0$  the system will evolve towards the equilibrium point. However, for tiny values of  $c_1$  the system will diverge from the equilibrium point ( $y_1$  is a stable manifold and  $y_2$  unstable - saddle).

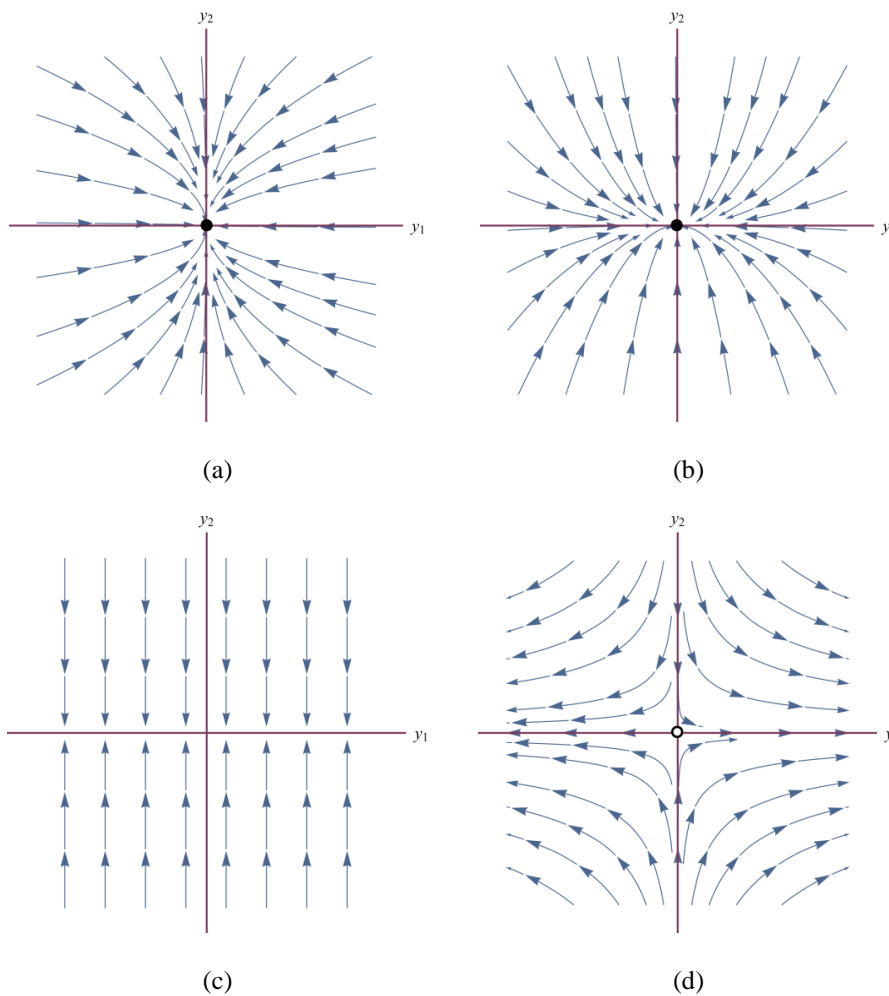


Figure 4. Phase diagram for (a)  $a < -1$ , (b)  $-1 < a < 0$ , (c)  $a = 0$  and (d)  $a > 0$ . A black dot indicates a stable fixed point (stable node, attractor), while an open circle indicates an unstable one (unstable node-repeller or saddle).

In the general case (see Figure 5) of real eigenvalues the manifolds (eigenvectors) are not perpendicular (except if  $\underline{\underline{A}}$  is symmetric). If the real part of both eigenvalues of  $\underline{\underline{A}}$  is zero and they have different non-zero imaginary parts the equilibrium is neutrally stable (stable in the Lyapunov sense for a linear system, see definitions in paragraph 2.2 and 2.3). If the eigenvalues are complex with negative real part then we have oscillations of reducing amplitude until equilibrium (Figure 6). If the real part is positive and the imaginary part non-zero then we diverge from equilibrium (oscillations with increasing amplitude, see also Figure 1). In the case of repeated but non-null eigenvalues, if the eigenvectors are distinct, then we have a star node, and when there is only one eigenvector the fixed point is called degenerated node (Figure 7). For a nice online application for generating phase diagrams for various  $\underline{\underline{A}}$  we refer to [Che16].

Figure 8 summarizes the various types of fixed points in function of  $\tau$  and  $\Delta$ . In the bifurcation example of the previous section  $\tau=0$ . Therefore, we had either saddle points (unstable equilibria) or centers (neutrally stable equilibria).

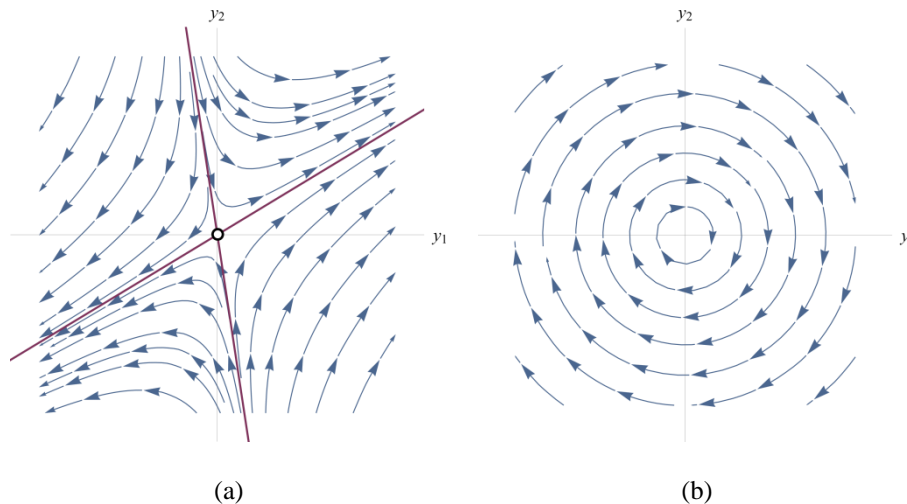


Figure 5. (a) Unstable fixed point with non-orthogonal eigenvectors (saddle). (b) Neutrally stable fixed point (center).

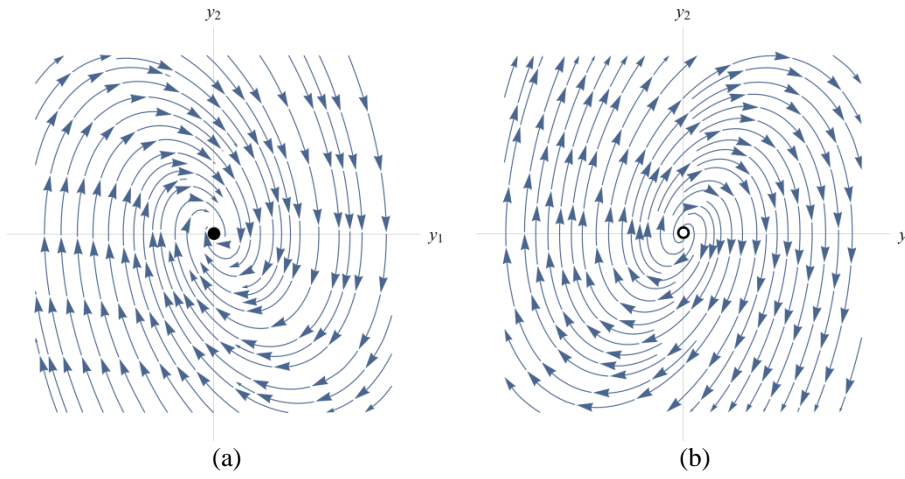


Figure 6. Stable (a) and unstable (b) spiral fixed points.

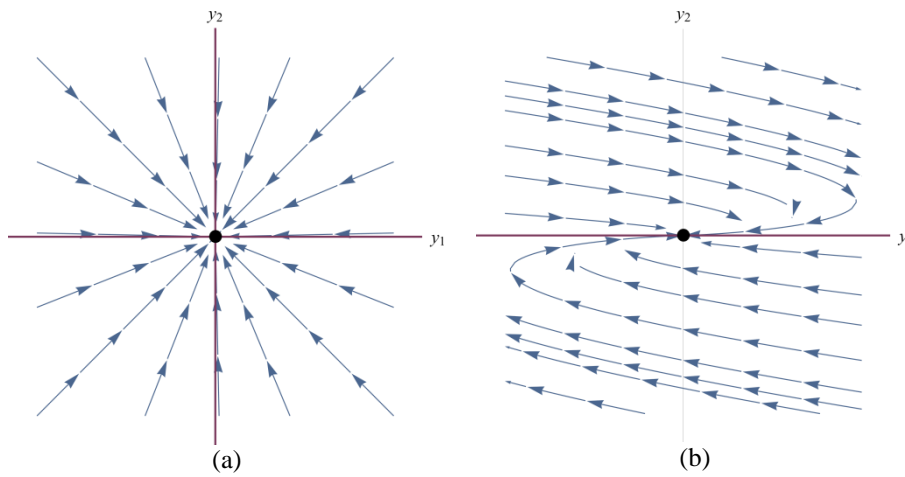


Figure 7. Degenerate cases: (a) star node and (b) degenerate node.

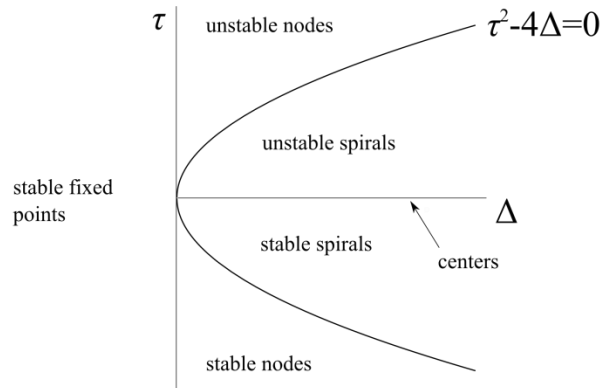


Figure 8. Classification of fixed points of a two dimensional dynamical systems.

### 3.2 Love mechanics: Romeo and Juliet

Two dimensional systems are certainly more interesting than one dimensional. While one dimensional systems can have nodes that are either stable or unstable and the solution might simply diverge or converge towards the equilibrium points, two dimensional systems involve richer dynamics, such as oscillations.

Strogatz (see [Spr04, Str88, Str94]) used a simple linear two dimensional system to describe the romantic affair between Romeo and Juliet! In his example  $y_1$  describes the love of Romeo for Juliet ( $R$ ) and  $y_2$  the love of Juliet for Romeo ( $J$ ):

$$\begin{aligned} \dot{R} &= aR + bJ \\ \dot{J} &= cR + dJ \end{aligned} \tag{17}$$

Positive values for  $J$  or  $R$  signify love and negative hate.  $J = R = 0$  signifies mutual indifference. The parameters  $a, b, c, d$  have a simple meaning as well.  $a < 0$  means that Romeo is a cautious lover. The more he realizes that he loves Juliet the more he is afraid, which reduces his affection. But if  $b > 0$  is great enough the affection of Juliet makes his feelings stronger ( $\dot{R} > 0$ ). Similarly, Juliet's love is characterized by the parameters  $c, d$ .

Let's investigate the scenario with  $a = d = 0$ ,  $b > 0$  and  $c < 0$ . Let's say that at the beginning Romeo is in love with Juliet and also Juliet with him. Though, the more Romeo loves her ( $R \uparrow$ ) the more Juliet is afraid and wants to run away ( $\dot{J} = cR < 0 \Rightarrow J < 0$ ). Romeo gets disappointed and backs off (

$\dot{R} = bJ < 0 \Rightarrow R < 0$ ). But then Juliet begins to find him again attractive ( $\dot{J} = cR > 0 \Rightarrow J > 0$ ) and after a while Romeo echoes her ( $\dot{R} = bJ > 0 \Rightarrow R > 0$ ). But then again Juliet loses her interest and so on... The sad outcome of this relation is a never ending cycle of love and hate (see Figure 5b)! If Romeo was also a cautious lover ( $a < 0$ ) then their love would end soon following a stable spiral towards the fixed point of mutual indifference  $J = R = 0$ . If Romeo was an enthusiastic lover ( $a > 0$ ) their relation would be an unstable spiral of increasing hate and love, but again if  $a > 0$  is very high the more Romeo loves Juliet the more she is afraid and draws away. However, if both Romeo and Juliet were attracted in the beginning, their love would become a love fest provided that their love characteristics  $a, b, c, d$  were such that to have an unstable node or saddle in the phase space (see Figure 5b). In other words, love is an instability!

Of course in reality the dynamics of love are much more complicated than this simple model and certainly non-linear. Non-linearities and more degrees of freedom were taken into account in [Spr04] and interesting dynamics were observed.

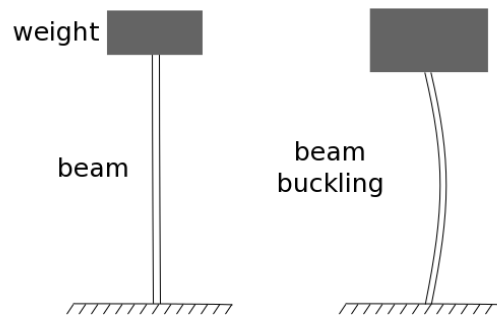


Figure 9. Sketch of beam buckling due to high load. Here, the load acts as a control (bifurcation) parameter, which determines the transition from axial deformation to a buckled, flexural state.

## 4 Common types of bifurcations

The evolution laws that we commonly use in Mechanics (and other scientific disciplines) can involve parameters that are unknown or non-constant (e.g. the loading of a beam or the elastic parameter of a spring). The dynamics of a system can significantly change with the variations of these parameters. For instance, in the example of section 2, the fixed point  $\theta_0 = 0$  becomes unstable for values of the normalized vertical load  $P^* > 1$  (see Figure 3). This is typical in many mechanical systems and central for the design of structures (see buckling of a beam due to high load, Figure 9).

In general, depending on the values of the parameters, fixed points can be created (appear) or destroyed (disappear) and/or their stability can change. These qualitative changes in the static and dynamic response of a system of equations are called *bifurcations* and the parameter values at which they first occur are called *bifurcation points*. The study of bifurcations is important since it provides the onset of instabilities and the transition across different states depending on the variation of the governing (bifurcation) parameters. In the following we will go through some of the most well-known (mathematical) bifurcation types for ODE's.

#### 4.1 Saddle-node bifurcation

The most fundamental bifurcation is the appearance and disappearance of equilibrium points for different values of a bifurcation parameter. This is the so called *saddle-node* (or *fold*) *bifurcation* of equilibria. In this case, as the parameter varies, two fixed points of the underlying system of equations move towards each other, collide and mutually annihilate. The following differential equation is a classic example of this kind of bifurcation:

$$\dot{y} = \mu + y^2 \quad (18)$$

where  $\mu$  is a real number that can admit any real value. When  $\mu$  is negative, the right-hand-side of equation (18) (equilibrium solution) has two fixed points, one stable and one unstable (see Figure 10).

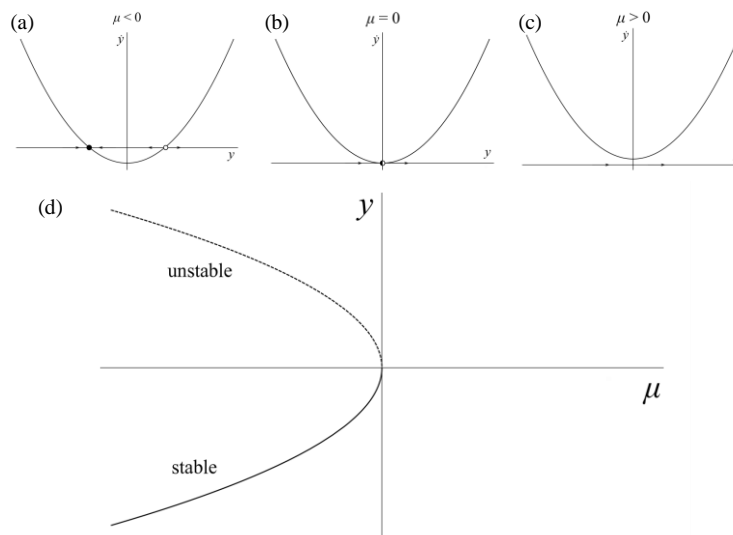


Figure 10. Saddle-node bifurcation. A half full circle denotes half stable fixed points.

As  $\mu \rightarrow 0$  from negative values, the two fixed points move towards each other and they collide to a half-stable point at  $y_0 = 0$  for  $\mu = 0$ . This is the bifurcation point, since for  $\mu > 0$  the dynamics change completely, equation (18) presents no fixed points and predicts infinite growth of  $y$  in time. This behavior is depicted in Figure 10a-c. As  $\mu$  plays the role of the independent variable, we can plot the steady state solutions of equation (18) in an  $\mu - y_0$  diagram (Figure 10d), where we can observe the number of steady state solutions in function of the parameter  $\mu$ , as well as their stability (calculated as described in section 2). As mentioned in section 2, such a diagram, where the fixed points of the equations (for a norm of the solution) are plotted against the bifurcation parameter is called *bifurcation diagram*.

Note that equation (18) along with its symmetric  $\dot{y} = \mu - y^2$ , are representative of all saddle-node bifurcations. This means that close to a saddle bifurcation, the dynamics of a given system are qualitatively the same with  $\dot{y} = \mu - y^2$  or  $\dot{y} = \mu + y^2$  (see Appendix). Equations like equation (18), which can characterize the dynamics of any system near a bifurcation point are called *normal forms* of that bifurcation.

#### 4.2 Transcritical bifurcation

The transcritical bifurcation happens when a pair of fixed points exchange stability as the bifurcation parameter varies. Its normal form is:

$$\dot{y} = \mu y - y^2 \quad (19)$$

As shown in Figure 11a-c, the point  $y_0 = 0$  is always a fixed point. Starting from negative values of  $\mu$ ,  $y_0 = 0$  is stable and there exists a second fixed point,  $y_0 = \mu$ , which is unstable. As the value of the parameter  $\mu$  increases, the second fixed point moves towards  $y_0 = 0$  and for  $\mu = 0$  (which is also the bifurcation point in this case) they collapse on a half-stable point. Upon further increasing of the parameter value, the two fixed points reappear but have opposite stability,  $y_0 = 0$  is unstable and  $y_0 = \mu$  is stable. Thus, we can say that the transcritical bifurcation is a mechanism for exchanging stability between two fixed points. This is more apparent if one observes the corresponding bifurcation diagram (Figure 11d).

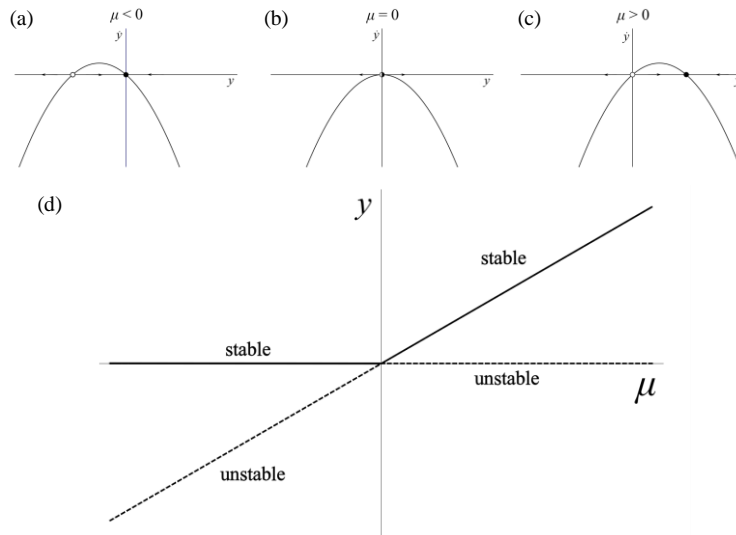


Figure 11. Transcritical bifurcation.

### 4.3 Supercritical and subcritical pitchfork bifurcation

Pitchfork bifurcation (both the super- and the sub-critical one) is common in problems that have symmetry and describe the appearance (or disappearance) of a symmetrical pair of fixed points after some critical value of the bifurcation parameter.

Revisiting the example of the buckling of a beam (see Figure 2 or Figure 9), after the load exceeds the critical threshold there exists no preferred direction for the deformation and only a defect in the mechanical problem or the perturbation itself can lead the beam to “choose” one direction or another, thus breaking its symmetry.

The normal form of the supercritical pitchfork bifurcation is:

$$\dot{y} = \mu y - y^3 \tag{20}$$

Notice that changing the variable  $y \rightarrow -y$  does not change the equation of the system. This symmetry justifies mathematically the aforementioned existence of a symmetrical pair of fixed points.

The fixed point  $y_0 = 0$  exists for all  $\mu \in \mathbb{R}$ . For  $\mu \leq 0$  it is stable. At  $\mu = 0$  the pitchfork bifurcation occurs and for  $\mu > 0$  a symmetric pair of stable fixed points

appears ( $y_0 = \pm\sqrt{\mu}$ ). Therefore, three fixed points exist ( $y_0 = \pm\sqrt{\mu}$  and  $y_0 = 0$ ) for  $\mu > 0$ .

The reason for which this type of bifurcation is called “pitchfork” becomes apparent upon observing the bifurcation diagram of Figure 12d.

The subcritical pitchfork bifurcation has the following normal form:

$$\dot{y} = \mu y + y^3 \tag{21}$$

As shown in Figure 13, the corresponding bifurcation diagram is similar to the one of Figure 12d, but the pitchfork is inverted. The pair  $y_0 = \pm\sqrt{-\mu}$  is unstable and it exists only for  $\mu < 0$ . In addition, even though the origin is a fixed point for all  $\mu \in \mathbb{R}$ , it is stable only for  $\mu < 0$ . For all  $\mu > 0$  there is no stable equilibrium solution and the system *blows up*, i.e.  $y \rightarrow \pm\infty$  as time elapses. Furthermore, one can show that the blow-up happens in finite time for all initial conditions. It is worth mentioning that this type of bifurcation is the normal form of the bifurcation of the example studied in sections 2 and 3 (see Figure 2 and Figure 3).

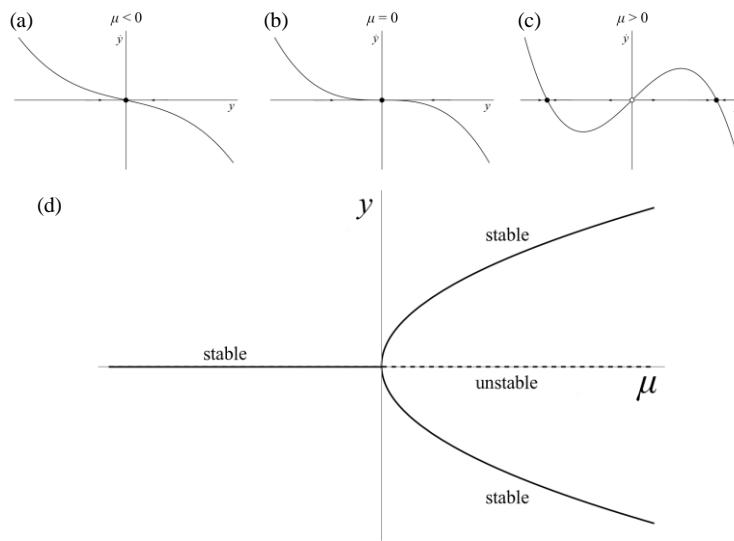


Figure 12. Supercritical pitchfork bifurcation.

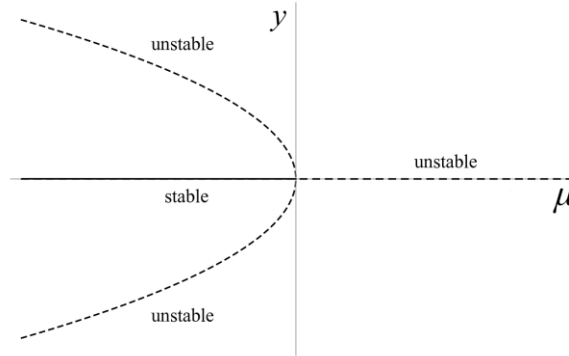


Figure 13. Bifurcation diagram of the subcritical pitchfork bifurcation.

#### 4.4 From one to two dimensions - Limit cycles

All the cases considered in the previous paragraphs concerned bifurcations of equilibrium solutions in one-dimensional problems. What about bifurcations in problems of high order?

Non-linear dynamical systems of order higher than one can present perfectly periodic solutions. Such solutions appear on the phase space as isolated closed orbits, which can attract or repel all neighboring trajectories, much like the fixed points. These orbits are called *limit cycles*. Limit cycles are an inherent phenomenon of two or higher dimensional systems that are non-linear. Even though, linear systems can present closed orbits, when the fixed point is a stable center (neutral stability, see Figure 5b), such solutions are non-isolated, i.e. if  $x(t)$  is a periodic solution, then  $c x(t)$  is also a periodic solution for all  $c \in \mathbb{R}^*$ .

An illustrative example of a system with a stable limit cycle in polar coordinates is:

$$\begin{aligned} \dot{r} &= r(1-r^2) \\ \dot{\theta} &= 1 \end{aligned} \quad (22)$$

where  $r \geq 0$ . It is easy to identify that the two equations are uncoupled and that the first one if treated alone, it has two fixed points, namely  $r=0$  (unstable) and  $r=1$  (stable). This means that all trajectories approach  $r=1$ . However, the system of two equations has no fixed points at all because  $\dot{\theta}=1 \neq 0$ .  $\dot{\theta}=1$  describes the angular velocity, which is constant. Therefore, all trajectories on the phase plane are approaching the unit circle ( $r=1$ ) monotonically. This can be visualized if we revert again to Cartesian coordinates (Figure 14 (a)), i.e.  $x(t) = r(t) \cos(\theta(t))$  and

$y(t) = r(t)\sin(\theta(t))$ . The evolution in time of the  $x$ -coordinate, for  $r(0) = 0.01$  and  $\theta(0) = 0$  is presented in Figure 14 (b). As we can see, the amplitude of the oscillations is  $r = 1$  and the period is  $T = 2\pi$ .

One of the most famous examples of equations that present limit cycles is the *van der Pol equation*,

$$\ddot{y} + \mu(y^2 - 1)\dot{y} + y = 0 \quad (23)$$

where  $\mu \geq 0$  is a parameter. In this equation, the non-linear term  $\mu(y^2 - 1)\dot{y}$  forces the oscillation. The limit cycle is no longer a circle (Figure 15a) and the waveform is not sinusoidal (Figure 15b).

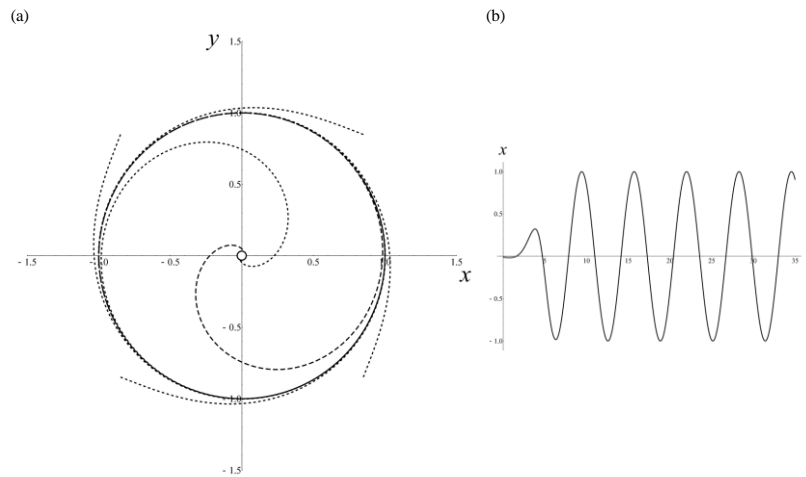


Figure 14. (a) Phase diagram of the system of Eq.22. We observe the trajectories moving towards the limit cycle of the system. (b) Evolution in time of the system of Eq.22 for  $r(0) = 0.01$  and  $\theta(0) = 0$ .

A question that follows naturally is if fixed points and limit cycles are the only possible attractors (or repellers) of the trajectories of a system of ODE's. The answer to that is negative for higher dimensions. In two dimensions, the dimensionality of the system (and thus the corresponding trajectories on the phase space) is equal to the dimensionality of the limit cycles (both equal to two) and hence all trajectories on the phase space can be attracted to either points or closed orbits. On the contrary, dynamical systems of order  $n \geq 3$  can have trajectories that might be in an open, bounded domain, yet, they can move freely inside it without settling into a fixed point or a closed orbit. They can be attracted to topological manifolds (called *stable manifolds*) or even to complex geometric objects that are called *strange attractors* or

*fractals*. The study of such complex (or chaotic) dynamics is out of the scope of the present chapter and the reader should refer to [Hal91, Str94] for a first introduction to these phenomena.

#### 4.5 Bifurcations in two dimensions - Supercritical and subcritical Hopf bifurcation

We are now ready to answer the question about bifurcations in two dimensional systems. In terms of bifurcations of fixed points, all the basic examples discussed in paragraphs 4.1-4.3 have their analogs in two (and in higher) dimensions. The corresponding normal forms in two dimensions are:

$$\begin{aligned}\dot{y}_1 &= \mu + y_1^2 \\ \dot{y}_2 &= -y_2\end{aligned}\tag{24}$$

$$\begin{aligned}\dot{y}_1 &= \mu y_1 - y_1^2 \\ \dot{y}_2 &= -y_2\end{aligned}\tag{25}$$

$$\begin{aligned}\dot{y}_1 &= \mu y_1 - y_1^3 \\ \dot{y}_2 &= -y_2\end{aligned}\tag{26}$$

$$\begin{aligned}\dot{y}_1 &= \mu y_1 + y_1^3 \\ \dot{y}_2 &= -y_2\end{aligned}\tag{27}$$

for the saddle-node, transcritical, supercritical pitchfork and subcritical pitchfork respectively. It is easy to prove that at the bifurcation point ( $\mu = 0$ ), the corresponding linearized problem has a zero eigenvalue. This means that they always involve the collision of fixed points. Furthermore, irrespectively of the dimensionality of the problem, these types of bifurcations are inherently one-dimensional phenomena in the sense that they occur on the one-dimensional unstable manifold of the unstable fixed point. There exists however another way for a fixed point to lose stability and it involves the creation or destruction of a limit cycle around it.

This case is the so-called *Hopf* (or *Andropov-Hopf*) bifurcation. Let us assume that the dynamical system at hand,  $\dot{y} = f(y, \mu)$ , has a stable fixed point. This means that the eigenvalues,  $\lambda_1, \lambda_2$ , of the Jacobian matrix of the system have negative real parts. The imaginary part is not necessarily zero. In other words the eigenvalues lie on the left half-plane of the complex plane  $\mathbb{C}$  (see Figure 16). For a two dimensional system, there are only two possible cases for its eigenvalues, either  $\lambda_1, \lambda_2 \in \mathbb{R}^-$  or they are complex conjugates. Let us then assume that there exists a value of the

parameter  $\mu = \mu_H$  for which the fixed point loses stability. In the first case, as we approach this bifurcation point by varying the parameter  $\mu$  one of the eigenvalues becomes zero. This corresponds to the cases of saddle-node, transcritical and pitch-fork bifurcations. In the second case, the pair of complex conjugate eigenvalues crosses simultaneously the imaginary axis into the right half-plane (Figure 16). The latter is the fundamental mechanism described by the Hopf bifurcation.

As mentioned before, the Hopf bifurcation describes the creation or destruction of a limit cycle around a fixed point when the latter loses stability. The first potential scenario is the creation of a limit cycle from a fixed point. In this case, for all values  $\mu < \mu_H$ , the system is stable and the fixed point is a stable spiral (Figure 6). As  $\mu$  increases it approaches and then surpasses the critical value  $\mu_H$  for which the spiral becomes unstable. This is the case of the supercritical Hopf bifurcation and its normal form is given by:

$$\begin{aligned}\dot{x} &= \mu x - y - x(x^2 + y^2) \\ \dot{y} &= x + \mu y - y(x^2 + y^2)\end{aligned}\tag{28}$$

or equivalently in polar coordinates:

$$\begin{aligned}\dot{r} &= \mu r - r^3 \\ \dot{\theta} &= 1\end{aligned}\tag{29}$$

It is worth mentioning that the unstable spiral is surrounded by a stable limit cycle. Notice that the system (29) is just a generalization of the system 22. For  $\mu < 0$  it yields that  $\dot{r} < 0$  and thus all oscillations have decreasing amplitude. This means that the only attractor is the origin and it is a stable spiral (Figure 17a). For  $\mu = 0$  the origin becomes a center. For  $\mu > 0$  as shown also in paragraph 4.4 the origin becomes an unstable spiral and is surrounded by a stable limit cycle (Figure 17b). If we consider  $x(t) = r(t)\cos(\theta(t))$  it is easy to show from the roots of  $\mu r - r^3$  that the amplitude of the oscillations is  $r = \sqrt{\mu}$  and the period  $T = 2\pi$ .

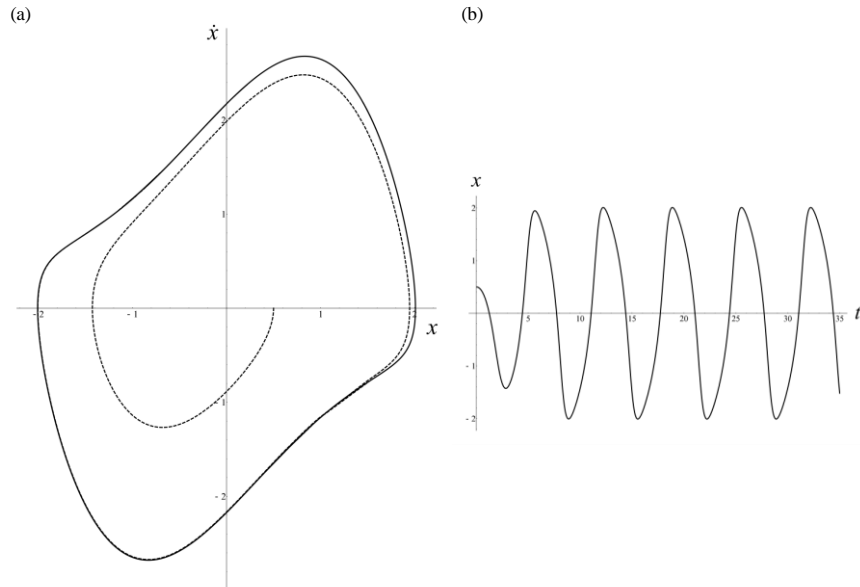


Figure 15. (a) Phase diagram of the van der Pol equation for  $\mu = 1$ . (b) Evolution of the solution of the van der Pol equation for  $y(0) = 0.5$  and  $\mu = 1$ .

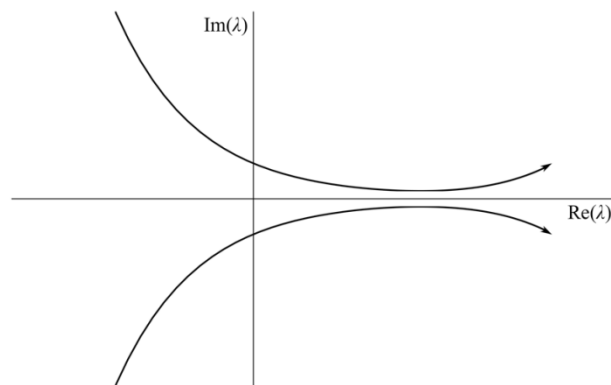


Figure 16. Sketch of a pair of complex eigenvalues crossing the imaginary axis.

We should notice here that the normal form represents the so-called *topological equivalent* of the Hopf bifurcation. This means that all limit cycles that are created by a Hopf bifurcation are equivalent (in a mathematical sense) to an oscillation of amplitude  $\sqrt{\mu}$  and period  $2\pi$  (in other words, of angular velocity  $\omega = 1$ ). Based on

the system 29 one can construct more general systems of equations that can admit different modes of sinusoidal wave forms as solutions. Such a system is:

$$\begin{aligned} \dot{r} &= \mu r - ar^3 \\ \dot{\theta} &= \omega + br^2 \end{aligned} \tag{30}$$

where  $\omega$  is the frequency of the infinitesimal oscillations (near  $\mu = 0$ ) and  $b$  describes the dependency of the frequency (and of the angular velocity) on the amplitude. For  $a > 0$  it can be shown that the amplitude is  $r = \sqrt{\mu/a}$  and the period is  $T = 2\pi / (\omega + br^2)$ .

The second potential scenario is the destruction of a limit cycle and it is called *subcritical Hopf bifurcation*. Its normal form is as follows:

$$\begin{aligned} \dot{x} &= \mu x - y + x(x^2 + y^2) \\ \dot{y} &= x + \mu y + y(x^2 + y^2) \end{aligned} \tag{31}$$

or equivalently in polar coordinates:

$$\begin{aligned} \dot{r} &= \mu r + r^3 \\ \dot{\theta} &= 1 \end{aligned} \tag{32}$$

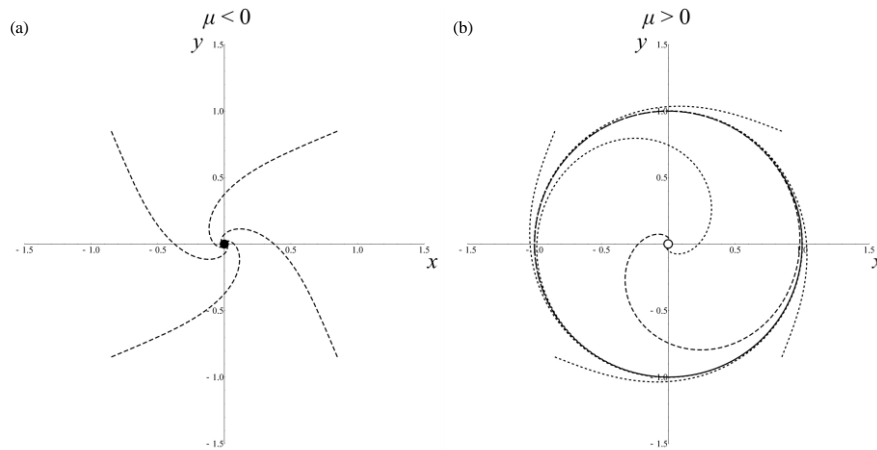


Figure 17. Phase diagram of the supercritical Hopf bifurcation. We observe the transition from a stable spiral in Figure (a) to an unstable one which is surrounded by a stable limit cycle (b).

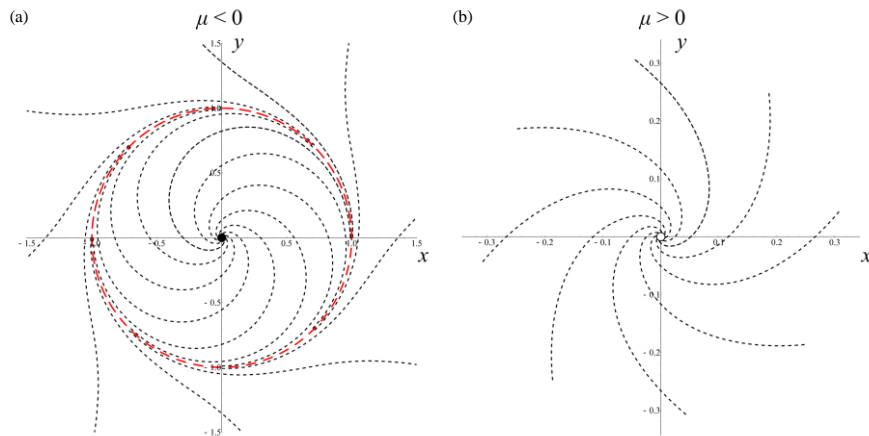


Figure 18. Phase diagram of the subcritical Hopf bifurcation. Figure (a) is for  $\mu < 0$  where we observe that origin is a stable spiral that is surrounded by an unstable limit cycle (marked with red dashed line). All trajectories starting from inside the cycle tend to the origin while those starting out of it diverge. The cycle radius decreases with increasing  $\mu$  until it collapses to the fixed point for  $\mu = 0$ . Figure (b) is for  $\mu > 0$  where we observe that there exists only the origin as a fixed point and it is an unstable spiral.

In this case, for  $\mu < 0$  the right-hand-side of the radial equation has two roots,  $r_0 = 0$  and  $r_0 = \mu$ . It is easy to show that the origin is a stable fixed point (stable spiral). However, the second root represents an unstable limit cycle for the system. This means that all trajectories that start inside the cycle move towards the origin whereas all the trajectories that start outside the cycle diverge since the cycle repels them (Figure 18a).

As the value of the parameter increases the radius of the cycle decreases and collapses to the origin for  $\mu = 0$ . For  $\mu > 0$  the limit cycle is destroyed and the origin exchanges stability with it becoming unstable (Figure 18b). This means that for  $\mu > 0$  there is no stable solution (fixed or periodic) for the system (32).

#### 4.6 Mathematical Bifurcations in PDE's

The bifurcations presented in the previous paragraphs are just indicative cases. As stated in paragraph 4.4 the higher the order of the system, the more complex the behavior can be. However, change in the number of the equilibrium solutions as well changes in the stability of equilibrium or periodic solutions are the most com-

mon and important bifurcations that can occur in systems of equations modelling problems in Mechanics. Even though the analysis was so far restricted in ODE's these mathematical bifurcations are observed in PDE's as well.

One famous example is the Bratu equation [Bra14, Gel63] here written as boundary value problem with symmetric boundary conditions and in one dimension:

$$\begin{aligned} 0 &= \frac{d^2 T(x)}{dx^2} + \lambda e^{T(x)} \\ T(-1) &= T(1) = 1 \end{aligned} \quad (33)$$

where  $x$  is the spatial coordinate and  $\lambda$  a bifurcation parameter. This equation can describe the time-independent behavior of an infinite layer under simple shear [Che89]. This means that it provides the steady state solutions ( $\frac{\partial T(x,t)}{\partial t} = 0$ ), which is the equivalent of the fixed points of ODE's. The steady state problem of equations (33) has two solutions for  $\lambda < \lambda_c$ , one for  $\lambda = \lambda_c$  and none for all  $\lambda > \lambda_c$ , where  $\lambda_c$  is the critical value of  $\lambda$  for which the bifurcation occurs. This type of bifurcation is a saddle-node bifurcation.

Notice that when dealing with PDE's, the equivalent of a fixed point is a time-independent solution which can either be homogenous (i.e. constant in space) or inhomogeneous (i.e. non-constant profile in space). One way of studying the stability of equilibrium solutions of PDE's (and their bifurcations to an extent) is using the so-called Linear Stability Analysis. An example of that method will be presented in paragraph 5.2. Such an analysis can predict the growth or decay of perturbations near an equilibrium solution, thus providing information about the stability of the equilibrium solution. By that means, one can derive when one steady state is preferred from another and determine the bifurcation point from the onset of instability. A famous example is the formation of Bénard (convection) cells in the Rayleigh-Bénard problem (Figure 19).

In this problem, there are various types of steady states and corresponding bifurcations. The critical parameter that governs these instabilities is called Rayleigh number and for low values, where conduction prevails, a linear temperature profile is predicted. Upon reaching a critical value though, a bifurcation occurs and convection becomes the dominant mechanism. In this case the flow appears to be steady in time but periodic in space (Figure 19b). For more information, the reader should refer to [Cha61] where the results of linear stability analyses for various boundary value problems of this type are presented.

In the following we will present the study of a problem that is more relevant to Geomechanics applications, the localization of shear and volumetric strain

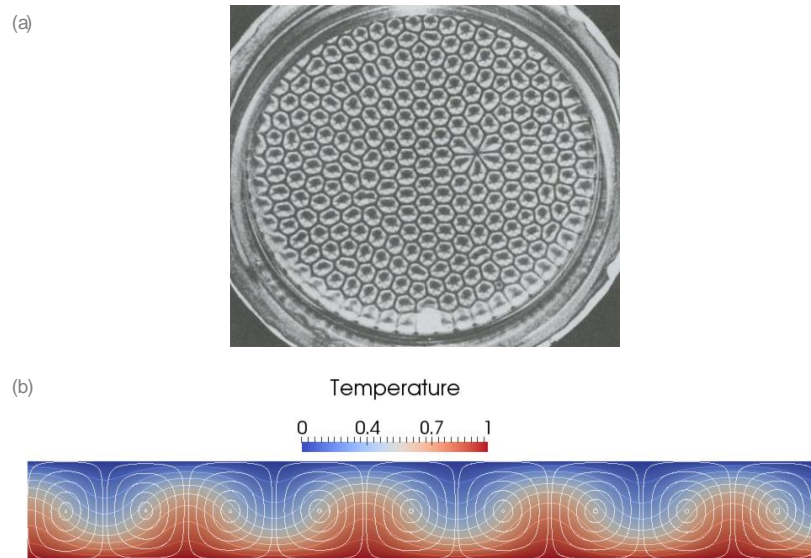


Figure 19. (a) Experiments on hydrothermal convection where the famous Bénard cells appear. (b) Streamlines and isotherms in numerical simulation of the corresponding two dimensional problem.

## 5 From ODE's to PDE's

The above sections were dedicated to the notion of stability and bifurcation focusing on ODE's. In this section we try to extend the above concepts to Partial Differential Equations (PDE's) who cover a variety of systems including mechanics of solids, in general, and geomechanics. A classical problem of bifurcation and instability is strain localization in materials. Strain localization is frequently manifested as thin bands where deformation is localized. Depending on the kinematics of strain localization three main types of deformation bands are distinguished. These are dilation (or extension) bands, shear bands and compaction bands [Ber02]. Whatever their type is, deformation bands appear at the moment that the homogeneous deformation of a system becomes an unstable equilibrium solution. In other words the system bifurcates to a non-homogeneous solution where the strain is localized. The classical approach for determining when this localization takes place is based on calculating the determinant of the acoustic tensor [Rud75].

### 5.1 Deformation bands and the acoustic tensor

Consider a homogeneous, homogeneously deformed solid subjected to quasi-static increments of deformation. Let's assume that after an increment, a deformation band

is formed, which breaks the aforementioned homogeneity of the deformation field (and consequently of the stress field) as shown in Figure 20. The displacement field remains continuous across the boundaries of the band, but its gradient does not (different strains inside the band):

$$\Delta u_i = 0 \quad \text{and} \quad \llbracket \Delta u_{i,j} \rrbracket = g_i n_j \quad (34)$$

where  $\llbracket [\cdot] \rrbracket$  denotes discontinuity across the deformation band boundary (e.g.  $\llbracket [a] \rrbracket = a^+ - a^-$ ),  $n_i$  is the orientation vector of the deformation band with  $i=1,2,3$  is the three-dimensional space,  $u_i$  the displacement field and  $\Delta$  denotes the increment of a field.  $(\cdot)_{,i}$  denotes derivation in terms of  $x_i$ .

The vector  $g_i$  describes the direction of the discontinuity and its inner product with the orientation of the band,  $n_i$ , determines the type of the deformation band (see Figure 20). In particular, if  $n_i g_i = 0$ , the deformation band is a pure shear band, if  $n_i g_i = -1$  a pure compaction band and if  $n_i g_i = +1$  a pure dilation (extension) band. The intermediate states,  $0 < n_i g_i < 1$  and  $-1 < n_i g_i < 0$  correspond respectively to dilatant and contracting shear bands.

In quasi-static conditions, the stress vector has to be continuous across the deformation band boundary:

$$\Delta t_i = \llbracket \Delta \sigma_{ij} \rrbracket n_j = 0 \quad (35)$$

Consider the class of materials that for a small increment  $\Delta$ , the constitutive law can be written (linearized) as follows:

$$\Delta \sigma_{ij} = L_{ijkl} \Delta u_{k,l} \quad (36)$$

The tensor  $L_{ijkl}$  can be continuous across the boundary of the band ( $\llbracket C_{ijkl} \rrbracket = 0$ ) or discontinuous in the sense that elastic unloading can occur outside the band, while continued inelastic loading continues within the band. In the first case we say that we have *continuous bifurcation*, while in the second *discontinuous bifurcation*. It is shown that continuous bifurcation precedes discontinuous bifurcation [Ric80].

By replacing Eq.(36) into (35) and using (34) we obtain:

$$\llbracket \Delta \sigma_{ij} \rrbracket n_j = L_{ijkl} \llbracket u_{k,l} \rrbracket n_j = n_j L_{ijkl} n_l g_k = 0 \quad (37)$$

The tensor  $\Gamma_{ik} = n_j L_{ijkl} n_l$  is called *acoustic tensor*. If its determinant is not zero, then the  $g_k$  has to be zero, which means that the deformation is continuous along the assumed deformation band. In other words no discontinuity of the gradient of the displacement field can appear across the boundary of the deformation band and the homogeneous solution prevails. Otherwise, if:

$$|\Gamma_{ik}| = 0 \quad (38)$$

the homogeneous solution ceases to be the only one and deformation bands are possible. For an orientation  $n_i$  the type of the deformation band is given by the (eigenvector  $g_i$ ).

The above condition for strain localization is independent of the material constitutive behavior as long as Eq.(36) can be written. For instance, for an elastoplastic material whose plastic behavior is a function of the first and second invariants of the stress tensor (Figure 21), Issen and Rudnicki [Iss00] (see also [Bes00]) showed that under axisymmetric compression conditions of loading strain localization is possible when the hardening modulus becomes smaller than a critical value  $h_{cr}$  for given values of  $\mu$  and  $\beta$  (see Figure 22).

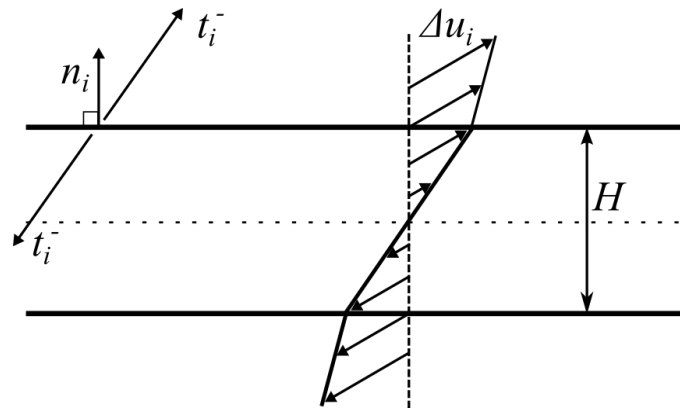


Figure 20. Schematic representation of a deformation band and of the discontinuity of the displacement field.

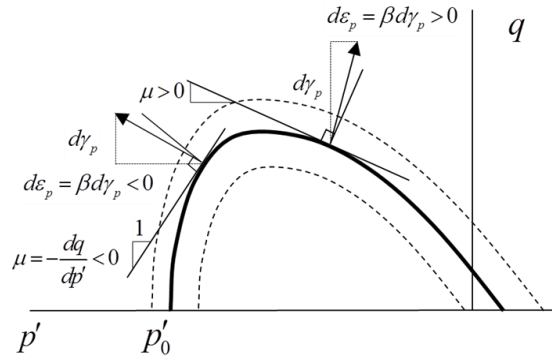


Figure 21. Elastoplastic yield envelope with hardening/softening (dotted lines). Compression is considered negative.

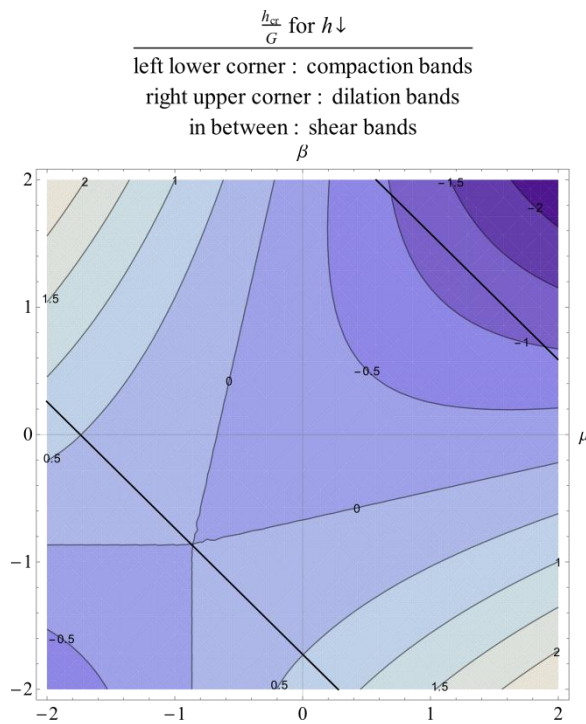


Figure 22. Critical hardening values in function of the  $\beta$  and  $\mu$  for strain localization [Iss00]. Notice that for non-associate plastic flow rule, localization can occur even with hardening ( $h_{cr} > 0$ ). The above diagram was derived by using the acoustic tensor criterion for localization (Eq.(38)).

For the above derivations we considered quasi-static conditions. If we remove this restriction, the jump of the shear stresses at the boundary of the shear band is not necessarily zero due to acceleration (not in equilibrium). From the linear momentum balance we obtain:

$$\Delta t_i = \llbracket \Delta \sigma_{ij} \rrbracket n_j = \rho c \gamma_i \quad (39)$$

where  $c$  is the velocity of a propagating discontinuity in direction  $n_i$  such that  $\llbracket [\gamma_i] \rrbracket = \llbracket [\Delta v_i] \rrbracket = c g_i$  (see Hadamard conditions on propagating discontinuities [Had03, Lem09]). Inserting Eq.(36) into (39) and using (34) we get:

$$\left( -n_j L_{ijkl} n_l - \rho c^2 \delta_{ik} \right) g_k = 0 \quad (40)$$

This equation shows that if there are accelerating waves ( $\llbracket [\gamma_i] \rrbracket = c g_i \neq 0$ ) the eigenvalues of the tensor  $-\Gamma_{ij}$  are equal to the square root of their wave velocity  $c^2$ . This is why  $\Gamma_{ij}$  is called *acoustic tensor*. The condition of localization derived in quasi-static conditions (Eq.(38)) corresponds to  $c = 0$  or in other words to the existence of stationary acceleration waves.

## 5.2 Deformation bands as an instability problem

The same condition with Eq.(38) can be derived by studying the stability of the homogeneous solution of the continuous system. In this case we do not have a system of ODE's anymore for which we saw how to investigate the stability of an equilibrium point, but a PDE. Nevertheless, the bifurcation analysis approach is similar. Stability is defined as in paragraph 2.1.

The general PDE's of the problem are:

$$\sigma_{ij,j} = \rho \ddot{u}_i \quad (41)$$

where  $\rho$  is the density of the material and the double dot represents the second time derivative (acceleration). Suppose again a homogeneous, homogeneously deformed solid that it is in equilibrium:

$$\sigma_{ij,j}^* = 0 \quad (42)$$

Considering the same class of materials that can be linearized around the above equilibrium point such as Eq.(36) to hold we get:

$$\sigma_{ij} = \sigma_{ij}^* + \Delta\sigma_{ij} = \sigma_{ij}^* + L_{ijkl}\Delta u_{k,l} \quad (43)$$

where, as in 5.1  $\Delta u_i$  is the increment in displacements, i.e.  $\Delta u_i = u_i - u_i^*$ .  $\Delta u_i$  can be seen also as a perturbation of the reference, homogeneous solution  $u_i^*$  (see paragraph 2.1). By injecting the above equation in (41) and using (42) we obtain:

$$L_{ijkl}\Delta u_{k,lj} = \rho \ddot{\Delta u}_i \quad (44)$$

Notice that  $L_{ijkl}$  is calculated at  $u_i^*$  and therefore it is independent of  $\Delta u_i$  (Taylor expansion of  $\sigma_{ij}$  around  $\varepsilon_{ij}^*$ ). Therefore, Eq.(44) is a linear PDE that can be solved by separation of variables (or Fourier transform). The linearization of the stress tensor around the equilibrium point (Eq.(36)) is central in strain localization analysis. Consequently, the conditions derived either in paragraph 5.1 or in the current one are valid as far as this linearization is possible.

Using the method of separation of variables,  $\Delta u_i = X(x_k)U_i(t)$ . Replacing in (44) we obtain:

$$L_{ijkl}X_{,lj}U_k(t) = \rho X \ddot{U}_i \quad (45)$$

This equation has sinusoidal solutions in terms of  $X$ . Moreover, we are looking for deformation bands, which are planar as shown in Figure 20. Therefore, the solution in terms of  $X$  takes the form:  $X(x_i) = e^{ikn_i x_i}$ , where  $n_i$  is the orientation vector of the deformation band as in the previous paragraph and  $k$  the wave number (of the perturbation). If  $\lambda$  is the wavelength corresponding to the wave number  $k$  ( $k = 2\pi / \lambda$ ), in order to satisfy the boundary conditions at the boundary of the deformation band  $\lambda = H / N$ , where  $N$  is a integer. Inserting  $X$  in Eq.(45) and by setting  $\dot{U}_i = V_i$  we obtain the following the following system of ordinary differential equations:

$$\begin{aligned} \dot{V}_i &= -\frac{1}{\rho} \left( \frac{2\pi}{\lambda} \right)^2 n_j L_{ijkl} n_l U_k \\ \dot{U}_i &= V_i \end{aligned} \quad (46)$$

In this way we transformed the PDE's of the problem to a system of ODE's, which we can study in the same way as in the previous sections. As shown in section 2, the above equations take solutions of the form  $U_k(t) = g_k e^{st}$ . After some algebraic manipulations the eigenvalue problem becomes:

$$\left[ -n_j L_{ijkl} n_l - \rho \left( \frac{\lambda s}{2\pi} \right)^2 \delta_{ik} \right] g_k = 0 \quad (47)$$

which is identical to (40) by setting  $c = \frac{\lambda s}{2\pi}$ . If the real part of  $\rho c^2 > 0$  then the homogeneous solution  $u_i^*$  is unstable and the system bifurcates to a non-uniform solution, a band, with direction  $n_i$ . As before, the type of the deformation band (compaction, shear, dilation band) is determined by the product  $n_i g_i$ . It is worth emphasizing that the above condition is independent of the specific constitutive law, provided that it is rate-independent. For rate dependent materials, a similar approach can be followed. The methodology is quite general and can be applied in many problems, including problems with multiphysical couplings, such as thermo-poro-chemo-mechanical couplings (e.g. [Ste14, Sul15]). Moreover, even though a Cauchy (Boltzmann) continuum was considered here, the same approach can be applied in Cosserat or even higher order continua (e.g. [Müh88, Sul11]).

If the eigenvalues of  $-\Gamma_{ij}$  do not depend on the (perturbation) wavelength  $\lambda$  and  $s$ , then the acceleration wave velocity  $c$  is constant (does not depend on  $\lambda$ ). If in addition they have a positive real part, the perturbation that propagates faster has zero wave length because  $s = 2\pi \frac{c}{\lambda}$  (for  $\lambda \rightarrow 0$ ,  $s \rightarrow \infty$ ). In other words the minor imperfection in size will propagate faster and dominate the other imperfections of larger wavelength. This is why in the classical Cauchy continuum, which has no internal lengths, the deformation band thickness is zero (the localization takes place on a mathematical plane). The fact that the smallest perturbation propagates faster justifies also the mesh dependency in Finite Element calculations. For instance, in the frame of classical simulations in elastoplasticity of Cauchy rate-independent continua with softening behavior (or even in perfect plasticity), the numerically predicted shear band thickness depends on the finite element discretization and on the element size (Figure 23).

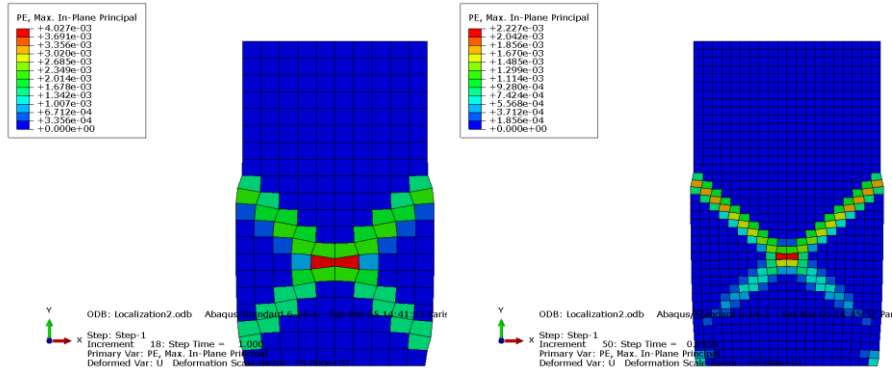


Figure 23. Shear band formation and mesh dependency for a rate-independent elastoplastic, von Mises, Cauchy medium with strain softening. The shear band thickness is always 1-2 elements thick and therefore mesh dependent. The plastic strains and the global energy dissipation are also mesh dependent. Abaqus v6.14 was used for the simulations.

## 6 Summary

The target of the present chapter was to give the basic ideas and tools of bifurcation theory and stability analysis. The definition of (Lyapunov) stability was given, as well as the fundamental theorems that allow studying the stability of linear and non-linear systems of ODE's. The notion of bifurcation was explained and illustrated through examples and a classification of the most common bifurcations and instabilities was presented. The focus was given on ODE's as their behavior is central for understanding bifurcation and stability. The study of PDE's is an extension of the ideas presented for ODE's and it was presented in the last section. The strain localization conditions of homogeneously deformed solids were derived as an example (acoustic tensor). After studying this chapter the reader would be able to distinguish the basic notions of stability and bifurcation and apply the different concepts in more complicated systems in geomechanics that are characterized of advanced constitutive law and multiphysical couplings.

## Appendix

Let  $\dot{y} = f(y, \mu)$  be a dynamical system with a bifurcation point at  $y = y_0$  for  $\mu = \mu_c$ . A Taylor expansion of the equation yields:

$$\begin{aligned} \dot{x} = & f(y_0, \mu_c) + (y - y_0) \left. \frac{\partial f}{\partial y} \right|_{(y_0, \mu_c)} + \\ & (\mu - \mu_c) \left. \frac{\partial f}{\partial \mu} \right|_{(x_0, \mu_c)} + \frac{1}{2} (y - y_0)^2 \left. \frac{\partial^2 f}{\partial y^2} \right|_{(y_0, \mu_c)} + \dots \end{aligned} \quad (48)$$

In the case of saddle-node bifurcations we have that the term  $f(y_0, \mu_c) = 0$  since  $y_0$  is a fixed point and  $\left. \frac{\partial f}{\partial y} \right|_{(y_0, \mu_c)} = 0$  by definition for this specific bifurcation. Therefore,

$$\dot{y} = a(\mu - \mu_c) + b(y - y_0)^2 + \dots \quad (49)$$

where,  $a = \left. \frac{\partial f}{\partial \mu} \right|_{(y_0, \mu_c)}$  and  $b = 1/2 \left. \frac{\partial^2 f}{\partial y^2} \right|_{(y_0, \mu_c)}$ . Thus, for  $(y, \mu)$  sufficiently close to  $(y_0, \mu_c)$  along with  $a, b \neq 0$ , we can neglect the higher order terms resulting to the normal forms:  $\dot{y} = \mu - y^2$  or  $\dot{y} = \mu + y^2$ .

## References

- [Ben00] Ahmed Benallal, Claudia Comi. On localization in saturated porous continua, *7742(00):847–853*, 2000.
- [Ben03] Ahmed Benallal, Claudia Comi. Perturbation growth and localization in uid-saturated inelastic porous media under quasi-static loadings, *51:851–899*, 2003.
- [Ber02] Xavier Du Bernard, Peter Eichhubl, Atilla Aydin. Dilation bands: A new form of localized failure in granular media, *Geophys. Res. Lett.* 29(24):2176, 2002.
- [Bes00] Pierre Besuelle, John W. Rudnicki. Localization: Shear Bands and Compaction Bands. In: , 219–322
- [Bés01] Pierre Bésuelle. Compacting and dilating shear bands in porous rock: theoretical and experimental conditions, *J. Geophys. Res.* 106(B7):13435–13442, 2001.
- [Big91a] Davide Bigoni, Tomasz Hueckel. Uniqueness and localization—I. Associative and non-associative elastoplasticity, *Int. J. Solids Struct.* 28(2):197–213, 1991.
- [Big91b] Davide Bigoni, Tomasz Hueckel. Uniqueness and localization—II. Coupled elastoplasticity, *Int. J. Solids Struct.* 28(2):215–224, 1991.
- [Bra14] G. Bratu. Sur les équations intégrales non linéaires, *Bull. la Société Mathématique Fr.* 42:113–142, 1914.
- [Bra69] F. Brauer, J.A. Nohel. *The Qualitative Theory of Ordinary Differential*

- Equations: An Introduction* : Dover Publications, 1969.
- [Cha04] René Chambon, Denis Caillerie, Gioacchino Viggiani. Loss of uniqueness and bifurcation vs instability: some remarks, *Rev. Française Génie Civ.* 8(5)–(6):517–535, 2004.
- [Cha61] S. Chandrasekhar. *Hydrodynamic and Hydromagnetic Stability - International Series of Monographs on Physics* : Oxford: Clarendon, 1961.
- [Che16] David Chelidze. *Fixed Point Eigenvalues and Phase Portrait*. URL <http://personal.egr.uri.edu/chelidz/courses/mce663/demos/FixedPointEigenvaluesAndPhasePortrait.nbp>. — The Wolfram Demonstrations Project.
- [Che89] H. Tz. Chen, A. S. Douglas, R. Malek-Madani. An asymptotic stability criterion for inhomogenous simple shear, *Q. Appl. Math.* XLVII:247–262, 1989.
- [Cro91] D.J. Crawford. Introduction to bifurcation theory, *Rev. Mod. Phys.* 63(4):991–1037, 1991.
- [Gel63] I.M. Gelfand. Some problems in the theory of quasi-linear equations, *Trans. Am. Math. Soc.* 29:295–381, 1963.
- [Had03] Jacques Hadamard. *Leçons sur la propagation des ondes et les équations de l'hydrodynamique*. Paris : Librairie Scientifique A.Hermann, 1903.
- [Hal91] J.K. Hale, H Kocak. *Dynamics and Bifurcations*. New York : Springer-Verlag, 1991.
- [Iss00] Kathleen A. Issen, John W. Rudnicki. Conditions for compaction bands in porous rock, *J. Geophys. Res.* 105(B9):21529, 2000.
- [Lem09] Jean Lemaitre, Jean-Louis Chaboche, Ahmed Benallal, Rodrigue Desmorat. *Mécanique des matériaux solides*. Paris : Dunod — ISBN 978-2-10-051623-0, 2009.
- [Lya66] Aleksandr Mikhailovich Lyapunov. *Stability of Motion*. New York : Academic Press, 1966.
- [Lya92a] Aleksandr Mikhailovich Lyapunov. *The general problem of the stability of motion*, University of Kharkov, 1892.
- [Lya92b] Aleksandr Mikhailovich Lyapunov. The general problem of the stability of motion, *Int. J. Control* 55:531–773, 1992.
- [Müh88] H.B. Mühlhaus, Ioannis Vardoulakis. The thickness of shear bands in granular materials, *Géotechnique* 38(3):331–331, 1988.
- [Per93] G Perrin, JB Leblond. Rudnicki and Rice's analysis of strain localization revisited, *J. Appl. Mech.* (93):842–846, 1993.
- [Ric76] James R Rice. The localization of plastic deformation. In: KOITER, W. T. (Hrsg.): *Theoretical and Applied Mechanics (Proceedings of the 14th International Congress on Theoretical and Applied Mechanics)*. Delft : NorthHolland Publishing Co., 207–220, 1976.
- [Ric80] James R Rice, J.W. Rudnicki. A note on some features of the theory of localization of deformation, *Int. J. Solids Struct.* 16:597–605, 1980.
- [Rud75] John W. Rudnicki, James R Rice. Conditions for the localization of deformation in pressure-sensitive dilatant materials, *J. Mech. Phys. Solids* 23(6):371–394, 1975.
- [Spr04] J C Sprott. Dynamical models of love., *Nonlinear Dynamics. Psychol.*

- Life Sci.* 8(3):303–14, 2004.
- [Ste14] Ioannis Stefanou, Jean Sulem. Chemically induced compaction bands: Triggering conditions and band thickness, *J. Geophys. Res. Solid Earth* 119(2):880–899, 2014.
- [Str88] S.-H. Strogatz. Love Affairs and Differential Equations, *Math. Mag.* 61(1), 1988.
- [Str94] S.-H. Strogatz. *Non linear dynamics and chaos* : Perseus Books, 1994.
- [Sul11] Jean Sulem, Ioannis Stefanou, Emmanuil Veveakis. Stability analysis of undrained adiabatic shearing of a rock layer with Cosserat microstructure, *Granul. Matter* 13(3):261–268, 2011.
- [Sul15] Jean Sulem, Ioannis Stefanou. Thermal and chemical effects in shear and compaction bands, *Geomech. Energy Environ.*, 2015.
- [Var95] Ioannis Vardoulakis, Jean Sulem. *Bifurcation Analysis in Geomechanics*. Glasgow : Blackie — ISBN 0203697030, 1995.
- [Vev12] Emmanuil Veveakis, Jean Sulem, Ioannis Stefanou. Modeling of fault gouges with Cosserat Continuum Mechanics: Influence of thermal pressurization and chemical decomposition as coseismic weakening mechanisms, *J. Struct. Geol.* 38:254–264, 2012.
- [Vev13] Emmanuil Veveakis, Ioannis Stefanou, Jean Sulem. Failure in shear bands for granular materials: thermo-hydro-chemo-mechanical effects, *Géotechnique Lett.* 3(April)-(June):31–36, 2013.

---

# Material instability and strain localization analysis

**Jean Sulem**

*CERMES-Laboratoire Navier, Ecole des Ponts ParisTech, Université Paris-Est, France*

---

*In this chapter, the principles of strain localization analysis as applied to geomaterials are presented. Conditions for the formation of different types of deformation bands are given. Extension of the analysis to fluid saturated porous media is also presented.*

## 1 Introduction

Failure of many engineering structures is characterized by the formation and propagation of a failure plane. Laboratory experiments as well as in field observations that the orientation of the failure plane (or fault surface) is controlled by the directions of the principal stresses. In the well-established Mohr-Coulomb's theory, the inclination  $\theta$  of the failure surface with respect to the direction of the minimum (in absolute value) principal stress is given as where  $\phi$  is the friction angle of the material. For typical values of Coulomb friction angle  $\phi$ ,  $30^\circ$  to  $50^\circ$ , values of  $\theta$  range from  $60^\circ$  to  $70^\circ$ , which is comparable with the range of observed failure plane inclinations. Mohr-Coulomb's theory is commonly used in geomechanics as the dominant feature in the behavior of geomaterials is its frictional character. The orientation of a failure surface can be deduced from the knowledge of the orientation of the principal stresses (not their magnitude) and of one material property (the internal friction angle). Inversely, the orientation of the principal stresses can be simply deduced, using Mohr-Coulomb's theory, from the orientation of the failure plane and the knowledge of the friction coefficient of the material.

Although the simplicity of this approach has made it very useful, the predictions of Mohr-Coulomb's theory have been criticized because it is commonly observed that the complete inelastic response of a material influences the conditions of incipient failure and not only one material parameter such as the internal friction angle.

Moreover for studying the response of a structure in the post-failure regime when the strength is suddenly dropping, one has to understand what failure physically means. The first observation was that what appears as a failure plane is in fact a zone of localized shear deformation. Thus the study and the modelling of strain localisation phenomena have proven to be very useful in the understanding of failure mechanisms. Based on the theoretical studies of material stability as developed by Hadamard [Had03] for elastic materials and later extended by Thomas [Tho61], Hill [Hil62] and Mandel [Man66] for inelastic materials, the localisation process is seen as an instability that can be predicted from the pre-failure constitutive behaviour of the material. The conditions for the onset of localisation are thus established by seeking the possible critical conditions for which the constitutive equations of the material (in the pre-localised stage) may allow the existence of a bifurcation point for which the deformation mode will localize into a planar band [Ric76, Var76]. In this approach, the initiation of failure in the form of the incipient of a shear band is modelled as a constitutive instability and consequently a great number of studies have been dealing with the development of appropriate constitutive relationships which can predict satisfactorily the onset of shear banding. Geomaterials are characterised by a non-associated and non-coaxial plastic behaviour and this has important effects on the localisation process [Rud75]. Numerous experimental studies on soils and rocks have been performed to understand the physical processes which control strain localization and validate the theoretical and constitutive concepts [e.g. Bés00, Des04, Sul99, Var80].

Shear band formation in the form of localized shear deformation is not the only possible localized deformation mode. Zones of localized deformation are sometimes observed in the direction normal to the maximum compressive stress as observed in highly porous rocks. These structures are interpreted as compaction bands [e.g. Bau04]. Deformation zones in the form of shear bands or compaction bands in geomaterials are observed on a very large range of scales from sub-millimetric (grain size) to kilometric scale (geological structure). The formation of deformation bands is associated with an induced heterogeneity of strength and of other material properties (e.g. porosity, grain size, pore size, permeability...) in relation with the transformation at the micro-scale of the microstructure of the rock inside the band. In geological structures, shear zones also play a major role in the nucleation of earthquakes, landslides and slope failure. They also are of prime importance in the flow of water, gas and oil in the subsurface as they can serve as conduits or barriers for fluid and heat fluxes. On the other hand, compaction bands are usually characterized by a significant reduction of the pore space, which in most cases is accompanied by an important reduction in permeability [Ols02]. Their presence can lead to largely anisotropic flow in fluid infiltrated porous rocks. Therefore, compaction bands are also of primary importance in reservoir mechanics for hydrocarbons production, CO<sub>2</sub> storage and mineral exploration.

The problem of modelling localized deformation in geomaterials is quite a challenging task, due to the difficulties which are encountered while dealing with softening materials and moving elastoplastic boundaries. It is however one of the most inter-

esting bifurcation problems [Ste16]. Asking the question of possible spontaneous change of the deformation mode for a given loading history and subsequent evolution of this secondary deformation mode, one may search for the conditions of uniqueness and stability of the corresponding boundary value problem. It turns out that the result of such analyses dealing with geomaterials depends primarily on the assumed physical non-linearities which are inherent to the underlying constitutive description and is in a lesser degree influenced by geometrical non-linearities.

It is not possible in a single paper to review the important literature published in the last forty years on the subject. We will thus choose to address some points in relation to the mathematical and physical background of bifurcation analysis as applied to geomechanics with some special emphasis on the effects of fluid and temperature.

## 2 Shear band model

Extensive presentation of shear band analysis in geomaterials can be found in [Var95] (see also [Bés04, Des02] for a review). The strain localization analysis consists in searching the incipient of a shear band in a solid as a mathematical bifurcation condition for the deformation field. Considering an infinitesimal neighborhood of a point in an elastic-plastic solid which is homogeneous as for the constitutive law and stress state, the strain localization phenomenon is understood as the appearance of a discontinuity in strain rates which marks the onset of non-uniform response. Such a bifurcation of the velocity gradient along a loading path can be caused by material destabilizing effects such as softening and lack of plastic normality in the constitutive law, as well as geometrical destabilizing effects such as large deformation affecting equilibrium equations. This bifurcation condition is obtained from (a) the constitutive relationships of the material, (b) the conditions of mechanical equilibrium across the shear band boundary and (c) the kinematic compatibility conditions which expresses that the velocity field is to be continuous (no material discontinuity). The latter condition implies that only the normal component of the velocity gradient across the shear band is discontinuous whereas the tangential one is continuous (weak discontinuity). The above conditions describe the so-called ‘continuous’ bifurcation modes. It has been shown that the critical state for continuous bifurcation precedes the one for ‘discontinuous’ bifurcation where a discontinuity of the velocity field itself (and not only its gradient) is considered [Sim93]. Non-trivial solution for the condition of continuous bifurcation is a necessary condition for the shear band existence and provides both the shear band orientation and the deformation jump across the shear band. Rudnicki and Rice [Rud75] and Rice [Ric76] have obtained solutions for realistic elasto-plastic constitutive relationships for geomaterials.

### 2.1 Strain localization criterion

According to the definition proposed by Hill [Hil62], a shear band is viewed as a thin layer that is bounded by two parallel material discontinuity surfaces of the incremental displacement gradient (Figure 1). These material discontinuity surfaces  $D^{(1)}$  and  $D^{(2)}$  are called shear-band boundaries and their distance,  $2d_B$ , is the thickness of the shear-band. Within the frame of constitutive theories without material length, the shear-band thickness  $d_B$  is undetermined.

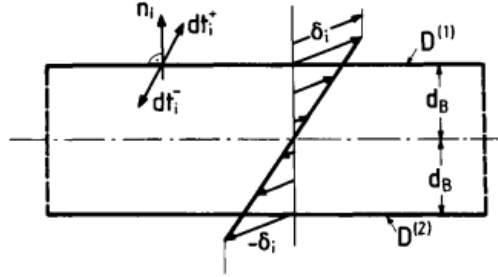


Figure 1: Model of a deforming shear-band with heat and fluid fluxes

Let denote by  $\mathbf{n}$  the unit vector normal to the band. Inside the band the incremental displacement field  $\Delta \mathbf{u}^1$  depends only on the position across the band; outside the band the rate of deformation is assumed to remain homogeneous. Assuming that the displacement field is continuous across the band, then according to Maxwell theorem, only the normal derivative of this field may be discontinuous across the band. Accordingly the following *kinematic compatibility conditions* hold:

$$[\Delta u_i] = 0 \text{ and } \left[ \partial_j \Delta u_i \right] = g_i n_j \quad (1)$$

where  $[\cdot]$  denotes the jump of the quantity across the shear band boundary. Note that as emphasized by [Bés04], the form of equation (1) requires that  $\left[ \partial_j \Delta u_i \right]$  has a vanishing intermediate eigenvalue and thus contains a plane of zero incremental displacement. Consequently, localization is favoured when the pre-bifurcation, homogeneous field contains a plane of zero extension rates, as in plane strain whereas highly destabilizing effects as strong softening behaviour is needed to generate shear band formation in axisymmetric deformation.

Incremental strains and stresses are linked through the constitutive relationships:

$$\Delta \sigma_{ij} = C_{ijkl} \partial_l \Delta u_k \quad (2)$$

Equilibrium across the shear band boundary implies the following *static compatibility condition*:

$$\left[ \Delta \sigma_{ij} \right] n_j = 0 \quad (3)$$

We observe that there are two possibilities, namely that the constitutive behaviour across the shear band boundaries is either continuous or discontinuous. Concerning discontinuous bifurcations one has to examine the possibility that elastic unloading occurs outside the shear band while continued elastic-plastic loading occurs within the band. If the elasto-plastic constitutive law admits a single smooth yield surface and plastic potential, [Ric80] have shown that continuous bifurcation analyses provide the lower limit to the range of deformations for which discontinuous bifurcations can occur. Accordingly, we restrict ourselves here to the first possibility of continuous constitutive behaviour, namely  $\left[ C_{ijkl} \right] = 0$ .

Using the constitutive relationships (2), the static compatibility condition (3) and the kinematic compatibility conditions (1), we finally obtain

$$\Gamma_{ik} g_k = 0 \quad (4)$$

where  $\Gamma_{ik} = C_{ijkl} n_j n_l$  is the acoustic tensor. It follows that weak stationary discontinuities for the incremental displacement exist only if the acoustic tensor is singular:

$$\det \Gamma = 0 \quad (5)$$

Equation (5) is the characteristic equation in terms of the direction cosines  $n_i$  of a statically, kinematically and materially admissible discontinuity surface. If the characteristic equation provides real solutions for the direction cosines  $n_i$ , discontinuity surfaces for the incremental displacement gradient exist and may also develop in due course of the deformation. Equation (5) is thus the *localization criterion*.

The vector dot product  $\mathbf{n} \cdot \mathbf{g}$  determines the nature of deformation band created at localization. The following classification describes the deformation band types (Figure 2):

$$\left\{ \begin{array}{ll} \mathbf{n} \cdot \mathbf{g} = 1 : & \text{pure dilation band} \\ 0 < \mathbf{n} \cdot \mathbf{g} < 1 : & \text{dilatant shear band} \\ \mathbf{n} \cdot \mathbf{g} = 0 : & \text{simple shear band} \\ -1 < \mathbf{n} \cdot \mathbf{g} < 0 : & \text{compactive shear band} \\ \mathbf{n} \cdot \mathbf{g} = -1 : & \text{pure compaction band} \end{array} \right. \quad (6)$$

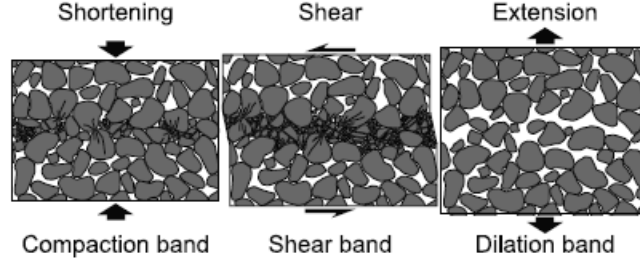


Figure 2: Localized deformation with shear, compaction and dilation modes [Ber02].

In a simple shear band the instantaneous relative movement is tangent to the band. In a dilatant (respectively compactive) shear band the angle between the unit vectors  $\mathbf{n}$  and  $\mathbf{g}$  is acute (respectively obtuse), and thus the band exhibits some form of instantaneous expansion (respectively contraction). Pure dilation and pure compaction bands exhibit little or no shear offset [Bor04].

## 2.2 Strain localization, loss of ellipticity and vanishing speed of acceleration waves

The governing equations of an incremental boundary problem are obtained from the equations of equilibrium  $\partial_j \Delta \sigma_{ij} = 0$  (for simplicity we omit here the body forces), the constitutive relationships of the form given by equation (2), and the boundary conditions (prescribed tractions or displacements at the boundary of the considered body). Incorporating the constitutive equations (2) into the equilibrium equations and assuming piecewise linear incremental constitutive equations yields the following second order differential system:

$$C_{ijkl} \partial_j \partial_l \Delta u_i = 0 \quad (7)$$

The *ellipticity condition* of the above differential system is expressed as follows:

$$\forall \mathbf{n}, C_{ijkl} n_j n_l \text{ is strictly definite positive.} \quad (8)$$

Consequently, the localization criterion (5) corresponds to the state of loss of ellipticity of the governing equations. They change type and from elliptic they turn to hyperbolic. Shear bands are thus identified with the characteristic lines of the governing hyperbolic partial differential equations.

Let us consider now the propagation of acceleration waves in a solid body along the direction  $\mathbf{n}$ . Acceleration waves are weak discontinuities of the various mechanical fields across wave-fronts which propagate with the speed  $c$ . One can show that the propagation speed  $c$  is the solution of an eigen-value problem [cf. Var95] and that  $c$  is obtained from the following equation:

$$\det(\Gamma_{ik} - \rho c^2 \delta_{ik}) \quad (9)$$

where  $\rho$  is the density of the material. Thus, if the acoustic tensor is strictly definite positive, all the velocities of acceleration waves are real. When all waves are able to propagate with real velocity, the material is stable in a dynamic sense. This is called the Hadamard's stability criterion [Had03] first established for hyperelastic materials. Consequently the localization criterion (5) corresponds to a state for which the velocity of wave propagation in the direction normal to the band is null (stationary wave).

### 3 Shear band formation in element tests on rocks

#### 3.1 Drucker-Prager model

As seen above, the localization criterion depends on the constitutive relation. The Drucker-Prager plasticity model with non-associate flow rule is commonly used for porous rocks. The yield surface and the plastic potential are expressed as

$$F = \bar{\tau} - \mu(q - \sigma); Q = \bar{\tau} + \beta\sigma \quad (10)$$

where  $\sigma = \sigma_{kk} / 3$  is the mean stress (negative in compression),  $\bar{\tau} = \sqrt{s_{ij}s_{ij} / 2}$  is the Mises equivalent stress (with  $s_{ij} = \sigma_{ij} - \sigma\delta_{ij}$ ),  $\mu$  is the friction coefficient and  $\beta$  is the dilatancy coefficient. For low-porosity rock, inelastic response is dilatant and  $\beta > 0$ ; however, compressed high-porosity rock typically experiences initial compaction, followed by either dilation or further compaction, depending upon the stress state. Negative values for the dilatancy coefficient and negative values for the friction coefficient at high mean stress can be thus observed as for cap yield surface. The critical value of the hardening modulus for which the localization is satisfied (equation (5)) is given by [Rud75]:

$$\frac{H_c}{G} = \frac{1+\nu}{9(1-\nu)}(\beta - \mu)^2 - \frac{1+\nu}{2} \left( N + \frac{\beta + \mu}{3} \right)^2 \quad (11)$$

where  $G$  is the elastic shear modulus,  $\nu$  is the Poisson's ratio,  $\mu$  is the friction coefficient and  $\beta$  is the dilatancy coefficient  $N$  is the normalized intermediate principal deviatoric stress ( $N_{ij} = s_{ij} / \bar{\tau}$ ) and varies from  $-1/\sqrt{3}$  for axisymmetric extension ( $\sigma_1 = \sigma_2 > \sigma_3$ ) to  $1/\sqrt{3}$  for axisymmetric compression ( $\sigma_1 > \sigma_2 = \sigma_3$ ). The value  $N=0$  corresponds to pure shear ( $\sigma_1 = -\sigma_3, \sigma_2 = 0$ ). The shear band is in a plane parallel to the intermediate principal stress and its normal is inclined with an angle

$\theta_B$  with respect to the  $\sigma_3$  - direction (most compressive direction) expressed as [Rud98]:

$$\theta_B = \frac{\pi}{4} + \frac{1}{2} \arcsin \alpha, \text{ with } \alpha = \frac{(2/3)(1+\nu)(\beta+\mu) - N(1-2\nu)}{\sqrt{4-3N^2}} \quad (12)$$

The above equations give the largest critical value of the hardening modulus and the shear band orientation as established by [Rud75]. As mentioned by Perrin and Leblond [Per93], these solutions are valid only if  $|\alpha| \leq 1$ , thus when the magnitude of  $\mu+\beta$  is small enough

$$\frac{N(1-2\nu) - \sqrt{4-3N^2}}{2(1+\nu)/3} \leq \beta + \mu \leq \frac{N(1-2\nu) + \sqrt{4-3N^2}}{2(1+\nu)/3} \quad (13)$$

The case for which  $\beta + \mu > \frac{N(1-2\nu) + \sqrt{4-3N^2}}{2(1+\nu)/3}$  corresponds to the formation of dilation bands in the direction normal to the least compressive principal stress,  $\theta_B = \pi/2$ , whereas, the case for which  $\beta + \mu < \frac{N(1-2\nu) - \sqrt{4-3N^2}}{2(1+\nu)/3}$  corresponds to the formation of compaction bands in the direction parallel to the least compressive principal stress,  $\theta_B = 0$  [Iss00]. The corresponding critical hardening modulus has the form

$$\frac{H_c^k}{G} = \frac{1+\nu}{9(1-\nu)} (\beta - \mu)^2 - \frac{1+\nu}{1-\nu} \left( \frac{1}{2} N_k - \frac{\beta + \mu}{3} \right)^2 - \left( 1 - \frac{3}{4} N_k^2 \right) \quad (14)$$

where  $k = 1$  for the dilation bands and  $k = 3$  for the compaction bands and  $N_1$  and  $N_3$  are the least and most compressive principal values of the normalized deviatoric stress tensor. These solutions for the critical hardening modulus and the orientation of the band are continuous over the limits of equation (13).

For plane strain deformation an approximate solution for the shear band inclination (equation (12)) has been given by [Var80]:

$$\theta_B = \frac{\pi}{4} + \frac{\phi_p}{4} + \frac{\psi_p}{4} \quad (15)$$

where  $\phi_p$  and  $\psi_p$  are respectively the friction angle and the dilatancy angle at peak values. This expression was first proposed by [Art77] on the basis of experimental observations.

### 3.2 Non coaxial plasticity

In classical flow theory of plasticity, the direction of the plastic deformation is fixed with respect to the normal to the plastic potential. Consequently, the direction is fixed by the current state of stress and does not depend upon the direction of the stress increment. The plastic deformation rate possesses the same principal axes as the stress tensor, which means that it is coaxial to the stress tensor. This is a strong assumption and its consequences on the prediction of shear localization have been discussed in many papers [e.g. Pap95, Rud75, Var80]. In order to arrive to better predictions for shear-band formation, one has to abandon the concept of classical coaxial plasticity flow rule and resort to *hypoplasticity* flow rules, which consider one way or the other the effect of stress rate. Rudnicki & Rice [Rud75] have considered the contribution of a non-coaxial term motivated by a yield vertex plasticity model. Other examples of non-coaxial constitutive models have been proposed in the form of a deformation theory of plasticity [e.g. Sul90, Ver86]. More generally, the incrementally non-linear laws of Darve [Dar85] and Chambon and Desrues, [Des89] developed for granular soils and rocks are non-coaxial.

These modifications of the plasticity flow rule result in significant changes in material response for non-proportional loading paths [Bés04, Des02].

### 3.3 Cataclastic shear banding

At high confinement, suppressed dilatancy may lead to grain crushing or *cataclasis* inside the shear band [Bie02] as shown in Figure 3 which in turn leads to substantial porosity and permeability reduction [Sul06]. At large scale, similar phenomena are observed in faulted zones when sheared. Usually in fault zones, two main domains can be identified: a fault core of small thickness constituted of highly comminuted ultra-cataclasites is surrounded with a damage zone which consists of fractured host rock [e.g. Che98]. The ultracataclastic structure is the results of numerous earthquake ruptures. As shown for example in a recent study of [Sul04] dedicated to the characterisation of Aigion fault material in the Gulf of Corinth (Greece), the permeability of the fault core is very low so that this zone acts as an impervious barrier to transverse fluid flow, whereas the highly fractured damage zone around acts mostly as conduits for nearly along-strike flow. Similar observations can be found in the work of Wibberley and Shimamoto [Wib02].

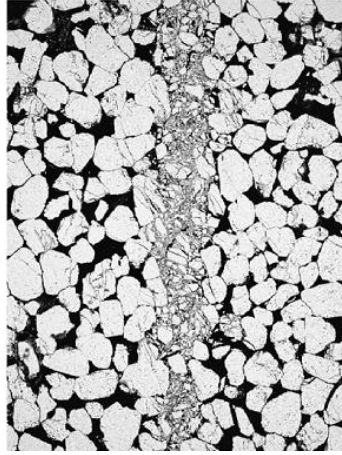


Figure 3: Cataclastic shear banding in Fontainebleau sandstone (El Bied et al. 2002)

### 3.3 Post-localization behavior

The various drawbacks and shortcomings of the classical continuum theory in connection with strain localization are related to the fact that in the post-bifurcation regime we deal in general with mathematically ill-posed governing equations. The origin of this undesirable situation can be traced back to the fact that conventional constitutive models do not contain material parameters with dimension of length, so that the shear band thickness (i.e. the extent of the plastically softening region) is undetermined. We can say that localization of deformation leads to a change in scale of the problem so that phenomena occurring at the scale of the grain cannot be ignored anymore in the modelling of the macroscopic behaviour of the material. Then it appears necessary to resort to continuum models with microstructure to describe correctly localization phenomena. These generalized continua usually contain additional kinematical degrees of freedom (Cosserat continuum) and/or higher deformation gradients (higher grade continuum). Cosserat continua and higher grade continua belong to a general class of constitutive models which account for the materials micro-structure. The contemporary formulation of these models are based on the work of Mindlin [Min64], Germain [Ger73a, Ger73b]. Rotation gradients and higher velocity gradients introduce a material length scale into the problem, which as already mentioned is necessary for the correct modeling of localization phenomena. This idea was widely publicized by the paper of Mühlhaus and Vardoulakis [Müh87]. In this case the underlying mathematical problem describing localization phenomena is 'regularized' and the governing equations remain elliptic. Moreover, this technique allows robust computations to follow the evolution of the considered system in the post-bifurcation regime and to extract additional information such as the shear band thickness or to assess the effect of scale. In the two last decades, large

scale numerical simulations which account for higher order continuum effects have been developed [Col06, Col16, Mat02, Pap16a, Pap16b, Pap92, Zer01].

## 4 Strain localization in fluid saturated porous media

### 4.1 Strain localization criterion in fluid saturated porous media

The rate constitutive equations for saturated porous elastic-plastic media can be written in the following two alternative forms [Ben03, Cou04]:

$$\begin{aligned}\dot{\boldsymbol{\sigma}} &= \mathbf{C}^d \dot{\boldsymbol{\varepsilon}} - \mathbf{K} \dot{p} \\ \dot{\boldsymbol{\sigma}} &= \mathbf{C}^u \dot{\boldsymbol{\varepsilon}} - \frac{1}{D} \mathbf{K} \dot{\zeta}\end{aligned}\quad (16)$$

where  $\mathbf{C}^d$  is the drained tangent modulus related to the stress rate under drained conditions (constant pore pressure  $p$ ) and  $\mathbf{C}^u$  is the undrained tangent modulus related to the stress rate under undrained conditions (constant fluid content  $\zeta$ )

$$\begin{aligned}\mathbf{C}^d &= \mathbf{C}_e^d - \frac{1}{H^d} \left( \mathbf{C}_e^d : \frac{\partial F}{\partial \boldsymbol{\sigma}} \otimes \frac{\partial Q}{\partial \boldsymbol{\sigma}} : \mathbf{C}_e^d \right) \\ \mathbf{C}^u &= \mathbf{C}_e^u - \frac{1}{H^u} \left( \mathbf{C}_e^u : \left( \frac{\partial F}{\partial \boldsymbol{\sigma}} - \frac{bM}{3K^u} \frac{\partial F}{\partial p} \mathbf{1} \right) \otimes \left( \frac{\partial Q}{\partial \boldsymbol{\sigma}} - \frac{bM}{3K^u} \frac{\partial Q}{\partial p} \mathbf{1} \right) : \mathbf{C}_e^u \right)\end{aligned}\quad (17)$$

In the above equations,  $\mathbf{C}_e^d$  (resp.  $\mathbf{C}_e^u$ ) is the drained (resp. undrained) elastic tensor,  $F$  is the yield function,  $Q$  is the plastic potential,  $b$  is the Biot elastic coefficient,  $M$  is the Biot modulus,  $K^u$  is the undrained elastic bulk modulus, with

$$\begin{aligned}H^d &= \frac{\partial Q}{\partial \boldsymbol{\sigma}} : \mathbf{C}_e^d : \frac{\partial F}{\partial \boldsymbol{\sigma}} + h^d \\ H^u &= H^d + \frac{1}{N} (\mathbf{K} \otimes \mathbf{L}) \\ \mathbf{K} &= b \mathbf{1} + \frac{1}{H^d} \left( \frac{\partial Q}{\partial p} - b \frac{\partial Q}{\partial \boldsymbol{\sigma}} : \mathbf{1} \right) \mathbf{C}_e^d : \frac{\partial F}{\partial \boldsymbol{\sigma}} \\ \mathbf{L} &= b \mathbf{1} + \frac{1}{H^d} \left( \frac{\partial F}{\partial p} - b \frac{\partial F}{\partial \boldsymbol{\sigma}} : \mathbf{1} \right) \frac{\partial f}{\partial \boldsymbol{\sigma}} : \mathbf{C}_e^d \\ D &= \frac{1}{M} + \frac{1}{H^d} \left( \frac{\partial F}{\partial p} - b \frac{\partial F}{\partial \boldsymbol{\sigma}} : \mathbf{1} \right) \left( \frac{\partial Q}{\partial p} - b \frac{\partial Q}{\partial \boldsymbol{\sigma}} : \mathbf{1} \right)\end{aligned}\quad (18)$$

and  $h^d$  is the drained plastic hardening modulus.

The stability of homogeneous deformation is investigated by considering an infinitesimal perturbation  $\delta\mathbf{X}$  to the set  $\mathbf{X}$  of all fields describing the response of the medium (displacements, stresses, pore pressure, etc.). The perturbation field is written in the form of  $\delta\mathbf{X} = \tilde{\mathbf{X}} \exp(i\xi\mathbf{n}\cdot\mathbf{x} + st)$  where  $\mathbf{n}$  is a unit vector,  $\xi$  is a wave-number,  $s$  is the rate of growth of the perturbation. Instability in the form of unbounded growth of the perturbation occurs when the following condition is met [Ben03]:

$$sD \det[\mathbf{n}\cdot\mathbf{H}^u\cdot\mathbf{n}] + k\xi^2 \det[\mathbf{n}\cdot\mathbf{H}^d\cdot\mathbf{n}] = 0 \quad (19)$$

where  $k$  is the permeability of the medium. Thus the rate of growth  $s$  is given by:

$$s = -\frac{k\xi^2 \det[\mathbf{n}\cdot\mathbf{H}^d\cdot\mathbf{n}]}{D \det[\mathbf{n}\cdot\mathbf{H}^u\cdot\mathbf{n}]} = 0 \quad (20)$$

From the above equation, it is seen that unbounded growth of the perturbation occurs whenever for some directions  $\mathbf{n}$  we have:

$$\det[\mathbf{n}\cdot\mathbf{H}^d\cdot\mathbf{n}] \cdot \det[\mathbf{n}\cdot\mathbf{H}^u\cdot\mathbf{n}] < 0 \quad (21)$$

Therefore, strain localization occurs when the drained or the undrained acoustic tensor becomes singular:

$$\begin{aligned} \det[\mathbf{n}\cdot\mathbf{H}^d\cdot\mathbf{n}] &= 0 \\ \text{or} & \\ \det[\mathbf{n}\cdot\mathbf{H}^u\cdot\mathbf{n}] &= 0 \end{aligned} \quad (22)$$

Thus the two conditions must be checked on the real deformation path (which is not necessarily drained or undrained.) to infer which one is met first. For associative behavior, it is shown that the singularity of the drained acoustic tensor occurs before the singularity of the undrained acoustic tensor which means that instability occurs when the condition of localization of the underlying drained deformation is met [Ben00]. On the other hand, for non-associative behavior, instability is controlled either by the drained or the undrained properties, depending on the constitutive equations and on the loading path.

## 4.2 Drucker-Prager model for saturated porous medium

For saturated porous media, the Drucker-Prager yield surface and plastic potential are expressed as:

$$F = \bar{\tau} - \mu(q - (\sigma + p_f)); Q = \bar{\tau} + \beta(\sigma + p_f) \quad (23)$$

The drained and undrained tangent moduli for the constitutive equations of a Drucker-Prager elasto-plastic model are

$$\begin{aligned}\mathbf{C}^d &= \mathbf{C}_e^d - \frac{\left(G \frac{\mathbf{s}}{\bar{\tau}} + K^d \beta \mathbf{1}\right) \otimes \left(G \frac{\mathbf{s}}{\bar{\tau}} + K^d \mu \mathbf{1}\right)}{h^u + G + K^d \mu \beta} \\ \mathbf{C}^u &= \mathbf{C}_e^u - \frac{\left(G \frac{\mathbf{s}}{\bar{\tau}} + K^u \beta^u \mathbf{1}\right) \otimes \left(G \frac{\mathbf{s}}{\bar{\tau}} + K^u \mu^u \mathbf{1}\right)}{h^u + G + K^u \mu^u \beta^u}\end{aligned}\quad (24)$$

where

$$K^u = K^d + b^2 M, \quad \mu^u = \mu \left(1 - \frac{bM}{K^u}\right), \quad \beta^u = \beta \left(1 - \frac{bM}{K^u}\right) \quad (25)$$

$K^u$  and  $K^d$  are the drained and undrained elastic bulk moduli respectively,  $b$  is the Biot coefficient,  $M$  is the Biot modulus and  $\frac{bM}{K^u} = B$  (Skempton coefficient). The undrained hardening modulus  $h^u$  is given by:

$$h^u = h^d + M \mu \beta \frac{K^d}{K^u} \quad (26)$$

In Figure 4, we represent the critical conditions for drained and undrained behavior assuming associative flow rule (Figure 4a) or non-associative flow rule (Figure 4b). Figure 4a shows that the singularity of the drained acoustic tensor precedes the one of the undrained tensor. On the contrary, Figure 4b shows that depending on the loading path (represented by parameter  $N$ ), the singularity of the undrained tensor may precedes the one of the drained tensor.

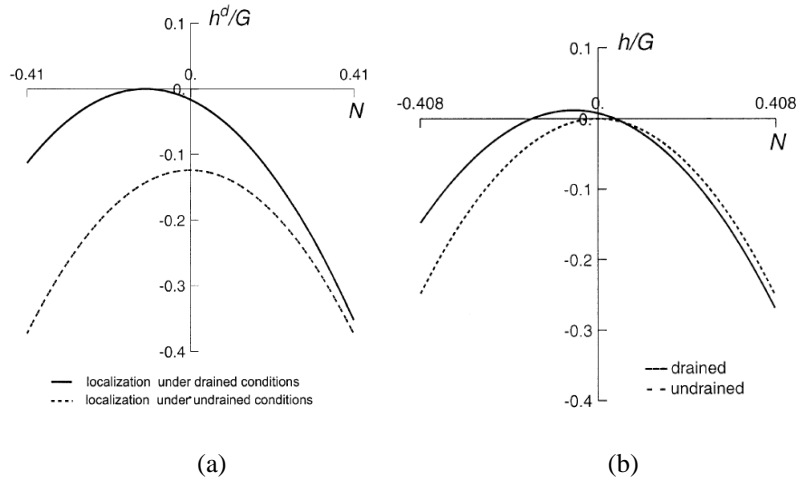


Figure 4: Critical hardening modulus at localization under drained and undrained conditions for (a) associative flow rule, (b) non associative flow rule ( $E = 60$  MPa,  $\nu = 0.3$ ,  $M = 7500$  MPa,  $b = 1$ ,  $\mu = 0.08$ ,  $\beta = 0$ ) [Ben03].

## 5 Conclusion

Bifurcation analysis and localization theory constitute the basis of contemporary continuum theory of failure as a natural extension of classical theory of strength of materials. The basic notions in relation with the shear band model are presented. The bifurcation condition corresponds to the singularity of the acoustic tensor. It is shown that the localization criterion corresponds to a state for which the velocity of wave propagation in the direction normal to the band is null. Extension to saturated fluid saturated media is presented. For associative behavior, it is shown that instability occurs when the condition of localization of the underlying drained deformation is met. On the other hand, for non-associative behavior, instability is controlled either by the drained or the undrained properties, depending on the constitutive equations and on the loading path.

## References

- [Art77] J. R. F. Arthur, T. Dunstan, K. S. Chua. Induced anisotropy in a sand, *Géotechnique* 27(1):13–30, 1977.
- [Bau04] Patrick Baud, Emmanuelle Klein, Teng Fong Wong. Compaction localization in porous sandstones: spatial evolution of damage and acoustic emission activity, *J. Struct. Geol.* 26(4):603–624, 2004.
- [Ben00] Ahmed Benallal, Claudia Comi. On localization in saturated porous

- continua, 7742(00):847–853, 2000.
- [Ben03] Ahmed Benallal, Claudia Comi. Perturbation growth and localization in uid-saturated inelastic porous media under quasi-static loadings, 51:851–899, 2003.
- [Ber02] Xavier Du Bernard, Peter Eichhubl, Atilla Aydin. Dilation bands: A new form of localized failure in granular media, *Geophys. Res. Lett.* 29(24):2176, 2002.
- [Bés00] P Bésuelle, J Desrues, S Raynaud. Experimental characterisation of the localisation phenomenon inside a Vosges sandstone in a triaxial cell, *Int. J. Rock Mech. Min. Sci.* 37(8):1223–1237, 2000.
- [Bés04] Pierre Bésuelle, John W. Rudnicki. Localization: Shear Bands and Compaction Bands. In: , 219–321, 2004.
- [Bie02] A El Bied, Jean Sulem, F Martineau. Microstructure of shear zones in Fontainebleau sandstone, *Int. J. Rock Mech. Min. Sci.* 39(7):917–932, 2002.
- [Bor04] Ronaldo I. Borja, Atilla Aydin. Computational modeling of deformation bands in granular media. I. Geological and mathematical framework, *Comput. Methods Appl. Mech. Eng.* 193(27)–(29):2667–2698, 2004.
- [Che98] Frederick M. Chester, Judith S. Chester. Ultracataclasite structure and friction processes of the Punchbowl fault, San Andreas system, California, *Tectonophysics* 295(1)–(2):199–221, 1998.
- [Col06] F. Collin, R. Chambon, R. Charlier. A finite element method for poro mechanical modelling of geotechnical problems using local second gradient models, *Int. J. Numer. Methods Eng.* 65(11):1749–1772, 2006.
- [Col16] F. Collin, P. Kotronis, B Pardoën. Numerical modelling of Multiphysics couplings and strain localization. In: *Numerical modeling of bifurcation: Applications to borehole stability, multilayer buckling, and rock bursting*, 2016.
- [Cou04] Olivier Coussy. *Poromechanics* : Wiley — ISBN 0470849207, 2004.
- [Dar85] Félix Darve. *Les lois incrementales non-linéaires, Manuel de rhéologie des géomatériaux*. Paris : Presse des Ponts et Chaussées, 1985.
- [Des02] Jacques Desrues, René Chambon. Shear band analysis and shear moduli calibration, *Int. J. Solids Struct.* 39(13)–(14):3757–3776, 2002.
- [Des04] Jacques Desrues, Gioacchino Viggiani. Strain localization in sand: an overview of the experimental results obtained in Grenoble using stereophotogrammetry, *Int. J. Numer. Anal. Methods Geomech.* 28(4):279–321, 2004.
- [Des89] J. Desrues, R. Chambon. Shear band analysis for granular materials: The question of incremental non-linearity, *Ingenieur-Archiv* 59(3):187–196, 1989.
- [Ger73a] P. Germain, E.H. Lee. On shock waves in elastic-plastic solids, *J. Mech. Phys. Solids* 21(6):359–382, 1973.
- [Ger73b] P. Germain. The Method of Virtual Power in Continuum Mechanics. Part 2: Microstructure, *SIAM J. Appl. Math.* 25(3):556–575, 1973.
- [Had03] Jacques Hadamard. *Leçons sur la propagation des ondes et les équations de l'hydrodynamique*. Paris : Librairie Scientifique A.Hermann, 1903.
- [Hil62] R. Hill. Acceleration waves in solids, *J. Mech. Phys. Solids* 10(1961):1–16,

- 1962.
- [Iss00] Kathleen A. Issen, John W. Rudnicki. Conditions for compaction bands in porous rock, *J. Geophys. Res.* 105(B9):21529, 2000.
- [Man66] J Mandel. Conditions de Stabilité et Postulat de Drucker. In: *Rheology and Soil Mechanics / Rhéologie et Mécanique des Sols* : International Union of Theoretical and Applied Mechanics, 55–68, 1966.
- [Mat02] Takashi Matsushima, René Chambon, Denis Caillerie. Large strain finite element analysis of a local second gradient model: application to localization, *Int. J. Numer. Methods Eng.* 54(4):499–521, 2002.
- [Min64] R.D. Mindlin. Micro-structure in linear elasticity, *Arch. Ration. Mech. Anal.* 16(1), 1964.
- [Müh87] H.B. Mühlhaus, Ioannis Vardoulakis. The thickness of shear bands in granular materials, *Géotechnique* 37(3):271–283, 1987.
- [Ols02] William A. Olsson, David Holcomb, John W. Rudnicki. Compaction Localization in Porous Sandstone: Implications for Reservoir Mechanics, *Oil Gas Sci. Technol.* 57(5):591–599, 2002.
- [Pap16a] Panos Papanastasiou, Antonis Zervos. Numerical modelling of strain localization. In: *Modelling of instabilities and bifurcation in Geomechanics, ALERT geomaterials doctoral school*, 2016.
- [Pap16b] Euripides Papamichos. Numerical modeling of bifurcation: Applications to borehole stability, multilayer buckling, and rock bursting. In: *Modelling of instabilities and bifurcation in Geomechanics, ALERT geomaterials doctoral school*, 2016.
- [Pap92] Panos C. Papanastasiou, Ioannis G. Vardoulakis. Numerical treatment of progressive localization in relation to borehole stability, *Int. J. Numer. Anal. Methods Geomech.* 16(6):389–424, 1992.
- [Pap95] E. Papamichos, Ioannis Vardoulakis. Shear band formation in sand according to non-coaxial plasticity model, *Géotechnique* 45(4):649–661, 1995.
- [Per93] G Perrin, JB Leblond. Rudnicki and Rice’s analysis of strain localization revisited, *J. Appl. Mech.* (93):842–846, 1993.
- [Ric76] James R Rice. The localization of plastic deformation. In: KOITER, W. T. (Hrsg.): *Theoretical and Applied Mechanics (Proceedings of the 14th International Congress on Theoretical and Applied Mechanics)*. Delft : NorthHolland Publishing Co., 207–220, 1976.
- [Ric80] James R Rice, J.W. Rudnicki. A note on some features of the theory of localization of deformation, *Int. J. Solids Struct.* 16:597–605, 1980.
- [Rud75] John W. Rudnicki, James R Rice. Conditions for the localization of deformation in pressure-sensitive dilatant materials, *J. Mech. Phys. Solids* 23(6):371–394, 1975.
- [Rud98] John W. Rudnicki, William A. Olsson. Reexamination of fault angles predicted by shear localization theory, *Int. J. Rock Mech. Min. Sci.* 35(4)–(5):512–513, 1998.
- [Sim93] J. C. Simo, J. Oliver, F. Armero. An analysis of strong discontinuities induced by strain-softening in rate-independent inelastic solids, *Comput. Mech.* 12(5):277–296, 1993.

- [Ste16] Ioannis Stefanou, S. Alevizos. Fundamentals of bifurcation theory and stability analysis. In: *Modelling of instabilities and bifurcation in Geomechanics, ALERT geomaterials doctoral school*, 2016.
- [Sul04] Jean Sulem, Ioannis Vardoulakis, Hichem Ouffroukh, Marc Boulon, Julien Hans. Experimental characterization of the thermo-poro-mechanical properties of the Aegion Fault gouge, *Comptes Rendus - Geosci.* 336:455–466, 2004.
- [Sul06] Jean Sulem, Hichem Ouffroukh. Shear banding in drained and undrained triaxial tests on a saturated sandstone: Porosity and permeability evolution, *Int. J. Rock Mech. Min. Sci.* 43(2):292–310, 2006.
- [Sul90] J. Sulem, I. Vardoulakis. Bifurcation analysis of the triaxial test on rock specimens. A theoretical model for shape and size effect, *Acta Mech.* 83(3)–(4):195–212, 1990.
- [Sul99] Jean Sulem, Ioannis Vardoulakis, Euripides Papamichos, Ahmed Oulahna, Johan Tronvoll. Elasto-plastic modelling of Red Wildmoor sandstone, *Mech. Cohesive-frictional Mater.* 4(3):215–245, 1999.
- [Tho61] T.Y. Thomas. *Plastic flow and fracture in solids* : Academic Press, 1961.
- [Var76] Ioannis Vardoulakis. Equilibrium theory of the shear bands in plastic bodies, *Mech. Res. Commun.* 3, 1976.
- [Var80] Ioannis Vardoulakis. Shear band inclination and shear modulus of sand in biaxial tests, *Int. J. Numer. Anal. Methods Geomech.* 4(January 1979):103–119, 1980.
- [Var95] Ioannis Vardoulakis, Jean Sulem. *Bifurcation Analysis in Geomechanics*. Glasgow : Blackie — ISBN 0203697030, 1995.
- [Ver86] P.A. Vermeer, G.J. Schotman. An extension to the deformation theory of plasticity. In: *2nd International Symposium Numerical Models in Geomechanics* : Jackson and Son, 33–41, 1986.
- [Wib02] Christopher A J Wibberley, Toshihiko Shimamoto. Internal structure and permeability of major strike-slip fault zones: The Median Tectonic Line in Mie Prefecture, Southwest Japan, *J. Struct. Geol.* 25:59–78, 2002.
- [Zer01] A. Zervos, P. Papanastasiou, I. Vardoulakis. Modelling of localisation and scale effect in thick-walled cylinders with gradient elastoplasticity, *Int. J. Solids Struct.* 38(30)–(31):5081–5095, 2001.



---

# Experimental investigation of the emergence of strain localization in geomaterials

**P. Bésuelle, P. Lanatà**

*Univ. Grenoble Alpes & CNRS, Lab. 3SR, Grenoble, France*

---

*Failures of geomaterials, including soils, rocks and concretes, are generally associated with a localized deformation. For about 40 years, strain localization phenomena have been investigated experimentally in different materials. Most of these studies have been motivated by the theoretical background of shear band analysis using bifurcation theory. Strain field measurements have been developed to characterize strain localization, especially for sand specimens. Full field methods, imaging tools and experimental loading apparatus have evolved considerably over past 15 years. This chapter looks at on the contributions of recent developments on the characterization of the strain localization process. The emergence of strain localization involves the progressive evolution from diffuse to localized deformation. The text introduces the methods used and then shows some selected experimental results obtained from some sands and porous rocks.*

## 1 Introduction

Localized deformation is a ubiquitous phenomenon in geomaterials (soils, rocks, concrete). It occurs over a vast range of size scales, from the microscale level of grains to faults extending over hundreds of kilometers. It occurs in a variety of forms, as a concentration or coalescence of cracks; a distinct, planar frictional surface; a gouge zone of finely comminuted material; or simply a region of higher shear strain or relative grain movements. In geomaterials, the severe shearing in regions of localized deformation may be accompanied by dilatancy (inelastic volume increase) and/or compaction (inelastic volume decrease) as well as by chemical alteration. If the material is fluid-saturated, as is frequently the case, inelastic volume changes can induce the flow of fluid or changes in pore pressure which will affect the response. Localization occurs under a variety of conditions that depend on the material and the loading process (*e.g.*, mean stress and loading rate). Although most frequently associated with the formation of faults under nominally brittle conditions or shear bands –semi-brittle

conditions—, localization can also occur by cataclastic flow of rocks at higher mean stresses and by ductile shearing at temperatures and pressures typical of depths of 10 to 15 km into the Earth's crust. A large transition zone bridges the brittle and ductile regimes. This distinction between the different types of localization can also be a matter of observation scale.

Sometimes, the occurrence of localization essentially coincides with failure. For example, in the axisymmetric loading of porous rock or sand specimens, more or less homogeneous deformation is terminated by the sudden appearance of a sharp fault or shear band in the sample and by rapid loss of strength. However, the transition from homogeneous deformation to clearly localized deformation is still an open question as far as eventual precursors are concerned. In other instances, incipient localization may be only the first step in a continuing process: a shear band can be de-activated but still exist (non reversible deformation) and can be potentially re-activated later. In other circumstances, a shear band can evolve as a fault, marking an inability of the material to support large strain or highly concentrated micro-deformation mechanisms, and switch to a material discontinuity.

Obviously, the phenomenon of localization in geological materials is both rich and complex and its consequences can be important. Seismic activity on large faults is a threat to human life and is a concern for the siting of structures. Shear zones and fractures of a more modest scale can be problems for foundations and underground structures of all types. The formation of a localized slip surface is frequently a predecessor to slope failure. More generally; however, features of localized deformation control not only the mechanical behavior but also the transport behavior of the crust. For example, faults often form impermeable barriers that trap hydrocarbons or bound aquifers. The presence of localized zones of deformation may disrupt efforts to withdraw or inject fluids into the subsurface. Although faults and shear zones typically inhibit flow perpendicular to their strike, they can also act as high-permeability channels for flow along the strike and carry fluid much further and more rapidly than predicted by assuming a homogeneous formation.

The importance of localization has motivated numerous experimental, theoretical and numerical works in the field of geomechanics, especially since the 1970s. However, open questions exist about how the occurrence of localization and its subsequent evolution are related to the stress state, deformation history, material properties and the coupling of deformation with the transport of fluid and heat and with chemical alteration.

In term of theoretical approach, ever since pioneering works of [Hil62] and [Ric76], bifurcation theory considers strain localization as a loss of uniqueness problem. If one considers a homogeneous body subjected to boundary conditions such that one possible solution for the next increment is additional homogeneous deformation, the bifurcation approach seeks conditions for which an alternative solution is possible, corresponding to localized deformation in a planar band (see [VS95] and [BR04] for comprehensive reviews).

Numerical modeling of strain localization concerns, in particular, the practical aspect of the band thickness. The absence of a length scale in the classical constitutive models causes numerical simulations to depend spuriously on the mesh size (in terms of band thickness and *de facto* energy dissipation). Recent developments have introduced a length scale in the continuum using micromorphic models ([Cos09], [MV87], [FH97], [CCM01]) or non-local models ([BLPC87], [BPC88], [VA91]), to cite a few studies.

Concerning experimental characterization, a large amount of work has also been produced, on soil and rock mechanics (see for example [VS95], [Des98], [PW05] for extended reviews). Pioneering studies have characterized strain localization by *post mortem* or destructive analysis (especially in rock mechanics). At the end of mechanical tests, after the specimens have been removed from the loading device, the patterns of localization, shear band orientation, local porosity and grain scale damage are analyzed with regard to experimental and loading conditions (boundary conditions, mean stress level, stress rate, material initial state, fluid saturation, etc.).

This chapter attempts to review recent experimental observations about *the progressive evolution from diffuse to localized deformation*. Spatial descriptions of physical quantities and the time evolution of these fields are needed for this aim, in contrast to more conventional measurement techniques based on global measurement by transducers positioned outside of the loading device and/or at the specimen boundaries (no field measurement) or on *post mortem* characterization (no time evolution). Such techniques which are referred to as full-field measurements became more and more popular during the last two decades ([VH12]). They are potentially well adapted to detecting, during laboratory tests, the transition from the initial (quasi-) homogeneous regime to the localized regime.

*Full-field methods* represent a long list of different techniques. Kinematic (displacement) field measurements seem obvious for detecting strain localization. Once the displacement field is measured, the strain field can be deduced quite easily by applying continuum mechanics. Many techniques exist, including among others, image correlation, the grid method, speckle interferometry and the moiré method ([Gr4], [VLMS02]). Other methods for non-kinematic measurements exist based on imagery techniques of physical processes, such as ray absorption, wave propagation or attenuation, temperature and electrical resistivity. Some methods use tracer emission detection (*e.g.*, gamma ray emission). Generally, these methods are not direct and need reconstruction algorithms to quantify the physical properties: X-ray tomography, neutron tomography, ultrasonic tomography, electrical resistivity tomography, magnetic resonance tomography, positron emission tomography, dynamic thermal tomography, etc. Acoustic emission monitoring is also interesting for geomaterials. The acoustic events (AEs) generated during deformation (due to micro-cracking) are detected by transducers on the specimen boundaries and are located by inverse analysis, giving a field of AEs resolved in time (*e.g.*, [FSDG09]). A review of the different full field measurement methods is beyond the scope of this chapter. We will simply present the digital image correlation (DIC) method because it is the most popular kinematic field

method in geomechanics. The method can be used with classical images from a digital high resolution camera (2D measurement) or combined with more complex imaging techniques such as X-ray tomography (3D measurements). The success of DIC in geomechanics comes, in 2D, from the relative simplicity of the specimen preparation in generating a needed random speckle, the availability of commercial codes and the trend in decreasing costs of digital cameras. Moreover, in 3D (volume), the possibility to use the natural heterogeneity of the geomaterial as a random speckle is crucial.

To continue the chapter, some selected results will be presented, to illustrate the transition from diffuse to localized deformation in sands and porous rocks. Note that we have chosen to present results coming, in large part, from our research group in Grenoble. We chose to select some results that we know well, and not necessarily the most advanced results from the literature each time. However, this selection should give quite a wide view of the subject. The first results concern the strain localization in a Hostun sand observed in plane strain compression. Then, the strain localization in sands will be presented at a smaller scale –at the scale of the grains –thanks to X-ray CT. Afterward, the localization in two porous rocks (a Vosges sandstone and a clayey rock) observed under plane strain compression will be discussed.

## 2 Methods

This part describes the methods and tools used to obtain the results presented in a later part. *Digital image correlation* (DIC) is first presented. The method became popular in geomechanics several years ago. It has superseded the *false relief stereophotogrammetry* (FRS) which was used in the '70s-'90s ([BHA70], [DV04]). FRS is based comparing of photographs taken from a fixed viewpoint at different times of the specimen's deformation. An essential feature of FRS is that the deformation is directly perceived as a fictitious relief (hence the name of the method) by using the well-known stereoscopic effect on successive pairs of photographs. The relief observed is due to the (plane) deformation taking place in the time interval between the two photographs, and not the real 3D geometry of the object. When two photographs are viewed in stereo, displaced regions appear elevated, with the elevation being proportional to the magnitude of the displacement. In the presence of a shear band, the deforming specimen appears as two planes of different elevation connected by a slope.

*X-ray computed tomography* is then described, which allows imaging of the specimens in 3D (volume). X-ray CT can directly detect the shear bands in specimens undergoing dilatancy or compaction (mass density change). However, the combination of X-ray CT with DIC is a much more powerful tool for detecting incipient shear bands because it measures the full strain tensor field (including shear strain) inside the specimen, and not only the mass density change (volume strain field).

The adaptation of experimental loading devices for geomaterial to full field measurements will be discussed. The devices need to be transparent to visible light (classical

camera) or to X-rays for X-ray computed tomography (X-ray CT). This adaptation of the loading device can become complex, especially for rock mechanics due to the high strength and stiffness of the specimens.

## 2.1 Digital image correlation (DIC)

Digital image correlation (DIC) provides a displacement field measurement between two images of the specimen. One of the images is called the reference image and the image corresponding to a deformed state of the specimen is called the deformed image. The displacement field corresponds to the transformation that matches the reference image to the deformed image. The measure at a discrete set of positions (nodes) using a correlation algorithm is based on a principle of optical flow conservation. Then, the strain tensor field can be deduced from the displacement vector field using spatial derivation methods for a discrete field. Note that an extended description of the method can be found in [Hal12] and a state of the art description of good practices can be found in [BBD<sup>+</sup>08].

The nodal displacements of the specimen are determined by correlating of small subsets (centered on the nodes) of the two digital images of the sample. Originally, DIC was applied to photographs of a plane surface of the specimen (*e.g.*, [PR82], [SWPM83]), but has been extended to volume 3D pictures of the specimen (*e.g.*, [BSFS99], [VvRH04]).

We call  $\underline{X}$  the position in the reference picture and  $\underline{x}$  the position in the deformed picture. The displacement is defined by  $\underline{u}(\underline{x}) = \underline{x} - \underline{X}$ .  $u$ ,  $v$  and  $w$  are the displacement components of  $\underline{u}$  in the space coordinates  $x$ ,  $y$  and  $z$  of  $\underline{X}$ , respectively. The displacement gradient tensor is defined by:

$$\underline{\underline{F}} = \underline{\underline{I}} + \frac{\partial \underline{u}}{\partial \underline{X}} = \begin{pmatrix} 1 + \frac{\partial u}{\partial x} & \frac{\partial u}{\partial y} & \frac{\partial u}{\partial z} \\ \frac{\partial v}{\partial x} & 1 + \frac{\partial v}{\partial y} & \frac{\partial v}{\partial z} \\ \frac{\partial w}{\partial x} & \frac{\partial w}{\partial y} & 1 + \frac{\partial w}{\partial z} \end{pmatrix}$$

The three main types of DIC can be described in the following:

- 2D-DIC needs one camera and two pictures of a flat surface of the specimen (defined as  $z = z_0$ ). The components of the displacement vector  $u(x, y, z_0)$  and  $v(x, y, z_0)$  are measured, which allows the components  $F_{xx}$ ,  $F_{xy}$ ,  $F_{yx}$  and  $F_{yy}$  to be determined. The surface of the specimen can be prepared with a random speckle.
- 3D-surface DIC (stereo-vision plus stereo-correlation) needs two cameras (and requires special calibration of the two cameras' frame) and two times two pictures of the surface of the specimen. The surface is not necessarily flat. The components of the displacement vector  $u(x, y, z_0)$ ,  $v(x, y, z_0)$  and  $w(x, y, z_0)$  are measured, which allow the components  $F_{zx}$  and  $F_{zy}$  to be determined, in

addition to the previous components. The derivative with respect to  $z$  is not accessible, it is still restricted to surface analysis. It is applicable to the evaluation of non-planar objects and out-of-plane deformations.

- 3D-volumetric DIC (also known as digital volume correlation or DVC) needs a 3D imaging device (*e.g.*, X-ray tomograph) and two 3D volume images. The three components of the displacement vector  $u(x, y, z)$ ,  $v(x, y, z)$  and  $w(x, y, z)$  are measured, which allow all of the gradient tensor's component to be determined. It is applicable to analysis of 3D deformation including internal deformation, but requires the object to have an internal “character” that may be followed (correlated) between images.

The Green-Lagrange strain tensor is defined as

$$\underline{\underline{E}} = \frac{1}{2} (\underline{\underline{F}}^T \cdot \underline{\underline{F}} - \underline{\underline{I}})$$

and the linearized strain tensor (for small strain assumption) is defined by

$$\underline{\underline{\varepsilon}} = \frac{1}{2} (\underline{\underline{F}}^T + \underline{\underline{F}})$$

The components of  $E_{xx} = 0.5 (F_{xx}^2 + F_{yx}^2 + F_{zx}^2 - 1)$ ,  $E_{xy} = 0.5 (F_{xx} \cdot F_{xy} + F_{yx} \cdot F_{yy} + F_{zx} \cdot F_{zy})$  and  $E_{yy} = 0.5 (F_{xy}^2 + F_{yy}^2 + F_{zy}^2 - 1)$  can be computed exactly with 3D-surface DIC, while they are approximated with 2D-DIC under the assumption that the out-of-plane displacement is quite homogeneous with respect to  $x$  and  $y$ , which is correct in plane strain deformation (no out-of-plane displacement). The approximation is also correct in the case of small stretching and small rotation, when  $\underline{\underline{E}}$  tends toward  $\underline{\underline{\varepsilon}}$ .

The displacement field is estimated for a set of nodes. 2D or 3D digital images correspond to some grey-level pixelated pictures. Each node is characterized by the grey-level distribution in its vicinity, called a subset, which is composed of pixels (2D) or voxels (3D). The subset from the reference image is associated with a subset in the deformed image that optimizes a similarity with the reference subset. The similarity is measured with a correlation coefficient. The difference in the positions of the two subsets corresponds to the displacement of the node. The process is repeated for each node selected on the reference image to obtain the displacement field.

The deformation of the subset, centered on the position  $\underline{X}_0$ , from the reference image to the deformed image can be approximated at the first order:

$$\phi(\underline{X}) = \underline{X} + \underline{u}(\underline{X}) \approx \underline{X} + \underline{u}(\underline{X}_0) + \frac{\partial \underline{u}}{\partial \underline{X}}(\underline{X}_0) \cdot (\underline{X} - \underline{X}_0)$$

where  $\underline{u}(\underline{X}_0)$  is the searched displacement of the subset. The main difference between the correlation methods comes from how to estimate the similarity between

the reference and the deformed subset, including the choice of correlation function and the assumptions on the transformation of the subset. The assumed transformation can simply be a rigid translation ( $\partial \underline{u} / \partial \underline{X}(\underline{X}_0) = 0$ ) or can take into account a rigid rotation and a stretching of the subset.

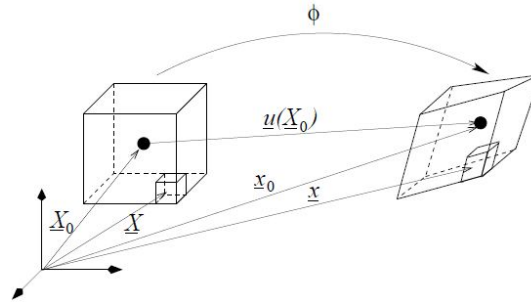


Figure 1: Material deformation of the subset (from [BCD<sup>+</sup>04]).

The DIC method is decomposed into several steps, including an approximation of the displacement at an integer number of pixels and a sub-pixel refinement (Fig. 2):

1. The set of nodes distributed on the reference image is defined. Generally the nodes are regularly spaced, with a given number of pixels for the distance between nodes.
2. The subset around the node is determined, which is generally a square (2D) or a cube (3D) with a size of a few pixels (voxels).
3. The zone of research (zone of interest) is determined and the most similar subset in the deformed image is searched.
4. For all possible positions in the research area, a correlation coefficient is measured corresponding to a displacement of an integer number of pixels, assuming a rigid displacement (no deformation of the subset). The position that maximizes the similarity coefficient is guessed as the best approximation.
5. The previous approximation is refined by a sub-pixel algorithm, because the true displacement rarely corresponds to an integer numbers of pixels. Generally, the subset size in this step is smaller than in step 2. Moreover, the zone of research (step 3) is reduced to very few pixels (voxels).

There are different kinds of sub-pixel approximations (*e.g.*, [PXD06]). The simplest is based on an interpolation of the correlation coefficient for positions around the approximation in 4. The coefficient is computed for rigid displacement of the subset with no stretching. The sub-pixel approximation corresponds to a maximum of the interpolation of the correlation coefficient. More complex methods account for the stretching of the subset, which generally corresponds to a linear approximation (which can also be a second-order function). Then, the parameters of the transformation are searched to

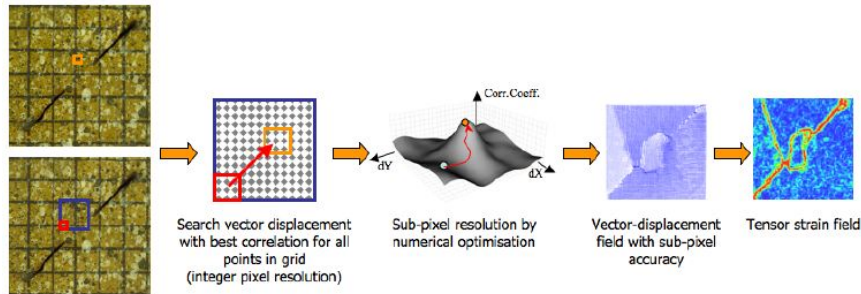


Figure 2: Schematic of a 2D-surface DIC analysis approach (from [Hal12]).

optimize the correlation coefficient. The optimization can concern the displacement, rotation and stretching parameters. However, this process can be time consuming; to reduce the computation time, the stretching of the subset is sometimes determined out of the optimization loop ([BCD<sup>+</sup>04]) and can be updated during an iterative algorithm. The zone of research during the sub-pixel correlation needs to be restrained to maintain a reasonable computation time. Several optimization algorithms exist, that are more or less robust and efficient (Newton-Raphson, Levenberg-Marquart, etc.). The sub-pixel correlation needs an interpolation of one of the two images to work on a continuous grey-level picture (not pixelated). The selection of the interpolation scheme is a key factor and directly affects the calculation's accuracy and convergence efficiency. A first and second-order continuity is preferable to assure the smoothness of the intensity function and its derivatives.

The grey-level distribution in the subset can be interpreted as the signature of the central node. This implies the need of a "character" of the image to be able to distinguish the subset in a unique manner. With some geomaterials, the natural heterogeneity of their material structure is sufficient to serve as speckle pattern. This is especially important for volume-3D DIC. With the surface DIC methods, a synthetic pattern can be deposited onto the specimen surface. The speckle pattern acts as a fixed reference that follows the movements of the material, meaning that its morphology is an important parameter that directly affects the accuracy of the measured displacements. A synthetic pattern can be obtained using by a layer of white paint and an ultra-fine layer of black paint droplets such as using an airbrush. The speckle density, grey-level contrast and characteristic size affect the quality of the measure. This implies that each speckle pattern must comply with a predetermined quality requirement to be considered appropriate for imaging. It should be adapted to the pixel(voxel) size of the digital images (see [BBD<sup>+</sup>08]).

DIC can be adapted to a material's specificities. For example, for a granular material studied using X-ray CT, DIC can be used to measure a "continuous strain field", using the standard procedure described above. DIC can also be used to measure the kinematic displacement (and rotation) of each grain; this is the *discrete* volumetric

DIC ([HBD<sup>+</sup>10]). Before the DIC procedure, the grains have to be individually identified through image segmentation. Then, the DIC subset has to be mapped onto each grain, using an *ad hoc* mask for each grain. Then, the (quasi)standard DIC procedure can be used to search the rigid displacement and rotation that optimize the correlation coefficient of each grain between the two images.

## 2.2 X-ray computed tomography (X-ray CT)

X-rays are a high-frequency form of electromagnetic radiation discovered at the end of the 19th century by W. C. Röntgen. They have can penetrate matter, depending on the wavelength spectrum. Many interactions exist between X-ray photons and matter, including photoelectric absorption. This absorption depends on the X-ray's characteristics and the atomic number of the matter. X-rays are thus a type of radiation that is able to be transmitted through matter, and is sensitive to the atomic number of the material that it is radiating through. For geomaterials, this absorption depends on the mass density and the mineralogy.

An *X-ray radiograph* is a two-dimensional measurement of the amount of X-ray photons arriving at each point onto a detector during a given exposure time, which is an integration of the X-ray attenuation of the matter being traversed along the path of the X-rays.

*X-ray computed tomography* is a method of reconstructing a 3D field of an X-ray attenuation coefficient inside an object, starting from a series of different projections (radiographs) of the object. The different projections are generally acquired by a relative rotation of the object and an image acquisition system. The source and detector rotate in medical applications; in industrial/laboratory applications such as this one, the specimen is usually rotated – with a vertical axis of rotation – by a rotation stage. Note that this technique is fully detailed in a number of textbooks on tomography, such as [Hsi09].

The kind of X-ray source distinguishes medical/industrial/laboratory tomographs from synchrotron facilities. The firsts are X-ray vacuum tubes that emit a cone-beam in the direction of the object and detector. Synchrotron light sources are large particle accelerator facilities. The main differences with respect to the previous small sources, for our applications, are the considerably higher brightness (photon flux) and capability for quasi-parallel beams (which can be advantageous in term of imaging), which allow fast scanning, (quasi)monochromatic X-ray light, phase contrast reconstruction, etc. The cone-beam of a laboratory tomograph is also interesting because the field of view changes, depending on the relative position of the object with respect to the detector and the source and the specimen can be enlarged on the detector due to geometric magnification. See [KC01] for an introduction to X-ray CT for geomaterials. The experimental results on geomaterials that will be described in the next section come from the X-ray scanner in Laboratoire 3SR (Grenoble). A detailed description of the scanner can be found in [And15].

## 2.3 Experimental devices for *in situ* full field measurements

### 2.3.1 A plane strain apparatus for soils

Desrues and coworkers originally developed a plane strain compression apparatus adapted for full-field measurement using one classical camera. The design of this device (the biaxial apparatus, hereafter) shares its underlying concept with those developed by [VG81] and [DVH90], in that the biaxial apparatus was specifically conceived to allow free shear band formation in a soil specimen.

Within this device, a 35 mm thick prismatic sand specimen, surrounded by a latex membrane, is mounted between two rigid walls that induce plane strain conditions (see Fig. 3). The initial nominal height and width of the specimen (in the plane of deformation) can vary in the range of 75–350 mm and 90–175 mm, respectively. The side walls are 50 mm thick glass plates which allow photographs to be taken of a specimen's in-plane deformation during the test. All surfaces in contact with the specimen are enlarged and lubricated with silicone grease to minimize friction. The lower and upper loading platens house porous stones connected to drainage lines. The top platen is free to rotate and slide horizontally in the plane of deformation, although it can be locked. This allows free lateral displacement of the upper part of the specimen once a shear band forms due to deviatoric loading. A large cell, filled with silicone oil, surrounds the specimen. The cell can sustain up to 2 MPa; and has two opposite pairs of large Plexiglas windows on its lateral surface. Strain-controlled axial loading is applied through a screw jack that rests atop the device.

The jacket around the specimen can be observed through the glass plate. The jacket follows the deformation of the specimen. Because the full-field measurement used was FRS, a grid was drawn on the jacket; however, a random speckle pattern for DIC analysis can be deposited as well.

### 2.3.2 A true triaxial cell for rocks

A true triaxial apparatus was developed at Laboratoire 3SR in Grenoble (France), with the aim of characterizing the onset of localization and the post-localization regime in rocks (see [BL16] for more details). The device can apply three independent stresses along the three space directions of a prismatic rock specimen, and allows its visualization under loading. A simplified schematic of the apparatus is shown in Fig. 4. The specimen's surfaces, perpendicular to the principal stress (direction 1) and intermediate compressive stress (direction 2), are in contact with rigid platens, which are moved by two perpendicular pistons, as in some triaxial setups developed previously ([Mog71], [HC00]). The two surfaces of the specimen, perpendicular to the minor stress (direction 3), are free to deform because the stress is applied by a confining fluid (by means of a soft silicon membrane). Since deformation bands and cracks are generally parallel to the intermediate stress (at least for an isotropic material, or an

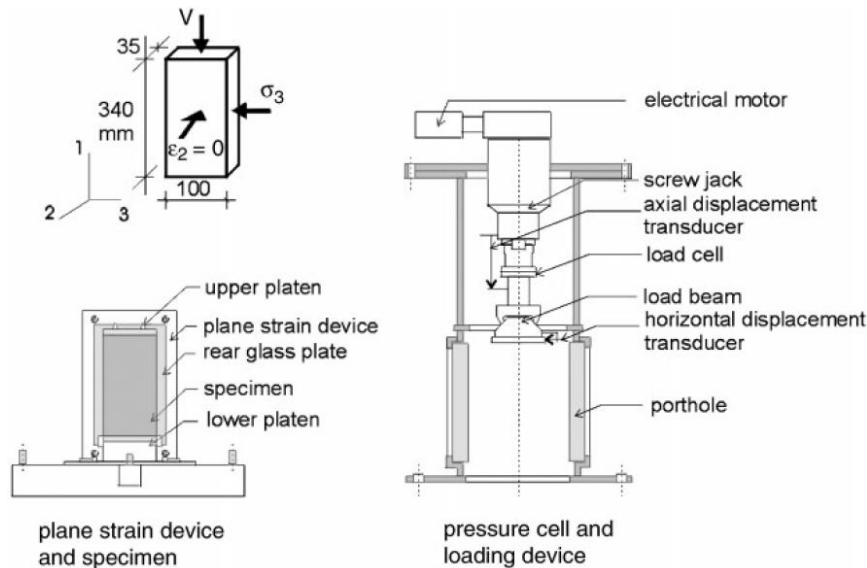


Figure 3: Schematic diagram of the plane strain apparatus for soils (from [DV04]).

anisotropic material with specific orientation of the symmetry directions), the specimen is free to deform and fail with no kinematic constraints imposed on the formation of the failure zone. Moreover, one of the two surfaces perpendicular to the intermediate stress (direction 2) is in contact with a hard window, in order to observe the specimen under loading. The two pistons can be controlled according to either a stress or displacement mode. The intermediate stress can be regulated to ensure that there is no deformation along this direction, thus allowing the application of plane strain loading, which implies that the kinematic of the surface in contact with the window is representative of the kinematic of the whole specimen, up to strain localization and beyond that level of stress. The surface of the specimen opposed to the horizontal piston is in contact with a thick, transparent, sapphire window (7), whose surfaces are optically polished. This surface of the specimen can be observed and photographed. For contact symmetry, the surface on the side of the horizontal piston is in contact with a thin sapphire platen, in order to ensure the same boundary conditions. The minor stress in direction 3 is applied to the two lateral surfaces of the specimen by a confining fluid. The specimen remains hydraulically isolated from this fluid by means of a silicone membrane (Fig. 5a). The membrane contains the specimen and wraps around the four loading caps (two caps along direction 1 and two along direction 2). This arrangement ensures that there is direct contact between the specimen and loading platens, particularly the sapphire window. It is worth noting that along the axial direction (direction 1), a special arrangement of platens with a wedge shape (8), placed between the specimen and the top and bottom loading caps, ensures that the loading

caps have the same thickness of the specimen along the intermediate stress (direction 2) (see Fig. 5b), and larger than the specimen along direction 3. If a compression or extension of the specimen occurs along direction 2, the set of wedges automatically adapt to this variation, thus avoiding an extrusion of the membrane during the deformation of the specimen. In both the axial and horizontal directions, a loading cap (Fig. 4, elements 9-10) is in contact with a piston by means of a spherical head, which allows the compensation, during the setup, of small parallelism offsets of the two opposite surfaces of the prismatic specimen. However, due to friction between the surfaces of the spherical head, once the contact is firmly established, they do not move anymore, and as such, this component does not show a degree of freedom (rotation) during the loading.

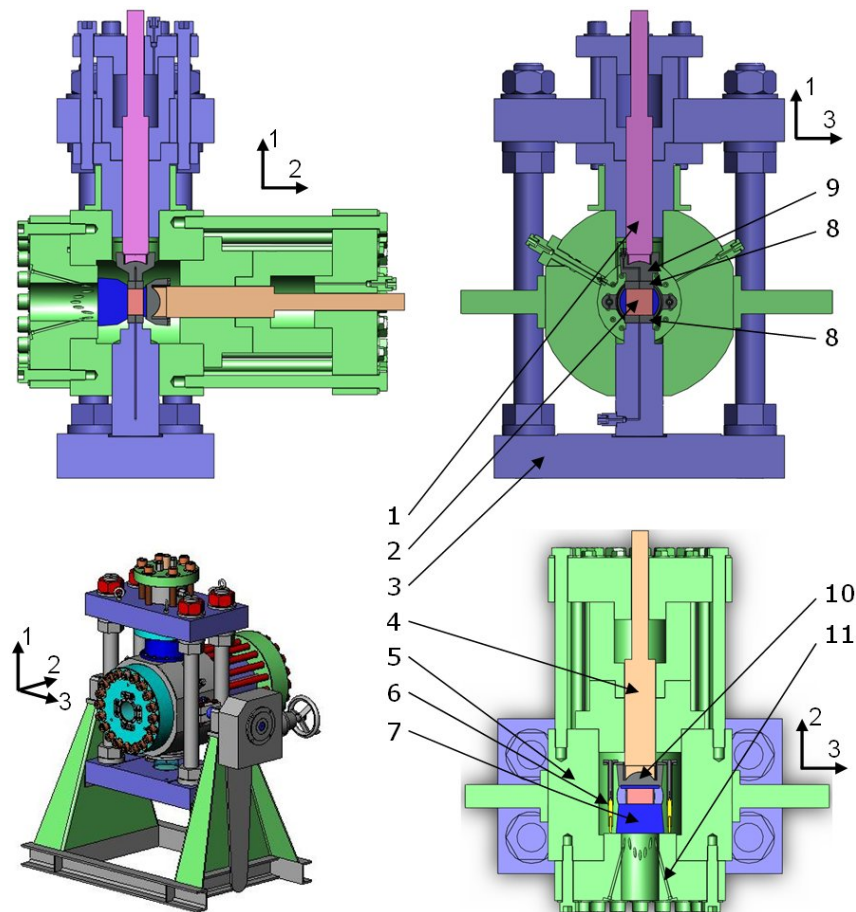


Figure 4: Schematic diagram of the plane strain apparatus for rocks (from [BL16]).

The surface of the specimen receives light through the sapphire window from a set of

20 LEDs, focused onto the sample surface using 20 optical fibers, which pass through orifices (11) made on the frame. These provide even and homogenous illumination for the taking of photographs, since the light power of each LED can be separately adjusted. Photographs of the visible surface of the specimen were taken throughout the loading with a high resolution camera. DIC analysis can thus be carried out on the resulting images to compute the displacement and strain fields. It is worth noting that to apply DIC, the observed specimen must have a random pattern, which is here artificial. The four surfaces of the specimen, which are in contact with the three rigid loading caps and the window, are lubricated. A thin layer of this lubricant is sufficiently transparent to allow good visualization of the pattern through the window.

The size of the specimen is 50 mm in the axial direction, 30 mm in the direction of intermediate stress and 25 or 50 mm in the direction of minor stress, which corresponds to slenderness ratios (the ratio between the height and width) of two and one, respectively. The loading cell can apply a maximum confining pressure of 100 MPa, while the axial and the horizontal pistons can apply forces of 500 and 700 kN, respectively. These values correspond to a differential stress, with respect to the confining pressures of 670 and 530 MPa, respectively, for a specimen with a slenderness ratio of two, and half of these values for a 50 mm width specimen.

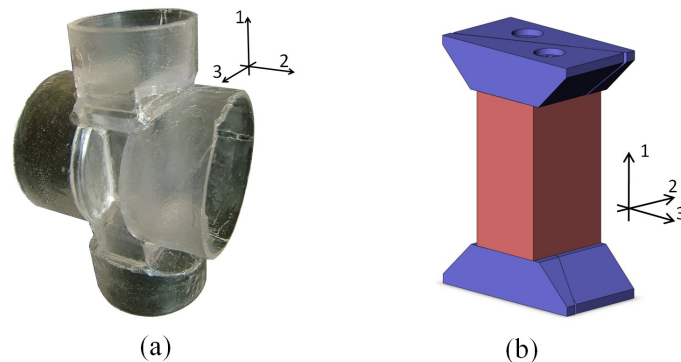


Figure 5: (a) Photograph of the silicon membrane that separates the specimen from the confining fluid and (b) scheme of the adaptable wedges at the top and bottom of the specimen. (from [BL16]).

### 2.3.3 An X-ray transparent triaxial cell

The system allows microtomography to be performed on a specimen under load (*in situ*), using a specifically built load frame that can be placed in the X-ray beam, either from a laboratory scanner or synchrotron microtomography beamline ([LBD<sup>+</sup>07]). Figures 6 and 7 show the experimental setup used at ESRF. The apparatus includes a small triaxial cell and a loading device designed specifically for microtomography on

small soil or rock specimens under load ([Len06]). The triaxial apparatus is practically the same as a conventional triaxial testing system, except for its much smaller size and the shape of its confining cell, which was designed to be as transparent as possible to the X-rays. A 10 mm thick confining cell made of polycarbonate was used, that is both transparent to the X-rays and capable of sustaining the 10 MPa confinement pressure and the tensile reaction force. The axial load and hence the deviator stress are applied in a displacement controlled manner using a motor-driven screw actuator. The loading system, which can be placed in the X-ray beamline without interfering with the tomographic scans, is quite compact and light, which is important because it sits directly on the translation and rotation stage during the experiment. The system has a maximum loading capacity of 7.5 kN. The same device can be used in a laboratory scan ([And15]).

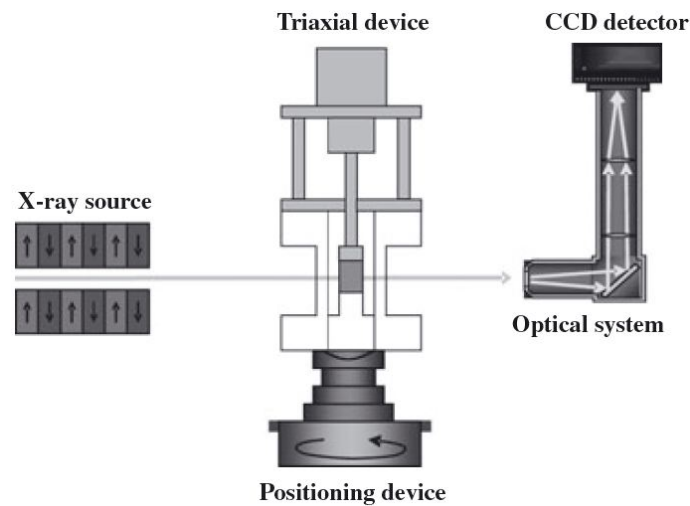


Figure 6: Schematic of the X-ray microtomography set-up for triaxial testing. (from [LBD<sup>+</sup>07]).

Higher capacity in terms of confining pressure and axial loading are needed to experiment on stiffer rocks. It can be necessary to work with stiffer (and with low X-ray absorbance) cell materials such as PEEK, aluminum, beryllium and carbon fiber (*e.g.*, [TO04]).

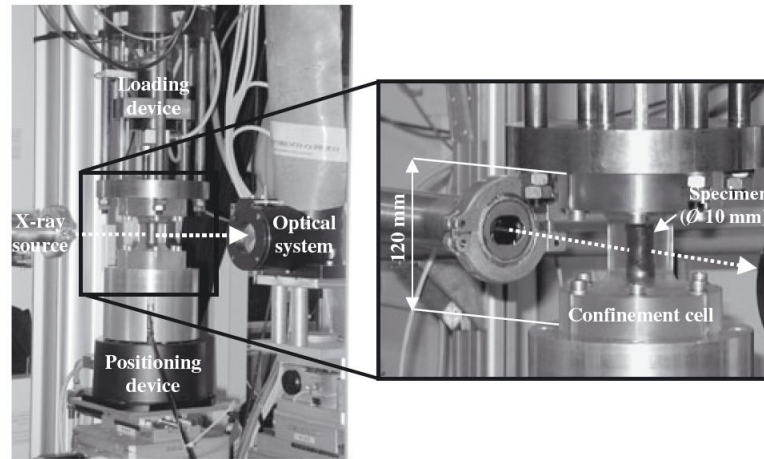


Figure 7: Tomography set-up for triaxial testing at the beamline ID15A at ESRF. Complete set-up on the beamline (left) and zoom on the rock specimen inside the triaxial cell (right). (from [LBD<sup>+</sup>07]).

### 3 Selected Materials

#### Hostun sand

Hostun sand is produced in a quarry close to the commune of Hostun in the department of Drôme, in the Rhône-Alpes region of France. It is approximately 60 km from Grenoble. The material is excavated as clumps made of a range of different silica grain sizes and lightly cemented by kaolin. The silica particles making up these clumps have been crushed *in-situ* from larger rocks, and consequently have not been transported very far. Since the particles were generated by crushing and have not been transported very far they are very angular. After quarrying, the clumps are washed to remove the kaolin, and are then sorted by grain size. Depending on the year of extraction (and the version of sieves), the  $D_{50}$  of the Hostun sand called S28 and then HN31 is about 0.34 mm. A uniform gradation of the natural sand was used, with 100 % of the material passing a 0:63 mm sieve and retained on a 0:16 mm sieve. The conventional minimum and maximum volumetric weights are 13.24 and 15.99  $kN/m^3$ , respectively, and the specific gravity  $G_s$  is 2.65 (see [FDP90], [DV04] and [And15] for more details).

### **Caicos ooids sand**

Caicos ooids are made of  $\text{CaCO}_3$  and more than 96 % of the material is Aragonite, the rest being calcite and “high-magnesium calcite.” The  $D_{50}$  of this material is around 0.42 mm. This sand comes from the Caicos platform in the British West Indies. Ooids grow from small seeds such as shell fragments, small quartz or calcite grains, and progressively become larger. They grow in marine environments, where the waves drive the accretion of material around the seed. Two principal mechanisms exist for an ooid to grow: by physical attachment of material as the ooid rolls (like a snowball), or by precipitation over the surface of the ooid. Both of these mechanisms tend to generate rounded grains – from whence the name comes – although the images acquired show some grains that are prolate spheroids (see [And15] for more details).

### **Vosges sandstone**

The tested rock is a natural sandstone coming from the Woustviller quarry in the Vosges mountains, Eastern France ([BDR00]). It is a pink quartz sandstone (quartz = 93 %), a few percent of which is feldspar and white mica. The sandstone is poorly cemented, its cohesion is due to the interpenetration between the grains. Its porosity is about 22 %. The dimension of the grains fluctuate between 0.15 and 0.45 mm with a mean value of about 0.30 mm. Its uniaxial compression strength is about 35 MPa.

### **Callovo-Oxfordian clayey rock**

The material tested is Callovo-Oxfordian argillite, which has been considered as a potential host rock for radioactive waste disposal facilities, from the ANDRA Underground Research Laboratory (URL) located in Bure (Meuse/Haute-Marne, Eastern France) at approximately 500 m below the ground surface. It is a sedimentary rock composed of phyllosilicates (20-60 %, mainly illite and interstratified illite-smectite, kaolinite, mica and chlorite), tectosilicates (10–40 %, mainly quartz and feldspars), carbonates (15–80 %, mainly calcite and dolomite) and pyrite (0–3 %) ([RSC<sup>+</sup>12]). Clay particles are clustered into aggregates, which are globally oriented along the stratification, whereas the other mineral inclusions have no preferential orientation. The structure presents a microscopic scale described by a microcrystalline and porous clay matrix and a mesoscopic scale related to the organization of the nonporous carbonate and tectosilicate grains (with grain size in the range of 1 to 50  $\mu\text{m}$ ) which are embedded into the clay matrix. Centimetric or multi-centimetric pipe shapes filled by heavy minerals (pyrite) are the markers of bioturbation ([DRM07]). At the investigated depth, the material has an extremely low permeability ( $10^{-20}$ – $10^{-22}$   $\text{m}^2$ ), a porosity of 15 % and a water content of about 6 %. Its uniaxial compressive strength is about 20 MPa.

## 4 Strain localization in sands

The progressive strain localization in sands is analyzed below. First, some results based on false relief stereophotogrammetry (FRS) of plane strain compression tests on Hostun sand are presented from the work of Desrues and co-workers ([DV04], [Des04]). In this application of FRS, the photographed image is the side of a sand specimen deforming under load, and the source of the differences between the successive images is the deformation process undergone by the specimen. FRS is now obsolete because of the relative low space resolution of the displacement field (with respect to DIC); however, experimental studies are still important. Then, a work that combines X-ray CT and DIC is presented. The analysis was in 3D, with a high space resolution and was extended for grain-scale analysis ([And15], [AHV<sup>+</sup>12]). A former work, based on *in situ* X-ray CT during triaxial tests is also presented to discuss the volume strain inside shear bands ([DCMM96]).

### 4.1 Plane strain compression by FRS

Three tests from [DV04] were selected to discuss the emergence of strain localization in Hostun sand. Tests were performed in the plane strain apparatus described in part 2.3.1, with a lateral pressure of 80-90 kPa and a slenderness ratio (H/W) of 2-2.2, and the two loading platens in contact with the specimen were locked (no translation, no rotation), excepted in test shf06 for which rotation was allowed. The initial densities of the specimens corresponded to a dense state for shf06, a loose state for shf03, and an intermediate state for shf00.

Figure 8 shows the corresponding stress strain response obtained for each selected test, in terms of the effective stress ratio  $t/s'$  vs. the global axial strain. Figures 9-11 show the stereophotogrammetry-based shear strain intensity ( $\varepsilon_s = (\varepsilon_1 - \varepsilon_3)/2$ ) and volumetric strain ( $\varepsilon_v = (\varepsilon_1 + \varepsilon_3)/2$ ) for each photographic increment. The size of the symbols is proportional to the value of the relevant quantity (note that the symbol scale is different for each increment). As far as volumetric strain is concerned, square symbols are for dilatancy and hexagons are for contractancy. The photograph numbers are noted on the relevant curve of the effective stress ratio  $t/s'$  vs the global axial strain, see Figure 8.

The evolution of the shear strain field of test shf00 (Figure 9) showed that the shear band pattern was partially in place at (or even just before) the stress peak (increment 4-5), as compared to the post-peak pattern (increment 5-6) which showed a shear band reflected on the top platen. The shear band was not yet reflected in increment 4-5. Two other bands were visible but less active; one was conjugated to the main shear band, and the second one was sub-parallel and initiated more or less from the top-left specimen corner. These two bands were de-activated in the next increment. The strain field was not homogeneous in the previous increments 3-4 and 1-2; however, the spatial resolution of FRS does not unambiguously show whether the deformation is

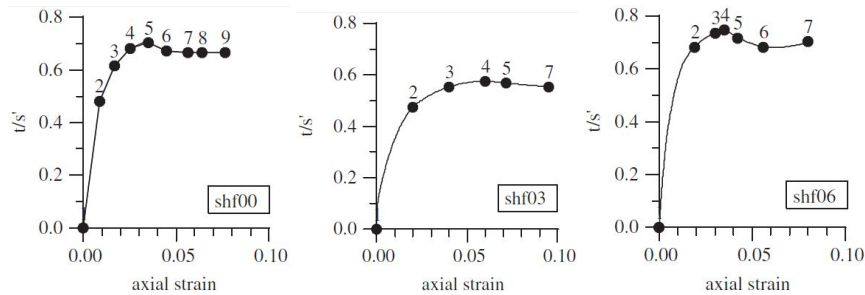


Figure 8: Stress strain responses from various tests; the numbers noted on each curve are the photographs numbers. (from [DV04]).

localized or not. Non-homogeneity can be a consequence of an initial heterogeneity in the specimen (void ratio heterogeneity) or early strain localization (or both). Volumetric strains were localized in the same band as the shear strains (increments 4-5 and 5-6) and are mostly dilative inside the shear band.

In test shf03 (Figure 10), the incremental shear strain fields (top row) indicated that a localized region first formed during increment 2-3 (before stress peak), showing two (or even three) parallel bands. Then, the pattern switched in the subsequent increment 3-4 (at the peak), resulting in a conjugate deformation pattern. A shear band could be observed in the last available photographic increment (4-5), which corresponded to the main band in increment 2-3 that was re-activated. In the first increment (1-2), the deformation was slightly non-homogeneous; however, the spatial resolution of FRS does not allow the deformation regime to state on. The final deformation pattern was characterized by volumetric strains that were localized in the same band as the shear strains. Both contractive and dilative incremental behaviors were exhibited inside the band.

In test shf06 (Figure 11), the shear strain fields (top row) indicated that two parallel zones of strain localization formed in the middle portion of the specimen in increment 3-4 (shortly prior to the stress peak). Note that the shear strains were always larger in the left shear band, which was the only one maintained throughout the test and finally intersected the entire specimen, whereas the other shear band eventually disappeared. A non-homogeneous deformation already existed during increment 2-3 if not, to a lesser extent, from the beginning of the test (increment 1-2). This heterogeneous shear strain field, could not clearly be qualified as localized (due to the FRS space resolution); however, it evoked a crossed shear bands pattern. The conjugated "bands" seemed very large; however that these large bands were an apparent combination of thinner parallel bands cannot be ignored. The authors of the paper called the apparent transformation of the deformation pattern a phenomenon of the progressive "condensation" of a centrally located heterogeneity of the deformation. However, from our experience and observations on thinner cohesive materials (presented later),

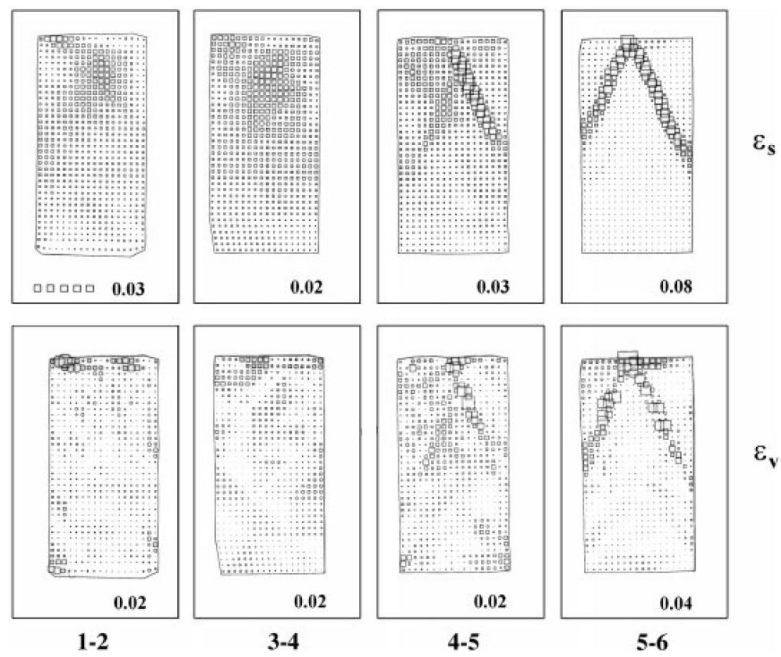


Figure 9: Test shf00: stereophotogrammetry-based incremental fields of shear strain intensity (top row) and volumetric strain (bottom row). (from [DV04]).

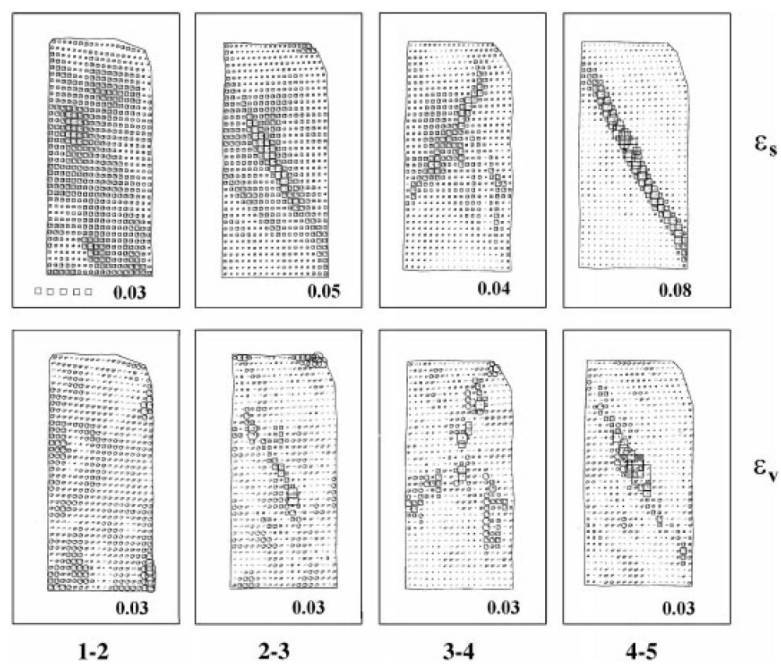


Figure 10: Test shf03: stereophotogrammetry-based incremental fields of shear strain intensity (top row) and volumetric strain (bottom row). (from [DV04]).

this apparent condensation could be interpreted as a phenomenon involving the selection of numerous bands in which some of them stay active and the others bands are de-activated. Volumetric strain fields (bottom row) essentially confirm such a picture. Note that the soil is always dilating in the localized regions.

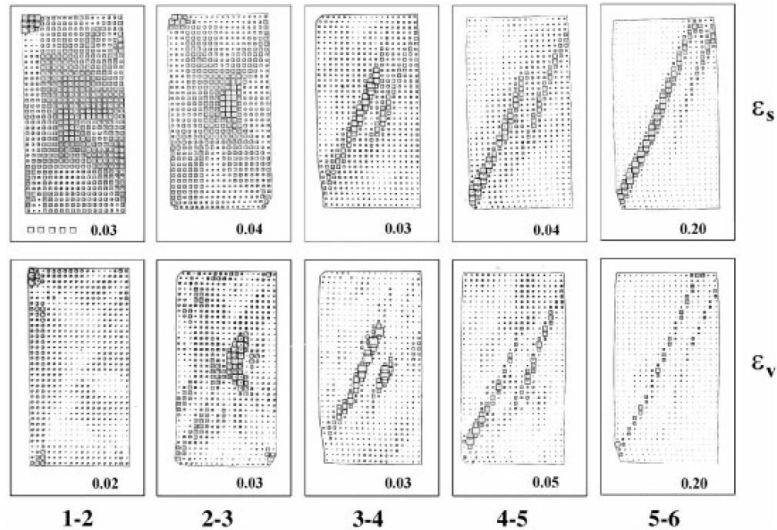


Figure 11: Test shf06: stereophotogrammetry-based incremental fields of shear strain intensity (top row) and volumetric strain (bottom row). (from [DV04]).

The understanding of the strain localization process in sands given by these results is limited by the space resolution of the FRS. However, it can be concluded that the strain localization is not a sudden appearance of shear bands in an initially homogeneous strain field. The evolution is quite progressive and heterogeneity starts well before the stress peak, probably by early strain localization. We can now consider more recent results obtained with more effective full-field methods.

## 4.2 Triaxial compression by X-ray CT and DIC

Here, we analyzed the COEA01 test on the Caicos ooid sand ([And15], [AHV<sup>+</sup>12], [AHD<sup>+</sup>12]). This triaxial compression test was performed with a confining pressure of 100 kPa on a small dense specimen (10 mm diameter and 20 mm height). The test was performed *in situ* in the X-ray CT apparatus of Laboratoire 3SR (Grenoble) with a voxel size of 15  $\mu\text{m}$ , using a transparent triaxial cell (see part 2.3.3). The axial loading was applied from the bottom of the specimen. The kinematic field was measured using

both continuous volumetric DIC (described in part 2.1) and a grain-tracking algorithm (based on grain identification and not on image correlation, see [And15]).

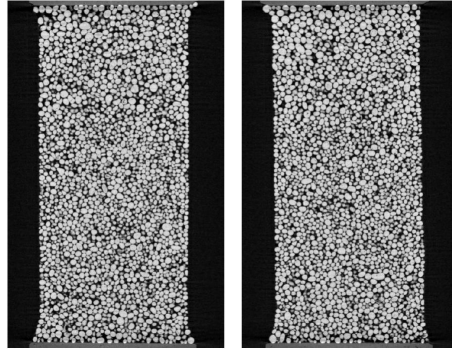


Figure 12: Test COEA01: Slices of the X-ray CT scan of specimen COEA01 in its initial configuration. These slices are taken at 90° from each other. (from [And15]).

Figure 12 shows two vertical slices taken from the 3D image of the specimen before the axial loading. Figure 13 shows the stress-strain response and global volume curve measured for this test. There was a stress peak followed by a strain softening. There was a small contraction at the beginning of the axial loading; thereafter, the specimen dilated.

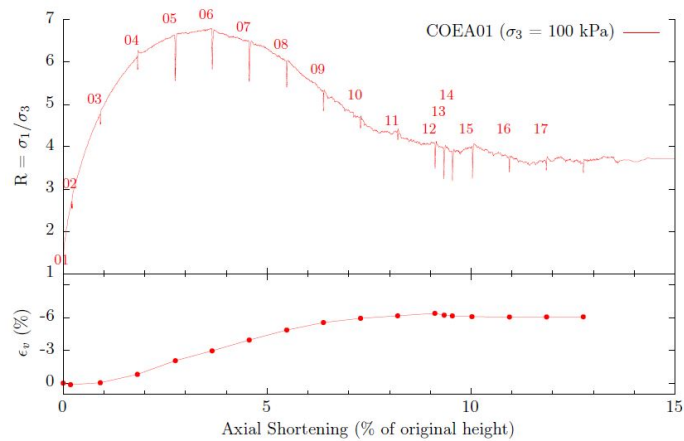


Figure 13: Test COEA01: Stress strain response; the numbers noted on curve are the X-ray CT scan numbers. (from [And15]).

The kinematic field was measured at the grain scale using a grain-tracking algorithm. The displacement vector and the Euler rotation angles were determined for each grain

(Figure 14). The grain displacement was higher at the bottom than at the top, due to the loading conditions. The displacement field showed an evolution from a diffuse deformation regime to a localized regime, clearly exhibiting an inclined shear band. The grain rotation field was more instructive. The rotation field was quite homogeneous at the beginning (increments 01-02 and 02-03), but was localized with a shear band at the end (from increment 09-10). The deformation pattern was more complex just before and after the stress peak (increments 05-06 and 06-07, respectively). Several bands could be identified; while some were parallel to the final main band, others were conjugated with respect to this final band. This pattern could also be identified in increment 04-05.

The equivalent continuum strain field was determined by two methods: i) using the grain displacement measured by the grain tracking and ii) by a continuous volumetric DIC (Figure 15). Note that the comparison and consistency of the two measures exclude the assumption of artifacts of the measure. The above observations of the rotation fields were confirmed. The transition from an initially homogeneous strain field (increment (01-02) and a localized regime with one active shear band at the end (from increment 09-10) was complex. The intermediate deformation pattern showed several shear bands that were parallel and conjugated, before and just after the stress peak. The number of active bands decreased during the subsequent loading step and was progressively reduced to a low number of shear bands –generally one band (for a small specimen size).

The same full-field analysis was extended to Ottawa sand ( $D_{50} = 0.25$  mm) and Hostun sand ( $D_{50} = 0.34$  mm) ([And15]). A comparison of the tests on the three sands is presented in Figure 16, which shows the deviatoric strain calculated in five key increments for these three tests:

- A: The first increment, close to the maximum slope of increase of porosity;
- B and C: Two increments at the maximum slope of local porosity increased, one at the beginning and one at the end;
- D: One increment when the gradient of porosity reduction started to change; and
- E: The last increment at the beginning of the plateau when the local porosity increased.

This figure shows that the beginning of the local change in porosity had a clear meaning: some very slight, diffuse features of localized strains could be seen for all specimens in increment A ([And15]). Increments B and C for every specimen lie on either side of the peak. For COEA01, some considerable conjugate structures are visible in states B and C, that were visible in specimen HNEA01 at state B. These were less visible in specimen OUEA06. In increment C, HNEA01 showed two parallel main bands. What was noticeable in all specimens for increments B and C was that the diffuse zone of localization visible in increment A was concentrated in space. There was a progressive process of shear band de-activation –a kind of selection in which very

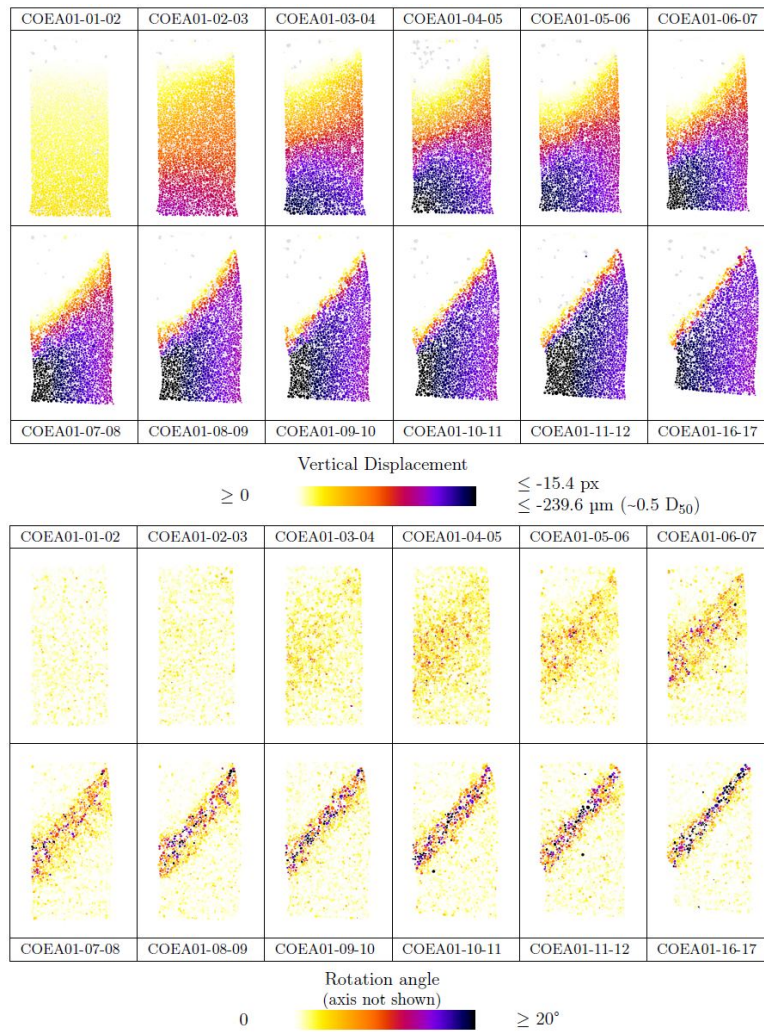


Figure 14: Test COEA01: (top) slice of the grain displacement field during the test (numbers corresponds the the scan numbers). (bottom) slice of the grain rotation. (from [And15]).

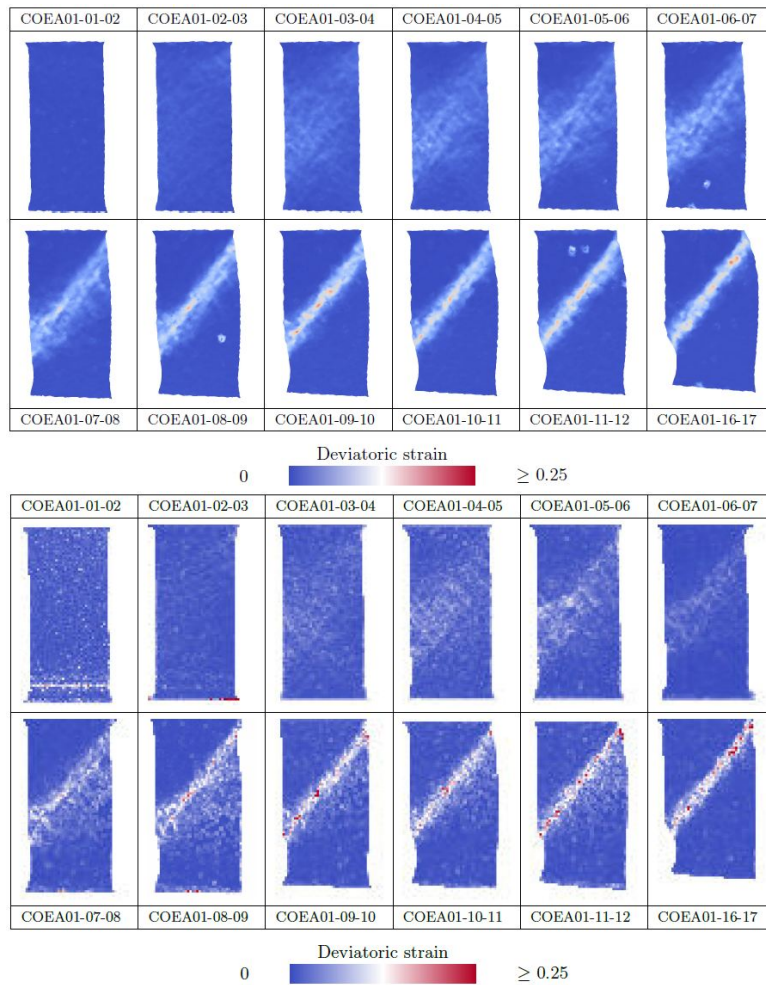


Figure 15: Test COEA01: (top) slice of the strain field during the test, measured from the grain displacement field by grain tracking algorithm (numbers corresponds the the scan numbers). (bottom) slice of the strain field, measured by a continous volumetric DIC. (from [And15]).

few bands stay to be active at the end. In increment D, the shear band was in a much more recognizable form compared to each specimen's residual state. By increment D, all of the specimens had started the "second phase" of localized strain in which the strain was concentrated in a very limited area. By increment E, the shear band was very close to fully mature: the second phase of strain concentration crossed all of the specimens, and the increments all corresponded to increments just at the end of strain softening.

To conclude, the results confirm that strain localization is not an abrupt process. Quite the contrary, there is a progressive evolution from a quite homogeneous deformation toward a relatively diffuse shear band pattern before the stress peak, and the number of active bands progressively decreases to converge to very few shear bands.

However, the observation of a pattern with several bands does not mean that all bands work at the same time. They can be active successively. This is suggested by [LBAS<sup>+</sup>14], which used spatially resolved diffusing wave spectroscopy to measure a strain quantity field on very short loading increments. The authors worked on a glass bead specimen with a plane strain compression apparatus. They showed the intermittency of the early bands, although the behavior of glass beads sometimes differs from that of natural sand.

### 4.3 Triaxial compression by X-ray CT, the critical void ratio

We report here some observations obtained by X-ray CT on the volume strain inside shear bands ([DCMM96]). The study used a medical tomography apparatus that had poor spatial resolution with respect to the actual standard: the voxel size was  $0.7 \times 0.7 \times 4 \text{ mm}^3$ . However, the results were interesting concerning the evolution of the void ratio in shear bands. The results introduced the notion of a *critical void ratio* inside shear bands. Several tests were performed on Hostun sand at the same confining pressure (60 kPa). Several initial specimen void ratio were obtained by sand pluviation, with different pluviation heights depending on the expected void ratio. The specimen size had a diameter and height of 100 mm. The local void ratio was determined from X-ray scanning, using a linear relation between the void ratio and X-ray absorption (grey-level in 3D pictures). The authors measured the void ratio before strain localization and then both inside and outside the shear bands after strain localization. They observed that, independently of the initial specimen void ratio (either loose or dense specimens), the void ratio inside the bands tended to move toward a unique value during the specimen loading (Figure 17). For dense specimens, the material dilated in the band, while for loose specimens, the porosity decreased lightly in the band.

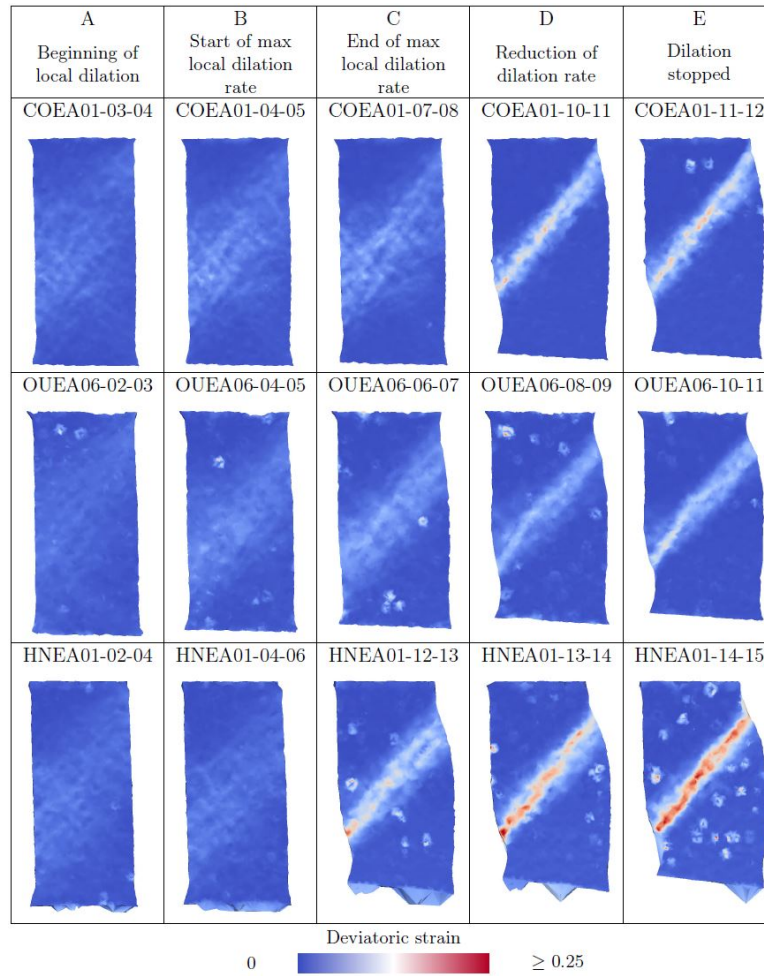


Figure 16: Comparison of the strain field during tests on three sands: (top) test COEA01 on Caicos ooids sand, (middle) test OUEA06 on Ottawa sand and (bottom) test HNEA01 on Hostun sand. (from [And15]).

To conclude, once the strain is localized in a specimen, the volume strain in the specimen is itself localized. The dilation (or compaction) of the specimen is mainly concentrated in the deformation bands. Here, both the space resolution and porosity change detection are too poor to clearly understand the transition from a homogeneous to a localized regime, compared to the previous part 4.2. However, we have to keep in mind that the first observations of the diffuse shear band patterns in the previous part were associated with the specimen dilation, suggesting that this dilation originates from the early strain localization.

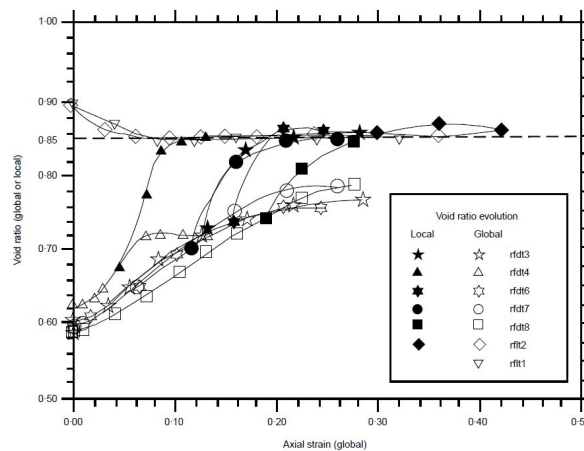


Figure 17: Comparison of triaxial tests on loose and dense Hostun sand specimens: void ratio evolution inside and outside shear bands. (from [DCMM96]).

## 5 Strain localization in porous rocks

We consider here the emergence of strain localization in some porous rocks. Many studies exist that characterized strain localization using *post-mortem* analysis (see [PW05] for a review), which are out of the scope of this chapter. Two experimental studies are considered here on two different rocks: Vosges sandstone and a clayey rock. Tests were performed on the true triaxial cell described in part 2.3.2, using 2D full-field measurement.

### 5.1 Strain localization in Vosges sandstone

The mechanical behavior and failure by strain localization in Woustviller red Vosges sandstone was extensively studied through axisymmetric compression and extension tests in [BDR00], [B99]. The recent work of [Lan14] –from which selected results



followed by an incurvation up to a stress peak and a progressive and then sudden strain softening. The loss of control during the softening was due to the relative low cell stiffness compared to the specimen's stiffness. The loop of the curve after the fast softening was due to a delay in the axial piston pressure control. The stress level stabilized at the end of the test. The global volume strain compacted at the beginning and then dilated. The maximum compaction corresponds more or less to the loss of linearity of the upper curve. At the end of the test, the volume strain rate vanished.

Some photographs were selected during the test (Figure 18): the incremental strain fields between these images are presented in Figure 19. The strain field was quite homogeneous during the linear part of the stress *vs.* strain curve (increment 8533-8549). The small fluctuations in both shear and volume strains correspond to the noise of the DIC measure. Once the stress *vs.* strain curve significantly left its quasi-linear regime, which corresponded to a significant reduction of the specimen volume compaction (increment 8593-8608), the shear strain field was no longer homogeneous. We distinguished a dense, diffuse strain localization band pattern: these bands were parallel and conjugated. This pattern was more visible in the next increment, 8608-8624. A similar pattern was visible in the volume strain field, showing dilatancy in the bands. This step corresponded to dilatancy in the global volume. Before the stress peak (increment 8624-8655), the complex pattern was less dense and some shear bands still existed (plastic strain) but were de-activated. The active shear bands continued to dilate. After the peak (increment 8655-8675), the number of active bands significantly decreased and the shear and volume dilatancy became increasingly concentrated in a decreasing number of bands. During the abrupt softening (the position of photograph 8676 on Figure 18 is not well defined due to a fast failure), one main shear band started to propagate from the bottom left corner and dominated the other bands. After the softening, the band was fully propagated through the specimen and was still dilating. The dilatancy decreased later (not shown). The inclination of the early bands before the stress peak, with respect to the axial loading direction, was about  $45^\circ$ , which decreased to around  $30^\circ$  at the end of the test.

Figure 20 shows the stress-strain response and global volume curve measured for the test BxR\_GVR\_11. The curve is similar to that of test BxR\_GVR\_06, but less brittle. There is first a quasi linear part in the stress *vs.* strain curve, followed by an curve up to a stress peak and a progressive and then a plateau on the curve. The global volume strain compacted from the beginning to the end. This kind of response was already described in [BDR00]. At the end of the test, the volume strain rate almost vanished.

Some photographs were selected during the test (Figure 20) and the incremental strain fields between these images are presented in Figure 21. The strain field was quite homogeneous during the linear part of the stress *vs.* strain curve (increment 3138-3158). The small apparent strain concentration on the right side of the specimen was probably an artifact due to the optical effect of the thin lubricant layer deposited on the specimen's surface. Once the stress *vs.* strain curve significantly left its quasilinear regime (increment 3196-3213), the shear strain field was no longer homogeneous. We distinguished a dense, diffuse strain localization band pattern: these bands were

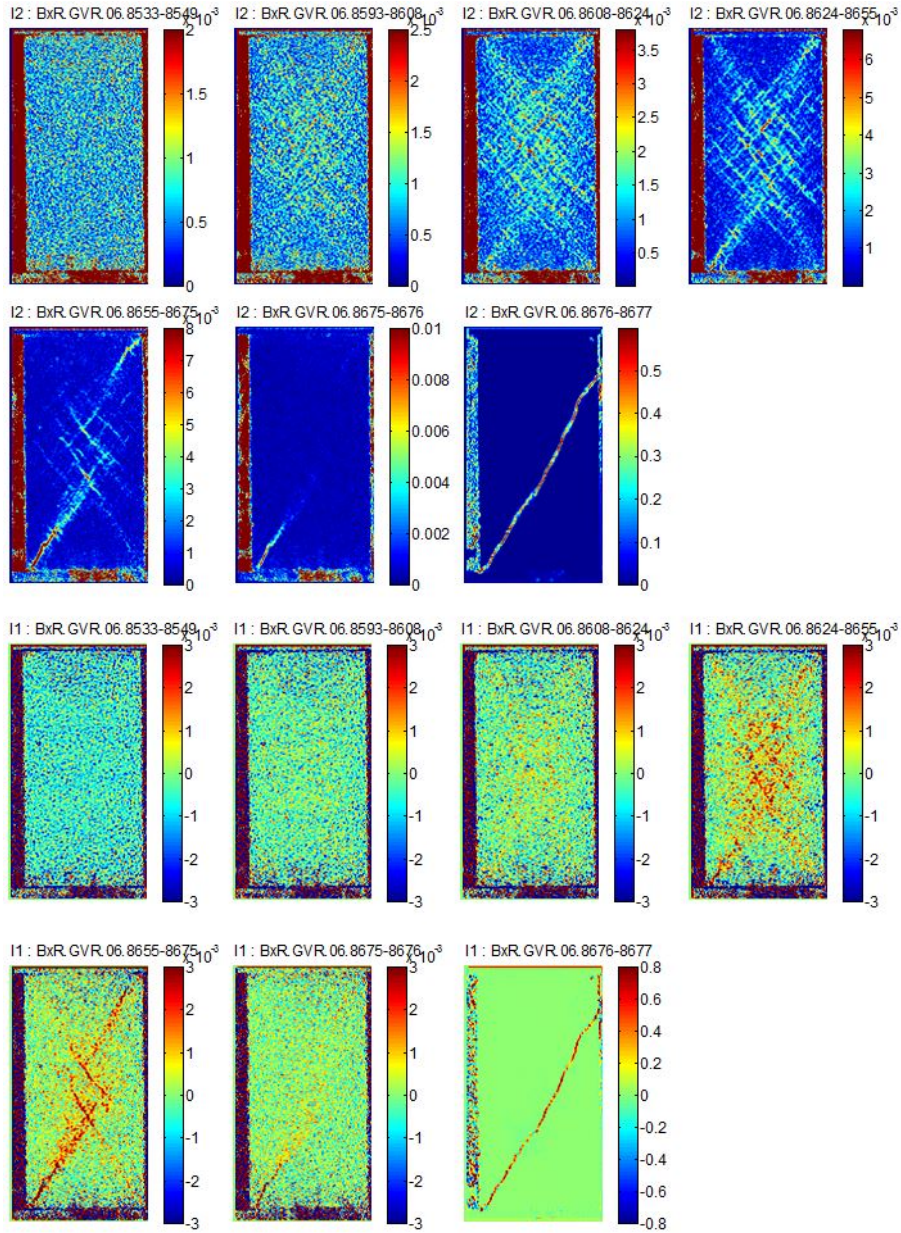


Figure 19: Test BxR\_GVR\_06: (the two first lines) incremental second strain tensor invariant (shear strain) fields; the numbers at the top of pictures correspond to the photographs numbers. (the two last lines) incremental first strain tensor invariant (volume strain) fields. (from [Lan14]).

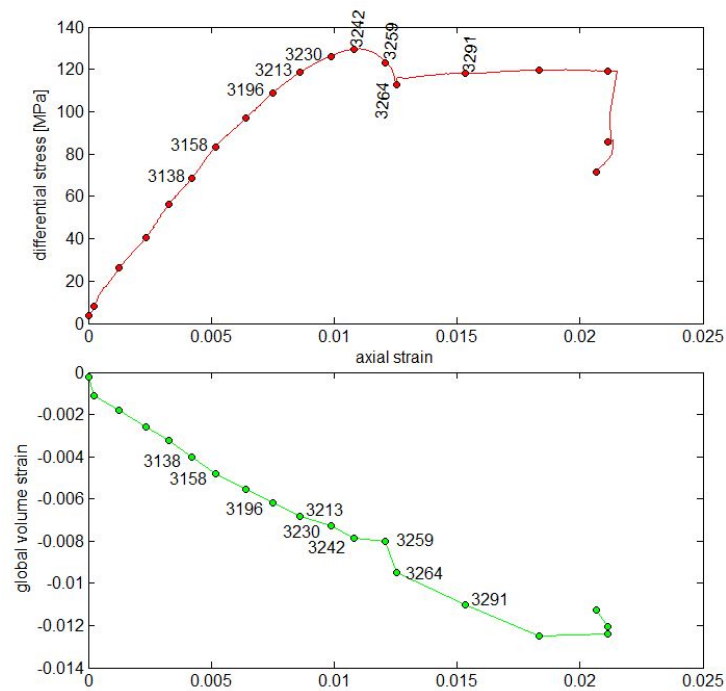


Figure 20: Test BxR\_GVR\_11: (top) differential stress ( $\sigma_1 - \sigma_3$ ) vs axial strain and (bottom) volume strain vs axial strain ; the numbers noted on each curve are the selected photographs numbers. (from [Lan14]).

parallel and conjugated. This pattern was more visible in the next increment, 3213-3230. A similar pattern was visible on the volume strain field, showing compaction in the bands. Before the stress peak (increment 3230-3242), the complex pattern was less dense and some shear bands still existed (plastic strain) but were de-activated. The active shear bands continued to be compactant. After the peak (increment 3242-3259), two main conjugated bands were still active and were around several short bands. The main bands were not very straight and they seemed to result from the coalescence of many smaller bands. In the following strain softening, only one band persisted, which crossed the top-left specimen corner. It also seems to result from the coalescence of many smaller bands. In the residual step (on the stress plateau), a second main band appeared, parallel to the previous one. Additionally, several conjugated small bands existed in the relay area between the main band. The bands persisted in the next increments (not shown). The volume strain was compactant in the bands. The inclination of the early bands before the stress peak, with respect to the axial loading direction, was about  $45^\circ$ , which stayed around  $45^\circ$  at the end of the test. This was also observed in [BDR00], based on *post-mortem* X-ray CT scans.

To conclude, these observations show the progressive nature of the strain localization process in porous sandstone. The strain localization is dependent on mean stress. A common observation between the two tests, one of which was performed at 20 MPa lateral stress and the other at 50 MPa, was the early diffuse strain localization, well before the stress peak. Once the stress *vs.* strain curve lost its linearity, a complex pattern of parallel and conjugated bands appeared, oriented at about  $45^\circ$  with respect to the axial direction. At 20 MPa, the bands dilated and induced a global volume dilatancy, while they were compactant at 50 MPa and extended the global specimen compacting regime. The number of active bands decreased during the subsequent loading to a very small number after the peak. The inclination of the bands, after the peak, stayed constant at 50 MPa, while it decreased significantly at lower mean stress.

## 5.2 Strain localization in a clayey rock

We selected two tests performed on Callovo-Oxfordian clayey rock. Tests BxR\_COx\_06 and BxR\_COx\_13 were performed at a lateral stress of 12 MPa, which corresponded to the *in situ* stress of the material.

Figure 22 shows the stress-strain response and global volume curve measured for the test BxR\_COx\_06. There was small curvature at first, then a quasi linear part in the stress *vs.* strain curve, followed by an curvature up to a stress peak and a progressive and then sudden strain softening. The loss of control during the softening was due to the relative low cell stiffness compared to the specimen's stiffness. The loop of the curve after the fast softening was due to a delay in the axial piston pressure control. The stress level stabilized at the end of the test (plateau). The global volume strain

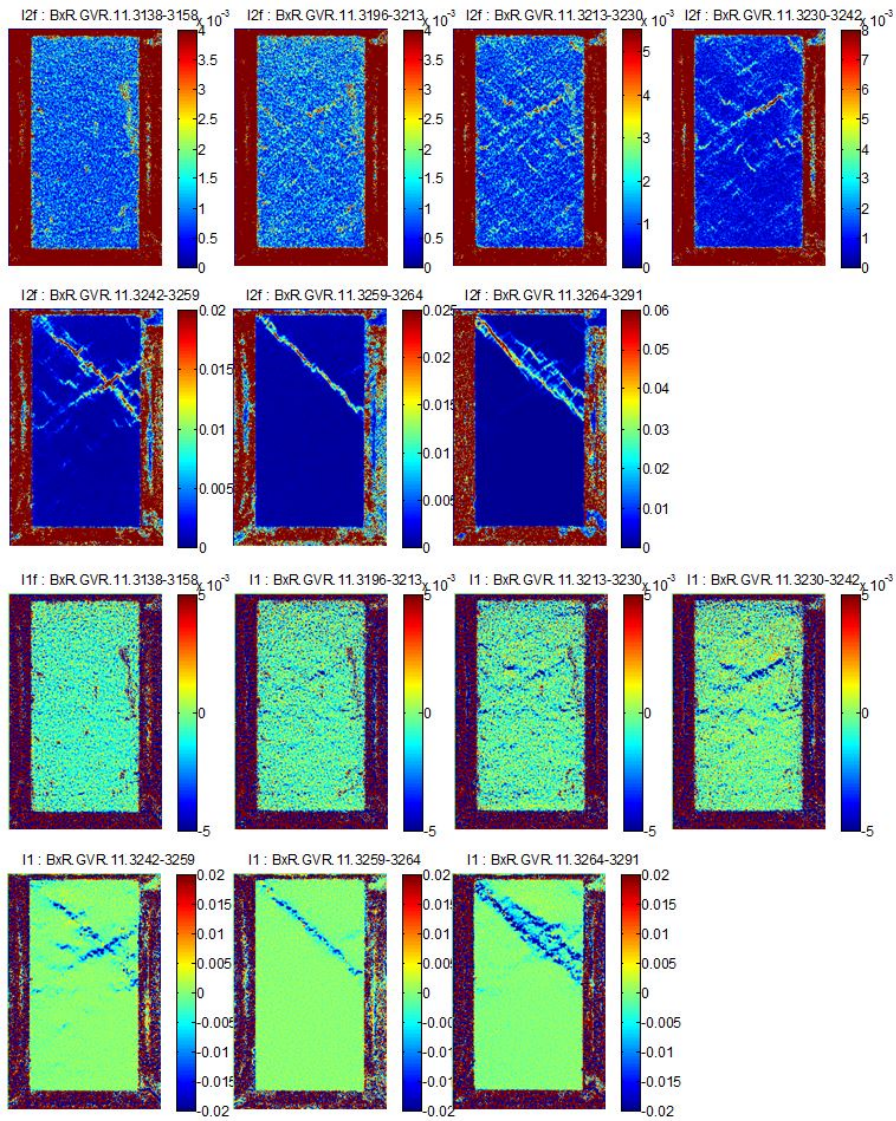


Figure 21: Test BxR\_GVR\_11: (the two first lines) incremental second strain tensor invariant (shear strain) fields; the numbers at the top of pictures correspond to the photographs numbers. (the two last lines) incremental first strain tensor invariant (volume strain) fields. (from [Lan14]).

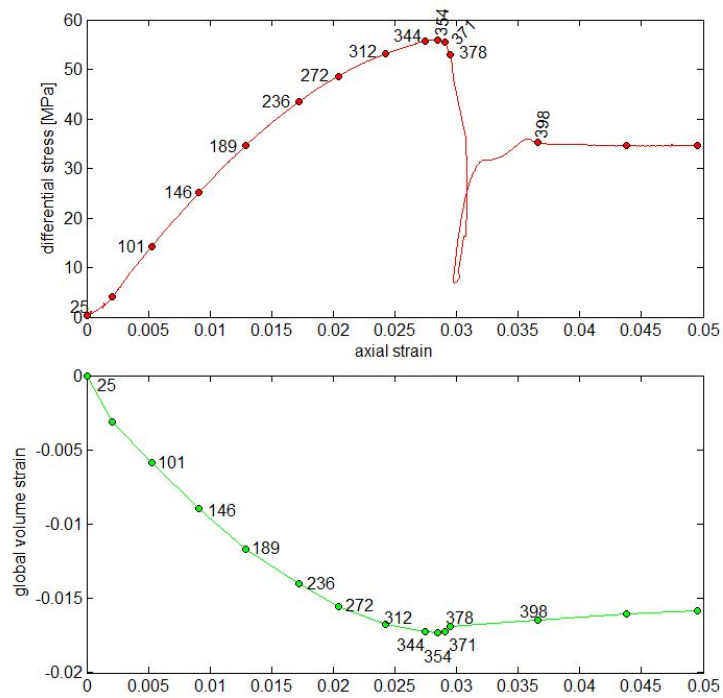


Figure 22: Test BxR.COx\_06: (top) differential stress ( $\sigma_1 - \sigma_3$ ) vs axial strain and (bottom) volume strain vs axial strain ; the numbers noted on each curve are the selected photographs numbers. (from [B12]).

compacted at the beginning and the compaction was progressively reduced up to a maximum, after which the specimen dilated slightly and, then the volume strain rate vanished. The maximum compaction corresponded to the stress peak of the upper curve.

Some photographs were selected during the test (Figure 22) and the incremental strain fields between these images are presented in Figure 23. The strain field is quite homogeneous during the linear part of the stress *vs.* strain curve (increment 0025-0101). The small fluctuations in both shear and volume strains corresponded to the noise of the DIC measure. However, at the lower third of the specimen there was a shear stress concentration on the left side. This area corresponded to a large calcite inclusion very close to the observed surface of the specimen, which was observed by X-ray CT after the test. The contrast in stiffness between the large inclusion and the rock matrix induced this strain concentration. Once the stress *vs.* strain curve showed a small curvature (increment 0146-0236), the appearance of shear strain field changed. It was not noisy like the previous increment but instead seemed structured. A very dense pattern of parallel and conjugated shear bands seemed to emerge. This pattern was confirmed in the next increments 0169-0272, 0272-0312 and 0312-0344. During these increments, one first observes that the initial strain concentration detected in the first increment propagated progressively as a shear band. Moreover, during the pre-peak steps, the number of active bands of the pattern decreased progressively. Only three bands were still active at the stress peak (increment 0344-0354), two of them propagated from the top-right and bottom-left corners. These two bands continued to propagate during the strain softening (increment 0371-0378). The term *fault propagation* should be more appropriate here; indeed, the strong strain intensity suggests a material discontinuity. Only one fault was active on the stress plateau: the fault initiated from the top-right corner. The propagation of this fault during the previous increment (0371-0378) showed that the process zone in front of the fault was itself composed of several parallel and conjugated shear bands.

As far as the volume strain fields are concerned, some horizontal "bands" were observed, that corresponded to a well-known artifact of the DIC method, generally due to the subpixel step. They had no physical meaning. The first volume strain localization was observed at increment 0371-0378, where the fault dilated (propagation in a mixed mode I and II). This corresponded to the global dilatancy of the specimen. The volume strain in the last increment showed some area of compaction and dilatancy around the fault. This is probably evidence of roughness in the fault, where some areas resist sliding more. The inclination of early bands before the stress peak, with respect to the axial loading direction, was about 45°.

Figure 24 shows the stress-strain response and global volume curve measured for the test BxR\_COx\_13, performed in the same conditions as for BxR\_COx\_06. It differed a little from the previous test because of the strong initial curvature of the stress *vs.* strain curve and its lower stress peak. This questions the low experimental reproducibility on such materials, mainly due to their natural heterogeneity.

The incremental strain fields are presented in Figure 25. The quality of the digital

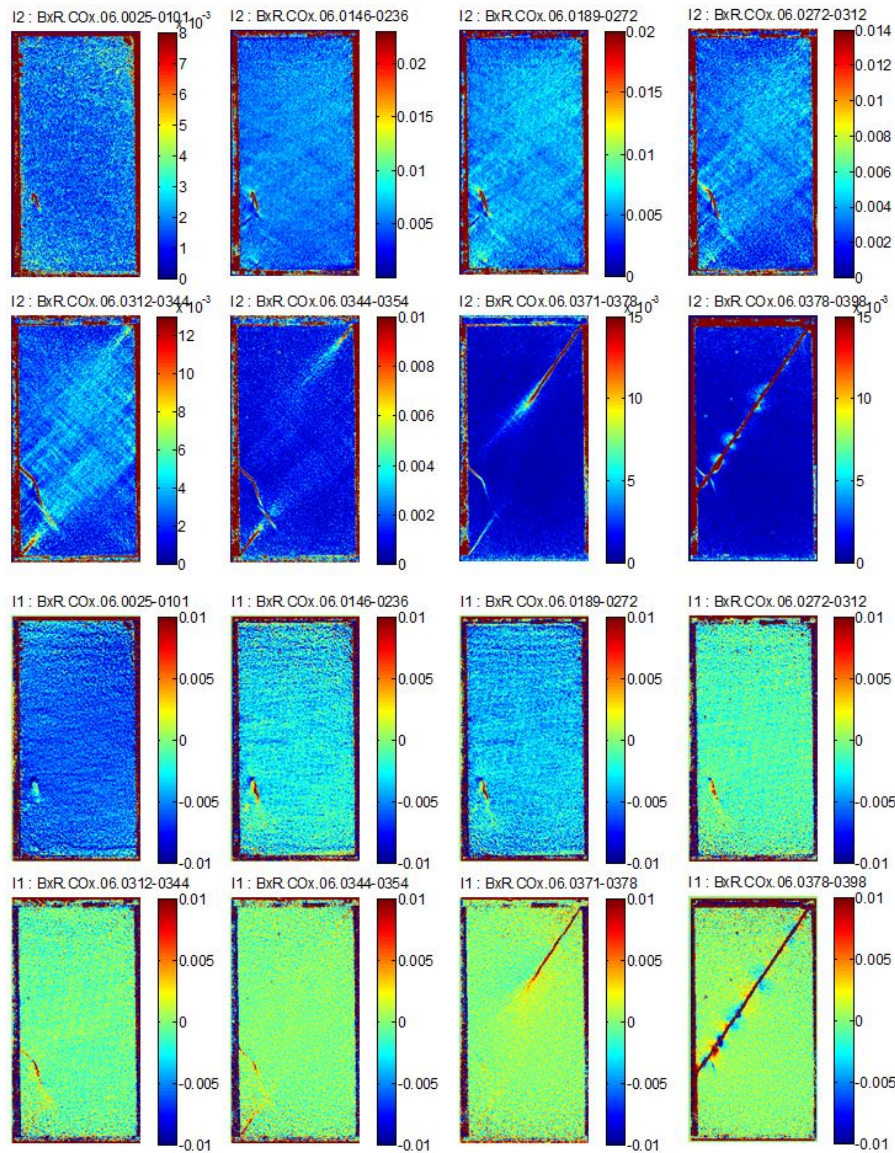


Figure 23: Test BxR\_COx\_06: (the two first lines) incremental second strain tensor invariant (shear strain) fields; the numbers at the top of pictures correspond to the photographs numbers. (the two last lines) incremental first strain tensor invariant (volume strain) fields. (from [B12]).

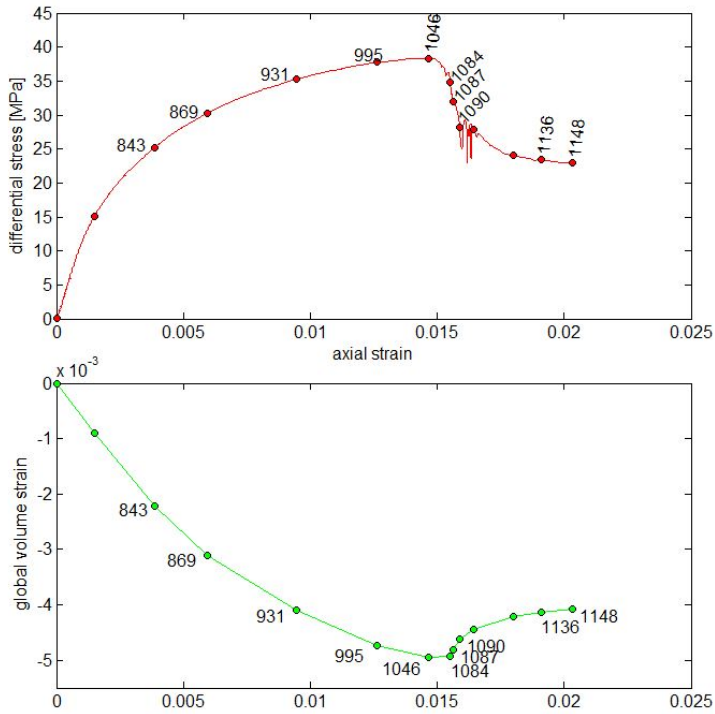


Figure 24: Test BxR\_COx\_13: (top) differential stress ( $\sigma_1 - \sigma_3$ ) vs axial strain and (bottom) volume strain vs axial strain ; the numbers noted on each curve are the selected photographs numbers. (from [B12]).

image is not as good as in the previous test. This can be due to the quality of the synthetic speckle or the camera's focus adjustment, which impacted the quality of the DIC results and the ability to detect small details. The results were not as fine as those for test BxR\_COx\_06. However, the usual dense pattern of parallel and conjugated shear bands was observed in increments 0931-0995 and 0995-1046. More interesting was the evolution after the stress peak. A large band composed of several parallel and conjugated bands was observed in increment 1046-1084. During the following increment, the width of the large band decreased progressively to converge to one band, which became a fault. The transition from strain localization to a fault here resulted from a condensation, during which the external bands were progressively de-activated, and the central band stayed active to evolve toward a fault.

Also the process of localization was progressive in a clayey rock and showed some early shear bands in a complex pattern, well before the stress peak. The early bands were very numerous, thin and close together. The thickness of the shear bands in a material with such a fine microstructure could not be measured with the digital camera used here. However, the band thickness was quite obvious directly linked with the microstructure internal's lengths. The volume strain inside the band showed a small dilatancy for this clay rock and the mean stress level used here. The two tests showed two examples of transition from shear bands to faults. One was by a fault propagation in a strain-localized pattern, with evidence of strain localization in the process zone. The other came from a phenomenon of condensation: a large band comprised several thinner bands became condensed by a de-activation of external thin bands. The few remaining bands became faults that coalesced to form a major fault.

## 6 Conclusions

Until now, the phenomenon of strain localization in geomaterials was understood as a propagation of shear bands or the birth of an abrupt shear band from a diffuse strain field associated with the stress peak of the specimen's response. The strain softening of the material in the bands induced a global softening of the specimen. Historically, this aspect came from observations of the specimens after the tests, in which relatively simple patterns of shear bands or faults were generally observed. This was also enforced by the theoretical approach of shear band analysis using bifurcation theory. This approach is generally quite consistent with experimental results at the stress peak.

The development of more efficient imaging tools and methods for full-field measurement has allowed better quantification of the deformation with better space and time resolutions and at a smaller scale. The recent results on a broad range of soil and porous rock suggest that the transition from a diffuse regime to a localized regime is more progressive than what is recalled above. A complex pattern of numerous parallel and conjugated shear bands appears well before the stress peak. These diffuse shear-band patterns can generate volume strain, dilatancy or compaction, depending

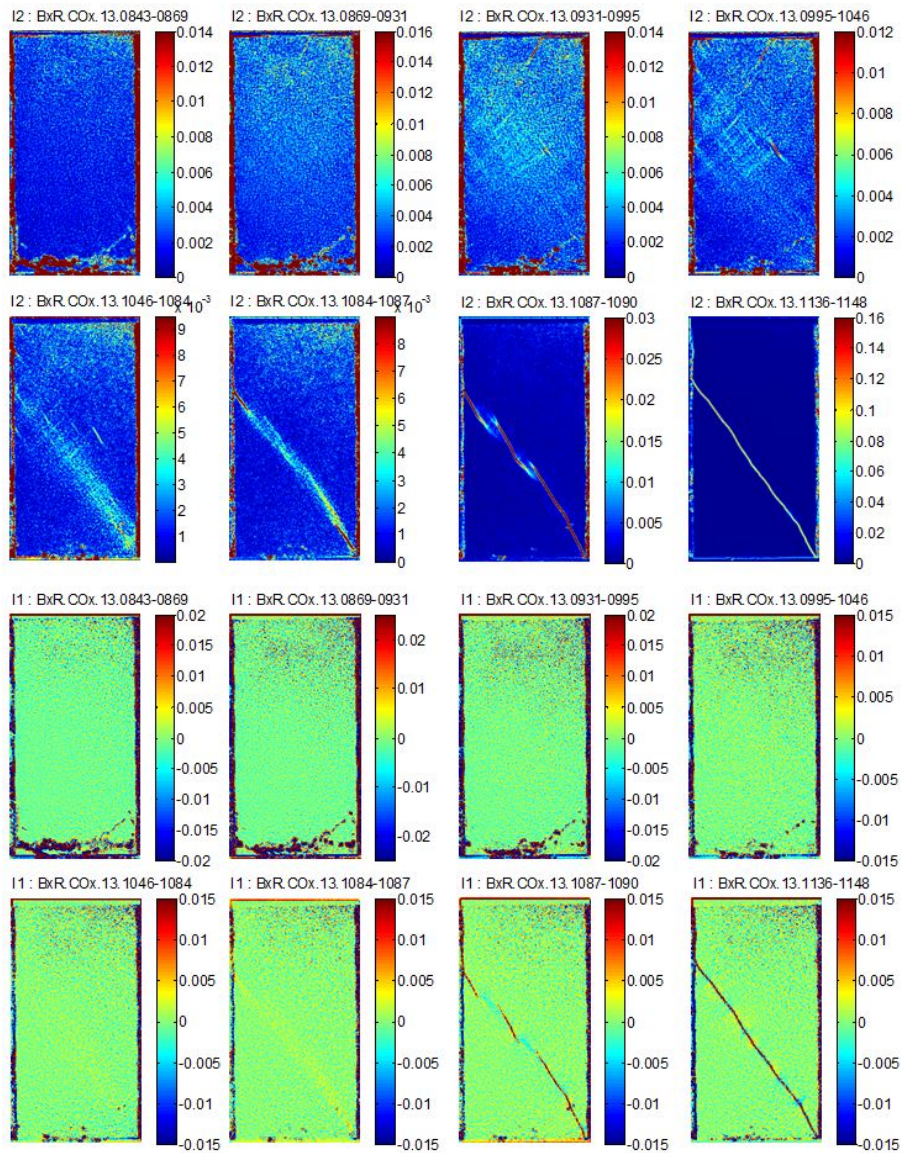


Figure 25: Test BxR\_COx\_13: (the two first lines) incremental second strain tensor invariant (shear strain) fields; the numbers at the top of pictures correspond to the photographs numbers. (the two last lines) incremental first strain tensor invariant (volume strain) fields. (from [B12]).

on the material and stress state. Some bands are progressively de-activated, and close to the stress peak, only a few shear bands stay active which concentrates the deformation. They are generally prone to strain softening, inducing global strain softening. In cohesive materials, these shear bands can evolve as faults or gouge zones of granular materials.

The recent trend of developing *in situ* micro-experiments to quantify the micro mechanisms of deformation at the scale of the microstructure should improve our understanding of early strain localization. In parallel, early band prediction appears to be a challenge for constitutive law development and numerical computation.

## References

- [AHD<sup>+</sup>12] E.C. Andò, S.A. Hall, J. Desrues, G. Viggiani, and P. Bésuelle. Experimental micromechanics: a triaxial test on sand observed at the grain scale. *Géotech. Lett.*, 2(3):107–112, 2012.
- [AHV<sup>+</sup>12] E. Andò, S.A. Hall, G. Viggiani, J. Desrues, and P. Bésuelle. Grain-scale experimental investigation of localised deformation in sand: a discrete particle tracking approach. *Acta Geotechnica*, 7(1):1–13, 2012.
- [And15] E.C. Andò. *Experimental investigation of microstructural changes in deforming granular media using x-ray tomography*. PhD thesis, University of Grenoble, France, <https://tel.archives-ouvertes.fr/tel-01144326>, 2015.
- [B99] P. Bésuelle. *Déformation et Rupture dans les Roches Tendres et les Sols Indurés : Comportement Homogène et Localisation*. PhD thesis, University of Grenoble, France, <https://tel.archives-ouvertes.fr/tel-00069471>, 1999.
- [B01a] P. Bésuelle. Compacting and dilating shear bands in porous rock: Theoretical and experimental conditions. *J. Geophys. Res.*, 106(B7):13435–13442, 2001.
- [B01b] P. Bésuelle. Evolution of strain localisation with stress in a sandstone: Brittle and semi-brittle regimes. *Phys. Chem. Earth, Part A*, 26(1-2):101–106, 2001.
- [B12] P. Bésuelle. Localisation des déformations dans l’argilite du Callo-Oxfordien. In *Internal communication*, 2012.
- [BBD<sup>+</sup>08] M. Bornert, F. Brémand, P. Doumalin, J.-C. Dupré, M. Fazzini, M. Grédiac, F. Hild, S. Mistou, J. Molimard, J.-J. Orteu, L. Robert, Y. Surrel, P. Vacher, and B. Wattrisse. Assessment of digital image correlation measurement errors: methodology and results. *Experim. Mech.*, 3:353–370, 2008.

- [BCD<sup>+</sup>04] M. Bornert, J.M. Chaix, P. Doumalin, J.C. Dupré, T. Fournel, Dominique Jeulin, E. Maire, M. Moreaud, and Hervé Moulinec. Mesure tridimensionnelle de champs cinématiques par imagerie volumique pour l'analyse des matériaux et des structures. *Instrumentation, Mesure, Métrologie*, 3-4:43–88, 2004.
- [BDR00] P. Bésuelle, J. Desrues, and S. Raynaud. Experimental characterisation of the localisation phenomenon inside a Vosges sandstone in a triaxial cell. *Int. J. Rock Mech. Min. Sci.*, 37(8):1223–1237, 2000.
- [BHA70] R. Butterfield, R.M. Harkness, and K.Z. Andrawes. A stereophotogrammetric method for measuring displacements fields. *Géotechnique*, 20(3):308–314, 1970.
- [BL16] P. Bésuelle and P. Lanatà. A new true triaxial cell for field measurements on rock specimens and its use in the characterization of strain localization on a Vosges sandstone during a plane strain compression test. *Geotech. Test. J.*, 39(5):1–12, 2016.
- [BLPC87] Z. Bažant, F.-B. Lin, and G. Pijaudier-Cabot. Yield limit degradation: Nonlocal continuum model with local strain. In D.R. Owen, E. Hinton, and E. Oñate, editors, *Computational Plasticity. Models, Software and Applications*, pages 1757–1780. Pineridge Press, Swansea, 1987.
- [BPC88] Z. Bažant and G. Pijaudier-Cabot. Nonlocal continuum damage, localization instability and convergence. *J. Appl. Mech.*, 55(2):287–293, 1988.
- [BR04] P. Bésuelle and J.W. Rudnicki. Localization: Shear bands and compaction bands. In Y. Guéguen and M. Boutéca, editors, *Mechanics of Fluid-Saturated Rocks*, pages 219–321. Academic Press, Elsevier, 2004.
- [BSFS99] B. K. Bay, T.S. Smith, D.P. Fyhrie, and M. Saad. Digital volume correlation: three-dimensional strain mapping using x-ray tomography digital volume correlation : three-dimensional strain mapping using x-ray tomography. *Experim. Mech.*, 39(3):217–2264, 1999.
- [CCM01] R. Chambon, D. Caillerie, and T. Matsushima. Plastic continuum with microstructure, local second gradient theories for geomaterials: localization studies. *Int. J. Solids Struct.*, 38(46-47):8503–8527, 2001.
- [Cos09] E. and F. Cosserat. *Théorie des Corps Déformables*. Hermann, Paris, 1909.
- [DCMM96] J. Desrues, R. Chambon, M. Mokni, and F. Mazerolle. Void ratio evolution inside shear bands in triaxial sand specimens studied by computed tomography. *Géotechnique*, 46(3):529–546, 1996.

- [Des98] J. Desrues. Localisation patterns in ductile and brittle geomaterials. In R. de Borst and E. van der Giessen, editors, *Material Instabilities in Solids*, pages 137–158. Wiley, New York, 1998.
- [Des04] J. Desrues. Experimental characterization of failure, degradation and instability in geomaterials. Progressive deformation and failure observed in laboratory specimens using strain field measurement methods. In I. Vardoulakis and P. Mira, editors, *ALERT Doctoral School 2004 - Failure, degradation and instabilities in geomaterials*, volume 8, pages 563–592, *Revue Française de Géotechnique*, 2004.
- [DRM07] C. David, P. Robion, and B. Menéndez. Anisotropy of elastic, magnetic and microstructural properties of the Callovo-Oxfordian argillite. *Phys. Chem. Earth, Part A*, 32:145–153, 2007.
- [DV04] J. Desrues and G. Viggiani. Strain localization in sand: an overview of the experimental results obtained in Grenoble using stereophotogrammetry. *Int. J. Numer. Anal. Meth. Geomech.*, 28:279–321, 2004.
- [DVH90] A. Drescher, I. Vardoulakis, and C. Han. A biaxial apparatus for testing soils. *Geotech. Test. J.*, 13(3):226–234, 1990.
- [FDP90] E. Flavigny, J. Desrues, and B. Palayer. Note technique : le sable d’Hostun ’RF’. *Rev. Franç. Géotech.*, 53, 1990.
- [FH97] N.A. Fleck and J.W. Hutchinson. Strain gradient plasticity. *Advances Appl. Mech.*, *Academic Press*, 33:295–361, 1997.
- [FSDG09] J. Fortin, S. Stanchits, G. Dresen, and Y. Guéguen. Acoustic emissions monitoring during inelastic deformation of porous sandstone: Comparison of three modes of deformation. *Pure Appl. Geophys.*, 166(1):823–841, 2009.
- [Gr4] M. Grédiac. The use of full-field measurement methods in composite material characterization: interest and limitations. *Composites: Part A*, 35:751–761, 2004.
- [Hal12] S.A. Hall. Digital image correlation in experimental geomechanics. In G. Viggiani, S.A. Hall, and Romero E., editors, *ALERT Doctoral School 2012 - Advanced experimental techniques in geomechanics*, pages 69–102, [http://www.alertgeomaterials.eu/internal/2012/school/2012\\_ALERT\\_school.pdf](http://www.alertgeomaterials.eu/internal/2012/school/2012_ALERT_school.pdf), 2012.
- [HBD<sup>+</sup>10] S.A. Hall, M. Bornert, J. Desrues, Y. Pannier, N. Lenoir, G. Viggiani, and P. Bésuelle. Discrete and continuum analysis of localised deformation in sand using x-ray  $\mu$ CT and volumetric digital image correlation. *Géotechnique*, 60(5):315–322, 2010.
- [HC00] B. Haimson and C. Chang. A new true triaxial cell for testing mechanical properties of rock, and its use to determine rock strength and deforma-

- bility of Westerly granite. *Int. J. Rock Mech. Min. Sci.*, 37(1-2):285–296, 2000.
- [Hil62] R. Hill. Acceleration waves in solids. *J. Mech. Phys. Solids*, 10:1–16, 1962.
- [Hsi09] J. Hsieh. *Computed Tomography Principles, Design, Artifacts, and Recent Advances*. Wiley, New York, 2nd edition, 2009.
- [KC01] R.A. Ketcham and W.D. Carlson. Acquisition, optimization and interpretation of X-ray computed tomographic imagery: applications to the geosciences. *Comput. Geosci.*, 27:381–400, 2001.
- [Lan14] P. Lanatà. *Full-field experimental characterization of mechanical behaviour and failure in a porous rock in plane strain compression: homogeneous deformation and strain localization*. PhD thesis, University of Grenoble, France, <https://tel.archives-ouvertes.fr/tel-01224997>, 2014.
- [LBAS<sup>+</sup>14] A. Le Bouil, A. Amon, J.-C. Sangleboeuf, H. Orain, P. Bésuelle, G. Viggiani, P. Chasle, and J. Crassous. A biaxial apparatus for the study of heterogeneous and intermittent strains in granular materials. *Granul. Matt.*, 16(1):1–8, 2014.
- [LBD<sup>+</sup>07] N. Lenoir, M. Bornert, J. Desrues, P. Bésuelle, and G. Viggiani. Volumetric digital image correlation applied to X-ray microtomography images from triaxial compression tests on argillaceous rock. 43:193–205, 2007.
- [Len06] N. Lenoir. *Comportement mécanique et rupture dans les roches argileuses étudiées par micro-tomographie à rayons X*. PhD thesis, University of Grenoble, France, <https://tel.archives-ouvertes.fr/tel-00011996/>, 2006.
- [Mog71] K. Mogi. Effect of the triaxial stress system on the failure of dolomite and limestone. *Tectonophysics*, 11:111–127, 1971.
- [MV87] H.-B. Mühlhaus and I. Vardoulakis. The thickness of shear band in granular materials. *Géotechnique*, 37(3):271–283, 1987.
- [PR82] W. Peters and W. Ranson. Digital imaging techniques in experimental stress analysis. *Opt. Eng.*, 21(3):427–431, 1982.
- [PW05] M.S. Paterson and T.-f. Wong. *Experimental Rock Deformation - The Brittle Field*. Springer, Berlin, second edition, 2005.
- [PXD06] B. Pan, H.-m. Xie, and F.-l. Dai. Performance of sub-pixel registration algorithms in digital image correlation. *Meas. Sci. Technol.*, 17:1615–1621, 2006.

- [Ric76] J.R. Rice. The localization of plastic deformation. In W.T. Koiter, editor, *Theoretical and Applied Mechanics*, pages 207–220, North-Holland Pub. Comp., Delft, 1976. Proc. 14th Int. Cong. Theor. Appl. Mech.
- [RSC<sup>+</sup>12] J.-C. Robinet, P. Sardini, D. Coelho, J.-C. Parneix, D. Prêt, S. Sammartino, E. Boller, and S. Altmann. Effects of mineral distribution at mesoscopic scale on solute diffusion in a clay-rich rock: Example of the Callovo-Oxfordian mudstone (Bure, France). *Water Resour. Res.*, 48:W05554, 2012.
- [SWPM83] M. Sutton, W. Wolters, W. Peters, and S. McNiell. Determination of displacements using an improved digital correlation method. *Image Vis. Comput.*, 1:133–139, 1983.
- [TO04] T. Takemura and M. Oda. Microstructure observation in deformed geomaterials using microfocus x-ray computed tomography. In J. Otani and Y. Obara, editors, *X-ray CT for geomaterials, soils, concrete, rocks*, pages 299–304, Kumamoto, 2004. Balkema, Rotterdam.
- [VA91] I. Vardoulakis and E.C. Aifantis. A gradient flow theory of plasticity for granular materials. *Acta Mechanica*, 387:197–217, 1991.
- [VG81] I. Vardoulakis and M. Goldscheider. Biaxial apparatus for testing shear bands in soils. In *10th ICSMFE*, number 4/61, pages 819–824. v, 1981.
- [VH12] G. Viggiani and S.A. Hall. Full-field measurements in experimental geomechanics: historical perspective, current trends and recent results. In G. Viggiani, S.A. Hall, and Romero E., editors, *ALERT Doctoral School 2012 - Advanced experimental techniques in geomechanics*, pages 3–67, [http://www.alertgeomaterials.eu/internal/2012/school/2012\\_ALERT\\_school.pdf](http://www.alertgeomaterials.eu/internal/2012/school/2012_ALERT_school.pdf), 2012.
- [VLMS02] A. Vautrin, J.R. Lee, J. Molimard, and Y. Surrel. Full-field optical techniques: applications to strain measurement and mechanical identification. In *Invited keynote at the 10th European conference on composite materials (ECCM10)*, [http://www.nottingham.ac.uk/home/eaziaj/photmechanics/Lee Full-field optical methods applications to strain measurement and mechanical identification\\_ECCM10\\_2002\\_keynote.pdf](http://www.nottingham.ac.uk/home/eaziaj/photmechanics/Lee%20Full-field%20optical%20methods%20applications%20to%20strain%20measurement%20and%20mechanical%20identification_ECCM10_2002_keynote.pdf), 2002.
- [VS95] I. Vardoulakis and J. Sulem. *Bifurcation Analysis in Geomechanics*. Blackie Academic & Professional, Glasgow, 1995.
- [VvRH04] E. Verhulp, B. van Rietbergen, and R. Huiskes. A three-dimensional digital image correlation technique for strain measurements in microstructures. *J. Biomech.*, 37:1313–1320, 2004.



---

## Numerical modelling of strain localization

**Panos Papanastasiou\* – Antonios Zervos\*\***

*\*Department of Civil and Environmental Engineering  
University of Cyprus  
P.O. Box 20537, 1678 Nicosia, Cyprus  
[panospap@ucy.ac.cy](mailto:panospap@ucy.ac.cy)*

*\*\*Faculty of Engineering and the Environment  
University of Southampton,  
Southampton SO17 1BJ, U.K.  
[az@soton.ac.uk](mailto:az@soton.ac.uk)*

---

*ABSTRACT. We present two higher order continua with microstructure that are used to regularize the ill-posed mathematical problem of strain-softening material to enable the modelling of progressive localization of deformation in zones of intense shearing that leads to failure of geomaterials and underground structures. The first model is based on a Cosserat plasticity model which in addition to the translational degrees of freedom of the classical continuum possesses independent rotation as well. The independent rotation introduces in the model curvatures and coupled stresses. The second higher order continuum is of gradient type and is called Gradient Elastoplasticity in which higher order deformation strains and internal length scales are present in both the elastic and the elastoplastic regime. The existence of the higher order strains requires numerical discretisation based on displacement formulation with a  $C1$  finite element. In both models the introduction of internal length, related to grain size, improve the computational stability and allows for robust progressive localization modelling in the post failure regime. It is demonstrated through examples that the models are capable of predicting advanced deformation modes such as surface buckling and localization of deformation in shear bands that may cause failure in a structure. As illustration we present results of two applications from geotechnical and petroleum geomechanics: the modelling of failure in thick walled cylinders under external and internal pressure and the stability of elliptical shape perforations. The obtained results show clearly a progressive failure mechanism and the computed modes are in a good qualitative agreement with laboratory and field observations*

## 1. Introduction

Failure in soil and rock masses is often accompanied by the concentration of deformation into narrow bands of intense shearing such as shear bands or shear interface layers. These bands may intersect the boundary of a free surface leading to failure. Near a failure state, the material inside these localisation zones, which are shown by experiments to have a finite thickness [Muh87], undergoes significant deformation and degradation, while the rest of the material remains rather inert.

During the last three decades numerous researches described localization phenomena in solids by utilizing the theory of equilibrium bifurcation. These studies were mainly analytical for the infinite-domain problem with various constitutive models and yielded mainly expressions for the critical hardening modulus and the localization band orientation angle at bifurcation; see for example in [Rud75]. Shear-band analyses for more complicated boundary-value problems and, more importantly, for post-localization analyses leading to failure can only be carried out computationally.

In order to link the above analytical bifurcation studies with the post-failure analysis we will explain here the terminology used in numerical analyses of stability and bifurcation problems. According to Figure 1 we distinguish among the primary branch (I) and the secondary branch (II), which intersects (I) at the bifurcation point. The primary path (I) corresponds to the trivial or homogeneous deformation solution whereas the secondary path corresponds to the localized deformation solution. The analytical studies mentioned above were restricted in the primary path and to the location of the bifurcation point [Var88, Pap89, Pap95a, Pap95b]. The bifurcation point is a singular point; thus the global stiffness matrix has at least one zero eigenvalue. In order to model localization at bifurcation point and beyond one has to switch from the primary to the secondary path. The method of switching from branch (I) to branch (II) is to perturb the primary solution with the eigenvector of the vanishing eigenvalue at the bifurcation point. Alternatively, one can introduce a material or a geometry imperfection to resort to an 'imperfect' structure which will follow the smooth branch (III), and is asymptotic to branches (I) and (II) in the relevant regimes. The introduction of a small imperfection transfers the bifurcation problem to a limit problem of branch III. At the limit point the slope of the load-displacement response is zero. We found that the Cosserat model and gradient models follow smoothly the branch (III) without the need to disturb the solution with the eigenvector of the zero eigenvalue [Pap92, Pap94]. The deformation pattern at the first equilibrium point after bifurcation is consistent with the eigenvector of the lowest eigenvalue.

Modelling of failure in rocks near underground openings requires the incorporation of 'extreme' dilation and 'extreme' strength loss in the material constitutive law [Ewy93]. Local or material softening can be considered as a macroscopic reflection of inhomogeneities at the microscopic scale (i.e. micro-cracks, weak spots, fissures etc.). The simplest way to account for these inhomogeneities in a continuum is by

smearing them in a strain-softening constitutive model. The material softening is the physical mechanism which triggers and promotes localization. However, a major drawback of strain-softening models is that it leads to loss of ellipticity of the governing equations [Var95] resulting in mathematically ill-posed boundary value problems, whose numerical analysis is sensitive to mesh refinement and convergence problems. Since in classical constitutive models there is no material length, the discretization sets the length scale. The localization region which is associated with strain softening, depends on the size of the mesh used for spatial discretization; i.e. the thickness and spacing of the shear-band are governed by the mesh size. A constitutive theory without internal length leads often to a softening zone of negligible thickness and hence at zero energy dissipation. Consequently, numerical computations based on classical theories give spurious or mesh dependent results in the post-peak regime.

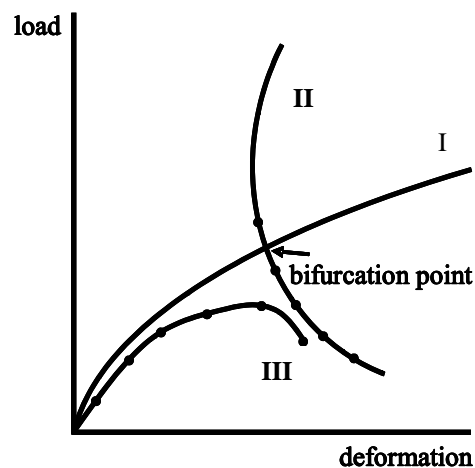


Figure 1: Primary and secondary branches in a bifurcation problem.

The governing equations can be regularised by resorting to higher order continuum theories. These theories take into account the micro-structure of the deforming solid through additional parameters of material length. These parameters are typically related either to the mean grain diameter or to some other, larger characteristic scale such as the microcrack length. The shear band thickness scales with this material length and is no longer indeterminate, allowing robust post-localisation numerical computations. In addition, the introduction of material lengths permits modelling of the scale effect that is often observed in geomechanics problems but cannot be modelled by classical theories.

Different methods for regularizing quasi-static, boundary-value problems with strain softening were proposed in the literature. Higher order theories found in the

literature include the Cosserat continuum theory [Cos09, Muh87, Pap92, Sul95], the Mindlin theory [Min64, Zer08a], non-local continua [Pij87], gradient plasticity, where higher-order derivatives of the plastic strain enter the yield function or certain constitutive quantities [Var91, Bor92, Aif92, Var92a, Var92b, Var94a, Var94b, Sul95, Cha98, Mat02], and gradient elastoplasticity [Zer01a, Zer01b, Zer07, Zer08b], where higher-order derivatives of the strain are used in both the elastic and the elastoplastic regime. The inclusion of gradient terms in both regimes ensures that the governing equations remain of the same order throughout the whole deformation history, avoiding the need for boundary conditions at the elastoplastic boundary. There is no a clear consensus which of the higher order continua is preferable, based on a better agreement of computational results with the experimental evidences. In order to decide among the various competing models one has to take into account the physics of the problem. For example if one considers stability of underground openings in sandstones in which there are evidences that initial localization is accommodated by grain rotations as sheared [Zer00] the Cosserat model appears to be appropriate. In applications characterized by strong deformation inhomogeneity the gradient models could be the choice.

In this chapter we describe the implementation of two higher order continua in finite element analysis to solve the ill-posed mathematical problem and mesh dependence problem of strain softening and to model localization of deformation and failure in boundary value problems. The first model is based on a Cosserat plasticity continuum which possesses micro-structure [Muh96]. The second model is of a gradient type and it is called gradient elastoplasticity. In this chapter we present first the Cosserat model in section 2. We describe briefly the governing equations in section 2.1, the numerical implementation in section 2.2, the material parameters in section 2.3 and two applications of localization modelling near underground openings of cylindrical cavity in section 2.4 and elliptical cavity in section 2.5. In the second part we present briefly the theory and the numerical formulation of gradient elastoplasticity, and use them to model the emergence of localisation of deformation in biaxial test specimens and in the cases of collapsing or expanding cylindrical cavities. The theory and numerical formulation are presented in Section 3.1. Sections 3.2 and 3.4 present numerical results and discussion for biaxial loading and expanding cavities respectively. Through the presented examples it is shown that the theories and the numerical formulations enable the tracking of emergent instabilities, robust modelling of the post-peak material behaviour leading to localisation of deformation and capturing quantitative details of the final localised failure mechanism. The final conclusions are drawn in section 4.

## 2. Cosserat Modelling

### 2.1 Governing equations

We describe briefly in this section the essentials of the Cosserat model [Cos09]. A full description of Cosserat plasticity theory can be found in [Muh87] and [Var95]. A Cosserat continuum possesses at material points, in addition to their translational degrees of freedom  $u_i$ , independent rotational degrees of freedom  $\omega_c$  as well (Figure 2). The displacements are defined by the motion of the material points, while the rotations are given independently by the micro-rotations represented by the orthogonal tensor. Point rotation and its gradient give rise to a non-symmetric stress tensor and to couple stresses, such that the non-symmetric part of the stress tensor is in equilibrium with the divergence of the couple stresses (Figure 2). A dimensional analysis reveals that micro-rotation gradients and couple stresses introduce an internal length into the problem. Considering a two-dimensional analysis, the state of deformation is described by the four components of the relative deformation

$$\begin{aligned} \varepsilon_{11} &= u_{1,1} & \varepsilon_{12} &= u_{1,2} + \omega^c \\ \varepsilon_{21} &= u_{2,1} - \omega^c & \varepsilon_{22} &= u_{2,2} \end{aligned} \quad (1)$$

and the two components of curvature given by the micro-rotation gradient

$$\kappa_1 = \omega_{,1}^c \quad \kappa_2 = \omega_{,2}^c \quad (2)$$

The above six kinematic quantities are conjugate in energy to six stress quantities. In the absence of body forces and body couple forces, force and moment equilibrium result in

$$\sigma_{ij,j} = 0, \quad m_{k,k} + \sigma_{21} - \sigma_{12} = 0 \quad \text{in } V \quad (3)$$

$$\sigma_{ij} n_j = t_i, \quad m_i n_i = m \quad \text{on } \partial V \quad (4)$$

where  $t_i$  and  $m$  prescribe tractions and couples on a part  $\partial V$  of the boundary of  $V$ . The symmetry of the stress tensor follows from equation (3) in the special case when the couple stresses or their divergence vanishes. As in classical plasticity in a Cosserat plasticity theory, generalized incremental strains are decomposed into an elastic and a plastic part

$$\varepsilon_{ij} = \varepsilon_{ij}^e + \varepsilon_{ij}^p \quad (5)$$

Elastic and plastic strains are defined here by generalizing the definition of elastic strain-energy potential, as well as the definitions for the yield surface and the plastic potential of the classical plasticity theory. The relationship between elastic strain and stress increment can be written as

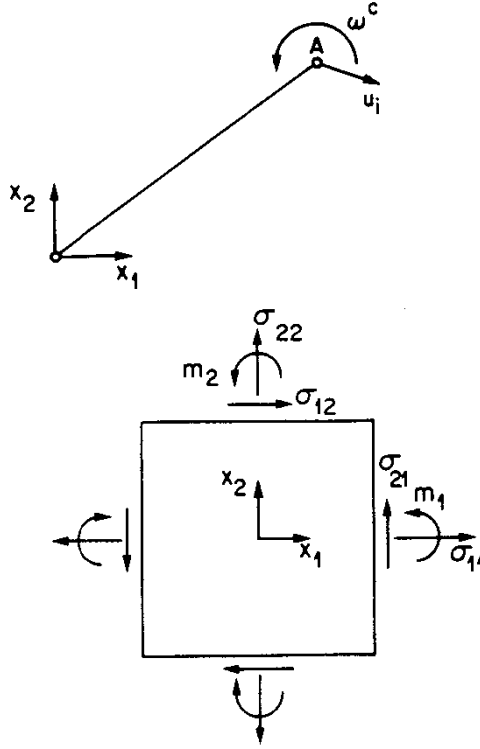


Figure 2: (a) Displacement and rotation field, (b) stresses and couple stresses in a Cosserat continuum.

$$d\epsilon_{ij}^e = \left\{ 2(h_1\delta_{ik}\delta_{jl} + h_2\delta_{jk}\delta_{il}) - \frac{k-1}{2k}\delta_{ij}\delta_{kl} \right\} \frac{d\sigma_{kl}}{2G} d\kappa_i^e = h_3 \frac{dm_i}{GR^2} \quad (6)$$

with  $\kappa=K/G=1/(1-2\nu)$ .  $G$ ,  $K$  and  $\nu$  are the elastic shear modulus, the compression modulus and Poisson ratio, respectively.  $R$  is the internal length which is defined through constitutive equations and  $h_i$  will be given below.

As in the classical flow theory of plasticity, plastic strains are generated when the yield condition is satisfied. The Mohr–Coulomb yield criterion can be written as

$$F = \frac{\tau}{p_0 + p} - \mu = 0 \quad (7)$$

where the material parameters are the mobilized friction coefficient  $\mu$  and the intercept  $p_0$  of the yield surface with the  $p$ -axis which is related to the material

cohesion,  $p_0=c/\tan\phi$ . In equation (7)  $p$  and  $\tau$  are invariant measures of average normal and shear contact tractions over the periphery of a macrocell of the ‘‘static’’ Cosserat model medium given in [Muh87]

$$p = \frac{\sigma_{kk}}{2} \quad \tau = \sqrt{(3s_{ij}s_{ij} - s_{ij}s_{ji})/4 + m_i m_i / R^2} \quad (8)$$

where  $s_{ij}$  is the deviatoric stress,  $s_{ij} = \sigma_{ij} + p\delta_{ij}$ . In the above definitions the internal length  $R$  can be identified as an equivalent radius of a typical grain or assembly of grains.

In this friction hardening/softening plasticity model we assumed that the friction coefficient  $\mu$  is a function of a plastic hardening parameter,  $\mu = \mu(\gamma^p)$  and the intercept  $p_0$  of the yield surface with the  $p$ -axis is a material constant. Hardening is taking place when  $\mu$  is monotonously increasing and softening when  $\mu$  is monotonously decreasing with increasing  $\gamma^p$ . The hardening parameter is defined as the integral over the entire loading history of the increment of the generalized plastic shear strain,  $\gamma^p = \int d\gamma^p$ .

The plastic shear-strain increment,  $d\gamma^p$ , is defined so that it is energy conjugate to the generalized shear stress intensity  $\tau$  in equation (8)

$$d\gamma^p = \sqrt{(3d\varepsilon_{ij}^p \varepsilon_{ij}^p + \varepsilon_{ij}^p \varepsilon_{ji}^p) / 2 + R^2 dk_i^p dk_i^p} \quad (9)$$

where  $d\varepsilon_{ij}^p$  is the deviator of the plastic relative deformation. When the couple stresses  $m_i$  and curvatures  $dk_i^p$  vanish, the definitions of  $\tau$  and  $d\gamma^p$  in equations (8) and (9) coincide with those of the classical plasticity.

In analogy of the yield surface, we postulate a plastic potential to which the normality condition is applicable as

$$Q = \frac{\tau}{p_0 + p} - \beta \quad (10)$$

where  $\beta = \beta(\gamma^p)$  is the mobilized dilatancy coefficient. Plastic strain and plastic curvature increments are derived from the flow-rule

$$d\varepsilon_{ij}^p = d\gamma^p \frac{\partial Q}{\partial \sigma_{ij}} \quad (11)$$

For the case of  $\mu = \beta$  the material obeys an associated flow rule and the incremental plastic strain vector in stress space is normal to the yield surface. In the most general case geomaterials obey a non-associated flow rule. The actual value of  $d\gamma^p$  is determined from Prager’s consistency condition,  $F=0$  and  $dF=0$ .

## 2.2 Finite Element Formulation of Cosserat Model

The numerical implementation of the Cosserat model can be easily constructed with simple extension of the algorithms used in classical elastoplasticity to include the additional terms as it is explained below [Bor91, Pap92].

For finite element analysis it is convenient to express the equilibrium conditions (3) and (4) in a matrix form through the principle of virtual work

$$\int_V \{\delta \varepsilon\}^T \{\sigma\} dV = \int_{\partial V} \{\delta u\}^T \{t\} dS \quad (12)$$

where the vectors for the generalized displacement  $\{u\}$ , strain  $\{\varepsilon\}$ , stress  $\{\sigma\}$  and tractions  $\{t\}$  are defined by

$$\begin{aligned} \{u\}^T &= \{u_1, u_2, \omega^c\} & \{\varepsilon\}^T &= \{\varepsilon_{11}, \varepsilon_{22}, \varepsilon_{12}, \varepsilon_{21}, \kappa_1 R, \kappa_2 R\} \\ \{\sigma\}^T &= \{\sigma_{11}, \sigma_{22}, \sigma_{12}, \sigma_{21}, m_1 / R, m_2 / R\} & \{t\}^T &= \{t_1, t_2, m\} \end{aligned} \quad (13)$$

The introduction of  $R$  in the form of equation (13) makes the components of generalized stress and strain vectors to have the same dimensions and closer order of magnitude.

In Cosserat plasticity theory, the generalized incremental strains are decomposed into elastic and plastic parts as in classical plasticity

$$\{d\varepsilon\} = \{d\varepsilon^e\} + \{d\varepsilon^p\} \quad (14)$$

The relationship between elastic strain and stress increment is written in a single matrix equation

$$\{d\sigma\} = [D^e] \{d\varepsilon^e\} \quad (15)$$

where the matrix  $[D^e]$  contains the elastic parameters of a two dimensional, linear-elastic, isotropic Cosserat continuum defined by

$$[D^e] = \begin{bmatrix} K+G & K-G & 0 & 0 & 0 & 0 \\ K-G & K+G & 0 & 0 & 0 & 0 \\ 0 & 0 & G+G^c & G-G^c & 0 & 0 \\ 0 & 0 & G-G^c & G+G^c & 0 & 0 \\ 0 & 0 & 0 & 0 & M & 0 \\ 0 & 0 & 0 & 0 & 0 & M \end{bmatrix} \quad (16)$$

where  $G^C$  is the elastic stiffness of the Cosserat medium with respect to relative rotations and  $M$  is the normalized bending stiffness. For the so-called static Cosserat model in [Muh87] proposed

$$\frac{G^C}{G} = \frac{1}{2}, \quad \frac{M}{G} = R^2 \quad (17)$$

The plastic strain and plastic curvature increments are derived from the flow-rule

$$\{d\varepsilon^p\} = d\gamma^p \left\{ \begin{array}{c} \frac{\partial Q}{\partial \sigma} \end{array} \right\} \quad (18)$$

As mentioned before, the actual value of  $d\gamma^p$  is determined from Prager's consistency condition,  $F=0$  and  $dF=0$ ; the last equation results in

$$d\gamma^p = \frac{\left\{ \frac{\partial F}{\partial \sigma} \right\} \left( [D^e] \{d\varepsilon\} \right)}{\left\{ \frac{\partial F}{\partial \sigma} \right\} \cdot \left( [D^e] \left\{ \frac{\partial Q}{\partial \sigma} \right\} \right) + (p_0 + p)h_t} \quad (19)$$

where  $h_t = d\mu / d\gamma^p$  is the plastic modulus.

The stress increment  $\{d\sigma\}$  can be expressed in terms of the total strain increment

$$\{d\sigma\} = [D^{ep}] \{d\varepsilon\} \quad (20)$$

where the elastic-plastic stiffness matrix  $[D^{ep}]$  is given by

$$[D^{ep}] = [D^e] - \langle 1 \rangle \frac{\left( [D^e] \left\{ \frac{\partial Q}{\partial \sigma} \right\} \right) \cdot \left( [D^e] \left\{ \frac{\partial F}{\partial \sigma} \right\} \right)^T}{\left\{ \frac{\partial F}{\partial \sigma} \right\} \left( [D^e] \left\{ \frac{\partial Q}{\partial \sigma} \right\} \right) + (p_0 + p)h} \quad (21)$$

Loading of the yield surface  $F=0$  takes place when  $d\gamma^p > 0$  and accordingly the switch function  $\langle 1 \rangle$  in equation (22) is defined such that

$$\langle 1 \rangle = \begin{cases} 1 & \text{if } F = 0 \text{ and } d\gamma^p > 0 \\ 0 & \text{if } F < 0 \text{ or } \{F = 0 \text{ and } d\gamma^p \leq 0\} \end{cases} \quad (22)$$

Robustness in the computations and insensitivity of the results to general mesh refinement for the present Cosserat model has been demonstrated in [Pap92]. In contrast, computations based on classical elastoplasticity with the same material

parameters are mesh sensitive due to the implementation of the material softening in the constitutive equations.

### 2.3 Material Parameters

In the next computations the material parameters for the Mohr–Coulomb elastoplastic constitutive model were derived from triaxial compression tests on Castlegate sandstone and a calibration procedure.

The elastic parameters were found to be  $E=8,100$  MPa and  $\nu=0.35$ . The parameter related to the material cohesion is  $p_0=9.81$  MPa. The calibration of the friction coefficient,  $\mu=\sin\phi_m$  as a function of the plastic shearing strain  $\gamma^p$  was based on interpolation of pre-peak triaxial data. Post-peak softening behavior was modeled by extrapolation of a function which was fit to the pre-peak data. The corresponding curve-fit was given by the hyperbolic function

$$\mu = \mu_0 + \frac{(1 - c_0 \gamma^p) \gamma^p}{c_1 + c_2 \gamma^p} \quad (23)$$

where  $\mu_0=463$  is the value of the friction coefficient that defines the state of initial yield;  $c_1=0.0077$ ,  $c_2=7.5$  and  $c_0=12$  is a control parameter of the rate of softening.

The dilation coefficient  $\beta=\sin\psi_m$  was taken equal to the mobilized friction coefficient  $\mu$  because the Castlegate sandstone exhibits pronounced dilation in the low confinement pressure triaxial tests, i.e., an associated flow rule was assumed

$$\beta = \mu \quad (24)$$

The internal length required by the Cosserat model is set equal to  $R=0.2$  mm. This value is related to the microstructure of the sandstone, e.g., the grain size. We emphasize here that the inclusion of the grain size in the constitutive equations provides the Cosserat model with the capability to predict the scale effect observed in the thick walled cylinder tests.

### 5.1 Failure in thick walled cylinder test

We modeled the problem of a thick-walled cylinder under external pressure. The results are compared with those of a physical experiment. The main dimensions of the cylinder are the internal radius,  $r_a=1.45$  cm and the external radius,  $r_b= 7.5$ cm. The external pressure was applied incrementally while the internal pressure was maintained zero.

Figure 3 shows a comparison of the experimental results with model predictions in terms of the applied external pressure versus normalized hole closure. The solid line shows the closure in the direction of breakouts and the dashed line shows the closure in the direction  $90^\circ$  from the breakouts. The initial part of the curve is almost linear although initial yielding at the hole wall takes place quite early, below 10 MPa. The first signs of failure in the experiment were observed after the pressure had reached 35 MPa. This prediction is well compared with the bifurcation point detected by the break of axisymmetry at pressure 34.75 MPa.

After bifurcation the deformation is characterized by a warping mode of finite wave number  $m=10$ , caused by surface buckling. As mentioned earlier the Cosserat model switches to the localized branch smoothly, without the need to perturb the primary solution with an imperfection. The computations confirmed that in the primary path the Cosserat rotation remains inactive everywhere, whereas after localization it increases by more than three orders of magnitude only on the boundaries of the shear bands due to the intense shearing [Pap92]. The predicted failure mode is depicted in Figure 4 where the contours of the plastic strain have been drawn in the vicinity of the hole after localization of deformation has taken place. Once localization of deformation starts, almost all the region close to the borehole wall unloads elastically, except the narrow zones of the forming shear bands, which continue to plastically soften and progress towards the interior. The shear bands bend further until they finally meet their symmetric image, leading to a familiar breakout form. Similar computations and extensive analysis can be found in [Pap92, Pap10].

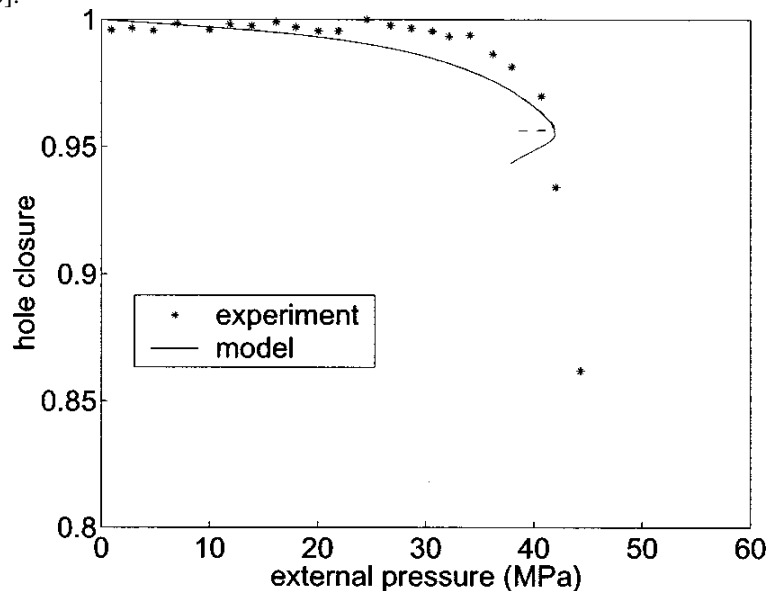


Figure 3: External pressure vs normalized hole closure.

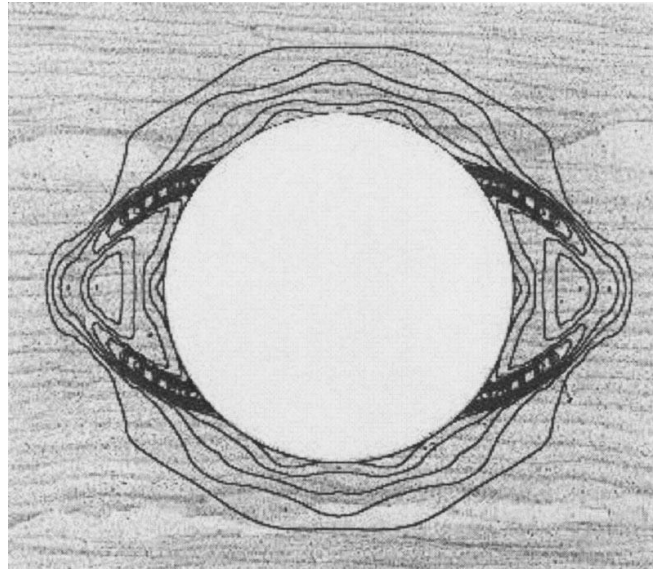


Figure 4: Contours of the shear plastic strain after localization of deformation.

We carried out a series of computations to investigate the issue of scale effect. Experimental results showed that small holes, compared to large holes, fail at higher external pressure [Hai89, Pap95, Hoe00, Pap10]. Computations were performed for models with different internal radii but with fixed ratio 5:1 of the external radius to the internal. The results are shown in Figure 5 where we plotted the load at which bifurcation takes place (dashed line) and the peak load (solid line) as a function of the hole radius normalized by the internal length. It is clear that both bifurcation and peak loads increase as the hole radius decreases. For very small holes bifurcation does not take place and limit point is reached. Smaller holes bifurcate with lower warping modes. The scale effect fades out rapidly with increasing hole size. As the hole gets bigger, the scale effect becomes less pronounced, a tendency also observed in the experiments of [Hai89, Pap95]. The scale effect also fades out for very small hole size because bifurcation disappears and the load reaches a limit value. This finding is also supported by experimental results discussed in detail by [Hoe01]. Bifurcation in the limit of a large borehole, which approaches a half space, is expected to take place with infinite wavelength mode once the stress state enters the softening regime for associated material.

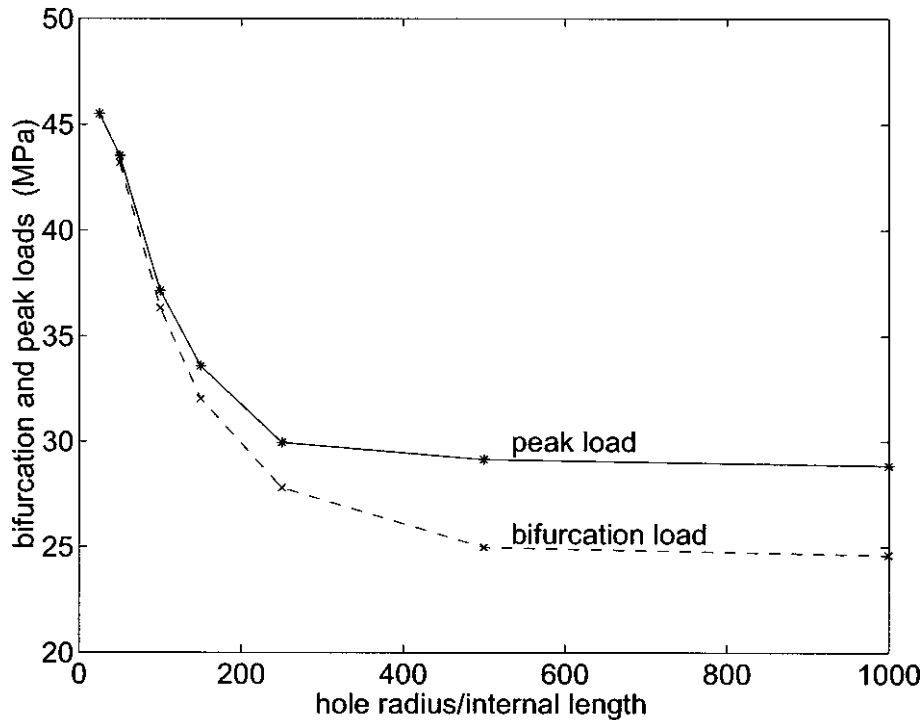


Figure 5: Bifurcation load and peak load vs normalized hole radius.

## 5.2 Stability analysis of elliptical shape perforations

In another illustration we present in this section a stability analysis of elliptical shape perforations embedded in a compressive stress field. The material parameters are those of the Castlegate sandstone which were used in the above computations. The application is related to the stability of perforation tunnels that are used for the flow of hydrocarbon in the wellbores. It is demonstrated that it is essential to carry out advanced localization analysis in order to reach correct results upon which a new perforation shape design can be based. Classical stress analysis predicts that an elliptical hole suffers less stress concentration than a circular hole when its major axis is aligned with the direction of the major principal stress and its axis ratio is the same as the applied stress ratio. However, this failure analysis based on localization of deformation will show that an elliptical hole is stronger if its axis ratio is greater than the ratio of the applied stresses.

Figure 6 shows the hole closure in terms of a change in cross-sectional area vs applied maximum insitu stress ( $\sigma_{\max}/\sigma_{\min}=1.5$ ) for a circular hole,  $a/b=1$ , and the elliptical holes with axis ratio  $a/b=1.5, 3$ .

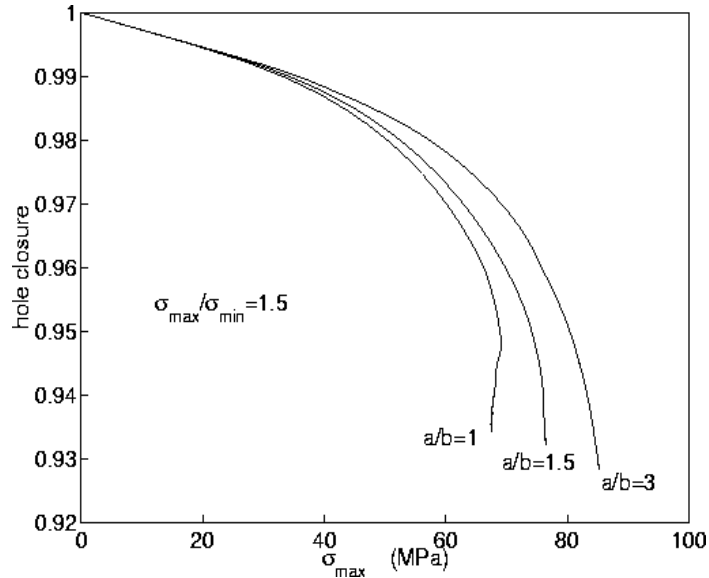


Figure 6: Hole closure vs applied stress for a circular hole and elliptical perforations with different ratio of the major/minor axis,  $a/b$ .

The predicted failure mode is depicted in Figures 7 and 8 where the displacement fields after localization and the contours of the plastic shear strain were drawn for the circular hole and for an elliptical hole. Although an elastic stress analysis suggests through the stress concentration near the hole that the more stable ellipse is the one with its axis ratio the same as the ratio of the applied stresses, this localization analysis has shown that an ellipse with axis ratio greater than the ratio of the applied in situ stress is even stronger. More computations and details can be found in [PAP 00].

To mention few other applications, [Tei93] analysed interface mechanisms in silos filled with granular medium which was simulated by the aforementioned Cosserat plasticity model. [Adh97] used Cosserat model for layered materials. More recently [Pap10] studied the stability of a borehole in anisotropic stress field and compared the predictions of the Cosserat model with experimental data.

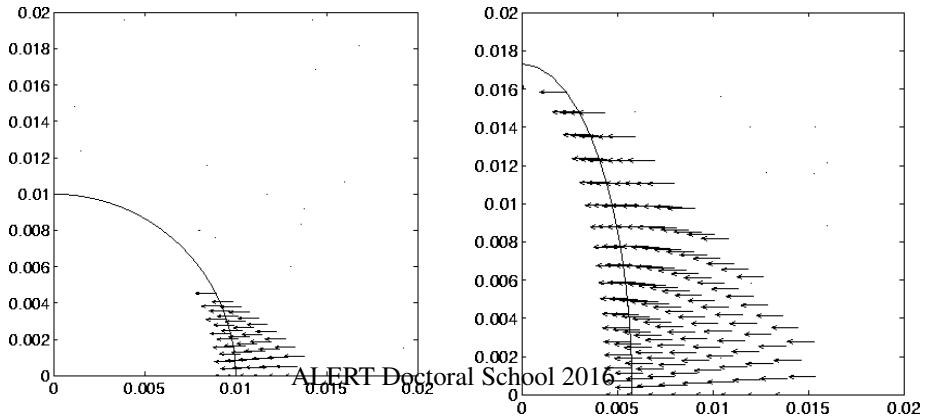


Figure 7: Incremental displacement field after localization of deformation around a circular hole and elliptical hole.

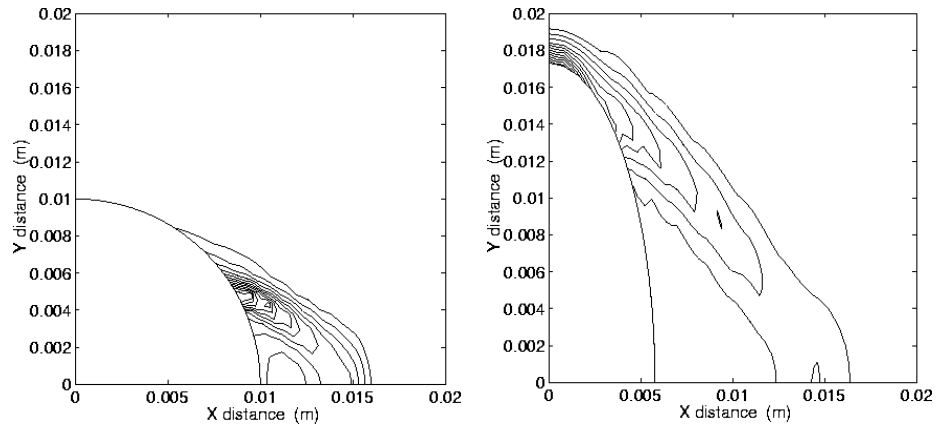


Figure 8: Contours of shear plastic strain around a circular hole and an elliptical hole.

### 3. Gradient Elastoplasticity

#### 3.1 Governing equations

Following decomposition of the total strain rate  $\dot{\epsilon}_{ij} = \dot{\epsilon}_{ij}^e + \dot{\epsilon}_{ij}^p$  into an elastic part  $\dot{\epsilon}_{ij}^e$  and a plastic part  $\dot{\epsilon}_{ij}^p$ , we define the total (equilibrium) stress rate  $\dot{\sigma}_{ij}$  in terms of the elastic strain rate and its Laplacian, as

$$\dot{\sigma}_{ij} = C_{ijkl}^e \left( \dot{\epsilon}_{kl}^e - l_e^2 \nabla^2 \dot{\epsilon}_{kl}^e \right) \quad (25)$$

Here  $C_{ijkl}^e$  is the tensor of elastic moduli and  $l_e$  is a material parameter with dimension of length, called the *elastic material length*. Also, we omitted the first spatial derivative from equations (25) to avoid introducing directionality in the

material response. Plastic deformations develop when the stress state meets the yield condition  $F(\tau_{ij}, \psi) = 0$ . The plastic strain rate is defined through the flow rule

$$\dot{\epsilon}_{ij}^p = \dot{\psi} \frac{\partial Q}{\partial \tau_{ij}} \quad (26)$$

where  $Q(\tau_{ij}, \psi)$  is a plastic potential and the scalar quantity  $\dot{\psi}$  is the plastic multiplier. In the special case of associative plasticity,  $Q \equiv F$ .

The yield function  $F$  and the plastic potential  $Q$  depend on the reduced stress  $\dot{\tau}_{ij} = \dot{\sigma}_{ij} - \dot{\alpha}_{ij}$  and on a hardening/softening parameter  $\psi$ . The back stress  $\dot{\alpha}_{ij}$  evolves according to the constitutive law

$$\dot{\alpha}_{ij} = -l_p^2 C_{ijkl}^e \nabla^2 \dot{\epsilon}_{kl}^p \quad (27)$$

where the scalar  $l_p$  is another material parameter with dimension of length, called the *plastic material length*. As back stresses are expected to develop due to micro-inhomogeneities in the plastic flow, an assumption that the back stress is proportional to the plastic strain as well as its Laplacian would be more accurate. However, here we confine ourselves to the simpler assumption that back stresses develop only where the deformation becomes sufficiently inhomogeneous, allowing for the region surrounding a material point to contribute to its strength.

The plastic strains are determined from the consistency condition of plasticity,

$$F(\tau_{ij}, \psi) = 0 \quad , \quad \text{and} \quad \dot{F}(\tau_{ij}, \psi) = \frac{\partial F}{\partial \tau_{ij}} \dot{\tau}_{ij} + \frac{\partial F}{\partial \psi} \dot{\psi} = 0 \quad (28)$$

which ensures that during plastic deformation the stress state remains on the evolving yield surface.

Substituting equations (25), (26) and (27) into equation (28), using the strain rate decomposition and the definition of the reduced stress, and assuming that  $\partial F / \partial \tau_{ij}$  and  $\partial Q / \partial \tau_{ij}$  vary slowly in space, the plastic multiplier is expressed as

$$\left[ 1 - \frac{H_0}{H} (l_e^2 + l_p^2) \nabla^2 \right] \dot{\psi} = \frac{1}{H} \frac{\partial F}{\partial \tau_{ij}} C_{ijkl}^e (\dot{\epsilon}_{kl} - l_e^2 \nabla^2 \dot{\epsilon}_{kl}) \quad (29)$$

Where

$$\text{where } H = H_0 + H_t, \quad H_0 = \frac{\partial F}{\partial \tau_{ij}} C_{ijkl}^e \frac{\partial Q}{\partial \tau_{kl}} \quad \text{and} \quad H_t = - \frac{\partial F}{\partial \psi}$$

An approximate solution of equation (29) can be obtained by noting that  $H_0/H \approx 1$  and that both  $l_e$  and  $l_p$  are small, since they represent some microstructural length scale of the material. The differential operator applied on the left hand side of equation (29) can then be inverted and transferred to the right hand side. Neglecting higher order terms, equation (29) then yields [Zer01a]

$$\dot{\psi} = \frac{1}{H} \frac{\partial F}{\partial \tau_{ij}} C_{ijkl}^e (\dot{\epsilon}_{kl} + l_c^2 \nabla^2 \dot{\epsilon}_{kl}) \quad (30)$$

where

$$l_c^2 = \frac{H_0}{H} l_p^2 - \frac{H_t}{H} l_e^2 > 0$$

The assumption of slow spatial variation of  $\partial F / \partial \tau_{ij}$  and  $\partial Q / \partial \tau_{ij}$ , on which the derivation of equation (29) is based, is only valid for an initial bifurcation from a relatively homogeneous ground state of plastic straining. In the post-bifurcation regime this assumption progressively breaks down as deformations localise. Then terms  $\nabla^2 (\partial F / \partial \tau_{ij})$  and  $\nabla^2 (\partial Q / \partial \tau_{ij})$  are not necessarily negligible. However the inclusion of such terms would necessitate a rather complicated numerical treatment of the consistency condition and lead to strongly non-linear and expensive calculations.

Here we use equations (29) and (30) even in the post-localization regime, bearing in mind their approximate nature. Numerical results obtained using this approach have been shown to reproduce in a realistic manner localization phenomena observed in experiments [Zer01a, Zer01b, Zer02].

For a total strain increment  $\dot{\boldsymbol{\epsilon}}_{ij}$ , equations (26) and (30) can be used to calculate the plastic part  $\dot{\boldsymbol{\epsilon}}_{ij}^p$ . The elastic part is then  $\dot{\boldsymbol{\epsilon}}_{ij}^e = \dot{\boldsymbol{\epsilon}}_{ij} - \dot{\boldsymbol{\epsilon}}_{ij}^p$ . Substituting to Equations (25) and (27), the constitutive quantities can be expressed in terms of total, rather than elastic and plastic strain increments as follows:

$$\dot{\boldsymbol{\sigma}}_{ij} = \mathbf{C}_{ijkl}^{ep} \dot{\boldsymbol{\epsilon}}_{kl} - \mathbf{C}_{ijkl}^m \nabla^2 \dot{\boldsymbol{\epsilon}}_{kl} \quad (31)$$

$$\dot{\boldsymbol{\alpha}}_{ij} = -l_p^2 \mathbf{C}_{ijkl}^p \nabla^2 \dot{\boldsymbol{\epsilon}}_{kl} \quad (32)$$

Here  $\mathbf{C}_{ijkl}^p$  is the known plastic stiffness matrix of classical plasticity

$$\mathbf{C}_{ijkl}^p = \frac{\langle 1 \rangle}{H} \mathbf{C}_{ijmn}^e \frac{\partial Q}{\partial \tau_{mn}} \frac{\partial F}{\partial \tau_{st}} \mathbf{C}_{stkl}^e \quad (33)$$

where  $\langle 1 \rangle = 1$  for loading (i.e.  $F = 0$  and  $\dot{\psi} \geq 0$ ) and  $\langle 1 \rangle = 0$  for unloading (i.e.  $F < 0$ , or  $F = 0$  and  $\dot{\psi} < 0$ ).  $\mathbf{C}_{ijkl}^{ep} = \mathbf{C}_{ijkl}^e - \mathbf{C}_{ijkl}^p$  is the usual elastoplastic stiffness matrix and

$$\mathbf{C}_{ijkl}^m = l_e^2 \mathbf{C}_{ijkl}^{ep} + l_c^2 \mathbf{C}_{ijkl}^p \quad (34)$$

is a stiffness matrix for the higher order terms.

Due to the approximation introduced to arrive to equation (30), the consistency condition is satisfied to an approximation  $\mathcal{O}((l_e^2 + l_p^2)^2)$ . In the numerical implementation presented in the next subsection, errors are prevented from accumulating by checking that the stress state of points undergoing plastic or neutral loading remains on the evolving yield surface and mapping it back if needed [Zer01a].

To derive the equation of virtual work, the above equations are reinterpreted within the framework of Mindlin's theory of microstructure [Min64]. It follows that they describe a restricted Mindlin continuum, i.e. a Mindlin continuum whose microscopic and macroscopic deformations coincide. To that end, equation (31) is rewritten as

$$\dot{\sigma}_{ij} = \dot{\sigma}_{ij}^{(0)} + \dot{\sigma}_{ij}^{(2)}, \quad \dot{\sigma}_{ij}^{(0)} = C_{ijkl}^{ep} \dot{\epsilon}_{kl}, \quad \dot{\sigma}_{ij}^{(2)} = -C_{ijkl}^m \nabla^2 \dot{\epsilon}_{kl} \quad (35)$$

In Mindlin's terminology  $\dot{\sigma}_{ij}^{(0)}$  is the Cauchy stress rate, which is identified as the constitutive stress rate tensor of classical elastoplasticity. The second term is seen as a relative stress rate. We postulate the existence of a double stress rate  $\dot{m}_{kij}$ , whose gradient equilibrates the relative stress. Then

$$\dot{\sigma}_{ij}^{(2)} + \dot{m}_{kij,k} = 0 \Rightarrow \dot{m}_{kij} = C_{ijmn}^m \dot{\epsilon}_{mn,k} \quad (36)$$

In the absence of body forces and inertial terms, the principle of virtual work is written as [Var95; Zer01a, Var91]

$$\int_V (\sigma_{ij}^{(0)} \delta \dot{\epsilon}_{ij} + m_{kij} \delta \dot{\epsilon}_{ij,k}) dV = \int_{S_\sigma} (t_i \delta \dot{v}_i + \mu_i n_k \delta \dot{v}_{i,k}) dS \quad (37)$$

where  $S_\sigma$  is the part of the boundary where Neumann-type boundary conditions are applied and  $n_i$  is its unit normal.  $t_i$  is the applied boundary traction vector,  $\mu_i$  the applied boundary double traction vector and  $\delta \dot{v}_i$  the virtual displacement rate vector.

### 3.2 Finite element formulation

Since the rate of all constitutive quantities can be expressed in terms of the total strain rate and its derivatives, the usual displacement formulation of the finite element method is suitable for solving boundary value problems of gradient elastoplasticity. However, the existence of strain gradients in the virtual work demands that strains be continuous. Therefore the interpolation of displacements must be  $C^1$ -continuous, instead of  $C^0$  that is adequate for classical elastoplasticity.

In the following we restrict the analysis to 2D plane strain and use the three-noded  $C^1$  triangle with 18 degrees of freedom for each interpolated field (namely the displacement and all its spatial derivatives of first and second order at each node) [Das90]. The displacement field varies as a complete quintic with a cubic normal derivative along the element edges. The displacement  $\mathbf{u}$  is interpolated as

$$\mathbf{u} = \mathbf{N} \cdot \hat{\mathbf{u}} \quad (38)$$

where  $\mathbf{N}$  are the shape functions and  $\hat{\mathbf{u}}$  the nodal degrees of freedom.

Strain rates, their gradients and their Laplacians are written in vector form as

$$\dot{\boldsymbol{\varepsilon}} = \mathbf{L}_1 \cdot \mathbf{N} \cdot \hat{\mathbf{u}} = \mathbf{B}_1 \cdot \hat{\mathbf{u}} \quad (39)$$

$$\dot{\boldsymbol{\varepsilon}}_x = \frac{\partial}{\partial x} \dot{\boldsymbol{\varepsilon}} = \mathbf{L}_{2x} \cdot \mathbf{N} \cdot \hat{\mathbf{u}} = \mathbf{B}_{2x} \cdot \hat{\mathbf{u}}, \quad \dot{\boldsymbol{\varepsilon}}_y = \frac{\partial}{\partial y} \dot{\boldsymbol{\varepsilon}} = \mathbf{L}_{2y} \cdot \mathbf{N} \cdot \hat{\mathbf{u}} = \mathbf{B}_{2y} \cdot \hat{\mathbf{u}} \quad (40)$$

$$\nabla^2 \dot{\boldsymbol{\varepsilon}} = \mathbf{L}_3 \cdot \mathbf{N} \cdot \hat{\mathbf{u}} = \mathbf{B}_3 \cdot \hat{\mathbf{u}} \quad (41)$$

where  $\mathbf{L}_1$ ,  $\mathbf{L}_{2x}$ ,  $\mathbf{L}_{2y}$  and  $\mathbf{L}_3$  are appropriate differential operators. The constitutive relations of equations (32), (35) and (36) are then written in vector form as

$$\dot{\boldsymbol{\sigma}}^{(0)} = \mathbf{C}^{ep} \cdot \dot{\boldsymbol{\varepsilon}} \quad (42)$$

$$\dot{\mathbf{m}}_x = \mathbf{C}^m \cdot \dot{\boldsymbol{\varepsilon}}_x, \quad \dot{\mathbf{m}}_y = \mathbf{C}^m \cdot \dot{\boldsymbol{\varepsilon}}_y \quad (43)$$

$$\dot{\mathbf{a}} = -l_p^2 \cdot \mathbf{C}^p \cdot \nabla^2 \dot{\boldsymbol{\varepsilon}} \quad (44)$$

where  $\mathbf{C}^{ep}$ ,  $\mathbf{C}^m$  and  $\mathbf{C}^p$  are the tensors  $C_{ijkl}^{ep}$ ,  $C_{ijkl}^m$  and  $C_{ijkl}^p$  in matrix form.

Substitution in the virtual work equation (37) results in the following linear system of equations for the nodal degrees of freedom:

$$\int_V (\mathbf{B}_1^T \mathbf{C}^{ep} \mathbf{B}_1 + \mathbf{B}_{2x}^T \mathbf{C}^m \mathbf{B}_{2x} + \mathbf{B}_{2y}^T \mathbf{C}^m \mathbf{B}_{2y}) dV \cdot \hat{\mathbf{u}} = \int_{S_\sigma} \left[ \mathbf{N}^T \hat{\mathbf{t}} + \left( n_x \frac{\partial \mathbf{N}^T}{\partial x} + n_y \frac{\partial \mathbf{N}^T}{\partial y} \right) \hat{\mathbf{m}} \right] dS \quad (45)$$

where  $\mathbf{n} = [n_x, n_y]$  is the outward unit normal to the boundary.  $\hat{\mathbf{t}}$  and  $\hat{\mathbf{m}}$  are the boundary traction and the boundary double traction vectors respectively.

The stiffness matrix on the left hand side of equation (45) is integrated using an  $O(h^7)$ -accurate, 13-point Gauss quadrature scheme, which is adequate to preserve convergence [Zer01a]. Equation (45) is solved iteratively for the degrees of freedom with the Newton-Raphson method.

### 3.3. Material model

We consider that the material behaviour is approximated adequately by a non-linear Mohr-Coulomb yield criterion and plastic potential. To avoid numerical problems related to the apex of the yield function at the point  $\tau_1 = \tau_3$ , the corner is “rounded” by a circular arc of radius  $R$ . The arc is taken tangent to the Mohr-Coulomb line, so that the derivative of the yield function remains continuous. The modified function is depicted in Figure 1 with a solid line and is written as

$$F(\tau_1, \tau_3) = \begin{cases} m\tau_1 - \tau_3 - \sigma_c = 0 & \text{if } H(\tau_1, \tau_3) \leq 0 \\ (\tau_1 - \tau^K)^2 + (\tau_3 - \tau^K)^2 - R^2 = 0 & \text{if } H(\tau_1, \tau_3) > 0 \end{cases} \quad (46)$$

where  $m = (1 + \sin \phi)/(1 - \sin \phi)$  is a friction coefficient and  $\sigma_c = 2c \cos \phi/(1 - \sin \phi)$  is the *equivalent stress*.  $\phi$  is the angle of internal friction and  $c$  is the material cohesion.  $\tau^K$  defines the centre of the arc and  $H = (\tau_1 - \tau_1^T) + m(\tau_3 - \tau_3^T) = 0$  is the line normal to the Mohr-Coulomb line, passing from its point of contact with the arc. Geometrical considerations lead to

$$\tau^K = \frac{1}{1+m} \left[ (1+m^2)\tau_1^T - m\sigma_c \right] \quad (47)$$

$$R^2 = \left( \frac{1}{1+m} \right)^2 \left\{ (m^2+1) \left[ (m-1)\tau_1^T - \sigma_c \right]^2 \right\} \quad (48)$$

The arc is defined uniquely by the abscissa  $\tau_1^T$  of the contact point, which here is taken such that the arc covers 1/10 of the tensile part of the function. Equation (22) is also used for the plastic potential, which is defined by the angle of dilatancy  $\psi$  in place of the angle of friction  $\phi$ . The condition for associative plasticity is  $\psi = \phi$ . The hardening/softening behaviour is described by assuming dependence of  $\sigma_c(\varepsilon_p)$  on the accumulated *equivalent plastic strain*  $\varepsilon_p$ . The latter is defined as the rate of dissipated work divided by the equivalent stress. The hardening/softening law is:

$$\sigma_c(\varepsilon_p) = \sigma_{c,0} + \frac{(1 - C_0 \varepsilon_p) \varepsilon_p}{C_1 + C_2 \varepsilon_p} \quad (49)$$

which is fitted on experimental data.  $C_1$  and  $C_2$  are calibration constants, while  $\sigma_{c,0}$  defines the state of initial yield. The constant  $C_0$  controls the rate of softening and it is an open parameter because, due to bifurcations and end restraints, standard laboratory calibration tests cannot determine the “true” material softening. The material lengths  $l_e$  and  $l_p$  are also open parameters, although they are usually considered to relate to a characteristic micromechanical length scale of the material, such as the average grain size [Muh87]. As the role of microstructure in the elastic regime is not expected to be significant, extra information on the shear-band thickness and the scale effect could, in principle, be inverted using the gradient elastoplasticity model to obtain the unknown softening rate and plastic material length  $l_p$ . The elastic material length  $l_e$  can then be taken to be a proportion of  $l_p$ .

The introduction of two material lengths gives gradient elastoplasticity the advantage that boundary conditions need only be prescribed on the external boundary. In gradient plasticity theories, where only one material length is used, the order of the governing equations changes at the elastoplastic boundary, necessitating a special treatment. In gradient elastoplasticity this is unnecessary, as gradient terms are introduced in the elastic regime as well. However, it is the plastic material length that dominates the behaviour of the material, as deformation gradients are much higher in the plastic than in the elastic regime.

The material parameters used in the computations correspond to a weak reservoir sandstone. The elastic parameters were found to be  $E = 8100 \text{ MPa}$  and  $\nu = 0.35$ . The friction angle is considered constant and equal to  $\phi = 32.5^\circ$ . The calibration constants for the hardening behaviour were determined as  $C_1 = 1.323 \cdot 10^{-5}$  and  $C_2 = 6.1271 \cdot 10^{-2}$ , while the equivalent stress at initial yield is  $\sigma_{c,0} = 25 \text{ MPa}$ . The material lengths are set to  $l_e = l_p = 0.2 \text{ mm}$ . The constant controlling the softening rate is taken  $C_0 = 80$ .

### 3.3 Modelling of the Biaxial Test

Modelling of the biaxial test has been consistently used in the literature as a “benchmark” for localization computations, as it readily demonstrates a model’s ability to capture localised zones of finite thickness. Although it would be interesting from the practical point of view to compare the predictions of the theory presented here with predictions of other existing higher-order theories, meaningful comparisons cannot be made without access to the relevant raw experimental data for calibration purposes. We will therefore consider such comparisons outside the scope of this paper.

The geometry of the test and the applied boundary conditions are shown in Figure 9. The sample is 5x10cm and is assumed to deform in plane-strain. Deviatoric load is applied by prescribing the vertical displacement increment of the top platen. The platen is considered to be rigid and lubricated, allowing the sample to slip without friction. Due to the initial uniformity of the stress and strain fields an imperfection is needed to trigger localization, so the initial cohesion has been reduced by 10% at a region 0.5x0.5cm at the lower right hand-side corner of the sample. The size of the imperfection does not influence the computed failure mode [Zer01a].

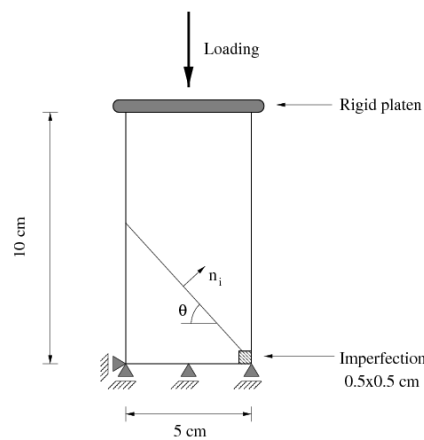


Figure 9: Biaxial geometry, loading and boundary conditions.

A parametric study was conducted to examine the effect of non-associativity on shear-band geometry. The dilatancy angle  $\psi$  was varied every  $5^\circ$  between  $\psi = 0^\circ$  (zero plastic volumetric strain) and  $\psi = 32.5^\circ$  (maximum plastic volumetric strain). The results were obtained with a mesh of  $21 \times 41 = 861$  nodes and 10,332 degrees of freedom. It has been shown that this mesh provides converged results [Zer01a].

The calculated vertical load vs vertical displacement curves are shown in Figure 10. The initial branch, which corresponds to uniform deformation, is identical for all dilatancy angles but the curves differ in the softening branch. In all cases the observed failure mechanism is a shear-band. In the associative case the deformation starts localizing at peak load. However, as non-associativity increases, localization starts earlier, in the hardening branch. This result agrees with the predictions of bifurcation theory [Var76; Ric76] and experimental observations [Ord91]. For the non-associative cases the curve is steeper, suggesting more severe structural softening.

The thickness  $d$  of the formed shear-bands is shown in Table 1. It decreases with decreasing dilatancy angle. Comparison of the associative case with the case of  $\psi = 0^\circ$  reveals a decrease of more than four times. This is visualised in Figure 11 where the equivalent plastic is plotted. The material outside the shear-band points unloads elastically. The difference of shear-band thickness between the associative case (Figure 11a) and the non-associative ones (Figures 11b, 11c and 11d) is obvious.

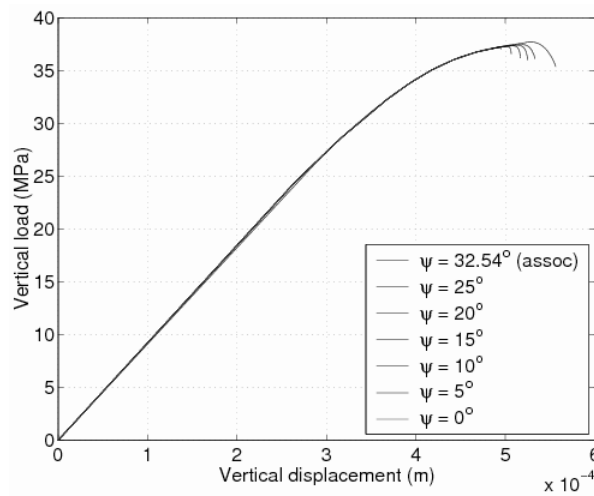


Figure 10: Vertical load vs. vertical displacement.

Table 1: Normalized shear-band thickness for different dilatancy angles and constant friction angle  $\phi = 32.5^\circ$

Dilatancy angle $\psi$	Band thickness $d/l_p$
32.50°	56.0
25.00°	45.8
20.00°	42.3
15.00°	35.2
10.00°	31.7
5.00°	24.7
0.00°	14.1

The inclination of the shear-band (angle  $\theta$  between the shear-band and the x-axis in Figure 9) also decreases with decreasing dilatancy angle. As shown in Table 2, the maximum inclination occurs for the associative case. The effect of non-associativity is better seen in Figure 11, where contours of the equivalent plastic strain are

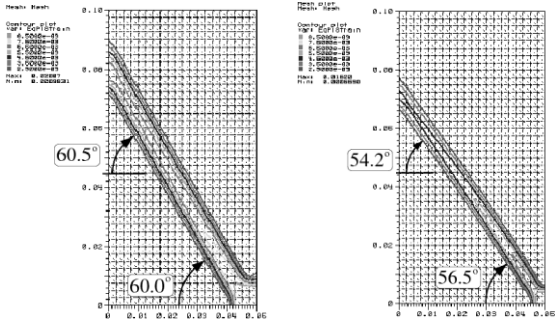
plotted. Plastic deformation is localised inside the shear-band allowing for the inclination to be graphically determined from the direction of the contour lines. Again, the difference between the associative case (Figure 12a) and the non-associative ones (Figures 11b, 11c and 11d) is clear. These results are in close agreement with the predictions of bifurcation analysis which relate the shear-band inclination to the angles of friction and dilatancy [Ric76, Var80]. A comparison is shown in Table 2. In Figure 11 we also observe that the inclination of the shear-band changes as it approaches the left hand-side boundary of the specimen. Similar shear-band re-orientations have been observed experimentally [Var95, Fin97, Bes00]. The explanation is that the shear-band is influenced by the natural boundary conditions as it approaches and subsequently intersects the free boundary. The inclination  $\theta^b$  at the boundary can then be approximated by the *Roscoe solution*,  $\theta^b \approx \theta^R = \pi/4 + \psi/2$  [Ben89]. The measured intersection angles are shown in Figure 11, at the upper left corner of each plot, and compared in Table 3 with the Roscoe solution. The difference is within the error of measurement. In the associative case the angle remains constant, while for  $\psi = 0^\circ$ ,  $\theta^b \approx 45^\circ$ .

Table 2: Theoretically predicted and numerically determined shear-band inclination, for different values of the dilatancy angle  $\psi$  and constant friction angle  $\phi=32.5^\circ$ .

Dilatancy angle $\psi$	Numerical $\theta$	Theoretical $\theta^{bif}$
32.50°	60.0°	61.27°
25.00°	58.0°	59.35°
20.00°	56.5°	58.05°
15.00°	55.0°	56.74°
10.00°	53.5°	55.42°
5.00°	53.5°	54.11°
0.00°	52.5°	52.80°

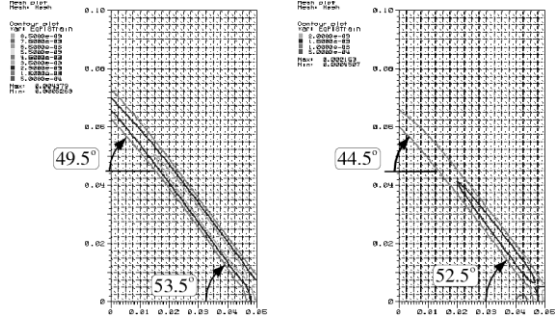
Table 3: of numerical results on shear-band inclination next to the free boundary with the Roscoe solution, for different dilatancy angles and constant friction angle  $\phi = 32.5^\circ$ .

Dilatancy angle $\psi$	Numerical $\theta^b$	Theoretical $\theta^R$
32.50°	60.5°	61.27°
20.00°	54.2°	55.00°
10.00°	49.5°	50.00°
0.00°	44.5°	45.00°



(a) Associative

(b) Non-associative,  $\psi = 20^\circ$



(c) Non-associative,  $\psi = 10^\circ$

(d) Non-associative,  $\psi = 0^\circ$

Figure 11: Contours of the equivalent plastic strain  $\epsilon_p$

### 3.4 Modelling cavity expansion

The problem of cylindrical cavity expansion is of significant interest in petroleum engineering, in the design of hydraulic fractures. Hydraulic fracturing is a technique of stimulating oil and gas reservoirs by inducing and propagating fractures through the injection of a high viscosity fluid [Eco00]. The pressure level at which a tensile fracture is initiated, i.e. the breakdown pressure, can be determined assuming that the crack forms when the hoop stress exceeds the tensile strength of the rock. For weaker rocks, however, where plastic deformations develop, analyses predict either higher breakdown pressures than the ones observed, or even that a tensile state of stress cannot be achieved during pressurisation. Nevertheless, significantly lower breakdown pressures are observed in the experiments [Pap95b]. In this section we investigate the possibility that tensile failure is preceded by the onset of shear localisation.

We model internal pressurisation of four thick-walled cylinders of a weak sandstone, with  $R_i = 5, 10, 20$  and  $40$  cm, and  $R_o = 6R_i$ ; a detailed account appears in [Zer08b]. The material parameters of Section 4 are used. Both internal pressure  $p_i$  and external pressure  $p_e$  are applied: first the cylinders are loaded with  $p_i=p_e=30$  MPa and subsequently  $p_i$  is increased under constant  $p_e$ . A mesh with a total of 32, 640 degrees of freedom is used, which suffices to provide converged results.

Initially, while  $p_i = p_e$ , no yielding occurs. In the second stage, as  $p_i$  increases, the material near the hole yields first. Deformation is initially axisymmetric, however, as  $p_i$  approaches 110MPa, axisymmetry is lost and the radial displacement increment in the vicinity of the hole assumes the sinusoidal form shown in figure 12. This happens spontaneously, and the relevant discussion of Section 4 applies here as well. Subsequently, regions near the cavity progressively unload while the deformation localises into thin bands of softening material that continue to shear. These are shown in Figure 12 with black points, while grey points show material still in the hardening regime. As can be seen, the shear-bands initiate from the cavity wall and propagate towards the outer boundary. The development of similar shear-bands has been observed experimentally on sand specimens [Als92]. The hoop stress  $\sigma_{\theta\theta}$  remains below the tensile strength, excluding the possibility of tensile failure before shear failure.

The corresponding internal pressure vs hole expansion curve is presented in figure 13, where the trivial deformation path, corresponding to axisymmetric expansion, is also shown for comparison. The two curves coincide up to the bifurcation point, where axisymmetry is lost. Then they slowly separate, as the curve corresponding to the bifurcated solution levels off at a pressure lower than the limit pressure, to which the trivial path asymptotically tends. The mechanism of localised shear failure is thus more critical than the attainment of limit pressure under axisymmetric deformation. From a practical point of view, this suggests that rupture in cavity pressurisation may occur at lower internal pressure than the limit pressure, which is

used in the interpretation of geotechnical tests or in fracture initiation prediction in weak rock formations.

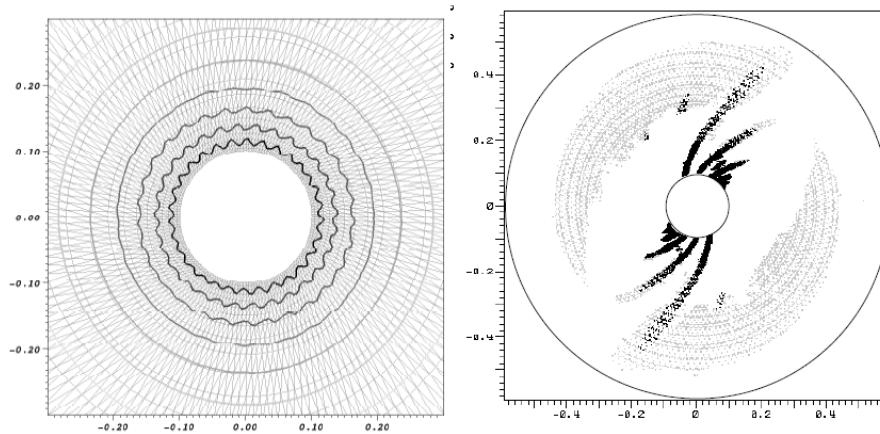


Figure 12: Radial displacement increment at bifurcation (left) and final material state (right) for the  $R_i = 10\text{cm}$  model.

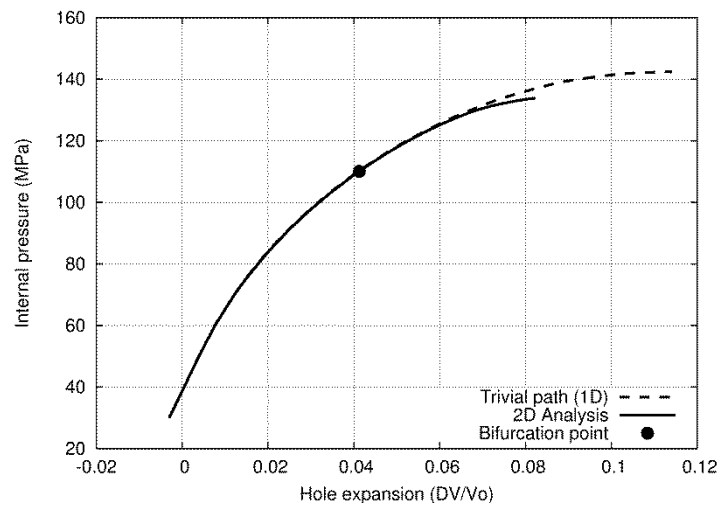


Figure 13: Internal pressure vs hole expansion for the  $R_i = 10\text{cm}$  model.

#### 4. Conclusion

In this review paper we presented two advanced theories with higher order continua one based on a Cosserat continuum and the other on Gradient Elastoplasticity. Numerical results were presented for different problems and load paths, showing that in all cases the Cosserat continuum and the gradient elastoplasticity can regularise the ill-posedness caused by strain-softening. It is able to track the spontaneous emergence of instabilities and to provide robust predictions of the post-localisation deformation, capturing quantitatively details of the localised mechanism. In other words, both models are capable of modelling the localization of deformation in shear bands which often leads to failure in geomaterials. The model are also capable of predicting the existence of the scale effect, observed in thick-walled cylinders, which is essential for interpreting the small-scale laboratory tests and for extrapolating the results to field wellbore dimensions.

The use of localization theories in practical applications is still limited by the issue of material parameters determination. Appropriate procedures or values for the internal lengths and the softening rate must be determined. We identify this as an open issue which requires further research investigation. We see more applications of these theories with microstructure in the problem of sand prediction as the geometry dealing with small holes perforations in reservoir sandstones [Hoe01]. As mentioned earlier, small holes show in experiments a pronounced strength that cannot be predicted by classical plasticity theories. Furthermore, we showed that localization analysis predicts that an elliptical hole with long axis parallel to the major insitu stress is more stable than a circular hole. This finding can be used in the design of new perforations based on elliptical shape.

## 5. Acknowledgements

The majority of this work was supported by Schlumberger Cambridge Research. We are grateful to the late Professor Ioannis Vardoulakis: inspiration and invaluable guidance, also for the work presented here, were among the many things he freely offered us during the time we spent working with him.

## 7. Bibliography/References

- [Adh97] Adhikary D.P. and Dyskin A.V. A Cosserat Continuum Model for Layered Materials Computers and geotechnics'', 20: 15-45, 1997.
- [Aif92] Aifantis E. On the role of gradients in the localization of deformation and fracture, *Int. J. Engng Sci.*, 30: 1279-1299, 1992.
- [Als92] Alsiny A., Vardoulakis I., Drescher A. Deformation localization in cavity inflation experiments on dry sand, *Géotechnique*, 42: 395-410.1992.
- [Ben89] Benallal A., Bilardon R., Geymonat G. Conditions de bifurcation à l'interieur et aux frontières pour une classe de matériaux non standard, *C. R. Acad. Sci. Paris, vol. 308, num. série II ;893-898*, 1989.
- [Bes00] Besuelle, P., Desrues, J., and Raynaud, S. Experimental characterisation of the localization phenomenon inside a vosges sandstone in a triaxial cell, *Int. J. Rock Mech. Min. Sci.*, 37: 1223-1237, 2000.
- [Bor91] de Borst R. Simulation of strain localization: a reappraisal of Cosserat continuum, *Eng. Comput*, 8: 317–32, 1991.
- [Bor92] de Borst R., Mühlhaus H.-B. Gradient-dependent plasticity: formulation and algorithmic aspect, *Int. J. Num. Meth. Engng*, vol. 35: 521-539, 1992.
- [Cos09] Cosserat E., and Cosserat F. *Théorie des Corps Déformables*, A. Hermann, Paris, 1909.
- [Cha98] Chambon R., Caillerie D., El Hassan N. One-dimensional localization studied with a second grade model, *Eur. J. Mech. A/Solids*, vol. 17, num. 4:637- 656, 1998
- [Das90] Dasgupta S., Sengupta D. A higher-order triangular plate bending element revisited, *Int. J. Num. Meth. Engng*, vol. 30, 1990, p. 419-430.
- [Eco00] Economides M. J., Nolte K. G., *Reservoir Stimulation*, 3rd edition, John-Wiley and Sons, 2000.
- [Ewy89] Ewy R. Yield and closure of directional and horizontal wells, *Int. J. Rock Mech. Min. Sci. Geomech. Abstr.*, 30 (7): 1061–1067, 1993.
- [Fin97] Finno, R. J., Harris, W. W., Mooney, M. A., and Viggiani, G. Shearbands in plane strain compression of loose sand, *Géotechnique*, 47(1): 149-165, 1997.
- [Hai89] Haimson B. and Herrick C. Borehole breakouts and in situ stress, in *Proc., Drilling Symp. at ATCE-ASME Conference, Houston*, Rowle, J.C. (ed.) 17–22, 1989.
- [Mat02] Matsushima T., Chambon R., Caillerie D. Large strain finite element analysis of a local second gradient model: application to localization, *Int. J. Num. Meth. Engng*, 54: 499-521,2002.
- [Min64] Mindlin R.D. Microstructure in linear elasticit, *Arch. Rat. Mech. Anal.*, 10: 51-78, 1964.
- [Muh87] Mühlhaus H.-B., and Vardoulakis I. The thickness of shear bands in granular materials, *Geotechnique*, 37: 271–283, 1987.

- [Ord91] Ord, A., Vardoulakis, I., and Kajewski, R. Shearband formation in gosford sandstone', *Int. J. Rock Mech. Min. Sci. & Geomech. Abstr.*, 28(5): 397-409, 1991.
- [Pap10] Papamichos E. Borehole failure analysis in a sandstone under anisotropic stresses, *Int. J. Numer. Analyt. Meth. Geomech.*, 34: 581-603, 2010.
- [Pap95a] Papamichos E., and van den Hoek P. Size dependency of castlegate and berea sandstone hollow-cylinder strength on the basis of bifurcation theory. *Proc., 35th U.S. Symp. Rock Mechanics*, 301-306. 1995.
- [Pap89] Papanastasiou P., and Vardoulakis I. Bifurcation analysis of deep boreholes: I scale effect, *Int. J. Numer. Analyt. Meth. Geomech.*, 13: 183-198, 1989.
- [Pap92] Papanastasiou P., and Vardoulakis I. Numerical treatment of progressive localization in relation to borehole stability, *Int. J. Numer. Analyt. Meth. Geomech.*, 16, p.389-424, 1992.
- [Pap94] Papanastasiou P., and Vardoulakis I., Numerical analysis of borehole stability problem, in *Numerical analysis and modelling of soil structure interaction*, J. Bull, ed., E&FN Spon, 673-711, London, 1994.
- [Pap95b] Papanastasiou P., and Durban D. Bifurcation of elastoplastic pressure-sensitive hollow cylinders." *Proc., 35th U.S. Symp. on Rock Mechanics*, J. K. Daemen et al. eds., Balkema, Rotterdam, The Netherlands, 301-306, 1995.
- [Pap97] Papanastasiou P., and Durban D. Elastoplastic analysis of cylindrical cavity problems in geomaterials, *Int. J. Numer. Analyt. Meth. Geomech.*, 21: 121-132, 1997.
- [Pap00] Papanastasiou P. Localization of deformation and failure around elliptical perforations based on a polar continuum, *Computational Mechanics*, 26: 352-361, 2000.
- [Pap09] Papanicolopoulos S.-A., Zervos A., Vardoulakis I. A three dimensional C1 finite element for gradient elasticity, *Int. J. Num. Meth. Engng.*, 77: 1396-1415, 2009.
- [Pij87] Pijaudier-Cabot G., Bazant Z. P. Nonlocal damage theor, *J. Engrg. Mech, ASCE*, 113: 1512-1533, 1987.
- [Rud75] Rudnicki J.W. and. Rice J.R. Conditions for the localization of the deformation in pressure sensitive dilatants materials, *J. Mech. Phys. Solids*, 23: 371-394, 1975.
- [Sul95] Sulem J., Vardoulakis I., and Papamichos E. Microstructure and scale effect in granular rocks, in *Mühlhaus H.-B. (ed.) Continuum Models for Materials with Microstructure*, John Wiley, 1995.
- [Tej93] Tejchman J. and Wu W. Numerical study on shear band patterning in a Cosserat continuum, *Acta Mech.*, 99: 61-74, 1993.
- [Hoe01] van den Hoek P. Prediction of different types of cavity failure using bifurcation theory, *U.S. Rock Mech. Symp.*, Washington, D.C. 2001
- [Hoe00] van den Hoek P., Hertogh G., Kooijman A., de Bree P., Kenter C., and Papamichos, E. A new concept of sand production prediction: Theory and laboratory experiments, *SPE Drill. Completion*, 15: 261-273, 2000.

- [Var80] Vardoulakis I. Shear band inclination and shear modulus of sand in biaxial tests, *Int. J. Num. Anal. Meth. Geomech.*, 4: 103-119, 1980.
- [Var88] Vardoulakis I. and Papanastasiou P. Bifurcation analysis of deep boreholes: I. surface instabilities, *Int. J. Numer. Analyt. Meth. Geomech.*, 12: 379–399, 1988.
- [Var91] Vardoulakis I., Aifantis E.C. A gradient flow theory of plasticity for granular materials”, *Acta Mechanica*, vol. 87, 1991, p. 197-217.
- [Var92a] Vardoulakis I., Frantziskonis G. Micro-structure in kinematic-hardening plasticity, *Eur. J. Mech. A/Solids*, 11(4): 467-486, 1992.
- [Var92b] Vardoulakis I., Shah K. R., Papanastasiou P. Modelling of tool-rock shear interfaces using gradient-dependent flow theory of plasticity, *Int. J. Rock Mech. Min. Sci. & Geomech. Abstr.*, vol. 29(6): 573-582, 1992.
- [Var94a] Vardoulakis I., Aifantis E. C. On the role of microstructure in the behavior of soils: Effects of higher order gradients and internal inertia, *Mech. Mater.*, 18:151-158, 1994.
- [Var94b] Vardoulakis I., Papamichos E., and Sulem J. A second gradient plasticity model for granular rocks., in *Fracture and damage in quasibrittle structures*, Z. P. Bazant, Z. Bittmar, M. J. and J. Mazars, eds., E&FN Spon, London, 1994.
- [Var95] Vardoulakis I. and Sulem, J. *Bifurcation Analysis in Geomechanics*, Blackie Academic and Professional, Glasgow, 1995.
- [Zer00] Zervos A., Vardoulakis I., Jean M., and Lerat P. Numerical investigation of granular interfaces kinematics, *Int. J. Numer. Analyt. Meth. Geomech.*, 5: 305–324, 2000.
- [Zer01] Zervos A., Papanastasiou P., and Vardoulakis I. A finite element displacement formulation for gradient elastoplasticity, *Int. J. Numer. Methods Eng.*, 50: 1369–1388, 2001.
- [Zer01b] Zervos A., Papanastasiou P. and Vardoulakis I., Modelling of localization and scale effect in thick-walled cylinders with gradient elastoplasticity, *Int. J. Solids Struct.*, 38:5081–5095, 2001.
- [Zer07] Zervos A., Vardoulakis I., Papanastasiou P., Influence of Nonassociativity on Localization and Failure in Geomechanics Based on Gradient Elastoplasticity, *Int. J. Geomechanics*, 7 (1), 63-74, 2007.
- [Zer08a] Zervos A., Finite elements for Elasticity with Microstructure and Gradient Elasticity, *Int. J. Num. Meth. Engng*, 73 (4):564-595 2008.
- [Zer08b] Zervos A., Papanastasiou P., Vardoulakis I., Shear localisation in thick walled cylinders under internal pressure based on Gradient Elastoplasticity, *Journal of Theoretical and Applied Mechanics*, 38 (1-2): 81-100, 2008.



# **Numerical modeling of bifurcation: Applications to borehole stability, multilayer buckling, and rock bursting**

**Euripides Papamichos**

*Aristotle University of Thessaloniki and SINTEF Petroleum Research*

---

*Typical boundary value problems of bifurcation are presented such as (i) borehole stability with applications in the oil and gas industry and in tunneling, (ii) multilayer buckling with application in the folding of geological formations, and (iii) spalling and buckling of surface parallel cracks with application in rock bursting in mining. The formulation of the bifurcation problem in all these cases is described together with the numerical implementation and the main results. If the formulation is in terms of a continuum with microstructure, such as the Cosserat continuum, scale is introduced into the bifurcation problem, which leads to size effect. For example, in borehole failure smaller diameter holes fail at higher stresses than larger holes.*

## **1 Introduction**

Three typical bifurcation boundary value problems are formulated and solved numerically. In Section 2, borehole stability is formulated and analyzed within a finite element method scheme for elastoplastic Cosserat materials and the results are compared with experimental data. In Section 3, multilayer buckling in anisotropic elastic and viscoelastic materials under initial stress is analyzed using the matrix transfer method. Finally, in Section 4 buckling of anisotropic elastic half-spaces with surface parallel cracks under initial stress are analyzed using the displacement discontinuity boundary element method. Conclusions are presented in Section 5.

## **2 Borehole stability**

Borehole failure has been an important geomechanical problem for the assessment of the integrity of tunnels, wellbores and perforations in the field. The most common failure mode for dilatant rocks is the formation of breakouts. A relevant laboratory

experiment is the Hollow Cylinder (HC) test with or without fluid flow. HC experiments under various axial and lateral stress paths in Red Wildmoor sandstone [Pap10a] have demonstrated the lateral and axial borehole failure modes shown in Figure 1 as suggested by Maury [Mau92]. The first prevails when the tangential stress at the hole is the largest compressive principal stress and failure takes place in the form of shear bands concentrated on two diametrically opposed locations of the borehole. The second prevails when the axial stress at the hole is the largest compressive principal stress and failure takes place in the form of shear bands forming toroids around the hole perimeter.

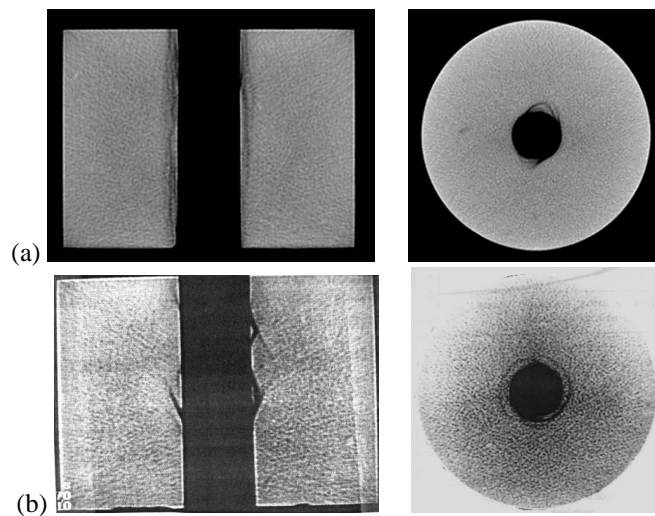


Figure 1: Vertical (left) and horizontal (right) X-ray CT scan images of hollow cylinder specimens demonstrating (a) lateral borehole failure with breakouts, and (b) axial borehole failure with toroids [Pap10a].

Analysis based on elasticity and a Mohr-Coulomb failure criterion for the rock has been traditionally used to predict borehole failure. However, comparisons with experimental results have long demonstrated that such an approach greatly underestimates the borehole failure strength. For successful predictions, the borehole failure problem has been treated as a bifurcation phenomenon [Var88] often in connection with continua with microstructure (Cosserat or gradient) (e.g. [Var95] and references therein) and elastoplastic constitutive laws. The advantage of this approach is that it describes naturally the observed failure patterns of shear bands and breakouts.

In the following the Cosserat elastoplastic model is implemented in a finite element scheme for the solution of the HC failure test. Figure 2 shows the geometric layout of the problem in the cylindrical  $(r, \theta, z)$ -coordinate system. A thick-wall cylinder of external radius  $r_e$ , internal radius  $r_i$  and height  $H$  is compressed radially with uniform external  $\sigma_{\text{ext}}$  and internal  $\sigma_{\text{int}}$  stresses with  $\sigma_{\text{ext}}/\sigma_{\text{int}} > 1$ . Axially a uniform strain  $\varepsilon_{zz}$  is applied to simulate the experiment where the axial load is applied through steel (i.e. rigid) loading platens. The strain  $\varepsilon_{zz}$  is controlled such that

it produces a prescribed axial load  $F_z$ . The uniform axial strain boundary condition means that the HC test is a 2d problem, i.e. it varies only in two dimensions in the  $r, \theta$ -plane normal to the hole. The effect of pore pressure on borehole failure is not included here for brevity but the reader is referred to Papamichos [Pap10b] for a description of the formulation with steady state fluid flow. As in the experiments  $r_e/r_i = 5$ . Section 2.1 presents the implementation for the axisymmetric solution of the primary path of cylindrical convergence of the HC hole and Section 2.2 formulates the bifurcation condition for borehole failure. Section 2.3 presents simulation results and comparison with experimental data. In Sections 2.1 and 2.2, standard mechanics notation of tension positive is employed for the stresses and strains. However, in Section 2.3, compressive stresses and strains are taken positive to avoid carrying the negative sign and plotting the results in negative axes.

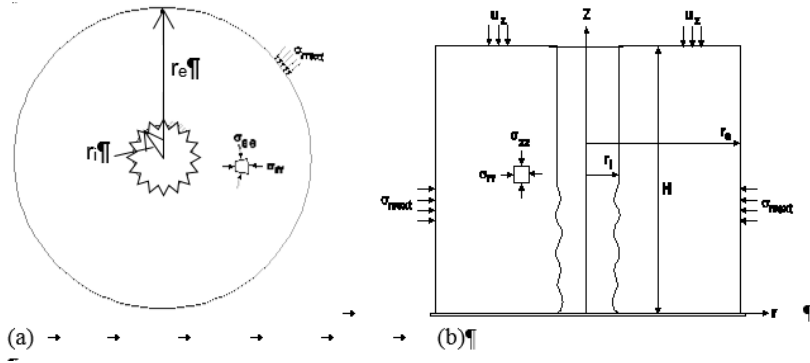


Figure 2: Geometric layout of the thick-wall hollow cylinder configuration: (a) plane view with lateral hole warping, and (b) vertical section with axial hole warping.

## 2.1 Primary loading path

During the axisymmetric deformations of the primary loading path, shear stresses and Cosserat couple stresses vanish and therefore the solution for the primary loading path can be significantly simplified and become 1d with dependence of the quantities only along the radial direction. The finite element formulation is based on the variational equation within a volume  $V$  with boundary  $\partial V$ , which in axisymmetric problems under uniform and prescribed axial displacement can be written in the cylindrical coordinate system  $(r, \theta, z)$  as

$$\int_V (\sigma_{rr} \delta \varepsilon_{rr} + \sigma_{\theta\theta} \delta \varepsilon_{\theta\theta}) dV = \int_{\partial V_\sigma} t_r \delta u_r dS \quad (1)$$

where  $\sigma_{rr}$  is the radial and  $\sigma_{\theta\theta}$  the tangential stress, dual in energy to the radial  $\varepsilon_{rr}$  and tangential  $\varepsilon_{\theta\theta}$  strains, respectively, and  $t_r$  is a prescribed traction on a part  $\partial V_\sigma$  of the boundary  $\partial V$ . Moreover,  $\delta \varepsilon_{rr}$ ,  $\delta \varepsilon_{\theta\theta}$  and  $\delta u_r$  are variations of the radial and tangential strains and the radial displacement  $u_r$ , respectively. The integrands in Eq.(1) are

independent of the  $\theta$  and  $z$ -coordinates and thus Eq.(1) can be integrated with respect to these coordinates and written in matrix form as

$$\int_{r_i}^{r_e} \{\delta\mathcal{E}\}^T \{\sigma\} r dr = -\delta u_r|_{r=r_i} \sigma_{rint} r_i + \delta u_r|_{r=r_e} \sigma_{rext} r_e \quad (2)$$

where the strain variation  $\{\delta\mathcal{E}\}$  and the stress  $\{\sigma\}$  vectors are defined as

$$\{\delta\mathcal{E}\}^T = \{\delta\mathcal{E}_{rr}, \delta\mathcal{E}_{\theta\theta}\}, \quad \{\sigma\}^T = \{\sigma_{rr}, \sigma_{\theta\theta}\} \quad (3)$$

and the stress boundary conditions at the hole and the external surface have been considered in the left-hand side.

In an elastoplastic analysis, incremental and iterative methods are used to solve these equations, where the total external loads are added in increments step by step. At the  $(m+1)^{\text{th}}$  loading step

$$\int_{r_i}^{r_e} \{\delta\mathcal{E}\}^T \{d\sigma\} r dr = {}^{m+1} \left[ \delta u_r|_{r=r_i} \sigma_{rint} r_i + \delta u_r|_{r=r_e} \sigma_{rext} r_e \right] - \int_{r_i}^{r_e} \{\delta\mathcal{E}\}^T {}^m \{\sigma\} r dr \quad (4)$$

where the first term in the right-hand side of the first equation is the load at the  $(m+1)^{\text{th}}$  step,  ${}^m\{\sigma\}$  is the stress vector at the  $m^{\text{th}}$  step and  $\{d\sigma\}$  the stress increment vector. Using the constitutive relations of Cosserat elastoplasticity [Pap10a]

$$\{d\sigma\} = [C^{ep}] \{d\mathcal{E}\} \quad (5)$$

and taking into account the fact that  $d\mathcal{E}_{zz}$  is constant with  $r$ , Eq.(4) can be written as

$$\begin{aligned} \int_{r_i}^{r_e} \{\delta\mathcal{E}\}^T [C_A^{ep}] \{d\mathcal{E}\} r dr &= {}^{m+1} \left[ \delta u_r|_{r=r_i} \sigma_{rint} r_i + \delta u_r|_{r=r_e} \sigma_{rext} r_e \right] - \\ &- \int_{r_i}^{r_e} \{\delta\mathcal{E}\}^T {}^m \{\sigma\} r dr - d\mathcal{E}_{zz} \int_{r_i}^{r_e} \{\delta\mathcal{E}\}^T \{C_B^{ep}\} r dr \end{aligned} \quad (6)$$

where the constitutive matrix  $[C_A^{ep}]$  and vector  $\{C_B^{ep}\}$  are the following parts of matrix  $[C^{ep}]$  in Eq.(5)

$$[C_A^{ep}] = \begin{bmatrix} C_{11}^{ep} & C_{12}^{ep} \\ C_{21}^{ep} & C_{22}^{ep} \end{bmatrix}, \quad \{C_B^{ep}\} = \begin{Bmatrix} C_{13}^{ep} \\ C_{23}^{ep} \end{Bmatrix} \quad (7)$$

The finite element solution is obtained with a one-dimensional discretization along the radius  $r$ . A fine discretization is required close to the hole to obtain mesh insensitivity. This is achieved by discretizing the domain in 100 elements according to a geometric progression with common ratio 1.05. Three-node elements with Lagrange polynomial basis functions of second-order are used. Each node has one degree of freedom, the radial displacement  $u_r$ .

In nonlinear constitutive models such as elastoplasticity, in contrast with linear elasticity, if a uniform along the radius axial strain is applied, the result will be a non-uniform axial stress  $\sigma_{zz}$  along the HC radius. The experiments in the laboratory are performed by applying a uniform axial strain such that it produces a prescribed axial load  $F_z$ . Numerically, this can be accomplished by implementing an axial load servo-control algorithm to control the applied axial strain [Pap10b].

## 2.2 Hole failure

In this section, the bifurcation condition for lateral HC failure is formulated and implemented in the finite element scheme. For axial HC failure the reader is referred to Papamichos [Pap10b]. The underlying hypothesis of the bifurcation theory is that spalling and shear banding in rocks are the result of material instabilities, termed equilibrium bifurcations. The bifurcation approach associates failure with the occurrence of the instabilities in contrast to classical procedures where failure is usually assumed ad hoc to be an intrinsic material property associated with the elastic-plastic limit. The analysis here focuses on the prediction of the bifurcation point of warping of the hole that subsequently may lead to spalling or shear banding as it has been demonstrated in post-bifurcation numerical analyses (e.g. [Pap92], [Pap10c]).

The bifurcation condition is formulated on the basis that in addition to the trivial solution of cylindrical convergence of the hole during the primary loading path, there exists another non-trivial warping solution that fulfils homogeneous boundary conditions. Thus, the bifurcation problem for the HC failure can be formulated with the homogeneous and incremental form of the virtual work equation for a Cosserat continuum

$$\int_V \{\delta d\hat{\varepsilon}\}^T \{d\hat{\sigma}\} dV = 0 \quad (8)$$

where  $\{d\hat{\sigma}\}$  and  $\{d\hat{\varepsilon}\}$  are the generalized stress and strain increment vectors, respectively, that correspond to the non-trivial bifurcation solution. This solution involves the Cosserat rotations and couple stresses, in contrast to the solution of the primary path, and therefore the bifurcation condition depends on the internal length.

The bifurcation condition for lateral failure which corresponds to warping of the hole on the  $(r, \theta)$ -plane normal to the HC axis, as shown in Figure 2a, is obtained by solving Eq.(8) for the non-trivial, plane-strain, displacement and microrotation increment field

$$\begin{aligned} d\hat{u}_r(r, \theta) &= V_r(r) \cos(m\theta) , & d\hat{\omega}_z^c(r, \theta) &= W_z(r) \sin(m\theta) \\ d\hat{u}_\theta(r, \theta) &= V_\theta(r) \sin(m\theta) , & d\hat{\omega}_r^c &= 0 \\ d\hat{u}_z &= 0 , & d\hat{\omega}_\theta^c &= 0 \end{aligned} \quad (9)$$

where  $m = 1, 2, 3, \dots$  is the wavenumber of the warping mode. The wavelength of the deformation is given as  $W = 2\pi r_i / m$ . For this displacement and microrotation

field, the generalized displacement, strain and stress increment vectors reduce to

$$\begin{aligned}\{d\hat{u}\}^T &= \{d\hat{u}_r, d\hat{u}_\theta, d\hat{w}_z^c\} \\ \{d\hat{\varepsilon}\}^T &= \{d\hat{\varepsilon}_{rr}, d\hat{\varepsilon}_{\theta\theta}, d\hat{\varepsilon}_{r\theta}, d\hat{\varepsilon}_{\theta r}, Rd\hat{\kappa}_{\theta z}, Rd\hat{\kappa}_{rz}\} \\ \{d\hat{\sigma}\}^T &= \{d\hat{\sigma}_{rr}, d\hat{\sigma}_{\theta\theta}, d\hat{\sigma}_{r\theta}, d\hat{\sigma}_{\theta r}, d\hat{\mu}_{\theta z}/R, d\hat{\mu}_{rz}/R\}\end{aligned}\quad (10)$$

For small deformation analysis the strain-displacement relation is given by

$$\{d\hat{\varepsilon}\} = [B]\{dU\} \quad \text{or} \quad \{\delta d\hat{\varepsilon}\} = [B]\{\delta dU\} \quad (11)$$

where  $\{dU\}$  is the displacement increment vector of nodal points related to the distributed displacement  $\{d\hat{u}\}$  by

$$\{du\} = [N]\{dU\} \quad (12)$$

in which  $[N]$  is the matrix of shape functions. The strain-displacement matrix  $[B]$  is defined as

$$[B] = [L][N] \quad (13)$$

and  $[L]$  is a differential operator matrix such that

$$\{d\hat{\varepsilon}\} = [L]\{d\hat{u}\} \quad (14)$$

Following the analysis of axisymmetric problems submitted to non-symmetrical loading [Zie89], a typical term of the  $[N]$  matrix of shape functions for the generalized velocity field Eq.(10) is

$$[N_i] = \begin{bmatrix} N_i \cos(m\theta) & 0 & 0 \\ 0 & N_i \sin(m\theta) & 0 \\ 0 & 0 & N_i \sin(m\theta) \end{bmatrix} \quad (15)$$

On substitution of the shape functions (15) into Eq.(13), a typical term of  $[B]$  is

$$[B_i] = \begin{bmatrix} N_{i,r} \cos(m\theta) & 0 & 0 \\ \frac{1}{r} N_i \cos(m\theta) & \frac{m}{r} N_i \cos(m\theta) & 0 \\ -\frac{m}{r} N_i \sin(m\theta) & -\frac{1}{r} N_i \sin(m\theta) & N_i \sin(m\theta) \\ 0 & N_{i,r} \sin(m\theta) & -N_i \sin(m\theta) \\ 0 & 0 & RN_{i,r} \sin(m\theta) \\ 0 & 0 & \frac{mR}{r} N_i \cos(m\theta) \end{bmatrix} \quad (16)$$

which is conveniently separated to

$$[B_i] = [B_i^s] \sin(m\theta) + [B_i^c] \cos(m\theta) \quad (17)$$

By combining Eqs.(8) and (11) with the incremental constitutive equations (5), the governing equation, may be written as

$$\int_V [B]^T [D] [B] dV \{dU\} = 0 \quad (18)$$

where  $[D]$  contains only the relevant components of the tangent constitutive matrix  $[C^{ep}]$  in Eq.(5). Equation (18) can be simplified by using Eq.(17) and performing the integration with respect to the  $\theta$  and  $z$ -coordinates, reducing to

$$[K] \{dU\} = 0, \quad [K] = \int_{r_i}^{r_o} \left\{ [B^s]^T [D] [B^s] + [B^c]^T [D] [B^c] \right\} r dr \quad (19)$$

which results in an eigenvalue problem for the critical bifurcation loads  $\sigma_{rim}$ ,  $\sigma_{rest}$  and  $\varepsilon_{zz}$ . Within a finite-element discretization scheme, the solution to this eigenvalue problem is obtained by requiring that the global stiffness matrix  $[K]$  becomes singular, i.e.

$$\det[K] = 0 \quad (20)$$

which is the bifurcation condition for lateral instability.

The governing Eq.(19) gives significant computational advantages because it reduces the two-dimensional problem to an one-dimensional finite element discretization with respect to the  $r$ -coordinate. The finite element solution of the eigenvalue problem Eq.(20) for hole failure is obtained with the same one-dimensional discretization along the radius  $r$  of the thick-wall HC used for obtaining the solution for the primary path. Each node has now three degrees of freedom. These are the radial  $V_r$  and tangential  $V_\theta$  displacement amplitude and the Cosserat microrotation  $W_z$  amplitude. The initial failure bifurcation condition requires that the global stiffness matrix  $[K]$  becomes singular. In inhomogeneous problems like the present, failure of local stability conditions does not necessarily imply loss of uniqueness [Pap92]. In fact, the obtained bifurcation points correspond to loading states where elements close to the hole have entered the softening regime. Although at these elements the local stability criterion is violated, the global stiffness matrix remains positive. The loading stresses at which the bifurcation condition is satisfied depend on the wavenumber  $m$  of the bifurcation mode. In a Cosserat continuum there exists for the HC problem a critical wavenumber  $m_{cr}$  that corresponds to the least required loads. It is obtained by solving the bifurcation condition for various  $m$  and selecting the  $m_{cr}$  corresponding to the least required loads. It maybe, therefore, assumed that the hole would fail under  $m_{cr}$ .

### 2.3 Simulation of hollow-cylinder experiments

Theoretical results from finite element simulations of HC tests under various loading paths are presented and compared to experimental data [Pap10a]. The bifurcation predictions for failure depend on the Cosserat internal length  $R$ . The internal length cannot be calibrated from standard triaxial test data. For this reason a parametric study with various internal lengths between  $R = 2$  and  $20 \mu\text{m}$  was performed, in order to select the internal length  $R$  from back calibration of the experimental results on hole failure. Once the internal length is selected, a size effect analysis can be performed for failure predictions of holes of various sizes.

For lateral failure, isotropic, plane-strain and radial loading tests at 3.6, 7.2, 12.5 and 14.5 MPa (average) axial stress were simulated and the results were compared with experimental data. In these tests, the hole remains unsupported while axial and external radial stresses are applied. In the isotropic tests, the applied axial and external radial stresses are the same. In the plane-strain tests, external radial stress is applied under zero axial strain. Finally, in the radial-loading test after an initial isotropic loading to 3.6 or 7.2 or 12.5 or 14.5 MPa, the external radial stress is increased while the axial stress is kept constant.

Figure 3 shows the bifurcation stresses for various  $R$  together with experimental failure stresses. The bifurcation point for the smallest  $R$  is found immediately after the material at the hole begins to soften. As  $R$  increases, the external stresses for failure increase. The theoretical predictions show that to capture the experimental data,  $R$  must be between 10 and  $15 \mu\text{m}$ . This is the case for all loading paths leading to lateral failure, which means that once  $R$  is back calibrated on experimental data for one loading path, e.g. isotropic loading, then it can be used to forward predict failure at other loading paths. The average grain diameter  $d_g$  of Red Wildmoor sandstone is  $107 \mu\text{m}$ . Thus the ratio of the back-calibrated  $R$  to the grain diameter is  $R/d_g = 0.09 - 0.14$ .

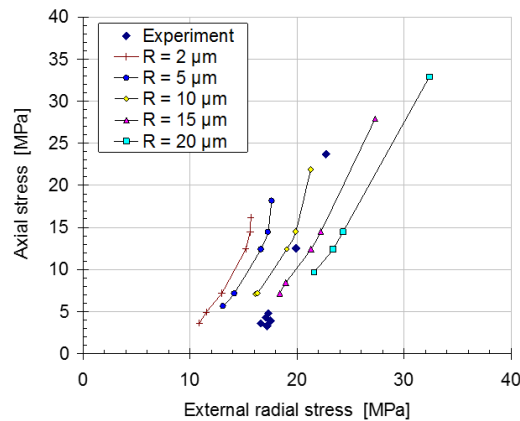


Figure 3: Experimental data and theoretical results for lateral hole failure for various loading paths and internal lengths.

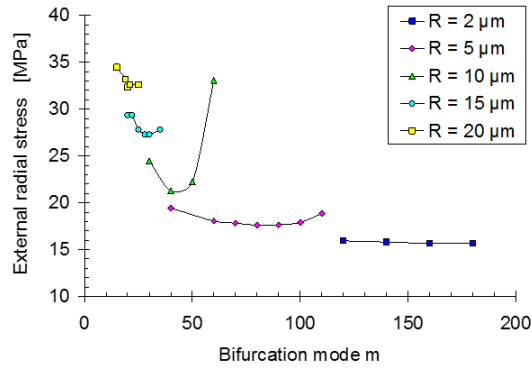


Figure 4: External radial stress at bifurcation failure vs. bifurcation mode  $m$  and internal length  $R$  for isotropic loading. The minimum in each curve leads to the selection of the critical mode  $m_{cr}$  corresponding to the least external radial stress.

Figure 4 shows the selection of the critical bifurcation mode  $m_{cr}$  for isotropic loading where the dependency of the external radial stress for failure with the bifurcation mode  $m$  and the internal length  $R$  is illustrated. Although the actual evolution of the critical bifurcation mode requires post-bifurcation analysis, it can be assumed that high critical modes of small wavelength would lead to spalling all around the hole, whereas low modes would lead to more localized spalling. Experimental and numerical evidence show that although localization may initiate under a high mode, a lower mode may finally evolve. Indeed experiments show that an initial mode  $m = 6$  localization evolves to an apparent mode  $m = 3$  failure [Hai93]. At the same time, post-bifurcation computations show that an initial mode  $m = 12$  evolves into a single shear-band failure zone [Pap92]. The results show that the relation between the  $m_{cr}$  for lateral hole failure and  $R$  is independent of the loading path and that  $m_{cr}$  decreases with a power law with  $R$  that can be approximate as

$$m_{cr} = 0.074(R/r_i)^{-0.92} \quad (21)$$

Figure 5 compares, as an example, the simulation results for isotropic and plane strain loading with experimental data where the external radial stress is plotted vs. the internal and external tangential strains. The internal tangential strain corresponds to the normalized (with its radius) hole closure. In addition, the points of hole failure for  $R = 10 \mu\text{m}$  are indicated. The results compare well with the experimental data up to the failure point after which post-failure analysis is required to capture the deformations involved. Theoretical results on the stress profiles along the radius of the HC demonstrate that for isotropic loading the axial stress  $\sigma_{zz}$  is always the intermediate principal stress. Therefore,  $\sigma_{zz}$  does not influence plastic yielding since a Mohr-Coulomb yield surface is employed. However, for plane-strain loading  $\sigma_{zz}$  is not always the intermediate principal stress but it becomes the least principal stress away from the hole. This leads to a higher stress concentration at the hole for plane-strain and results in earlier hole failure.

The value  $R = 10 \mu\text{m}$  was chosen to construct scale effect diagrams in terms of the hole diameter for the various loading configurations. The results are illustrated in Figure 6 where the normalized external radial stress is plotted vs. the hole diameter. The normalization is done with the external radial stress for failure of the 20-mm diameter hole which is considered as the reference hole. The plot includes also the scale effect equation [Pap10a]

$$\frac{\sigma_F}{\sigma_{Fref}} = \frac{1}{3} + \frac{2}{3} \left( \frac{D_{ref}}{D} \right)^{2/5}, \quad D_{ref} = 20 \text{ mm} \quad (22)$$

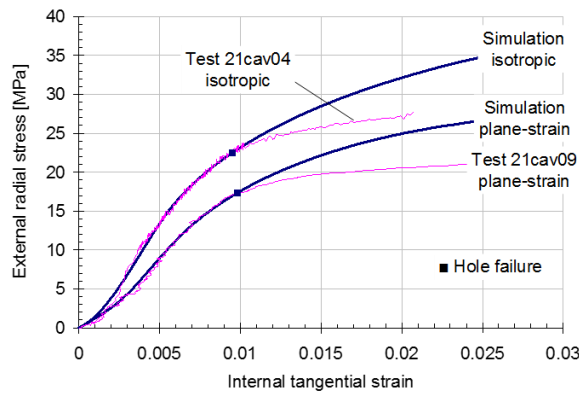


Figure 5: Isotropic and plane-strain loading. Numerical simulations and experimental results for the external radial stress vs. internal tangential strain. The hole failure points are indicated.

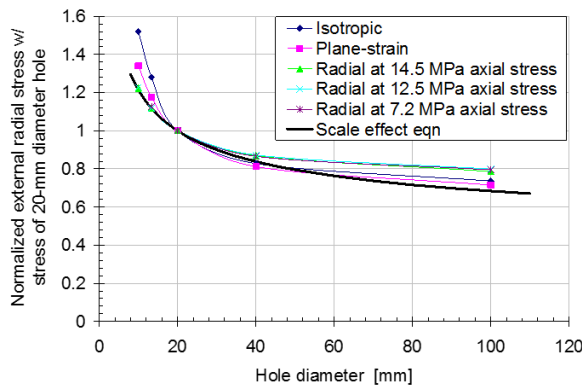


Figure 6: Theoretical predictions of scale effect for lateral hole failure during isotropic, plane-strain and radial loading tests at axial stress 7.2, 12.5 and 14.5 MPa and internal length  $R = 10 \mu\text{m}$ .

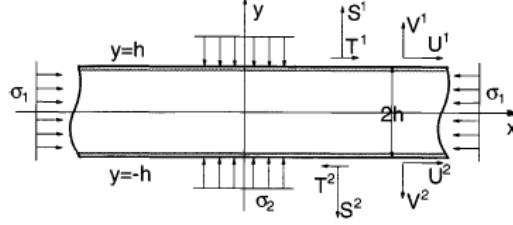
that was used to approximate experimental results. In Eq.(22),  $\sigma_F$  is the isotropic failure stress of a hole with diameter  $D$ , and  $\sigma_{Fref}$  the isotropic failure stress of a reference hole with diameter  $D_{ref} = 20$  mm. The results show that the scale effect is similar for all radial loading paths while a stronger size effect is predicted for the plane-strain and the isotropic loading paths.

### 3 Folding of elastic media as a bifurcation problem

The constitutive equations of large strain elasticity theory are utilized to study buckling of elastic layered media. These buckling modes can explain the occurrence of various periodic structures in geology such as folds. The analysis of the behavior of stratified elastic or viscoelastic media under compression is of interest to the structural geologist. Biot has presented an analysis of folding of stratified sedimentary rock in a series of pioneering papers and in his book ([Bio65] and references therein). The particular type of folding mechanism considered in Biot's theory is the spontaneous folding caused by instability under a compressive load acting in a direction parallel to the layers. From the geological viewpoint, a purely elastic theory is not sufficient to explain folding. Time-dependent phenomena such as viscous behavior must be taken into account. Biot [Bio57] developed a general theory of folding of a compressed viscoelastic layer embedded in an infinite medium of another viscoelastic material. He showed that, in general, there exists a lower and a higher critical load between which folding occurs at a finite rate with a dominant wavelength. This is the wavelength whose amplitude increases at the fastest rate. An experimental verification of Biot's theory of folding of stratified viscoelastic media in compression is presented by Biot et al. [Bio61].

#### 3.1 Buckling of a layer under initial stress

The problem considered here is the non-homogeneous, plane-strain deformation of a layer of thickness  $2h$ , due to constant horizontal and vertical compressions  $\sigma_1$  and  $\sigma_2$ , respectively, as shown in Figure 7. The theory in this analysis is based on incremental plane-strain deformations superimposed on the large strain uniform compression. The problem is formulated in terms of the first Piola-Kirchhoff stress  $\pi_{ij}$  with  $d\pi_{ij}$  being its increment referred to the deformed initially stressed state. In the case of constant body forces, the equations of equilibrium for the incremental problem take the form  $d\pi_{ij,j} = 0$ , where a subscript preceded by a comma denotes partial differentiation and repeated indices are summed. The incremental stress boundary conditions are  $d\pi_{ij}n_j = d\pi_i$ , where  $d\pi_i$  are the components of prescribed traction increments referred to the initial stressed state and  $n_j$  are the components of the outward unit normal of the boundary. Let  $du_i$  be the instantaneous incremental displacement components in the current configuration. The stress increment  $d\pi_{ij}$  is related to the Jaumann increments of the cororated Cauchy stress  $dT_{ij}$ , the initial stress field  $\sigma_{ij}$  and the incremental strain  $d\varepsilon_{ij}$  and spin  $d\omega_{ij}$  as follows

Figure 7: A single layer under initial stress  $\sigma_1$  and  $\sigma_2$ .

$$d\pi_{ij} = dT_{ij} + d\omega_{ik}\sigma_{kj} - \sigma_{ik}d\varepsilon_{kj} + \sigma_{ij}d\varepsilon_{kk} \quad (23)$$

The Jaumann stress increments are related directly to the strain increments through constitutive relations for anisotropic materials

$$\begin{aligned} dT_{11} &= C_{11}d\varepsilon_{11} + C_{12}d\varepsilon_{22} \\ dT_{22} &= C_{21}d\varepsilon_{11} + C_{22}d\varepsilon_{22} \\ dT_{12} &= 2Gd\varepsilon_{12} \end{aligned} \quad (24)$$

Using Eq.(23) and the constitutive Eq.(24), the equations of equilibrium become

$$\begin{aligned} C_{11}du_{1,11} + (G - \tau)du_{1,22} + (C_{12} + G + \tau)du_{2,12} &= 0 \\ (C_{21} + G - \tau)du_{1,12} + (G + \tau)du_{2,11} + C_{22}du_{2,22} &= 0 \end{aligned} \quad (25)$$

where  $\tau = (\sigma_1 - \sigma_2)/2$ . For the considered non-homogeneous deformation mode, the displacement field is assumed to be given in terms of two unknown amplitude functions of the dimensionless coordinates  $x = x_1/L$ ,  $y = x_2/L$

$$\begin{aligned} du_1 &= U(y)\sin(\beta x), & U(y) &= Ae^{\gamma y} \\ du_2 &= V(y)\cos(\beta x), & V(y) &= Be^{\gamma y} \end{aligned} \quad (26)$$

where  $L$  is a reference length associated with the wavelength  $W$  and  $\beta$  a dimensionless wavenumber. The wavelength  $W$  of the deformation mode can be written as  $W = 2\pi L/\beta$ . By substituting the displacement field (26) in the differential equations (25) and letting  $Z = \gamma/\beta$ , we obtain a system of two linear homogeneous algebraic equations with respect to the integration constants  $A$  and  $B$

$$\begin{aligned} A[-C_{11} + (G - \tau)Z^2] + B[-(C_{12} + G + \tau)Z] &= 0 \\ A[(C_{21} + G - \tau)Z] + B[-(G + \tau) + C_{22}Z^2] &= 0 \end{aligned} \quad (27)$$

For non-trivial solution in terms of  $A$  and  $B$ , the determinant of the system of equations (27) must vanish. This leads to the following biquadratic equation for  $Z$

$$aZ^4 - bZ^2 + c = 0 \quad (28)$$

where  $a = C_{22}(G - \tau)$ ,  $b = C_{11}C_{22} - C_{12}C_{21} - C_{12}(G - \tau) - C_{21}(G + \tau)$  and  $c = C_{11}(G + \tau)$ . The four roots of Eq.(28) correspond to four solutions  $U_k$  and  $V_k$  for the displacement field amplitudes. The complete solution for  $U(y)$  and  $V(y)$  is then given as a linear combination of the function base as

$$U(y) = \sum_{k=1}^4 a_k U_k, \quad V(y) = \sum_{k=1}^4 a_k V_k \quad (29)$$

where  $a_k$  are integration constants. The base functions  $U_k$  and  $V_k$  are given explicitly in [Pap88].

### 3.2 Eigendisplacements and tractions at layer boundaries

The incremental displacement amplitudes at the upper (1) and lower (2) boundaries of the layer are obtained directly from Eqs.(29)

$$\begin{aligned} U^1 &= \sum_{k=1}^4 a_k U_k(h/L), & V^1 &= \sum_{k=1}^4 a_k V_k(h/L) \\ U^2 &= \sum_{k=1}^4 a_k U_k(-h/L), & V^2 &= \sum_{k=1}^4 a_k V_k(-h/L) \end{aligned} \quad (30)$$

The boundary tractions  $d\pi_i = d\pi_{ij}n_j$  are written through Eqs.(23), and (24) as

$$d\pi_1 = \frac{\beta}{L} T(y) \sin(\beta x), \quad d\pi_2 = \frac{\beta}{L} S(y) \cos(\beta x) \quad (31)$$

$$\begin{aligned} S(y) &= \sum_{k=1}^4 a_k S_k, & S_k &= (C_{21} - \tau - p)U_k + C_{22}V_k'/\beta \\ T(y) &= \sum_{k=1}^4 a_k T_k, & T_k &= (G - \tau)U_k'/\beta + (G - p)V_k \end{aligned} \quad (32)$$

where  $p = (\sigma_1 + \sigma_2)/2$  and  $(\cdot)' = d/dy$ . The stress amplitudes  $S$  and  $T$  at the upper (1) and lower (2) boundaries of the layer, in accordance with Eq.(30), are

$$\begin{aligned} S^1 &= \sum_{k=1}^4 a_k S_k(h/L), & T^1 &= \sum_{k=1}^4 a_k T_k(h/L) \\ S^2 &= \sum_{k=1}^4 a_k S_k(-h/L), & T^2 &= \sum_{k=1}^4 a_k T_k(-h/L) \end{aligned} \quad (33)$$

In matrix form the general solution for the upper ( $i=1$ ) or lower ( $i=2$ ) boundary displacement and traction amplitudes is written

$$\begin{Bmatrix} U^i \\ V^i \\ S^i \\ T^i \end{Bmatrix} = \begin{bmatrix} U_1^i & U_2^i & U_3^i & U_4^i \\ V_1^i & V_2^i & V_3^i & V_4^i \\ S_1^i & S_2^i & S_3^i & S_4^i \\ T_1^i & T_2^i & T_3^i & T_4^i \end{bmatrix} \begin{Bmatrix} a_1 \\ a_2 \\ a_3 \\ a_4 \end{Bmatrix} \quad (34)$$

### 3.3 Buckling of a layer system—the transfer matrix technique

Buckling of a layer system can be analyzed and solved numerically using the solution for a single layer and the transfer matrix technique [Buf65]. Figure 8 shows a system of  $n$  layers of different materials and different initial stresses parallel to the layer axis with a global coordinate system located at the top layer. This medium is obtained by superposing adhering layers, each of which can be viewed individually as a single layer. The layers are numbered from 1 to  $n$  starting at the top. By assuming perfect adherence at the interfaces, the incremental stresses and displacements are continuous along the interfaces. Under these conditions, the equations for the buckling of the system of layers are derived immediately from the results of Section 3.2 provided that all local coordinates are expressed in the global coordinate system. From Eq.(34), the amplitude of the incremental stresses and displacements for the  $i^{\text{th}}$  interface of the  $j^{\text{th}}$  layer can be assembled in matrix form as

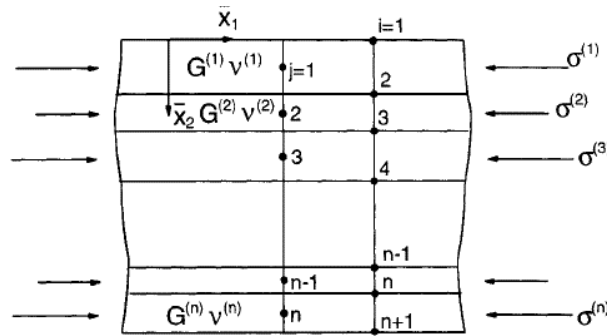


Figure 8: Multilayered medium under compressive initial stresses.

$$\begin{Bmatrix} U^{ij} \\ V^{ij} \\ S^{ij} \\ T^{ij} \end{Bmatrix} = \begin{bmatrix} U_1^{ij} & U_2^{ij} & U_3^{ij} & U_4^{ij} \\ V_1^{ij} & V_2^{ij} & V_3^{ij} & V_4^{ij} \\ S_1^{ij} & S_2^{ij} & S_3^{ij} & S_4^{ij} \\ T_1^{ij} & T_2^{ij} & T_3^{ij} & T_4^{ij} \end{bmatrix} \begin{Bmatrix} a_1^j \\ a_2^j \\ a_3^j \\ a_4^j \end{Bmatrix} \quad \text{or} \quad \{X^{ij}\} = [F^{ij}] \{A^j\} \quad (35)$$

By requiring continuity of the incremental displacements and tractions at all interfaces, the integration constants of every layer are linked to the integration constants of the top layer as follows

$$\{A^n\} = [F]\{A^1\}, \quad [F] = [F^n] \cdots [F^2], \quad [F^k] = [F^{kk}]^{-1} [F^{k(k-1)}] \quad (36)$$

In order to formulate the eigenvalue problem we have to consider boundary conditions only at the upper and lower boundary surfaces of the layered medium. As an example, the case of zero tractions at the upper boundary surface ( $i = 1, j = 1$ ) and zero displacements at the lower boundary surface ( $i = n+1, j = n$ ) is considered. These boundary conditions can be written in matrix form as

$$[Y^1]\{A^1\} = 0, \quad [Y^n]\{A^n\} = 0 \quad (37)$$

where  $[Y^1]$  contains the last two rows of  $[F^{11}]$  and  $[Y^n]$  the first two rows of  $[F^{(n+1)n}]$ . By taking into account Eq.(36), the matrix Eq.(37) can be assembled in a homogeneous algebraic system of equations for the integration constants  $\{A^1\}$

$$\begin{bmatrix} [Y^n] & [F] \\ [Y^1] & \end{bmatrix} \{A^1\} = 0 \quad \text{or} \quad [Y]\{A^1\} = 0 \quad (38)$$

The resulting homogeneous system of equations has non-trivial solutions in terms of the integration constants involved only if the determinant of the system is zero, i.e.  $\det([Y]) = 0$ . This provides an equation whose roots gives the corresponding eigenvalues. In this equation, we fix the wavenumber  $\beta$  and we consider it as an equation for the load. When monotonic loading is assumed, then the lowest loading level associated with the least eigenvalue provides the critical buckling load.

### 3.4 Buckling of layered half space

The buckling condition for a homogeneous half-space is independent of the wavelength of the considered mode. This is because no length appears in this problem and consequently the various modes corresponding to different wavelengths cannot be differentiated. The introduction of length leads to the selection of a particular buckling mode. An example is the buckling of a layer on top of a half-space due to a horizontal homogeneous strain field, as shown in Figure 9a. Both media are assumed isotropic and compressible with elastic parameters  $G, \nu$  and  $G_L, \nu_L$  for the half-space and the layer, respectively. Figure 9b presents the results for the critical buckling stress. The wave number is given as  $\beta = 2\pi h/W$  where  $h$  is the thickness of the layer and  $W$  the wavelength of the deformation field. For the two limiting cases of vanishingly short wavelength ( $\beta \rightarrow \infty$ ) and infinitely large wavelength ( $\beta \rightarrow 0$ ) the buckling stress corresponds to that of a homogeneous half-space. For short wavelengths, the layer behaves like a half-space whereas large wavelengths cannot ‘see’ the layer. If the layer is stiffer than the half-space then there is a dominant buckling mode, the wavelength of which depends on the

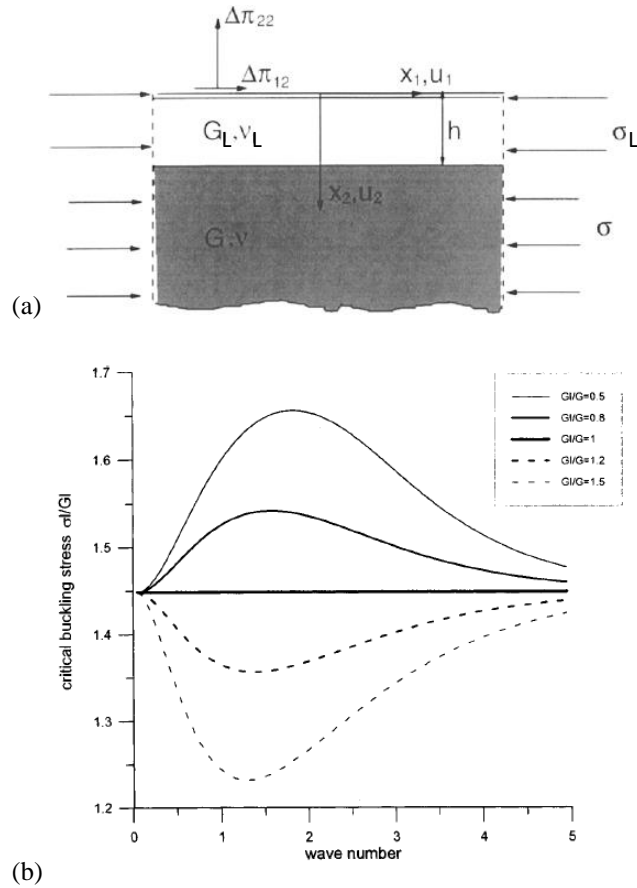


Figure 9: (a) Buckling of a layer on top of a half space, and (b) critical buckling stress as a function of wavenumber for various values  $G_L/G$ .

stiffness contrast  $G_L/G$ .

For viscoelastic behavior for the layer and the half space there exists a dominant wavelength for fastest growth [Pap88]. Figure 10 plots the critical buckling stress as a function of wavelength  $\beta$  for various rates of growth and relaxation constant  $r/r_L = 0.01$  Maxwell type viscoelastic materials are elastic for fast deformations ( $p \rightarrow \infty$ ) but in slow deformations ( $p \rightarrow 0$ ) exhibit Newtonian viscosity. In all cases the stiffness of the layer is sufficiently higher than that of the half-space and both are incompressible, i.e.  $\nu = \nu_L = 0.5$ . Figure 10 shows that for a given load there exists a wavenumber of fastest rate of growth, i.e. highest value of  $p$ . The possibility of buckling with multiple wavelengths is also possible. If e.g. more than one different loads are applied, the dominant wavelength of each load will be present and will be superposed. This fact is of great interest in the mechanics of folding and can reveal the stress states that the formations have experienced in the past.

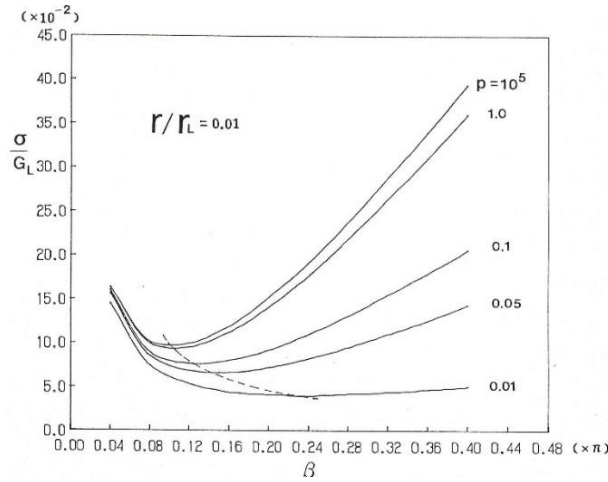


Figure 10: Critical buckling stress of a viscoelastic layer on a viscoelastic half space with relaxation constant ratio  $r/r_L = 0.01$  and rate of growth  $p$ .

#### 4 Axial splitting and spalling

Axial splitting in uniaxial loading, spalling of a free surface and rock bursting are common phenomena in brittle materials, like rock and concrete, under compressive stresses parallel to a free surface. A micromechanically-motivated mechanism is presented here that views axial splitting and spalling as a result of the interaction between surface instabilities and surface parallel Griffith cracks. According to this mechanism, surface instabilities in a uniformly stressed half-space, produce secondary tensile stresses, which, for material points close to a free surface remain unbalanced in the direction normal to the surface. These tensile stresses cause latent, surface parallel cracks to open and thus magnify the effect of diffuse bifurcation. Tensile stress concentrations develop at the crack tips resulting in unstable crack growth and finally axial splitting and spalling of the material.

Unstable crack growth and axial splitting correspond to some critical crack surface density (distributed material damage) which manifests itself in the mean spacing of forming spalls. The fractured material becomes much weaker than the intact one due to the lower buckling stress of individual columns. Keeping this model in mind, we may consider that rock bursting is the result of buckling of flaked rock surfaces, the flaking itself being triggered by surface instabilities. In order to investigate this mechanism, the buckling problem under plane-strain conditions due to a uniform compression of a semi-infinite medium containing surface parallel Griffith cracks is considered. Analytical solutions for these type of problems have been presented by Keer et al. [Kee82], who solved the buckling problem in solids containing a periodic array of coplanar cracks and by Nazarenko, who considered a single crack [Naz86]. Vardoulakis and Papamichos [Var91] and Papamichos [Pap92] have de-

veloped a numerical boundary element solution based on the displacement discontinuity method for solving the problems of an arbitrary number and/or geometry of surface parallel cracks in elastic, anisotropic media. In the following, the weakening of a medium due to the presence of periodic crack arrays is investigated.

#### 4.1 Buckling of a half-space with surface parallel cracks

The buckling problem of a half-space containing a single or periodic arrays of coplanar cracks is solved using a numerical solution for the eigendisplacements of the two crack faces and the free surface. The problem is formulated using the boundary element method for crack problems in semi-infinite anisotropic media under initial horizontal stress [Var91]. The method was constructed by modifying the Displacement Discontinuity Method [Cro11] to account for the existence of the initial stress field. It is based on the analytical solution to the problem of a constant displacement discontinuity over a finite line segment in a semi-infinite, anisotropic medium. For a line segment, the displacement discontinuity  $D_i$  is defined as the difference in displacement between the two sides of the segment. The formulation provides the functions that allow the determination of the displacement and first Piola-Kirchhoff stress increments at any point in a half-space due to a displacement discontinuity increment  $D_i$  over the line segment.

Figure 11 shows the deformed crack shape and the free surface due to buckling of a single crack for three values of the ratio  $h/a$ , where  $h$  is the distance of the crack from the free surface and  $a$  the crack half-length. At each point along the crack, the relative displacements between the two faces are the eigendisplacement discontinuities of the crack. The two sides of the crack deform by different amounts and, as expected, the disturbed region of the free surface localizes with the crack approaching the free surface. For a periodic crack array (Figure 12), the infinitely extended crack array is approximated with ten 25-element cracks. Such an approximation is considered satisfactory since it was found that an increase in the number of cracks does not affect significantly the results. Figure 13 presents the results where the normalized critical buckling stress  $\xi = -\sigma/G$  is plotted as a function of the dimensionless depth  $h/L$  and the dimensionless crack length  $\alpha/L$ , where  $L$  is the spacing between the cracks. Poisson's ratio has the value of 0.3 in all calculations. This is the solution for the first bifurcation mode which is antisymmetric and corresponds to cracks tending to open and close alternately, as shown in Figure 13a. The numerical results of the advanced solution for the symmetric mode of all open cracks are shown in Figure 13b. Higher stress is required for the all open mode and in fact, the critical stress in this case increases with decreasing spacing.

Once the periodic crack array problem is solved, additional crack arrays can be placed in the half-space to investigate the weakening of the medium due to the presence of additional crack arrays. The crack arrays were approximated with ten 20-element cracks. For  $\alpha/L = 0.5$ ,  $h/a$  between 0.5 and 5 and the lowest buckling mode, the second crack array reduces the critical buckling stress by approximately 6

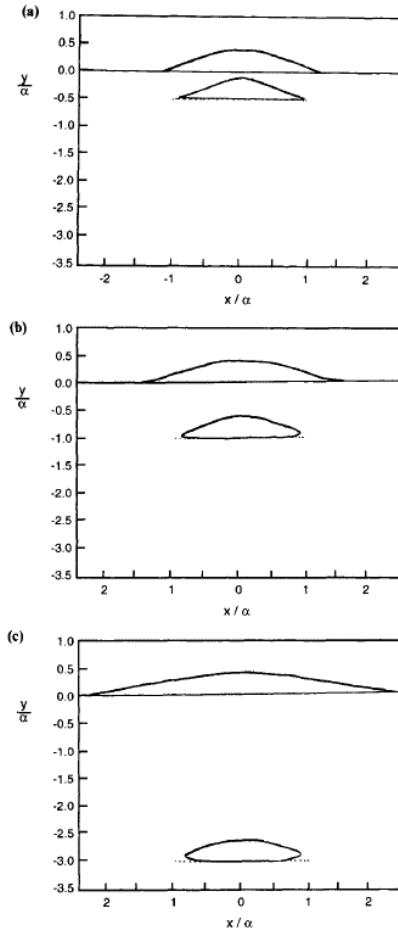


Figure 11. Deformed shape of crack and free surface due to buckling of the half-space for  $h/\alpha =$  (a) 0.5, (b) 1, and (c) 3 (boundary element solution,  $\nu = 0.3$ ).

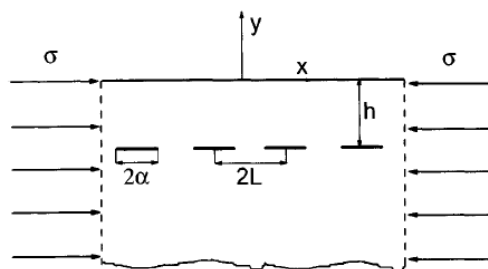


Figure 12. Half-space with periodic array of collinear cracks compressed by uniform horizontal stress.

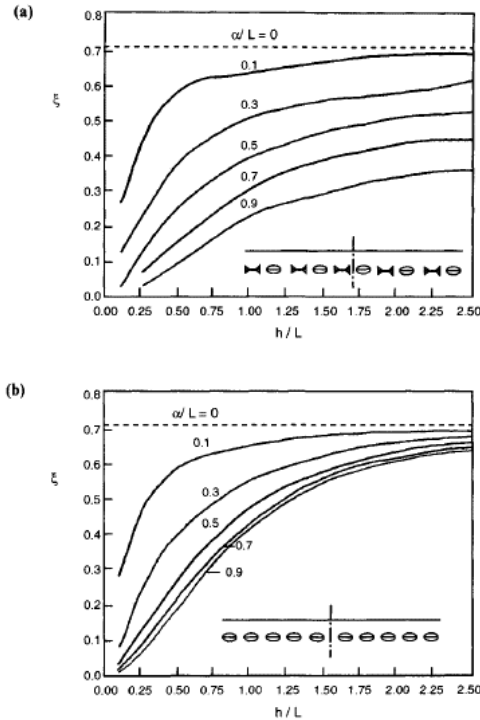


Figure 13. Critical buckling stress  $\xi = -\sigma/G$  of a half-space with a periodic array of collinear cracks, for (a) alternate open mode, (b) all open mode ( $\nu = 0.3$ ).

percent, while the third array reduces it by an additional 1.5 percent. This means that the buckling load is mainly determined by the cracks closer to the free surface.

Furthermore, the eigendisplacements at the critical state show that the buckling of the half-space affects primarily the crack array closer to the free surface, suggesting a progressive spalling behavior that starts close to the free surface and subsequently progresses deeper into the material. This spalling advancement was observed experimentally for example in Berea sandstone specimens tested in the surface instability detection apparatus [Pap94].

## 5 Conclusions

A three-dimensional Cosserat non-linear elastic, Mohr-Coulomb elastic-plastic model was formulated and calibrated based on generalizations of classical continuum models. The model was calibrated on Red Wildmoor sandstone data and applied to the bifurcation problem of borehole failure. The Cosserat internal length was calibrated on back analysis of borehole failure data from HC tests. Once calibrated, it can be used for forward predictions under different loading paths and

fluid flows. The lateral borehole failure mode was analyzed. This mode prevails when the tangential stress at the borehole is the largest compressive principal stress.

In elastic, semi-infinite media containing surface parallel Griffith cracks, the resistance to crack propagation is diminished as the critical stress for surface instability is approached. In particular, the effective stress intensity factor increases rapidly near the surface instability condition and therefore we may assume that any crack at this stress level will propagate. Furthermore, the critical buckling stress of the media under consideration decreases rapidly with increases relative to the depth and length of the cracks. This suggests that in the case of a constant far-field stress (e.g. load control conditions in a laboratory setting), cracks close to the free surface will tend to become unstable once they begin to grow, leading to spalling of the surface. For a stable crack growth, a reduction in the value of the far-field stress will be necessary (e.g. displacement control conditions). Thus, a material with surface parallel cracks could be modeled as a softening material with respect to the crack length and spacing.

## Acknowledgments

The author wish to thank the sponsors of SINTEF Petroleum's Sand production project, ConocoPhillips Scandinavia, Total E&P Norge, Eni Norge, StatoilHydro and Norske Shell for supporting this research.

## References

- [Bio57] Biot MA. Folding instability of a layered viscoelastic medium under compression. *Proc. Roy. Soc. London, Ser. A* 242, 444–454, 1957.
- [Bio61] Biot MA. Theory of folding of stratified viscoelastic media and its implications in tectonics and orogenesis. *Geologic Society of America Bulletin* 72, 1595-1620, 1961.
- [Bio65] Biot MA. *Mechanics of incremental deformations*. John Wiley, New York, 1965.
- [Buf65] Bufler H. Die Drucksstabilität rechteckiger Verbundplatten. *Ingenieur Archiv* 34, 109–128, 1965.
- [Cro83] Crouch SL, Starfield AM. *Boundary element methods in solid mechanics*. Allen & Unwin, London, 1983.
- [Hai93] Haimson BC, Song I. Laboratory study of borehole breakouts in Cordova Cream: a case of shear failure mechanism. *International Journal for Rock Mechanics and Mining Sciences & Geomechanics Abstracts* 30, 7, 1047-1056, 1993.

- [Kee82] Keer LM, Nemat-Nasser S, Oranratnachai A. Surface instability and splitting in compressed brittle elastic solids containing crack arrays. *Journal of Applied Mechanics* 49, 761–767, 1982.
- [Mau92] Maury V. An overview of tunnel, underground excavation and borehole collapse mechanisms. In: *Comprehensive Rock Engineering, Vol 4: Principles, practice & projects*, Oxford: Pergamon Press, 369-412, 1992.
- [Naz86] Nazarenko VM. Theory of fracture of materials in compression along near surface cracks under plane-strain conditions. *Soviet Appl. Mech.* 22, 12, 1192–1199, The Faraday Press, New York, 1986
- [Pap88] Papamichos E. Numerical analysis of buckling phenomena in layered rock media. MSc Geo-Engineering Thesis, University of Minnesota, Minneapolis, Minnesota, USA, 1988.
- [Pap10a] Papamichos E, Tronvoll J, Skjærstein A, Unander TE. Hole stability of Red Wildmoor sandstone under anisotropic stresses and sand production criterion. *Journal of Petroleum Sciences and Engineering* 72, 78-92, doi:10.1016/j.petrol.2010.03.006, 2010.
- [Pap10b] Papamichos E. Analysis of borehole failure modes and pore pressure effects. *Computers and Geotechnics* 37, 141-152, doi:10.1016/j.compgeo.2009.08.006, 2010.
- [Pap10c] Papamichos E. Borehole failure analysis in a sandstone under anisotropic stresses. *Intl Journal for Numerical and Analytical Methods in Geomechanics* 34, 581–603, doi:10.1002/nag.824, 2010.
- [Pap92] Papanastasiou P, Vardoulakis I. Numerical treatment of progressive localization in relation to borehole stability. *International Journal for Numerical and Analytical Methods in Geomechanics* 16: 389-424, 1992.
- [Pap94] Papamichos E, Labuz JF, Vardoulakis I. A surface instability detection apparatus. *Rock Mechanics Rock Engineering* 27, 1, 37-56, doi:10.1007/BF01025955, 1994.
- [Var88] Vardoulakis I, Sulem J, Guenot A. Borehole instabilities as bifurcation phenomena. *International Journal of Rock Mechanics and Mining Sciences & Geomechanics Abstracts* 25(3): 159-170, DOI: 10.1016/0148-9062(88)92298-X, 1988.
- [Var95] Vardoulakis I, Sulem J. *Bifurcation analysis in geomechanics*. Glasgow: Blackie Academic & Professional, 1995.
- [Zie89] Zienkiewicz OC, Taylor RL. *The finite element method, Vol. 2, Solid and fluid mechanics dynamics and non-linearity*. 4th ed., London: McGraw-Hill, 1989.

# Multiphysics couplings and strain localization in geomaterials

**Jean Sulem and Ioannis Stefanou**

*CERMES-Laboratoire Navier, Ecole des Ponts ParisTech, Université Paris-Est, France*

---

*The purpose of this chapter is to provide a review of recent research regarding the effects of temperature, pore-pressure, chemical reactions and microstructure on strain localization in geomaterials. Examples have been taken in relation with seismic slip and with compaction banding. Strain localization is treated as an instability from a homogeneous deformation state.*

## 1 Introduction

Although strain localization in the form of shear band formation can occur with negative or positive rate of strain hardening, the latter being possible for deformation states close to plane strain [Rud75], softening behavior definitely favors shear banding. This softening behavior may correspond to a mechanical degradation of the rock properties (microcracking, grain crushing and grain size reduction...) [Das11], but various other physical processes can be responsible for it [Reg13]. The effect of an infiltrated pore fluid which interacts with a rock mass can lead to a hardening or softening behavior depending on the volumetric response of the rock (dilatant or contractant). The effect rapid heating of a saturated geomaterial leads to pore-fluid pressurization due to the discrepancy between the thermal expansion of water and solid grains. Thermal pressurization is a softening mechanism as it results in a decrease of the effective mean stress and thus of the shear strength. Chemical reactions such as dissolution/precipitation, mineral transformation at high temperature (dehydration of minerals, decomposition of carbonates, ...) affect the solid phase of the rock, sometimes release a new fluid phase in the system (dehydration reactions) and can induce a positive feedback in the progressive mechanical degradation. On the other hand, mechanical damage increases the reaction surface between the reactive fluid and the solid and enhances dissolution and further material weakening [Hu07a, Hu07b].

A key parameter when studying multi-physics effects on the formation and evolution of deformation bands is the actual width of the localized zone. Obviously, this parameter plays a major role in the energy budget of the system as it controls the feedback of the dissipative terms in the energy balance equation. As emphasized by [Ric14] narrow deforming zones concentrate the frictional heating, which leads to large temperature rises and thus to more rapid weakening. The width of the deforming zone is determined by the various physical processes involved in the weakening mechanisms but it also controls the multi-physics couplings which occur during dynamic slip.

It is well known that strain localization analyses performed for rate-independent materials within the frame of classical continuum theories lead to infinitesimally narrow localized zone. This reflects the ill-posedness of the underlying mathematical problem and can be traced to the absence of a material length in the constitutive equations. Viscous regularization by considering strain rate hardening is commonly considered to overcome this problem. Another approach is to resort to continuum models with microstructure to describe on a more physical basis the localization phenomena. These generalized continua usually contain additional kinematical degrees of freedom (Cosserat continuum) and/or higher deformation gradients (higher grade continuum). They introduce material internal lengths and also characteristic time scales. The internal length and the micro-inertia introduced from generalized continua permit to describe localization phenomena in zones of finite thickness and lead to a finite evolution rate of a deformation band like in strain rate dependent constitutive laws [Sul11, Vev12, Vev13].

In this paper, we review some multi-physics couplings, which enhance strain localization in geomaterials. The first part of the paper focusses on shear banding, emphasizing thermal and chemical effects in relation with shear heating. As mentioned above the localization zone thickness can be captured either by considering rate dependency of the constitutive law or by resorting to higher order continua that possess an internal length. In order to explore the link between the two different modeling approaches a comparison between a) rate dependent Cauchy continuum and b) rate independent Cosserat continuum is shown for the scaling of the localized zone thickness. The comparison is made on the basis of a simplified example in order to illustrate the main differences and aspects of each modeling strategy. The last part of the paper is focused on compaction band formation in porous materials triggered by dissolution as an example of another type of chemo-mechanically induced strain localization.

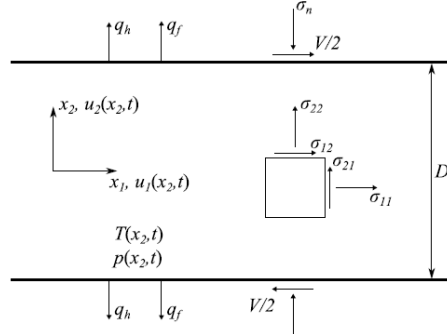


Figure 1: Model of a fault zone as an infinite layer under uniform shear strain rate

$$\dot{\gamma} = \frac{V}{D}.$$

## 2 Thermo-chemo-chemical couplings and stability of shear zones

### 2.1 Problem statement

We consider a layer of saturated rock with thickness  $D$  deformed in shear at a slip rate  $V$  (Figure 1). Several investigations have shown that the ultracataclastic gouge zones forming the fault core have a much lower permeability ( $< 10^{-19} \text{ m}^2$ ) than that in the surrounding damage zone (e.g. [Sul04, Wib02]). Therefore, as fluids and heat are trapped inside the slip zone during an earthquake, it is interesting to investigate the stability of undrained adiabatic shearing of such a gouge layer. This is done by assuming that drainage and heat flux are prohibited at the boundaries of the layer. It is also assumed that the normal stress  $\sigma_n$  acting on the layer is constant.

In this 1D-model the velocity components,  $u_1(x_2, t)$ , and  $u_2(x_2, t)$  in the direction parallel and normal to the fault respectively depend only on the time since the onset of slip and on the position  $x_2$  in the direction normal to the band. Inside such a shear-band the pore pressure  $p_f$  and the temperature  $T$  are assumed to be functions only of time  $t$  and of the position  $x_2$  in the direction normal to the band.

The governing equations of the system are the balance laws of linear momentum, mass and energy. Neglecting inertia effects [Ric06a], mechanical equilibrium leads to shear and normal stress which do not depend on  $x_2$ .

$$\frac{\partial \sigma_{12}}{\partial x_2} = 0 \quad , \quad \frac{\partial \sigma_{22}}{\partial x_2} = 0 \quad (1)$$

The fluid mass balance equation (equation (2)) is the sum of three terms: the diffusion term, the thermal pressurization term and the term corresponding to the effect on pore pressure of inelastic porosity change (for example dilatancy). Chemical effects and their impact on the localization zone will be discussed later in the paper.

$$\frac{\partial p_f}{\partial t} = c_{hy} \frac{\partial^2 p_f}{\partial x_2^2} + \Lambda \frac{\partial T}{\partial t} - \frac{1}{\beta^*} \frac{\partial n^p}{\partial t} \quad (2)$$

In equation (2),  $c_{hy}$  is the hydraulic diffusivity,  $\beta^*$  is the storage capacity,  $\partial n^p / \partial t$  is the rate of inelastic porosity change,  $\Lambda = n(\lambda_f - \lambda_n) / \beta^*$  is the undrained thermal pressurization coefficient, where  $\lambda_f$  is the pore fluid thermal expansion coefficient and  $\lambda_n$  is the thermal expansion coefficient of the pore volume, and  $n$  is the porosity of the rock. Typical values for  $\Lambda$  range from 0.1 to 1 MPa/°C [Gha08].

The energy balance equation (equation (3)) is the sum of two terms: the diffusion term and the source term corresponding to the frictional heat.

$$\frac{\partial T}{\partial t} = c_{th} \frac{\partial^2 T}{\partial x_2^2} + \frac{1}{\rho C} \tau \dot{\gamma}_0^p \quad (3)$$

In equation (3),  $c_{th}$  is the thermal conductivity,  $\rho C$  is the specific heat,  $\tau \dot{\gamma}_0^p$  is the plastic work which is assumed to be entirely converted into heat. The shear stress  $\tau$  is proportional to the effective Terzaghi stress:  $\tau = f(\sigma_n - p_0)$  where  $f$  is the friction coefficient.

Considering that the layer is homogeneous and uniformly sheared at a constant strain rate  $\dot{\gamma}_0 = V / D$  where  $V$  is the imposed slip rate, pore pressure and temperature are independent of  $x_2$ . A closed form solution for their evolution in time has been given by Lachenbruch [Lac80, Ric06b, Sul07]:

$$\begin{aligned}
 p_f &= p_{f0} + (\sigma_n - p_0) \left( 1 - \exp\left(-\frac{Vt}{L}\right) \right) \\
 T &= T_0 + \frac{(\sigma_n - p_0)}{\Lambda} \left( 1 - \exp\left(-\frac{Vt}{L}\right) \right)
 \end{aligned}
 , \text{ with } L = \frac{\rho C h}{f \Lambda} \quad (4)$$

The pore-pressure increases towards the imposed normal stress  $\sigma_n$  and the temperature increases towards  $T = T_0 + (\sigma_n - p_{f0}) / \Lambda$ . In due course of the shear heating and fluid pressurization process, the shear strength is reduced towards zero. We observe that the length scale  $L$ , which controls the shear stress evolution, is the same as the one which controls the temperature evolution.

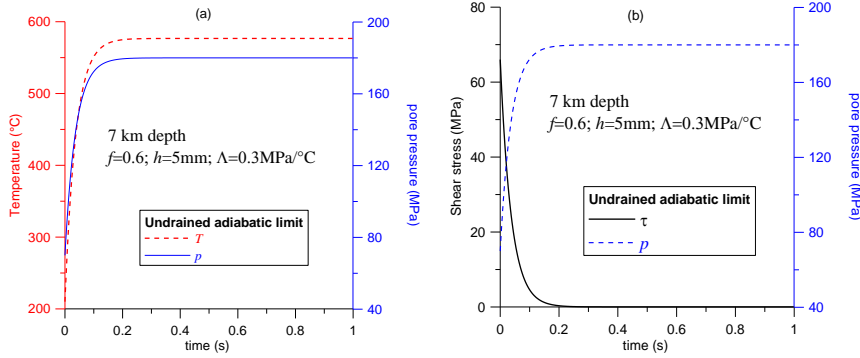


Figure 1. Homogeneous layer at 7 km depth ( $T_0 = 210^\circ\text{C}$ ,  $p_{f0} = 70\text{MPa}$ ,  $\sigma_n = 180\text{MPa}$ ), uniformly sheared at a constant strain rate (imposed slip velocity  $V = 1\text{m/s}$ ) under locally undrained and adiabatic conditions.

## 2.2 Stability of adiabatic undrained shear

The stability of the above undrained adiabatic (uniform) solution can be studied by performing a linear perturbation analysis. Details of such an analysis are found in the paper of [Ric14, see also Sul11]. Note that when performing this stability analysis, spatially-dependent perturbations are considered inside the layer so that heat and fluid diffusion is allowed inside the layer, whereas zero heat and fluid fluxes are imposed at the boundaries of the layer. If we assume constant friction coefficient, this solution is unstable for all wave lengths of the perturbation. Therefore, strain

will localize into a zone of zero thickness, which corresponds to the solution of slip on a plane given by [Ric06b] for which the temperature rise is  $\Delta T = \left(1 + \sqrt{c_{hy}/c_{th}}\right)(\sigma_n - p_{f0})/\Lambda$ . Considering the very low permeability of the fault gouge,  $c_{hy}$  and  $c_{th}$  are of the same order of magnitude so that the temperature is in that case about twice bigger than the undrained adiabatic uniform solution. As mentioned in the introduction, the infinitesimally thin localized zone is reflecting the lack of a material length in the model (for example the grain size) that will act as a localization limiter. [Ric14] have considered a rate-dependent friction coefficient derived from rate-and-state friction (RSF) laws which are commonly used in seismology [Die79],  $f = f_0 + a \log(\dot{\gamma}/\dot{\gamma}_0)$ , where  $a$  is a strain rate-hardening (or softening) parameter and it depends on temperature. Under temperature increase,  $a$  is not monotonous and experimental evidence shows that either thermal softening or thermal hardening takes place [Che92, Sch98]. This coupling is important as it plays a direct role on the stability of faults and of course on localization [Ale14, Pou14, Vev14]. The choice of the RSF law depends on the available experimental data and its mathematical form can lead to differences regarding temperature increase [Vev10]. As it will be shown in the next paragraphs, temperature increase and strain localization are key factors as far it concerns the interplay between mechanics, heat and pore-pressure diffusion and the activation of chemical reactions induced by frictional heating.

Neglecting the direct effect of temperature increase on the RSF law, Rice et al. (2014) have obtained that for strain-rate softening ( $a < 0$ ), the uniform solution of undrained adiabatic shearing is unstable for all wave lengths of the perturbation. For strain-rate hardening ( $a > 0$ ), only shear zones with a thickness  $h$  smaller than a

critical value  $h_{cr} = \pi \sqrt{\frac{a \rho C}{f_0 \Lambda} \frac{c_{th} + c_{hy}}{(f_0 + 2a) \dot{\gamma}_0}}$  can support stable homogeneous deformation.

This critical thickness is interpreted as the thickness of the localized shear zone and this statement was corroborated by numerical simulation in the post-localization regime performed by [Pla14]. Interestingly, this expression of the critical shear zone thickness exhibits two competing processes: Fluid and thermal diffusion and rate-dependent frictional strengthening tend to expand the localized zone, while thermal pressurization tends to narrow it. As emphasized above, strain localization in a narrow zone leads to faster and stronger temperature rise than that predicted if localization is ignored.

For representative values of the material parameters, stress and temperature conditions of a fault at a seismogenic depth of 7 km, [Ric14] have obtained typical values of few microns to few tens of microns for the thickness of the localized zone. This value is comparable to the gouge grain size and therefore it might be important to take into account the granular microstructure of the material. This has been proposed by Sulem et al. [Sul11] which studied localization in a fluid-saturated material accounting for the motion of individual grains using a Cosserat microstructure. In a Cosserat continuum, each material point possesses additional rotational degrees of

freedom so that a rolling resistance is attributed to the grains. Note that an internal length  $R$  related to the grain size of the material is introduced in the formulation of constitutive laws for a Cosserat material. A stability analysis of undrained adiabatic shearing of an elastoplastic layer with strain hardening and dilatancy has been proposed. It was shown that instability can occur even in the hardening regime of the underlying drained stress-strain response if dilatant hardening cannot compensate the thermal pressurization of the pore fluid. A remarkable result is that if we do not take into account the effect of microstructure and the associated micro-inertia, the underlying mathematical problem is ill-posed, i.e. for a hardening modulus lower than the critical hardening modulus at instability, the growth coefficient in time of the instability is infinite. The complete dynamic analysis for a Cosserat continuum shows that the growth coefficient of the instability is always finite and that it depends on the wavelength of the instability mode. The wavelength of the instability mode for which the growth coefficient is maximum will evolve faster and it will dominate the others. This selected wavelength is depicted in Figure 3. For representative values of a fault zone at 7 km depth, it was found that the selected wavelength is about  $200R$ . The localized zone thickness is half of this value, so that for typical values of a grain size of few microns for the fault gouge, this corresponds to a shear band thickness of few hundreds of microns which is compatible with field observations in fault zones.

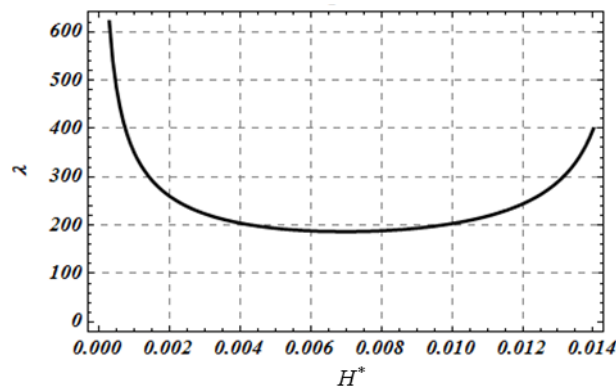


Figure 2. Wave length selection:  $\lambda$  is the wave length of the perturbation normalized by the Cosserat internal length  $R$ ,  $H^*$  is the strain hardening modulus of the elastoplastic model.

### 2.3 Chemical weakening and earthquake nucleation

An interesting situation corresponds to shear localization in a chemically weakening material. This case is relevant for understanding the nucleation of intermediate and

deep earthquakes within subduction zones. As discussed by Green [Gre07], deep earthquakes have been a paradox since their discovery in the 1920s. The combined increase of pressure and temperature with depth precludes brittle failure or frictional sliding beyond a few tens of kilometers. Nevertheless, earthquakes still occur in subduction zones to 700 km. Growing evidence suggests that the great majority of subduction zone earthquakes shallower than 400 km are initiated by breakdown of hydrous phases and that deeper ones probably initiate as a shearing instability associated with breakdown of metastable olivine to its higher-pressure polymorphs. Reaction weakening behavior has been extensively documented in the case of rocks containing dehydrating minerals such as gypsum and serpentinite. In the case of serpentinite dehydration, the reaction products may be weaker. This is the case for the dehydration of lizardite for which the produced ultra-fine grained olivine is weaker than the serpentinite aggregates [Rut88]:



This leads to a self-lubrication of the fault by the newly formed material. The intrinsic reaction-weakening process assumed here is thus an interesting possibility for dehydration-induced earthquakes at intermediate depths. Brantut and Sulem [Bra12] have assumed a simple evolution law for the friction coefficient  $f$  in order to describe chemical weakening during dehydration:

$$f = f_0 + a \ln(\dot{\gamma} / \dot{\gamma}_0) - b\mu \quad (5)$$

$f_0$  is a reference friction coefficient for a reference strain rate  $\dot{\gamma}_0$  and  $a$  and  $b$  are positive constitutive parameters. This friction law is similar to the commonly used RSF laws where the ‘state’ is identified as the reaction extent  $\mu$ .

The reaction rate is assumed to be of first order, which accounts for temperature dependency following an Arrhenius law and depletion:

$$\frac{\partial \mu}{\partial t} = A(1 - \mu) \exp\left(-\frac{E_a}{RT}\right) \quad (6)$$

where  $A$  is a pre-exponential factor,  $E_a$  is the activation energy of the reaction and  $R$  is the gas constant. It is shown that due to the endothermic character of the mineral decomposition reaction, the temperature is buffered during the reaction to a value close to the critical temperature  $T_c$  at which the reaction is triggered [Bra11, Sul09]. Therefore, the reaction rate can be linearized above  $T_c$ :

$$\frac{\partial \mu}{\partial t} \approx \begin{cases} 0 & \text{if } T < T_c \\ c_T (T - T_c) - c_\mu \mu & \text{if } T \geq T_c \end{cases} \quad (7)$$

The pore pressure evolution is given by the fluid mass balance [Bra11, Sul09]:

$$\frac{\partial p_f}{\partial t} = c_{hy} \frac{\partial^2 p_f}{\partial y^2} + \Lambda \frac{\partial T}{\partial t} + m_w \frac{1 - \xi}{\rho_f \beta^*} \frac{\partial \mu}{\partial t} \quad (8)$$

where  $m_w$  is the mass of water that is released due to the reaction per unit of rock volume and  $\xi$  is the ratio of pore volume creation to fluid volume release due to the dehydration reaction.

The temperature evolution is given by the energy balance equation. Heat is generated by dissipation of the frictional energy (shear heating), and is partitioned into temperature change and diffusion and reaction enthalpy, which is a heat sink for endothermic reactions. Denoting  $m_0$  the mass of reacting mineral per unit of total rock volume and  $\Delta H$  the reaction enthalpy, we obtain [Bra11, Sul09]:

$$\frac{\partial T}{\partial t} = c_{th} \frac{\partial^2 T}{\partial y^2} + \frac{\tau \dot{\gamma}}{\rho C} - m_0 \frac{\Delta H}{\rho C} \frac{\partial \mu}{\partial t} \quad (9)$$

where  $\tau$  is the applied shear stress on the fault and  $\dot{\gamma}$  is the strain rate.

The linear stability analysis of the above system of equations has been performed by Brantut and Sulem [Bra12] and they have obtained the following expression for the critical wavelength (smallest wave length for which the growth coefficient of the instability is positive), below which all perturbations vanish in time:

$$\lambda_{cr}^{ch} = 2\pi \sqrt{\frac{ac_{th} \rho C c_\mu}{\dot{\gamma}_0 b \tau_0 c_T}} \quad (10)$$

This value corresponds to the smallest wave length for which the growth coefficient of the instability is positive. We observe that it depends only on the thermo-chemical parameters and that it is not influenced by the pore pressure effect.

In order to illustrate this analysis, we use the parameter values given in Table 2. They are taken from Brantut & Sulem (2012) for lizardite dehydration of a layer at 30 km depth, which is sheared at a very low strain rate of  $10^{-6} \text{ s}^{-1}$ .

It is worth investigating the evolution of the localization zone in a simple case of a gouge layer of 5 m thickness. An initial small perturbation of the shear strain field is imposed with a wavelength equal to the gouge thickness. According to (10), this

wave length is unstable. In particular, the critical wave length given by (10) is 0.12 m.

Figure 4a shows the evolution of the shear stress and of the shear strain rate in the middle of the localization zone. Figure 4b presents the profile of the shear strain at various time instants showing the localization and the de-localization process when the reaction is depleted. Note that in this example, a very low strain rate corresponding to a subducting slab was assumed. For this strain rate and due to partial dehydration (the material in the middle is depleted but not in the adjacent zones) chemical traveling waves are triggered and travel towards the boundaries of the gouge layer. Figure 4c depicts the temperature increase due to shearing in the middle of the shear band. It is worth mentioning that after a point the (endothermic) chemical reaction buffers the temperature rise. Figure 4d shows the evolution of the chemical reaction and the pore pressure increase in the middle of the shear band.

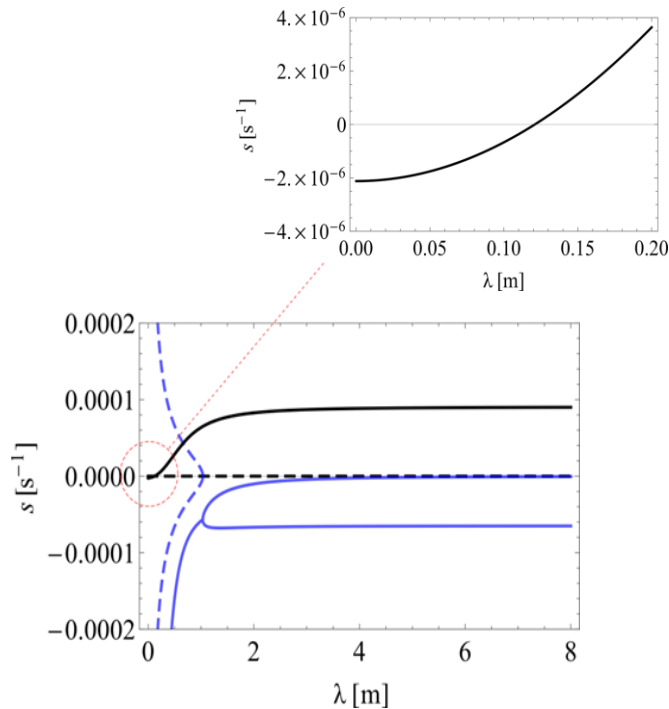


Figure 3. Growth coefficient (Lyapunov exponent) in terms of perturbation wavelength. The real part is plotted in solid line and the imaginary part in dotted line.

Black color signifies the mode related to chemical instability and blue the mode related to thermal pressurization ( $\text{Re}[s] < 0$  for this mode). The smallest wave length for which  $s$  becomes positive is given by equation (10).

Table 1. Parameter values for lizardite dehydration at a depth of around 30 km [Bra12].

Quantity	Value
Friction coefficient, $f_0$	0.6
Rate strengthening parameter, $a$	0.002
Reaction weakening parameter $b$	0.5
Specific heat capacity, $\rho C$	$2.7 \text{ MPa}^\circ\text{C}^{-1}$
Thermal dependency of the chemical kinetics, $c_T$	$2.58 \times 10^{-7} \text{ }^\circ\text{C}^{-1}\text{s}^{-1}$
Depletion dependency of the chemical kinetics, $c_\mu$	$2.12 \times 10^{-6} \text{ s}^{-1}$
Initial shear stress, $\tau_0$	240 MPa
Nominal strain rate, $\dot{\gamma}_0$	$10^{-6} \text{ s}^{-1}$
Thermal pressurization coefficient, $\Lambda$	$0.5 \text{ MPa }^\circ\text{C}^{-1}$
Thermal diffusivity, $c_{th}$	$10^{-6} \text{ m}^2 \text{ s}^{-1}$
Hydraulic diffusivity, $c_{hy}$	$10^{-6} \text{ m}^2 \text{ s}^{-1}$

It is worth investigating the evolution of the localization zone in a simple case of a gouge layer of 5 m thickness. An initial small perturbation of the shear strain field is imposed with a wavelength equal to the gouge thickness. According Figure 3, this wave length is unstable. In particular, the critical wave length given by (10) is 0.12 m (Figure 3).

Figure 4a shows the evolution of the shear stress and of the shear strain rate in the middle of the localization zone. Figure 4b presents the profile of the shear strain at various time instants showing the localization and the de-localization process when the reaction is depleted. Note that in this example, a very low strain rate corresponding to a subducting slab was assumed. For this strain rate and due to partial dehydration (the material in the middle is depleted but not in the adjacent zones) chemical traveling waves are triggered and travel towards the boundaries of the gouge layer. Figure 4c depicts the temperature increase due to shearing in the middle of the shear band. It is worth mentioning that after a point the (endothermic) chemical reaction buffers the temperature rise. Figure 4d shows the evolution of the chemical reaction and the pore pressure increase in the middle of the shear band.

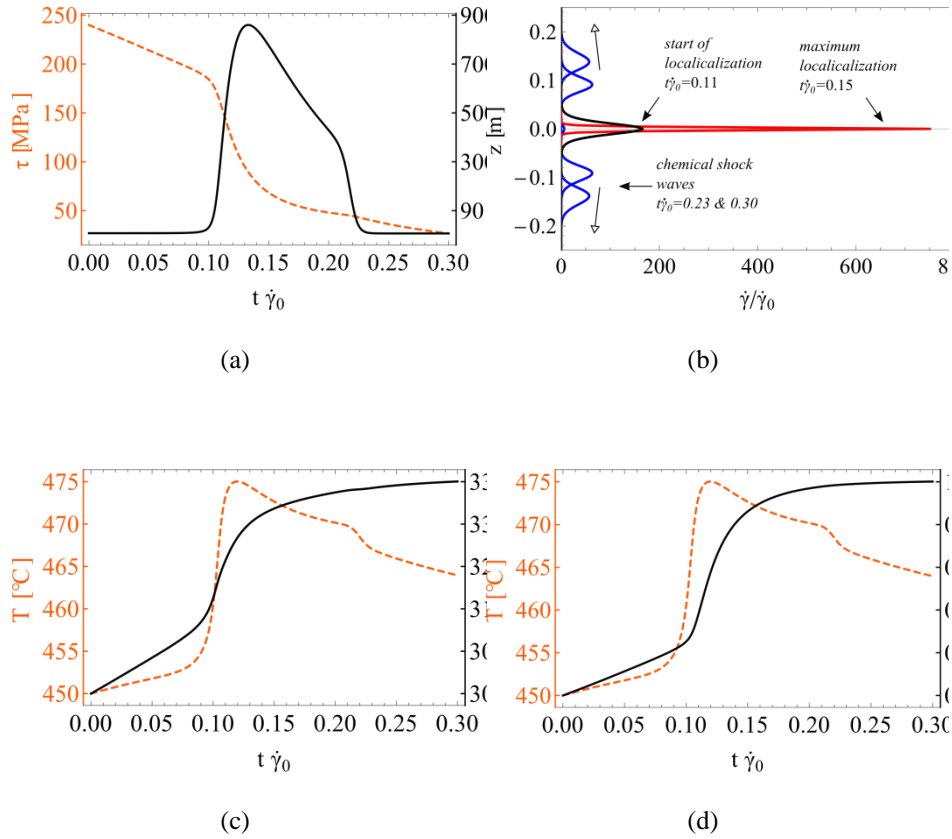


Figure 4. Strain localization due to chemical softening in a 5 m thick dehydrating gouge layer: (a) Shear stress drop in the middle of the shear band and shear strain evolution. The system localizes to a narrow band because of dehydration, but then it delocalizes due to depletion; (b) Evolution of shear band localization – profile of shear strain rate; (c) Temperature and pore pressure increase in the middle of the shear band. The chemical reaction buffers temperature rise; (d) Evolution of the chemical reaction in the middle of the shear band. At  $t\dot{\gamma}_0 \approx 0.1$  the reaction effects become important and the material is rapidly depleted in the middle of the gouge ( $\mu \rightarrow 1$ ) until  $t\dot{\gamma}_0 \approx 0.3$ . Due to partial depletion, chemical shock waves are triggered and travel towards the boundaries of the gouge.

### 3 Dissolution weakening and compaction banding

#### 3.1 Multi-scale modelling of strong chemo-poro-mechanical coupling

In a recent paper [Ste14], instabilities in the form of compaction bands as triggered by chemical degradation of the solid skeleton have been studied. Chemical dissolution and grain breakage have been considered. The interest of the approach is in the strong chemo-poro-mechanical coupling which was considered. As the stresses and the deformations evolve, the grains of the material break leading to an increase of their specific surface. As the dissolution rate depends upon the area of contact between the reactive fluid and the minerals, dissolution is accelerated by grain fracturing and grain breakage and chemical softening is further enhanced.

The effect of chemical dissolution is important in field and in reservoir applications. For instance, the experimental results of Xie et al. [Xie11] showed that the chemical dissolution of a limestone leads to a significant increase of the porosity (from 23% for the intact rock to 27% for the degraded one). According to the same authors, the plastic pore collapse threshold is also reduced from about 30 to 20 MPa and the chemically degraded materials become more collapsible and more ductile due to the increase in porosity and the degradation of the inter-granular cementation. This evidence is corroborated by other authors [e.g. Bus12, Cia14, Hu07c, Hu07a, Nov03] for a class of geomaterials and results in a contraction of the elastic domain only due to chemical reasons (chemical softening). In parallel, in a saturated porous geomaterial, the progressive mechanical damage of the solid skeleton during compaction has as a result the increase of the interface area of the reactants (i.e. of the solution with the solid) and consequently the acceleration of the dissolution rate of the solid phase [Rim80]. Thus, the solid skeleton is degraded more rapidly (mass removal because of dissolution), the overall mechanical properties of the system diminish (contraction of the elastic domain – chemical softening), deformations increase and the solid skeleton is further damaged (intergranular fractures, debonding, breakage of the porous network etc.). Figure 5 schematically shows this positive feedback process, whose stability is not guaranteed. Notice that chemical softening is central for compaction banding in the absence of other softening mechanisms such as mechanical softening.

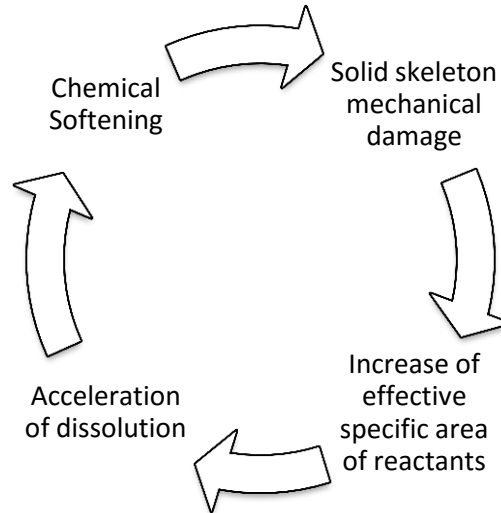
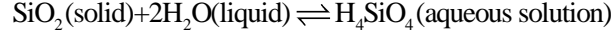


Figure 5. Positive feedback process due to dissolution and solid skeleton damage (e.g. intergranular fracturing, breakage of the porous network, matrix cracking, grain-matrix debonding etc.)

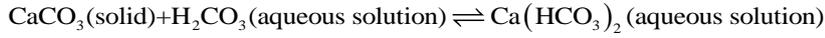
A two-scale approach was proposed as the reaction kinetics is considered at the micro-scale (grain level), whereas the balance and constitutive equations are written at the macro scale i.e. the RVE. Due to the existing heterogeneity of the microstructure (e.g. different grain sizes and constituents in the RVE) the dissolution rate may not be homogeneous over the RVE. The size of the RVE is a finite statistical quantity that depends upon the geomaterial at hand. The chemical softening rate of the yield surface is therefore related to the average, over the RVE, of the reaction rate at the grain level. This average procedure naturally introduces a characteristic length (size of the RVE). This approach is directly inspired from the development of non-local continuum theories. For heterogeneous materials, the constitutive law at a point of the continuum should involve weighted averages of a state variable over a certain neighborhood of that point. This leads to an integral type of constitutive equations. Along the same lines of thinking, gradient type constitutive models take into account the field in the vicinity of the considered point by enriching the local constitutive equations with higher order gradients of the deformation field [Ger73, Var95]. As emphasized by [Baž02], resorting to nonlocal continuum appears to be an effective means for regularizing boundary value problems with strain softening. In our problem, the introduction of this ‘chemical’ characteristic length gives a length scale to the problem and naturally leads to a selection of a particular wave length when performing a linear stability analysis of the system. Details of the analysis can be found in the paper of Stefanou & Sulem [Ste14]. We just recall in the following the main assumptions and the principal results.

*Micro-scale:*

We consider a dissolution process of the form:  $\text{solid}_{(3)} + \text{solvent}_{(1)} \rightleftharpoons \text{solution}_{(2)}$ . For example the dissolution/precipitation of quartz in water is described by the following chemical equation:



Another example is the dissolution of calcite with water that is saturated with carbon dioxide:



This equation represents a set of consecutive reactions that take place and are responsible for the dissolution of carbonate rocks [Grg11]. The reaction kinetics is written in a simplified manner as:

$$\frac{\partial w_2}{\partial t} = k^* \frac{S}{e} \left( 1 - \frac{w_2}{w_2^{eq}} \right) \quad (11)$$

where  $w_2$  is the mass fraction of the dissolution product in the fluid,  $k^*$  is a reaction rate coefficient,  $e$  is the void ratio,  $S$  is the specific surface of a single grain (which is inversely proportional to the grain size) and  $w_2^{eq}$  the mass fraction of dissolution product to the fluid mass at chemical equilibrium. It should be emphasized that Eq.(11) is written at the microscale and that  $w_2$ ,  $S$  and  $e$  represent local quantities, which are not necessarily homogeneous over the RVE. Grain crushing is also described at the micro-scale. We use here a simple empirical expression for the evolution of the grain size in terms of the mechanical work input as proposed by Lade et al. [Lad96]:

$$D = D_0 \left( \frac{a}{a + E_T} \right) \quad (12)$$

where  $D_0$  is the effective grain size of the initial gradation and  $E_T$  is the total energy input density,  $a$  is a fitting parameter, which represents the grain crushability. Considering that the specific effective surface of a grain  $S$  is inversely proportional to the grain diameter, it is natural to assume the same type of relationship:

$$S = S_0 \left( 1 + \frac{E_T}{a} \right) \quad (13)$$

*Macro-scale:*

At the macro-scale, the constitutive equations are derived from a modified Cam-Clay elasto-plastic model for which an associative flow rule is assumed for sake of simplicity:

$$F = q^2 + M^2 p'(p' - p'_c) = 0 \quad (14)$$

where  $p'$  and  $q$  are respectively the Terzaghi effective mean stress and the shearing stress intensity (square root of the second invariant of the deviatoric part of the stress tensor).  $p'_c$  is a material parameter (namely the yield stress under isotropic loading) which is assumed to decrease from  $p'_0$  (initial reference state) to  $p'_R$  (residual yield stress once the chemical reaction is completed) according to the following law  $p'_c \equiv p'_R - (p'_R - p'_0)\zeta^\kappa$ .  $\kappa$  is an exponent that can be experimentally determined for the material and the chemical process at hand and  $\zeta = M_s / M_0$  is the ratio of the current solid mass over its initial value, which is taken here as a chemical softening parameter.

This chemical softening parameter  $\zeta$  can be expressed in terms of the *average* mass fraction of the dissolution product over the RVE  $w_2^M = \frac{1}{V_T V_r} \int w_2 dV$ . Assuming that  $w_2 = w_2(z, t)$  (oedometric conditions) is a function that can be expanded into Taylor series up to the second order in  $z$ :

$$w_2^M \approx w_2 + \ell_c^2 \frac{\partial^2 w_2}{\partial z^2} \quad (15)$$

where  $\ell_c = \ell_{REV} \sqrt{\frac{1}{24}} \approx \frac{\ell_{REV}}{5}$  appears as a characteristic internal length and  $\ell_{REV}$  is the size of the RVE in  $z$ -direction.

### 3.2 Compaction banding in oedometric compression

In the following we refer to the main results obtained in [Ste14] for oedometric compaction in a carbonate reservoir at 1.8 km depth because of CO<sub>2</sub> injection. In Table 2 we present some typical values for the chemo-mechanical parameters of a porous carbonate rock. At this depth, we assume that the water pressure is  $p_f \approx 18\text{MPa}$  and the total vertical stress is  $\sigma_n \approx 45\text{MPa}$ .

Table 2. Indicative material properties of a carbonate grainstone.

Quantity	Value
Hydraulic diffusivity, $c_{hy}$	$10^{-3} \text{ m}^2 \text{ s}^{-1}$
Grain diameter, $D_0^{50}$	0.2 mm
Initial effective grain surface area to volume ratio, $S$	$25 \text{ mm}^{-1}$
Bulk modulus, $K$	5 GPa
Shear modulus, $G$	5 GPa
Porosity, $n$	0.25
CSL slope, $M$	0.9
Initial yield stress, $p'_0$	35 MPa
Residual yield stress, $p'_R$	30% $p'_0$
Chemical softening exponent, $\kappa$	2
Grain crushing parameter, $a$	1 MPa
Fluid density, $\rho_f$	$1 \text{ g cm}^{-3}$
Solid density, $\rho_s$	$2.65 \text{ g cm}^{-3}$
Dissolution rate, $k^*$	$1.6 \cdot 10^{-10} \text{ m/s}$

Stefanou and Sulem [Ste14] have derived the instability conditions for which compaction bands formation is possible from a Linear Stability Analysis. The details of the analysis can be found in the aforementioned paper. In particular, there is a region in the  $q-p'$  plane where compaction band formation is possible. In other words homogeneous deformations are unstable and the system bifurcates to non-homogeneous solutions. Figure 6 shows the instability zone for the chemo-poro-mechanical parameters of the carbonate grainstone considered in this example.

Inside the instability region there exists a minimum critical wavelength above which perturbations are unstable (positive growth coefficient). This critical wavelength is related to the characteristic internal length,  $\ell_c$ , which was introduced in the previous paragraph. If  $\ell_c = 0$  then the system is unstable for any perturbation wave length.

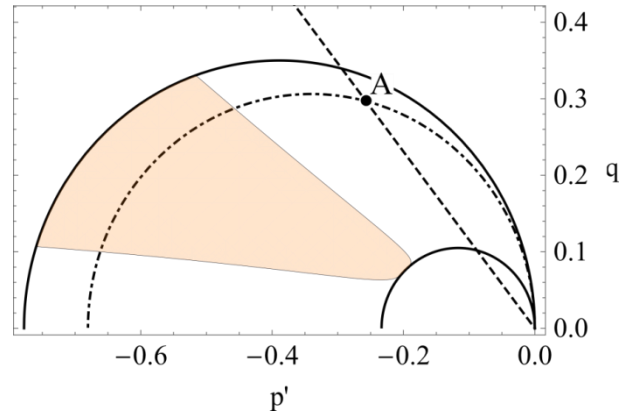


Figure 6. Instability region (shaded) for compaction bands under oedometric conditions for a carbonate grainstone. The outer envelope (solid line ellipse) represents the initial strength of the material. The straight dashed line depicts the linear elastic oedometric path. Point A corresponds to the initial stress state at 1.8km depth. The inner ellipse (solid line) represents the residual strength of the grainstone after complete dissolution of the rock. The stresses are normalized by the applied vertical stress at 1.8 km depth, which is constant.

Initially we assume that the material is in a state of elastic deformation (Point A) under the applied total vertical stress of 45 MPa. At time  $t=0$ , the injection of the  $\text{CO}_2$  solution starts. It is assumed that the  $\text{CO}_2$  solution is continuously renewed in such a way that practically open flow conditions hold ( $w_2(t > 0) = 0$ ). In field,  $\text{CO}_2$  injection open flow conditions would correspond to a zone outside the gas plume, where the formation fluid is saturated with  $\text{CO}_2$ , but is not in chemical equilibrium with the rock so that carbonate dissolution occurs continuously ( $w_2 < w_2^{eq}$ ).

As a result of  $\text{CO}_2$  injection, the system is not in chemical equilibrium and dissolution occurs. Consequently, the material is progressively degraded due to chemical softening and the chemical softening parameter decreases from its initial value  $\zeta_0 = 1$ . When  $\zeta = \zeta_A \approx 0.9$  the material yields, plastic strains are accumulated and solid skeleton damage occurs (Eq.(13)). This phase of deformation under constant applied loading (i.e. the overburden) corresponds to the creep behavior that is observed due to  $\text{CO}_2$  injection [Gue07, Lit09, Rut12].

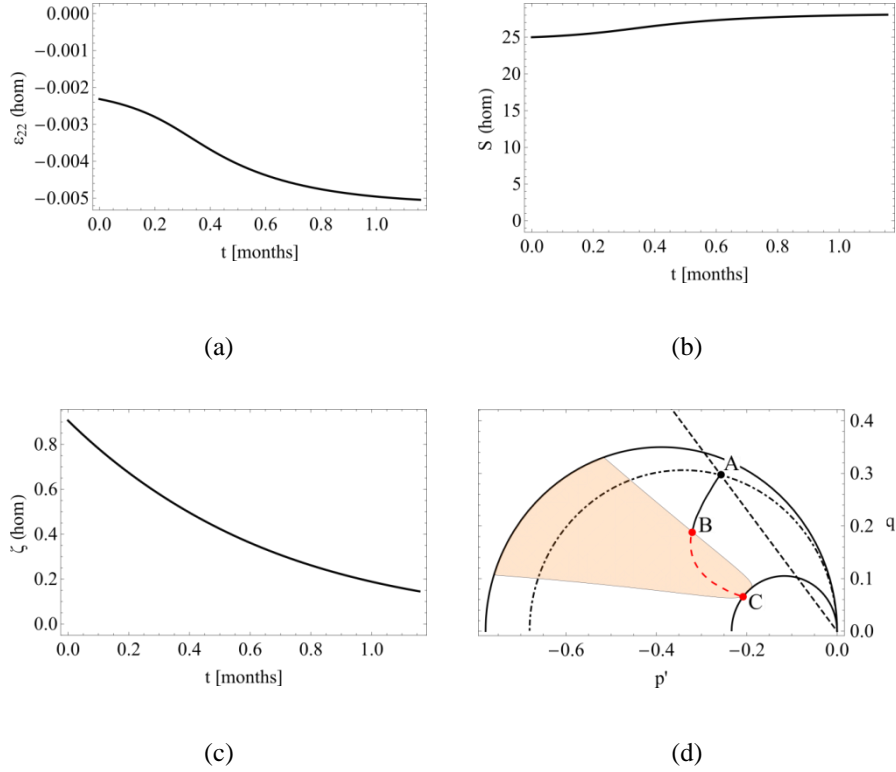


Figure 7. Evolution in time of (a) deformation, (b) the specific surface, (c) the chemical softening parameter and (d) of the stress path during imposed homogeneous dissolution of a specimen under oedometric conditions.

We emphasize that Linear Stability Analysis only gives the conditions for compaction band triggering. However, in order to assess the evolution of the system and the gradual strain localization inside the band one has to study the post-bifurcation [Sul16]. A numerical simulation is first performed by imposing homogeneous deformation. The conditions are oedometric and the numerical analysis starts from point A ( $\zeta_A = 0.9$ ). Figure 7 shows the evolution of the total (homogeneous) deformation, of the specific surface, of the chemical softening parameter  $\zeta$  and the stress path followed during combined dissolution and chemical softening. Due to dissolution, we observe a slow increase of the compressive deformations from  $2 \times 10^{-3}$  to  $5 \times 10^{-3}$  (creep) and a limited increase of the specific surface of the grains. At the end of the simulation, the grainstone is depleted ( $\zeta = 0$ ) and no more dissolution is possible. The situation is different when the unphysical constraint of homogeneous deformation is removed.

The system is now free to develop non-homogeneous deformation and strain localization in the form of compaction banding can occur. An initial perturbation with a

wavelength equal to the height of the sample and amplitude  $10^{-5}$  is imposed (200 mm). Compaction band formation is possible for this perturbation wavelength only when the stress state falls into the unstable zone (Figure 7d). At the beginning of  $\text{CO}_2$  injection the system creeps from point A to point B. No compaction band is triggered and the system behaves as in the previous case of homogeneous deformation. Once the stress path crosses the shaded area non-homogeneous deformations start to grow and a compaction band forms. Figure 8 shows the profile of the vertical deformation at various times. The deformations localize into a narrow band whose thickness depends on the characteristic internal length,  $\ell_c$ . Here we chose  $\ell_c = 4$  mm ( $\sim 20$  grains for a typical grain size of 200  $\mu\text{m}$ ). In Figure 9 we present the average vertical deformation over the entire sample, the vertical deformation at the peak of the compaction band and the vertical deformation of a point far from the localization zone. The vertical deformation at the peak of the compaction band is 14 times larger than the vertical deformation far from it. Figure 10 shows the stress path of the point at the peak of the compaction band and the stress path of a point far from the localization zone. In the beginning the stress paths coincide, but after entering in the instability zone they start to diverge due to compaction band formation.

It is worth emphasizing that compaction band thickness depends on the chosen characteristic length. This is shown by Linear Stability Analysis [Ste14] and it is corroborated numerically by choosing a different characteristic length,  $\ell_c = 16$  mm ( $\sim 80$  grains). Figure 11 shows how a larger characteristic length leads to larger compaction band thickness. On the contrary, in the absence of internal length ( $\ell_c = 0$ ) the compaction band thickness is zero.

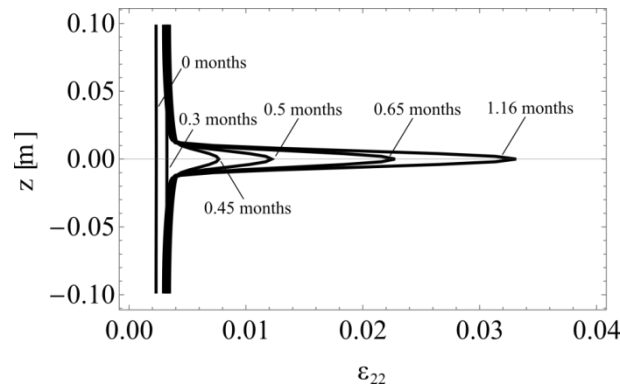


Figure 8. Profile of the vertical deformation at various times and for  $\ell_c = 4$  mm (20 grains). The deformations localize into a narrow band, i.e. compaction band.

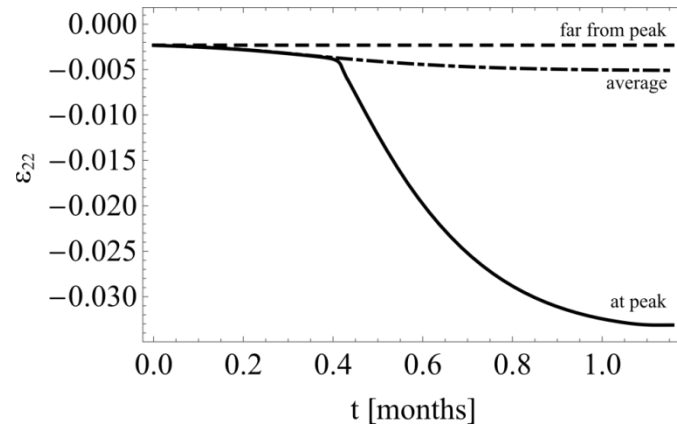


Figure 9. Vertical deformation in function of time: at the peak of the compaction band, average over the entire sample and at a point far from the localization zone.

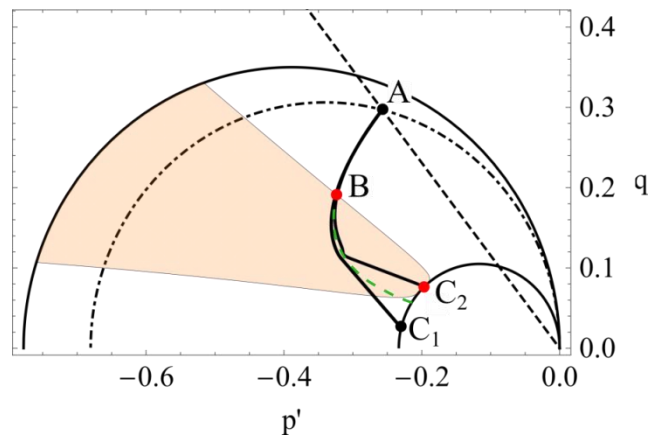


Figure 10. Stress paths of the point at the peak of the compaction band ( $ABC_2$ ) and of a point far from the localization zone ( $ABC_1$ ). The dashed line corresponds to the stress path of the homogeneous deformation (see Figure 7d).

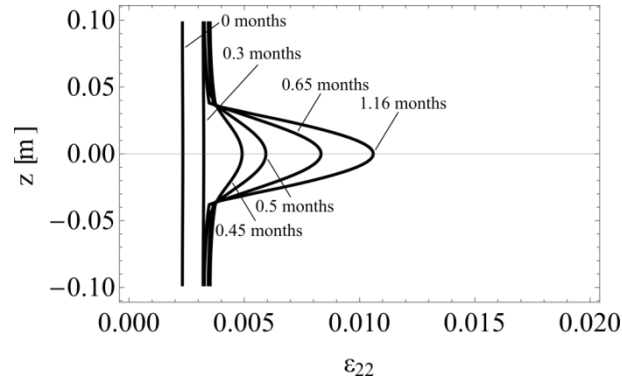


Figure 11. Profile of the vertical deformation at various times for  $\ell_c = 16\text{mm}$  (80 grains). The deformations localize into a band which is thicker than in the case of  $\ell_c = 4\text{mm}$  (20 grains, see Figure 8).

## 5 Conclusions

We have reviewed in this paper some recent work on the effect of temperature, pore pressure and chemical reactions on strain localization in geomaterials. Examples have been taken in relation with seismic slip and with compaction banding. Strain localization is triggered by the softening of the material strength. Weakening mechanisms can be of various origins: mechanical (e.g. microcracking), hydraulic (e.g. pore fluid pressurization), thermal (e.g. shear heating), chemical (e.g. dissolution).

We have presented the framework of localized failure in earthquake rupture as the result of instability of the deformation process. It was shown that it is necessary to introduce a localization limiter in order to obtain a finite thickness for the localized shear zone. Rate independent constitutive models for a classical (Cauchy) continuum lead to an infinitesimally thin zone. On the contrary, a rate dependent friction law or a Cosserat framework lead to a finite value for the critical wave length of the perturbation, above which, homogeneous deformation is unstable.

We have also analyzed compaction banding induced by dissolution. A strong chemo-mechanical coupling is considered: the material softens in due course of dissolution whereas the dissolution process accelerates with increasing damage (because of the increase of the specific surface of the grain and thus of the area of contact between the reactive fluid and the minerals). A two-scale approach has been proposed in order to account for the heterogeneity of the dissolution process over the RVE. This naturally introduces a ‘chemical’ material length related to the non-local character of the relation between the softening rate of the yield surface (at the macro-scale) and the dissolution process (at the grain scale). Here again, the introduction

of this material length is crucial to limit the compaction band thickness to a finite value. Post-localization robust computations have been performed to simulate the progressive evolution of compaction band under open flow conditions.

Some challenging open questions remain such as the modelling of coupled thermo-chemo-hydro-mechanical phenomena with evolution of the microstructure of the material through various mechanical and chemical processes. This would require methods for cross scale couplings, advanced homogenization techniques and enriched continua models.

## References

- [Ale14] S. Alevizos, T. Poulet, Emmanuil Veveakis. Thermo-poro-mechanics of chemically active creeping faults. 1: Theory and steady state considerations, *J. Geophys. Res. Solid Earth* 119(6):4558–4582, 2014.
- [Baž02] Zdeněk. P. Bažant, Milan Jirásek. Nonlocal Integral Formulations of Plasticity and Damage: Survey of Progress, *J. Eng. Mech.* 128(11):1119–1149, 2002.
- [Bra11] Nicolas Brantut, Jean Sulem, Alexandre Schubnel. Effect of dehydration reactions on earthquake nucleation: Stable sliding, slow transients, and unstable slip, *J. Geophys. Res. Solid Earth* 116(July 2010):1–16, 2011.
- [Bra12] Nicolas Brantut, Jean Sulem. Strain Localization and Slip Instability in a Strain-Rate Hardening, Chemically Weakening Material, *J. Appl. Mech.* 79(3):031004, 2012.
- [Bus12] Giuseppe Buscarnera. A conceptual model for the chemo-mechanical degradation of granular geomaterials, *Géotechnique Lett.* 2(July)-(September):149–154, 2012.
- [Che92] Frederick M. Chester, N. G. Higgs. Multimechanism friction constitutive model for ultrafine quartz gouge at hypocentral conditions, *J. Geophys. Res.* 97(B2):1859, 1992.
- [Cia14] Matteo Oryem Ciantia, Riccardo Castellanza, Claudio di Prisco. Experimental Study on the Water-Induced Weakening of Calcarenites, *Rock Mech. Rock Eng.* :441–461, 2014.
- [Das11] Arghya Das, Giang D. Nguyen, Itai Einav. Compaction bands due to grain crushing in porous rocks: A theoretical approach based on breakage mechanics, *J. Geophys. Res.* 116(B8):1–14, 2011.
- [Die79] James H. Dieterich. Modeling of rock friction: 1. Experimental results and constitutive equations, *J. Geophys. Res.* 84(B5):2161, 1979.
- [Ger73] P. Germain. The Method of Virtual Power in Continuum Mechanics. Part 2: Microstructure, *SIAM J. Appl. Math.* 25(3):556–575, 1973.
- [Gha08] Siavash Ghabezloo, Jean Sulem. Stress dependent thermal pressurization of a fluid-saturated rock, *Rock Mech. Rock Eng.* 42(1):1–24, 2008.
- [Gre07] Harry W Green. Shearing instabilities accompanying high-pressure phase transformations and the mechanics of deep earthquakes., *Proc. Natl. Acad. Sci. U. S. A.* 104(22):9133–8, 2007.

- [Grg11] D. Grgic. Influence of CO<sub>2</sub> on the long-term chemomechanical behavior of an oolitic limestone, *J. Geophys. Res.* 116(B7):B07201, 2011.
- [Gue07] Y. Le Guen, Francois Renard, R. Hellmann, E. Brosse, M. Collombet, D. Tisserand, J.-P. Gratier. Enhanced deformation of limestone and sandstone in the presence of high P CO<sub>2</sub> fluids, *J. Geophys. Res.* 112(B5):B05421, 2007.
- [Hu07a] Liang-Bo Bo Hu, Tomasz Hueckel. Creep of saturated materials as a chemically enhanced rate-dependent damage process, *Int. J. Numer. Anal. Methods Geomech.* 31(14):1537–1565, 2007.
- [Hu07b] Liang Bo Hu, Tomasz Hueckel. Coupled chemo-mechanics of intergranular contact: Toward a three-scale model, *Comput. Geotech.* 34(4):306–327, 2007.
- [Hu07c] Liang-Bo Hu, Tomasz Hueckel. Coupled chemo-mechanics of intergranular contact: Toward a three-scale model, *Comput. Geotech.* 34(4):306–327, 2007.
- [Lac80] Arthur H. Lachenbruch. Frictional heating, fluid pressure, and the resistance to fault motion, *J. Geophys. Res.* 85(B11):6097, 1980.
- [Lad96] Poul V. Lade, Jerry A. Yamamuro, Paul A. Bopp. Significance of Particle Crushing in Granular Materials, *J. Geotech. Eng.* 122(4):309–316, 1996.
- [Lit09] Emilia Liteanu, Christopher J. Spiers. Influence of pore fluid salt content on compaction creep of calcite aggregates in the presence of supercritical CO<sub>2</sub>, *Chem. Geol.* 265(1)–(2):134–147, 2009.
- [Nov03] Roberto Nova, Riccardo Castellanza, C. Tamagnini. A constitutive model for bonded geomaterials subject to mechanical and/or chemical degradation, *Int. J. Numer. Anal. Methods Geomech.* 27(9):705–732, 2003.
- [Pla14] John D. Platt, John W. Rudnicki, James R Rice. Stability and localization of rapid shear in fluid-saturated fault gouge: 2. Localized zone width and strength evolution, *J. Geophys. Res. Solid Earth* 119(5):4334–4359, 2014.
- [Pou14] T. Poulet, Emmanuil Veveakis, Klaus Regenauer-lieb, D. A. Yuen. Thermo-poro-mechanics of chemically active creeping faults: 3. the role of serpentinite in episodic tremor and slip sequences, and transition to chaos, *J. Geophys. Res. Solid Earth* 119:4606–4625, 2014.
- [Reg13] Klaus Regenauer-lieb, Emmanuil Veveakis, Thomas Poulet, Florian Wellmann, Ali Karrech, Jie Liu, Juerg Hauser, Christoph Schrank, u. a. Multiscale coupling and multiphysics approaches in earth sciences : Theory, *J. Coupled Syst. Multiscale Dyn.* 1(1):49–73, 2013.
- [Ric06a] James R Rice. Heating and weakening of faults during earthquake slip, *J. Geophys. Res.* 111(B5):B05311, 2006.
- [Ric06b] James R Rice. Heating and weakening of faults during earthquake slip, *J. Geophys. Res.* 111(B5), 2006.
- [Ric14] James R Rice, John W. Rudnicki, John D. Platt. Stability and localization of rapid shear in fluid-saturated fault gouge: 1. Linearized stability analysis, *J. Geophys. Res. Solid Earth* 119(5):4311–4333, 2014.
- [Rim80] J.D. Rimstidt, H.L. Barnes. The kinetics of silica-water reactions, *Geochim. Cosmochim. Acta* 44(11):1683–1699, 1980.

- [Rud75] John W. Rudnicki, James R Rice. Conditions for the localization of deformation in pressure-sensitive dilatant materials, *J. Mech. Phys. Solids* 23(6):371–394, 1975.
- [Rut12] Jonny Rutqvist. The Geomechanics of CO<sub>2</sub> Storage in Deep Sedimentary Formations, *Geotech. Geol. Eng.* 30(3):525–551, 2012.
- [Rut88] E. H. Rutter, K. H. Brodie. Experimental “sytectonic” dehydration of serpentinite under conditions of controlled pore water pressure, *J. Geophys. Res.* 93(B5):4907, 1988.
- [Sch98] Christopher H. Scholz. Earthquakes and friction laws, *Nature* 391:37–42, 1998.
- [Ste14] Ioannis Stefanou, Jean Sulem. Chemically induced compaction bands: Triggering conditions and band thickness, *J. Geophys. Res. Solid Earth* 119(2):880–899, 2014.
- [Sul04] Jean Sulem, Ioannis Vardoulakis, Hichem Ouffroukh, Marc Boulon, Julien Hans. Experimental characterization of the thermo-poro-mechanical properties of the Aegion Fault gouge, *Comptes Rendus - Geosci.* 336:455–466, 2004.
- [Sul07] Jean Sulem, P. Lazar, Ioannis Vardoulakis. Thermo-poro-mechanical properties of clayey gouge and application to rapid fault shearing, *Int. J. Numer. Anal. Methods Geomech.* 31(3):523–540, 2007.
- [Sul09] Jean Sulem, V. Famin. Thermal decomposition of carbonates in fault zones: Slip-weakening and temperature-limiting effects, *J. Geophys. Res.* 114(B3):B03309, 2009.
- [Sul11] Jean Sulem, Ioannis Stefanou, Emmanuil Veveakis. Stability analysis of undrained adiabatic shearing of a rock layer with Cosserat microstructure, *Granul. Matter* 13(3):261–268, 2011.
- [Sul16] Jean Sulem, Ioannis Stefanou. Thermal and chemical effects in shear and compaction bands, *Geomech. Energy Environ.*, 2016.
- [Var95] Ioannis Vardoulakis, Jean Sulem. *Bifurcation Analysis in Geomechanics*. Glasgow : Blackie — ISBN 0203697030, 1995.
- [Vev10] Emmanuil Veveakis, S. Alevizos, Ioannis Vardoulakis. Chemical reaction capping of thermal instabilities during shear of frictional faults, *J. Mech. Phys. Solids* 58(9):1175–1194, 2010.
- [Vev12] Emmanuil Veveakis, Jean Sulem, Ioannis Stefanou. Modeling of fault gouges with Cosserat Continuum Mechanics: Influence of thermal pressurization and chemical decomposition as coseismic weakening mechanisms, *J. Struct. Geol.* 38:254–264, 2012.
- [Vev13] Emmanuil Veveakis, Ioannis Stefanou, Jean Sulem. Failure in shear bands for granular materials: thermo-hydro-chemo-mechanical effects, *Géotechnique Lett.* 3(April)-(June):31–36, 2013.
- [Vev14] Emmanuil Veveakis, T. Poulet, S. Alevizos. Thermo-poro-mechanics of chemically active creeping faults: 2. Transient considerations, *J. Geophys. Res. Solid Earth* 119(6):4583–4605, 2014.
- [Wib02] Christopher A J Wibberley, Toshihiko Shimamoto. Internal structure and permeability of major strike-slip fault zones: The Median Tectonic Line in Mie Prefecture, Southwest Japan, *J. Struct. Geol.* 25:59–78, 2002.

- [Xie11] S.Y. Xie, J.F. Shao, W.Y. Xu. Influences of chemical degradation on mechanical behaviour of a limestone, *Int. J. Rock Mech. Min. Sci.* 48(5):741–747, 2011.



---

# Thermo-poro-mechanics of chemically active faults

**Manolis Veveakis**

*University of New South Wales (e.veveakis@unsw.edu.au)*

---

*Shear zones in outcrops and core drillings on active faults commonly reveal two scales of localization, with centimeter to tens of meters thick deformation zones embedding much narrower zones of mm- to cm-scale. The narrow zones are often attributed to some form of fast instability such as earthquakes or slow slip events. Surprisingly, the double localisation phenomenon seem to be independent of the mode of failure, as it is observed in brittle cataclastic fault zones as well as ductile mylonitic shear zones. In both a very thin layer of chemically altered, ultra fine grained ultracataclasite or ultramylonite is noted. We present an extension to the classical solid mechanical theory where both length scales emerge as part of the same evolutionary process of shearing the host rock. We highlight the important role of any type of solid-fluid phase transitions that govern the second degree localisation process in the core of the shear zone. In both brittle and ductile shear zones chemistry stops the localisation process caused by a multiphysics feedback loop leading to an unstable slip. The microstructural evolutionary processes govern the time-scale of the transition between slow background shear and fast, intermittent instabilities in the fault zone core. The fast cataclastic fragmentation processes are limiting the rates of forming the ultracataclasites in the brittle domain, while the slow dynamic recrystallisation prolongs the transition to ultramylonites into a slow slip instability in the ductile realm.*

## 1 Introduction

The geologist in the field is often confronted with two scales of localisation when investigating shear or fault zones[CC98, BZS03]. Brittle fault zones show striking examples of extremely localized slip events, occurring within a thin shear zone,  $< 1 - 5$  mm thick, called the principal slipping zone (PSZ) [Sib03]. This localized PSZ lies within a finely granulated fault zone of typically tens to hundreds millimeter thickness. These fault zones are either cataclastic in the brittle regime or mylonitic in the ductile regime.

Exhumed field examples for the morphology of these brittle fault zones can be found in the North Branch San Gabriel fault [CEB93], the Punchbowl fault of the San Andreas system in southern California [CC98], the Median Tectonic Line fault in Japan [WS03], and in the Hanaore fault in southwest Japan [NS05]. Active faults have been intersected in wells in e.g. the Aigion system, central Greece, where the fault zone of clay size particles consists of finely crushed radiolarites, extended to about 1 *m*. This localized zone of deformation was found to be intercepted by a “fresh” distinct slip surface of sub-millimeter size [SLV07, CDMB04]. Other wells that have been specifically designed to intersect active faults are the completed San Andreas Fault project [HvDS<sup>+</sup>11] and the ongoing Alpine Fault drilling project [Tow09]. The San Andreas Fault project revealed a fault zone of 1-2.5 m width at 3km depth, with several ultralocalized PSZ's.

Similarly, in the ductile field the dynamic recrystallization of the matrix minerals is telltale of crystal plastic or diffusion creep, forming shear zones of vast thickness interrupted by ultralocalized anastomosing patterns of extreme grain size reduction in the ultramylonite. Exhumed thrusts in creeping carbonates around the world like the Naukluft thrust in Namibia [RFMM12], the McConnell thrust in Alberta Canada [KL97] or the Glarus Thrust in Switzerland [HHp<sup>+</sup>08], all present a common structure of a meter-wide (1 – 5 meters) zone which accomodates several thin (mm-cm at most) veins of ultralocalized deformation and chemical alteration.

The brittle field features micro-mechanisms, governed by grain breakage, rolling, cleavage and brittle fragmentation processes. The ductile field features dislocation, diffusion and dissolution mechanism. Although these mechanisms are completely different they surprisingly exhibit the same dual pattern of localisation: a broad meter wide shear zone with ultra localised PSZ's in its middle.

Each of the different phenomena can be explained independently but to date no comprehensive theory has been suggested that can investigate the reason for the double degree localisation process and the potential commonalities between brittle and ductile localisation. This is because the dynamic process of the extreme localisation and the quasi static response of the background flow of the shear zone are treated as two different fundamental theories. The former instability is described in Solid Mechanics and the latter flow in Fluid Dynamics.

While Solid Mechanics is capable of accurately describing the conditions for failure it does not emphasise the long term post-failure behaviour. This is due to the nature of the solid materials that maintain a high degree of structural integrity after failure and are not significantly affected by the elapsed time. The consequence of this is that a quasi static approach is preferred thus making it possible to cast the weak rate effects into approximate laboratory determined hardening laws.

Fluid Dynamics on the opposite does not have the concept of failure, it knows nothing about the processes that happen prior to failure and is totally concerned with the description of the rate of flow of the material under an applied stress. Since most mantle convection codes are based on the fluid dynamical approach, the geophysical commu-

nity has over the recent years expended a lot of effort into incorporating the theory of Solid Mechanics.

The fact that both theories apply to geology has been universally acknowledged and the after dinner contribution of Reiner on the 'Deborah Number' [Rei64] is well worth reading. The number is defined as the ratio of the stress relaxation time over the time of observation. Reiner's quote "the mountains flowed before the lord" implies that given enough time one may smoothly transition from one to the other theory. This can be easily conceptualized in a Newtonian (linear viscous) viscoelastic framework, however, the inclusion of non-linear temperature dependence of the creep processes gave rise to the Time-Temperature Superposition (TTS) in polymer sciences [TA45]. The TTS principle implies that the temperature dependent behaviour of materials can be substituted by appropriate experiments at different time-scales for a reference temperature. It is thereby assumed that the time evolution described in the temperature equation is the only time-scale relevant for the long term mechanical behaviour of solids. This simple concept allows us to directly extend it for the nonlinear viscous behaviour of solids within a single theoretical framework incorporating elasticity, plastic failure and viscous post failure evolution.

In the present work we summarise a theory that couples the solid and fluid-like behaviour. This theory must be able to provide the framework for modeling both the formation of faults (refer, for more in depth reading, to [RLVP<sup>+</sup>13a, RLVP<sup>+</sup>13b]) and their post-failure evolution. We show that the formation and post failure evolution of faults depend strongly on the coupled multiphysical effects affecting pressure, temperature and chemical conditions. We thus aim at providing in this paper a comprehensive guide through the energetics of faults and explain how they apply to the different types of failure.

## 2 Time-independent formation of shear zones from Solid Mechanics

The theory describing the onset of localized failure from uniform deformation has been a direct extension of the classic Mohr's theory of the strength of materials, and is applied to geomaterials using the so-called Thomas - Hill - Mandel shear-band model [Hil62, Man66], which was introduced in the early 60s. A seminal paper was contributed by Rudnicki and Rice [RJ75]. More recently, the mathematical formulation of bifurcation and post-bifurcation phenomena and related instabilities were summarized in [VS95] to form the basis of an improved continuum theory of failure of geomaterials.

This theory defines failure as stationary elastic wave and does not consider time evolution as a degree of freedom. While velocity dependent solutions are sought, they are independent of their evolution in true time. This is known as quasi-static deformation. The fundamental stress and strain solutions therefore degenerate into a geometric

problem where failure lines appear with a finite width  $d$ .

These concepts of shear banding as material bifurcation of an elasto-plastic skeleton have led to the identification of a material length scale defining the width of shear bands. The critical stress, as well as the orientation and the thickness of the localized shear failure planes (shear zones) are calculated through the eigenvalues of the elasto-plastic stiffness modulus  $C_{ijkl}^{ep}$  of the material [RJ75] obeying a rate-independent rheology,  $\dot{\sigma}'_{ij} = C_{ijkl}^{ep} \dot{\epsilon}_{kl}$  (the prime denoting effective stress). Within the framework of the solid mechanical instabilities the shear (fault) zone thickness emerges as a solution depending on the microstructure [MV87, PV11].

This rate-independent regime is typically used as an adequate description of brittle processes, thus placing the formation of the shear zones (onset of localization) near the maximum deviatoric stress [RJ75]. For example, in linear elastic fracture mechanics brittle fracture occurs without thermal activation when a critical stress level is reached to split the bonds. At a critical energy threshold an elastodynamic fast time scale instability ensues where a variety of dissipative processes kick in such as grain/particle rotations which release heat in extremely fast timescales. The fast time scale instability simplifies the processes as temperature and fluids do not have time to diffuse. This regime is called undrained-adiabatic and is characterising extremely fast co-seismic slip [Ric06, SSV11] of brittle failure events.

Within this brittle, solid mechanical framework recent studies [SSV11, VSS12, VSS13] derived different levels of localisation corresponding to different energy (temperature) regimes. This result is a direct generalisation of the extension of the visco-elastic Deborah number concept to different temperatures using the time temperature superposition principle [TA45] for elasto-plastic media. This approach is generalising the concept of visco-elastic relaxation experiment at different temperatures to that of non-linear visco-elasto-plastic solutions where quasi static solutions are sought for different temperatures.

In order to so we first freeze time by adopting classical, rate-independent, elasto-plastic theory for a fault zone material incorporating chemical, hydraulic and thermal sensitivity. In the brittle field these fault zones are characterised by a damage zone surrounding the fault zone with an embedded PSZ as shown in Fig. 1 (a). In the brittle crust the width of this hierarchical damage zone can be up to 3-5 km wide [BZS03, ABZ12], containing in principle multiple localization zones [FLR03]. In order to keep the mathematical model tractable, we restrict the present work to the study of a single fault zone.

We therefore calculate the extent (thickness) of the brittle fault zone at different temperature regimes, marked by: (1) the temperature inferred from geothermal consideration for the boundary of the fault zone, (2) the activation temperature of the dominant chemical reaction observed in the PSZ. The details of the approach can be found in [SSV11, VSS12, VSS13] and the results are summarised in Figure 1 (b) and (c).

## 2.1 Shear Zone Thickness at Boundary Temperature Conditions

The general solution for a quasi static shear zone considers the average of the background particle size  $d_{50}$ , the fluid pressure and the dominant chemical reaction at a given temperature. Both fluid pressure and reaction rate are strongly affected by the temperature. At ambient geothermal temperatures of the shear zone the chemical reaction is inactive and the thickness of the shear zone is predominantly controlled by the thermal-elastic pressurisation of the poro-elastic skeleton (Fig. 1 (b)), characterized by the pressurization coefficient  $\Lambda = \frac{\alpha_f - \alpha_s}{K_s + K_f}$  (MPa/K). In this expression,  $\alpha$  is the thermal expansion coefficient and  $K$  the compressibility, with subscripts  $s, f$  denoting solid and fluid phases, respectively.

The solid mechanical thickness of the shear zone can be calculated directly as function of the average particle size  $d_{50}$ , and the thermal pressurisation  $\Lambda$  as well as a multiplier  $C$  representing the elasto-plastic material:

$$\frac{d}{d_{50}} = \sqrt{\frac{C}{\Lambda}} \quad (1)$$

For a Drucker-Prager, Cosserat material it was shown in [VSS13] that  $C = 17.5 \cdot 10^3 \text{ KMPa}^{-1}$ . For typical values of  $\Lambda$  between  $10^{-4}$  (MPa/K) [CZV11] and 1 (MPa/K) [Ric06], with  $d_{50}$  of the order of 1 mm, the shear zone width ranges between 0.1 and 13 meters.

## 2.2 Shear Zone Thickness at Elevated Temperature

The effect of chemical reaction can be incorporated by considering the reaction rate to follow Arrhenius kinetics. In this framework the reaction rate depends on the activation enthalpy  $Q_F$  and the reaction rate frequency  $k_F$ . The reaction is activated at elevated temperatures, near the activation temperature of the reaction at given pressure conditions. At these temperature conditions, and considering calcite decomposition as a typical reaction for a carbonate host rock [FNB<sup>+</sup>08, SF09], the thickness of the PSZ is several orders of magnitude smaller than the low temperature shear zone as shown in Fig. 1 (c).

This result is reconciling field observations from two different temperature regimes but has no predictive power on how these temperatures may have been achieved. The traditional concept of TTS is not extendable to obtain extended solution for non-linear solids. We therefore need a non-linear superposition that allows fault zone evolution through time. The non-linear concept in this work is introduced by a Taylor expansion of the plastic strain rate, accounting for higher-order terms describing the non-linearities.

In Geomechanics several studies have been devoted to the thickness of shear bands in soils. Under purely mechanical effects the thickness of the initial shear band (with thickness  $D$  in Figure 1) in a granular medium is around  $16d_{50}$  with  $d_{50}$  the average

(50% weight) grain diameter [MV87]. This zone appears to be too wide to be considered as the PSZ [Ric06]. In principle the PSZ represents a very fine shear localization, consisting of ultrafine particles that have usually undergone mechano-chemical degradation (gelification, decarbonation and dehydration reactions, melting, as thoroughly discussed by [THH<sup>+</sup>11]). Therefore, the initial mechanism such as the shear band formation from homogenous deformation [MV87] is a consequence of the solid mechanical failure while the formation of PSZ's may be considered an effect of the fluid-like deformation following the onset of the initial structure.

Such post-failure behaviour may for instance be significantly influenced by the presence of fluids interacting with the rock, hence inducing coupled effects including shear heating and pore fluid pressurization. These mechanisms are therefore expected to control the strength during fault slip [Sib73, Lac80, WS05] and the weakening effect displayed in catastrophic landslides [Var2a, VVD07, LA07, BE08, GAA10]. Thermo-poro-mechanical couplings due to shear heating [SJP05, Ric06] can be also associated to chemical effects such as dehydration of minerals or decomposition of carbonates, theoretically studied recently by [BSCS10, BSS11, SF09, VAV10] and reported to take place in real faults [Hea07] and experiments at laboratory conditions [HSH<sup>+</sup>07, FDHS10, BHS<sup>+</sup>11, PHM<sup>+</sup>11, CVTM13]

### 3 Time-dependent evolution of shear zones

To this end, we assume a smooth function of the effective stress, temperature  $T$  and additional internal variables  $\xi$ , expressing the constitutive behaviour of the material

$$\dot{\epsilon}_{ij}^p = f(\sigma'_{ij}, T, \xi) \quad (2)$$

The temperature and  $\xi$  obey their own evolution laws, namely the energy balance for  $T$  and experimentally deduced evolution laws for  $\xi$ . By expanding Eq. (2) around the effective yield stress  $\sigma'_Y$  we obtain

$$\dot{\epsilon}_{ij}^p = f' \left( \frac{\bar{\sigma}_{ij}}{\sigma'_n} \right) + \sum_{m \geq 2} f^{(m)} \left( \frac{\bar{\sigma}_{ij}}{\sigma'_n} \right)^m \quad (3)$$

where  $\bar{\sigma}_{ij} = \sigma'_{ij} - \sigma_Y$ ,  $\sigma'_n$  a reference stress and  $f^{(m)} = \frac{1}{m!} \left| \frac{d^m f(\sigma'_{ij}, T, \xi)}{d\sigma'^m_{ij}} \right|_{\sigma'_{ij} = \sigma'_Y}$ .

The first order of the Taylor expansion corresponds to the time independent solid mechanical regime presented earlier and describes the formation of the fault near initial yield. Once the fault has been formed after initial yield it continues to deform plastically (irreversible deformation) upon continuation of loading. This restricts our modelling efforts to the behaviour of the material inside the solid mechanical shear zone obtained from the first order expansion. Therefore, by considering explicitly the rate sensitivity emerging from the higher order terms of the expansion we study the

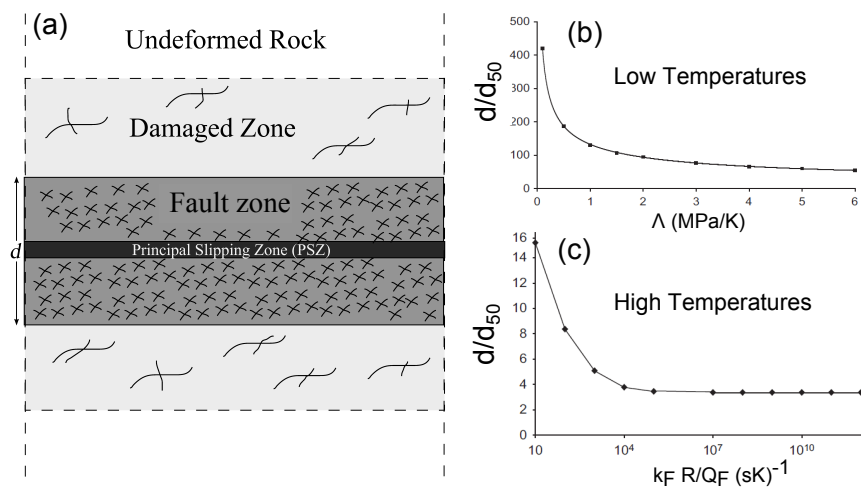


Figure 1: (a) Conceptual model of the internal structure of a fault described by two scales: the Principal Slipping Zone (PSZ) in the centre surrounded by the fault zone. (b) using the geothermal temperature as a thermal condition for the boundary of the fault zone we obtain the thickness of the fault zone as a function of its internal structure (average particle size) and the thermal pressurisation. (c) Using the higher temperature required for chemical reactions as recorded in the PSZ a much length scale down to 3 times the average grain/particle size is obtained.

non-linear (fluid-like) evolution of the mechanisms inside the solid mechanical fault zone solution.

The higher order terms of Eq. (3) give a natural extension of the classical TTS in the nonlinear visco-plastic space. If the solid mechanical yield is considered as a large scale reference state of our model we can describe the higher order terms in the nonlinear fluid dynamic space by the so-called overstress  $\bar{\sigma}_{ij} = \sigma'_{ij} - \sigma'_Y$ , defined as the stress that follows the evolution post the initial yield point [Per66], hence  $\bar{\sigma}_{ij} > 0$  is always satisfied. The rate of plastic strain is therefore expressed as

$$\dot{\epsilon}_{ij}^p = \sum_m f^{(m)} \left( \frac{\bar{\sigma}'_{ij}}{\sigma'_n} \right)^m \quad \text{when } \bar{\sigma}_{ij} > 0 \quad (4)$$

where  $f^{(m)}$  has now dimensions of  $(s)^{-1}$ , being thus a reference strain rate.

In this sense the nonlinear TTS expresses a straight forward extension of the linear TTS with the difference that the time scale now plays an explicit role. In the classical TTS the time scale is simply derived from relaxation experiments returning the system near to its equilibrium whereas in the nonlinear TTS the system is always driven far from equilibrium. In the nonlinear framework the relaxation experiments therefore must be replaced by far from equilibrium energy considerations which define the time scales over which the rate of processes exchange energy inside the fault zone [RLYF09].

### 3.1 Energy considerations

We introduce the Helmholtz free energy  $\psi$ , being a function of the elastic strain, temperature and the internal variables  $\xi$ . The energy balance equation, together with the second law of thermodynamics and Fourier's law of diffusion provide the local form of the entropy production equation [RRRH00, RLYF09]:

$$\frac{\partial T}{\partial t} + v_k^m \frac{\partial T}{\partial x_k} = c_{th} \frac{\partial^2 T}{\partial x_k^2} + \frac{q_e}{(\rho C)} + \frac{\Phi_m}{(\rho C)} + \frac{L}{(\rho C)} \quad (5)$$

where  $v_k^m$  is the barycentric velocity of the system,  $c_{th} = \frac{k_{th}}{(\rho C)}$  is the thermal diffusion coefficient of the mixture (usually depending weakly on temperature and strongly on the microstructure, here considered constant),  $C = -T \frac{\partial^2 \psi}{\partial T^2}$  is the specific heat capacity of the mixture under constant volume,  $q_e = \rho_m T \frac{\partial^2 \psi}{\partial T \partial \epsilon_{ij}^e} \dot{\epsilon}_{ij}^e$  is the thermoelastic rate of heating. Note that in the framework of solid mechanics the advective terms are neglected, thus  $v_k^m = 0$ .

The term  $L = \rho_m T \frac{\partial^2 \psi}{\partial T \partial \xi} \dot{\xi} = \Delta h r$  represents the latent energy produced or absorbed during a higher order energy transition ( $\Delta h$  is the enthalpy of the energy transition and  $r$  its rate). This includes any microstructural changes such as grain size reduction and damage in the case that the state variable is a grain size or a damage parameter

[LBZ14b, LBZ14a], respectively. In the case where the state variable refers to the chemical constituents it corresponds to the well known latent heat of a phase change. Finally  $\Phi_m$  is the local dissipation, i.e. the mechanical power that is converted into heat in the system. In generalised thermodynamics the dissipation is defined by the product of a thermodynamic force times a thermodynamic flux. In mechanics the thermodynamic force is the stress  $\sigma'_{ij}$  and the thermodynamic flux is the plastic strain rate  $\dot{\epsilon}^p_{ij}$ . In the generalised framework, when additional state variables/processes are considered the force becomes a generalised force such as a damage force  $E_\xi$  and the thermodynamic flux is the rate of change of the state variable  $\dot{\xi}$ .

$$\Phi_m = \sigma'_{ij} \dot{\epsilon}^p_{ij} - E_\xi \dot{\xi} = \chi \sigma'_{ij} \dot{\epsilon}^p_{ij}. \quad (6)$$

with  $E_\xi = \rho_m \frac{\partial \psi}{\partial \xi}$  the energy dual of the internal variable  $\xi$ . The Taylor-Quinney ratio  $\chi$  expresses the amount of the mechanical energy converted into heat [TQ34], and is in principle a history dependent quantity rather than a constant ( $0 < \chi < 1$ ). Its importance is discussed in the following section.

### 3.2 The Taylor-Quinney coefficient

The Taylor-Quinney coefficient is a function of the elastic strain, the temperature and the internal variables:

$$\chi = \chi(\epsilon^e_{ij}, \xi, T) = 1 - \frac{E_\xi \dot{\xi}}{\sigma'_{ij} \dot{\epsilon}^p_{ij}}. \quad (7)$$

The Taylor-Quinney coefficient is unity if all deformation work is converted into heat. For values smaller than unity and larger than zero it describes the portion of deformation work that is stored in microstructure. The coefficient can be derived through thermographic deformation experiments [RRRH00]. The Taylor-Quinney coefficient as derived from thermography often starts at initial yield being close to zero and progressively evolves in the transient deformation regime towards a steady state value of 0.9 for most materials [CB92]. Its evolution between these two values is therefore prescribed by the development of the internal state variables. As such it has a fundamental meaning for discriminating deformation mechanisms.

If the dissipation process is for instance a rapid fracture the evolution time of the Taylor-Quinney is extremely fast and obtained from the bond energy between the covalent or electronic bonds of the atoms. This equates macroscopically to an elastic interaction potential. In linear elastic fracture mechanics brittle fracture occurs at explosive timescales (of the order of seconds). The Taylor-Quinney coefficient prior to fracture is zero as all mechanical work is stored elastic deformation. At the critical threshold an elastodynamic fast time scale instability ensues where a variety of dissipative processes kick in such as grain/particle rotations which release heat therefore increasing the Taylor-Quinney coefficient. This is the typical mechanism for brittle fracture.

Similarly in ductile deformation processes the Taylor-Quinney coefficient is zero at initial yield, however, in contrast to brittle deformation the failure is thermally activated. A series of micro-mechanical processes such as dislocation and diffusion mechanisms kick in that feature a time scale that is relatively slow compared to the elastodynamic time scale. The thermal activation is often described by an Arrhenius temperature activation. This rate-dependent failure mechanism is known as ductile (or creep) fracture.

$$\Phi_m = \Phi_0 \chi(\xi) \left( \frac{\bar{\sigma}_{ij}}{\sigma'_n} \right)^{m+1} e^{-\frac{T_0}{T}} \quad (8)$$

where  $\Phi_0 = \sigma'_n \dot{\epsilon}_0$  is the reference dissipation,  $\sigma'_n$  is a reference stress value and  $T_0 = Q_d/R$  the thermal sensitivity (activation temperature) of dissipation.

### 3.3 Chemical reactions

From the analysis of the brittle regime (Section 2) we obtained that chemical reactions have a critical role in the system, defining the ultimate width of localization (the PSZ thickness). In this work we will emphasize on fluid release reactions, due to their fundamental importance in earth systems. Fluid-release reactions occur when either a hydrous mineral such as a clay mineral, serpentinite, mica, gypsum etc. loses its water at a critical activation enthalpy or when a mineral that is made of fluid phase and a solid constituent breaks down such as carbonate breaking to lime plus carbon dioxide upon critical activation enthalpy [FNB<sup>+</sup>08, SF09].

We treat these shear zone minerals as generalized solids characterised by the bonded chemical species  $A$  and  $B$  forming the solid composite  $AB$ . We assume  $B$  to represent fluid species filling the porous matrix of  $AB$  at initial conditions. At high temperatures the solid  $AB$  breaks down, producing excess  $B$  fluid, and increasing the fluid pore pressure through a general fluid-release reaction of the form  $\nu_1 AB_{(s)} \rightleftharpoons \nu_2 A_{(s)} + \nu_3 B_{(f)}$ .

The kinetics of this reaction are assumed to obey the standard Arrhenius dependency on temperature (see appendix A). Following these considerations, the rates of the forward ( $r_F$ ) and reverse ( $r_R$ ) first order reactions (and for  $\nu_1 = \nu_2 = \nu_3 = 1$ ) can be calculated to be

$$\begin{aligned} r_F &= \frac{\rho_{AB}}{M_{AB}} (1 - \phi)(1 - s) k_F e^{-Q_F/RT} \\ r_R &= \frac{\rho_A \rho_B}{M_A M_B} (1 - \phi) s \Delta \phi_{chem} k_R e^{-Q_R/RT} \end{aligned} \quad (9)$$

The total reaction rate is subsequently

$$r = \left[ (1 - s) - s \Delta \phi_{chem} \frac{\rho_A \rho_B}{\rho_{AB}^2} \frac{M_{AB}^2}{M_A M_B} K_c^{-1} e^{\Delta h/RT} \right] (1 - \phi) \rho_{AB} k_F e^{-Q_F/RT} \quad (10)$$

where  $K_c = k_F/k_R$  and  $\Delta h = Q_R - Q_F$ . In these expressions  $k_F, k_R, Q_F, Q_R$  are the pre-exponential factors and activation enthalpies of the forward and reverse reaction, respectively and  $M_i$  and  $\rho_i$  is the molar mass and density of the  $i$ -th constituent. The porosity  $\phi$  consists of an initial value  $\phi_0$  and the new interconnected pore volume created from the reaction  $\Delta\phi_{chem}$ ,  $\phi = \phi_0 + \Delta\phi_{chem}$ . The partial solid ratio  $s$  is the volume ratio of the produced solid  $A$  in the solid matrix. The expressions for the dependency of  $\phi$  and  $s$  on the reaction kinetics are given in [APV14] and are summarized here in appendix A. This formulation is essentially a damage mechanics formulation with porosity being the damage parameter being controlled by the physics of the chemical reactions.

## 4 Post failure evolution of a shear zone

We focus on the post failure evolution of a shear zone with thickness  $d$ , formed by material bifurcation (Fig. 2). Due to the small thickness of the shear zone compared to the thickness of the overburden, its momentum balance prescribes a constant stress profile across the shear zone, thus  $\sigma_{yx} = \tau_n(t)$  and  $\sigma_{yy} = \sigma_n(t)$  [Ric06, VAV10]. In addition, in the presence of a fluid, the stress can be decomposed according to Terzaghi's principle [VS95] to  $\sigma'_{ij} = \sigma_{ij} + p_f\delta_{ij}$ , with  $\delta_{ij}$  the Kronecker's delta and  $p_f = p_n + \Delta p$  the pore fluid pressure, consisting of a hydrostatic part  $p_n$  at the boundary and the excess pore pressure  $\Delta p$ . The final system of equations is obtained once the energy equation is coupled with the mass balance equation [VAV10, APV14, VPA14, VRL14]:

$$\frac{\partial \Delta p^*}{\partial t^*} = \frac{\partial}{\partial y^*} \left[ \frac{1}{Le} \frac{\partial \Delta p^*}{\partial y^*} \right] + \Lambda \frac{T_c}{\bar{\sigma}'_n} \frac{\partial \theta}{\partial t^*} + (1 - \phi)(1 - s)\mu_r e^{\frac{Ar\theta}{1+\theta}} \quad (11)$$

$$\frac{\partial \theta}{\partial t^*} = \frac{\partial^2 \theta}{\partial y^{*2}} + \delta \left[ Gr (1 - \Delta p^*)^m e^{\frac{aAr}{1+\theta}} - (1 - \phi)(1 - s) + (1 - \phi)s\Delta\phi_{chem}\eta K_c^{-1} e^{\frac{xAr}{1+\theta}} \right] e^{\frac{Ar\theta}{1+\theta}}$$

where the fields were normalised with the help of a reference temperature  $T_c$ :

$$t^* = \frac{c_{th}}{(d/2)^2} t, \quad y^* = \frac{y}{d/2}, \quad \theta = \frac{T - T_c}{T_c}, \quad \Delta p^* = \frac{\Delta p}{\bar{\sigma}'_n} \quad (12)$$

The kinetics of the reactions are normalised using the Arrhenius scaling

$$Ar = \frac{Q_F}{RT_c}, \quad a = 1 - \frac{Q_d}{Q_F}, \quad x = 1 - \frac{Q_R}{Q_F} \quad (13)$$

The remaining dimensionless quantities appearing in the system (11) are defined as

$$\begin{aligned}
 \delta &= \frac{|\Delta h|(d/2)^2}{k_{th}T_c} k_F \rho_{AB} e^{-Ar} & (14) \\
 \eta &= \frac{\rho_A \rho_B}{\rho_{AB}^2} \frac{M_{AB}^2}{M_A M_B} \\
 \mu_r &= \left( \frac{\rho_{AB}}{\rho_B} \frac{M_B}{M_{AB}} \right) \frac{(d/2)^2}{c_{th} \bar{\sigma}'_n} \frac{k_F}{(\beta_f + \beta_s)} e^{-Ar} \\
 Le &= \frac{c_{th} \mu_f (\beta_f + \beta_s)}{k} \\
 Gr &= \frac{\chi(\xi) \Phi_0}{k_F |\Delta h| (\rho_{AB} / M_{AB})}
 \end{aligned}$$

where  $k_{th} = c_{th}(\rho C)$  the thermal conductivity of the system. The system of Eqs. (11) is fully described when the 8 dimensionless numbers ( $a$ ,  $x$ ,  $\mu_r$ ,  $Le$ ,  $\delta$ ,  $Gr$ ,  $K_c$ , and the boundary temperature  $\theta_b$  since  $Ar$  is implicitly considered in these groups) are determined. However, the system has a much lower dimensionality which can be revealed through a comprehensive analysis of its steady state and transient responses. These analyses has been presented in [APV14, VPA14, PVRLY14], identifying the dominant parameters of the system. Of critical importance is the Gruntfest number  $Gr$ , as it incorporates the energetics of the microstructure through the Taylor-Quinney coefficient, as well as the mechanical loading and the characteristics of the chemical reaction. High values of  $Gr$  correspond to a regime where the mechanical input is sufficient to trigger the chemical reaction. Due to its fundamental nature,  $Gr$  will be treated as a bifurcation parameter.

The post-failure evolution of the shear zone is summarized in Fig. 3. The first panel (a) illustrates the fundamental three phase stability S-curve typical to all systems of the generalized type discussed above (Eq. 11) [YS77]. The first phase is illustrated in details in panel (b) showing a steady state creep solution acting as a global stable material response without instabilities. The panel (c) is the solution for the phase of elevated Gruntfest numbers but below the critical point B of Fig. 3 (a). For any initial conditions below line BC of (a) the system relaxes back to the stable branch AB. For any initial condition above line BC of (a) the system features a solitary oscillation. Panel (d) of Fig. 3 illustrates the behaviour in domain III where a stable oscillator emerges. This stable oscillator is self-sustained and has a fundamental role in the post-failure evolution of shear zones. This area, where  $Gr > Gr_B$ , is the domain where localisation of dissipation occurs owing to critical energy transitions. This means that the latent energy term  $L$  of Eq. 5 is triggered and energy is released. This domain does not depend on the exact micro mechanism, as shown in [VAV10], but describes a generalised material instability where the changes of the state variable form the localisation phenomenon. The state variable can be for instance a grain size, a damage or porosity change as discussed in this study.

Alevizos et al. [APV14] provided asymptotic criteria for the area of oscillations to be

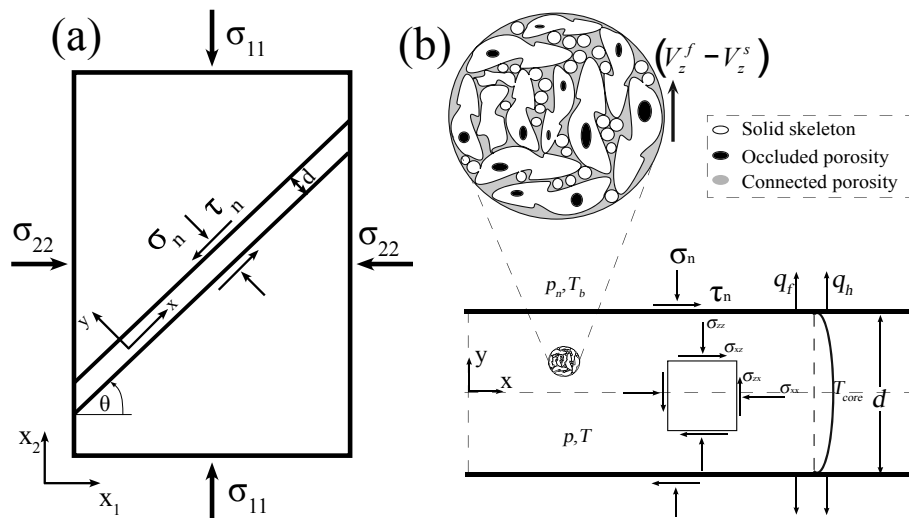


Figure 2: (a) Sketch of the continuum mechanical concept of shear failure as a material bifurcation [RJ75]. At a critical stress ratio of the original stresses (in the coordinate system  $x_1 - x_2$ ) a conjugate pair of shear zones emerge, having a thickness  $d$  and dipping at angles  $\pm\theta$  thereby defining the rotated coordinate system of failure,  $x - y$ . For visual purposes only the shear zone dipping at  $\theta$  is shown here. (b) Processes inside the shear zone of (a). The loading conditions and the filter velocity  $v_z^f - v_z^s$ , along the content of a saturated rock, are depicted. We assume that any chemical reaction is taking place at the solid-pore interface. Hence all the produced fluid contributes to the interconnected pore volume and is concentrated on the grain boundaries. We also assume that the produced solid is added to the skeleton, establishing a common velocity field  $v_z^s$  with the reactant solid.

admitted. This occurs when the following inequalities simultaneously hold:

$$Gr > \left(1 + \frac{e^{-Ar\theta_b}}{Ar\delta}\right) e^{-aAr}, \mu_r Le < Ar^{-3/2}, \log(K_c) \gg 1 \quad (15)$$

These inequalities correlate most of the dimensionless groups of the system, implying that in environments where strong (irreversible) endothermic reactions are favoured (hence  $\log(K_c) \gg 1$  is always satisfied) any 2 of the remaining groups can always be selected as control over oscillatory instabilities.

#### 4.1 Analysis of the system's response

The solution discussed in Fig. 3 is obtained under the assumption of a constant loading stress and chemistry as well as internal microstructure thus giving a constant Grunfest number. In the more general case either of these parameters can evolve in time thus allowing the system to cross all three areas of the phase diagram. This leads potentially to a multiplicity of chaotic responses marked by phases of self-organised chaos, transition from aseismic creep to seismic slip and back. For example if the system follows the hysteretic loop ABB'CA of Fig. 3 we find all three different system responses in one and the same shear zone.

Of particular interest for plate tectonic loading is the particular attractor depicted in Fig. 3 (d) where a constant plate velocity would lead to a constant shear stress over time, allowing for a steady state evolution of the microstructure and chemistry. The periodic instability that emerges in this regime corresponds to a stick-slip type of instability, as illustrated in Fig. 4 where the limit cycle is plotted in the logarithmic strain rate versus normalised time space. The limit cycle is characterised by two distinctly different time scale phenomena, the first being a long time scale of slow creep interrupted by a short time scale fast response owing to fluid the release reaction.

In addition to the two timescales characterizing the system's time evolution, its spatial manifestation also comprises two length-scales. Fig. 5 shows profiles of strain rate (red line), porosity (blue line) and solid product (green line) inside the solid mechanical shear zone, at their maximum points in the limit cycle. Starting from a flat initial profile when the solid mechanical shear zone is established, the strain rate localizes in an ultrathin core zone during the fast timescale. The extreme localisation of strain rate in the centre of the solid mechanical shear zone is a robust outcome for any chemical reaction. The thickness of this ultralocalized shear band inside the global mechanical shear zone depends on the activation enthalpy of the forward reaction. For large enthalpy reactions the localised zone is ultra-sharp and broadens with reducing enthalpy. This localisation is then followed by a chemical-mechanical localisation wave propagating towards the boundaries of the shear zone [VRL15, VRLW14, SS14].

We expect from this result two important outcomes. The first is that the shear zone will show at least two different scales of localisation, linked to the corresponding timescales. The broad solid mechanical zone acts as a vessel for the long creeping

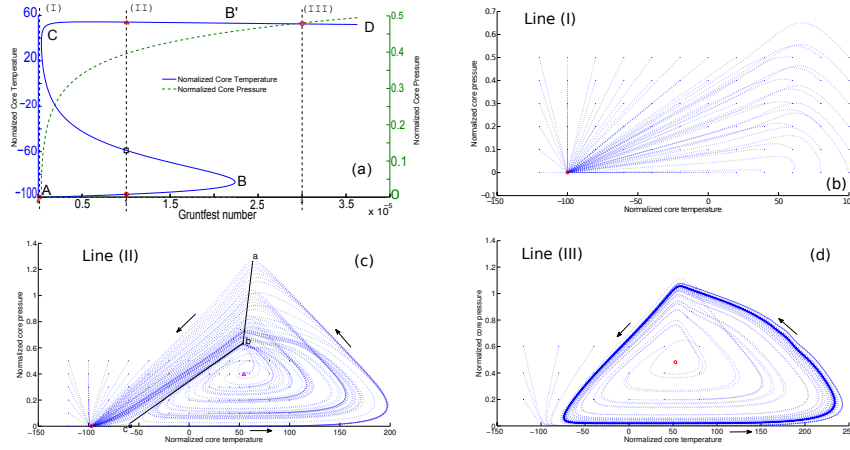


Figure 3: Summary of the system’s response when Eqs. (15) are satisfied. (a) Steady state response of the dimensionless core temperature (solid line) and the dimensionless core excess pore pressure (dashed line). The three lines annotated correspond to the three areas of interest, providing the phase diagrams of: (b) a stable, aseismic creep behavior (line I), where all the initial conditions in the  $\Delta p - T$  phase plane end up at the stable node depicted as a circle, (c) non-periodic events (line II), where the line a-b-c separates the linear paths towards the lower stable node (circle) from the homoclinic orbits tending to the circle via the unstable spiral orbit of the upper solution (triangle), and (d) periodic instabilities (line III), appearing in the  $\Delta p - T$  phase plane as stable limit cycles around the unstable upper steady state solution (circle). The magnitude of the cycle increases with decreasing  $Gr$ , obtaining its maximum amplitude at point B, where a homoclinic bifurcation takes place, with the periodic orbit colliding with the saddle point B. Note that values of  $\Delta p$  larger than 1 indicate possible hydraulic fracturing in the vicinity of the fault’s core, limiting the present model.

timescale, whereas the sharp fluid-dynamic length-scale accompanies the fast pressurization timescale. The second outcome is that the width of the fluid dynamic localization can be used to identify the activation energy of the chemical reaction involved. The spatial extent of the fluid release reaction is shown in the blue porosity curve in Fig. 5 to broaden with reducing enthalpy of the reaction. The same trend applies to the solid constituent of the reaction. This additional information may be used in the field as added constraint for identification of activation enthalpies.

### 4.2 Timescales of the system

We expand the temperature field with respect to  $\epsilon = 1/Ar$  [Fow97]. At leading order the chemical reaction is inactive, thus reducing the system to a single equation, known

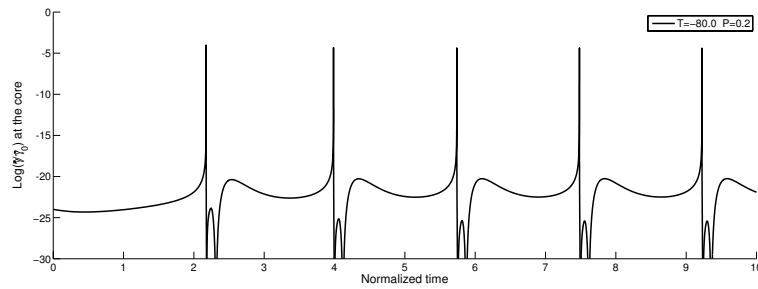


Figure 4: Evolution of the core strain rate on line III of Fig. 3 (a). Irrespectively of the initial conditions, the system in this area undergoes cycles of abrupt acceleration followed by prolonged relaxation.

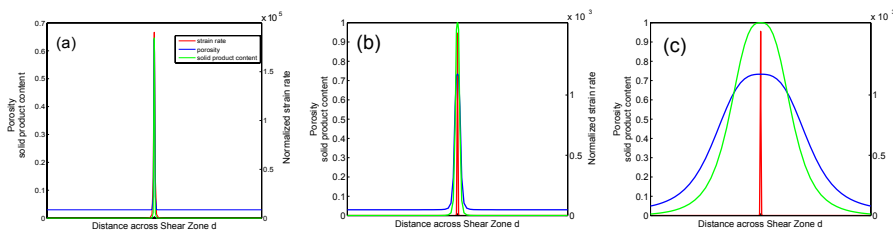


Figure 5: Influence of the characteristics of the reaction. Snapshots of the profiles of porosity  $\phi$ , solid product content and strain rate near the time of their maximum values (the point of maximum temperature in the limit cycle of Fig. 3d). (a) For  $\Delta h = Q_F$ , (b) for  $\Delta h = 3/4 Q_F$ , (c) for  $\Delta h = Q_F/2$ . We notice that as  $\Delta h$  decreases the reaction broadens its extent inside the shear zone  $d$ . For  $\Delta h \approx Q_F$  porosity and  $s$  are weakly produced at the core of the shear zone, and the strain rate is smaller in magnitude (a). Once  $s$  and  $\phi$  reach their maximum values (in this case  $s = 1$  and  $\phi = 0.75$ ) the reaction takes place in an increasingly broader zone as  $Q_R$  increases (b-c).

as the Frank-Kamenetskii limit:

$$\frac{\partial \theta}{\partial t^*} = \frac{\partial^2 \theta}{\partial y^{*2}} + \lambda e^\theta \quad (16)$$

where  $\lambda = \delta (Gr e^{aAr} - 1)$ . Equation (16) is correspondingly the Frank-Kamenetskii equation [Fuj69], known to have the semi-analytic solution [VVD07]:

$$\theta = \theta_{core} - \ln \left[ \lambda(t_I - t^*) + \frac{y^{*2}}{4(c_1 - \ln(t_I - t^*))} \right] \quad (17)$$

where  $\theta_{core}$  is the initial temperature at the core (maximum),  $t_I = 1/\lambda$  is the time that temperature presents a singularity (blow-up time), and the constant  $c_1$  is determined by the boundary conditions [VVD07]. We note that the initial condition should be the temperature at which the fault is initially formed. For flat, isothermal profile inside the shear zone,  $\theta_{core} = \theta_b$ .

As discussed in [VVD07], past a critical strain rate achieved at  $t \approx 0.88t_I$ , the analytical solution of Eq. (17) indicates that dissipation (strain rate) localizes towards the center of the shear band while abruptly increasing. When reaching the critical value of temperature to trigger chemical pressurization, then the system enters the pressurization regime and excess pore pressure is being generated from the reaction in an undrained adiabatic setting. The time at which the temperature at the center of the fault zone ( $y = 0$ ) reaches the activation temperature of the reaction,  $\theta_{cr}$ , is approximately the time-scale of the frictional (stable creep under zero overpressures) process,

$$t_{cr}^* = \frac{1}{\lambda} \left[ 1 - e^{(\theta_{core} - \theta_{cr})} \right] \quad (18)$$

Thus, the time at which chemical pressurization will set in is a function of the initial configuration of the system  $\theta_{core}$ , of the pressurization temperature  $\theta_{cr}$  and of all the material, chemical and loading parameters of the problem, incorporated into  $\lambda$ . Recalling that  $Gr$  (hence  $\lambda$ ) incorporates the Taylor-Quinney coefficient,  $t_{cr}^*$  is directly influenced by the evolution of the internal variables, thus of the microstructure.

Note that when  $\theta_{cr} = \theta_{core}$  then  $t_{cr}^* = 0$ , meaning that the fault will enter the pressurization regime directly, without admitting any period of creep. On the other hand, when  $\theta_{cr} \gg \theta_{core}$ , then  $t_{cr}^* = 1/\lambda$  and the fault will admit all its creeping capability. Once the chemical reaction is triggered it evolves in a fast timescale, estimated by the higher order of the expansion, where undrained-adiabatic conditions establish. In this regime, the timescale is inversely proportional to  $\mu_r$  [VAV10]

$$t_p^* \sim \frac{1}{\mu_r} \quad (19)$$

## 5 Comparison to Field Observations

We have identified in the above theoretical considerations two fundamentally different processes (rate/temperature independent and rate/temperature dependent) with similar

outcomes. Both processes lead to two scales of localisation. The large scale is associated with the solid mechanical solution and the small scale with the fluidised fault zone material inside the master shear zone.

In the rate/temperature independent solution the ultralocalised PSZ appears without a creeping phase. From Eq. (18) we conclude that the system is already in a critical state and does not require shear heating to be brought to criticality. In physical terms this could be seen as a transition that is equivalent to allowing phase changes, or grain size reduction, or damage to start at a negligible input of energy. This leads to the identification of the fast time-scale elastodynamic instability, where the energy released in the PSZ causes extreme localisation with an internal time scale governed by the energy change process. In our example we postulated a fluid release reaction and obtained the pressurisation time scale of Eq. (19). Other mechanisms, such as damage or grain-size, impose different time scales for instability based on their energetics. This dual localisation is therefore the hallmark of brittle shear zones as illustrated in Figure 6 (a).

In the case where the system is not close to criticality and is creeping the equivalent ductile localisation mechanism can emerge. Upon a finite time after release of deformational work into heat inside the creeping shear zone, the system can reach the critical point for a fast energy transition. At this point the creeping zone forms a PSZ upon which the micro mechanical or chemical changes of the fast energy process occur. We have discussed the example of a chemical breakdown reaction which results into an accelerated slip instability forming the PSZ. A number of other microstructural processes are often activated in the course of this instability leading to a rich microstructure inside the PSZ. This could be dynamic recrystallisation, fluid release, dissolution-precipitation etc. The complex nature of these instabilities leads to complex geometries and time series such as slow slip/earthquake signatures. The dual feature of creeping zone and ultralocalized PSZ, therefore is also a hallmark of ductile shear zones as illustrated in Figure 6 (b).

To juxtapose the outcomes of the theoretical approach with field evidence, we compare our solutions with observation from brittle and ductile shear zones. Figure 6 shows in (a) the famous Punchbowl cataclastic fault described by Chester and Chester [CC98]. The fault shows a cataclastic fault zone of the order of meter thickness with an ultralocalized, pulverised PSZ. The mineralogy of the host rock and PSZ indicate a transition from quartz and feldspar dominated to clay mineralogy in the cataclastic fault zone and ultimately higher ordered smectite and quartz in the PSZ [CC98]. This indicates a series of mineral dissolution-precipitation reactions that are typical for the ingress of water under lower temperature environments. The addition of water can decrease the activation temperature and thereby render the system critical at ambient conditions.

The same style of deformation is also recorded in the UNESCO world heritage Glarus fault that shows a meter-thick, chemically altered tectonite (known as Lochsite tectonite), blending the hanging wall and footwall minerals [PVH<sup>+</sup>14]. The tectonite is deformed and folded by ductile deformation and has an ultralocalised PSZ (Fig. 6b)

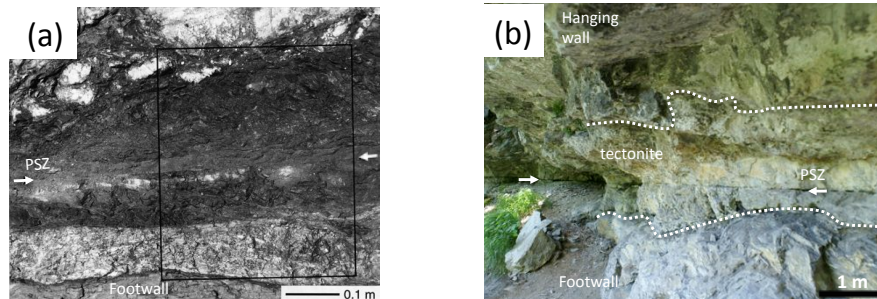


Figure 6: (a) Punchball fault from Chester and Chester [CC98] featuring two scales of localisation, the cataclastic fault zone and the ultracataclastic PSZ annotated by arrows. (b) The Glarus Thrust at the Lochsite, featuring two scales of localisation, the creeping zone forming the carbonate rich tectonite and the ultralocalized PSZ in its centre.

in its middle. Field evidence include a multiplicity of PSZ's inside the tectonite, implying repetitive fast events interrupting ductile creep. The key chemical reaction controlling both the tectonite formation and the thickness of the PSZ was identified to be carbonate decomposition and precipitation [HHp<sup>+</sup>08]. For the ductile localisation instability additional heat is required as the carbonate decomposition reaction happens at much larger temperature than the boundary of the thrust zone. The addition of temperature is readily available from the long-term dissipation of the creep process, which becomes a prerequisite for the ductile instability. Because the shear zone has a characteristic background temperature, the chemical reaction has a critical temperature to be triggered and the microstructure has equilibrated over time, to quasi-steady state, the ductile instability is inferred to have periodic signature in time. This implies a regular stick-slip type of behaviour for the ductile PSZ whereas the brittle PSZ is expected to be chaotic in time. The reason is that brittle instabilities are always at criticality while ductile instabilities require time to be brought to criticality.

## 6 Application to ETS sequences

The temporal predictions of the model presented can be tested against real measurements from Episodic Tremor and Slip events (ETS) at the plate interface during the subduction of oceanic plates below the continental ones. In these subduction environments, key minerals controlling both the rheology and the fluid-release reaction are the minerals of the serpentinite family [PVRLY14]. We may therefore specify the fluid release reaction to be the dehydration of serpentinite minerals. For the example of antigorite dehydration,  $AB$  could correspond to antigorite ( $Mg_{48}Si_{34}O_{85}(OH)_{62}$ ),  $A$  would represent all the solid products such as olivine ( $MgSiO_4$ ) and enstatite ( $MgSiO_3$ ) and  $B$  the fluid  $H_2O$ . In this section, we use the values presented by

[PVH<sup>+</sup>14] for the material properties of the system and study regular and irregular GPS signals from two different subduction environments.

## 6.1 Regular sequences - Cascadia ETS sequence

We begin with the periodically consistent case of the Cascadia ETS sequence in Canada (for a more detailed analysis refer to [APV14, VPA14, PVRLY14]). Episodic transient movements are continuously recorded from a network of GPS sensors revealing consistent periodicity between slip events over 20 years. The magnitude of the slip events is about 10 mm, being accumulated over approximately 2 weeks. We model the detailed displacement data available from the GPS stations in Vancouver Island [NAS], exhibiting a period of 14 months between the slow slip events. Because of the nearly perfect periodic sequence, it is expected that the model will be able to predict the evolution with a single fundamental mode of oscillation. All the GPS data used in this section were de-trended from the background to obtain a zero average velocity. No further geophysical techniques were used to remove annual effects, so that the model can be juxtaposed against the raw signals.

The model replicates the temporal sequence of the last 20 years, as shown in Fig. 7, highlighting the validity of the suggested interplay between dehydration reactions and the mechanical response. The inverted values of the parameters used [PVH<sup>+</sup>14] show that the serpentinite family minerals creep in an interface shear zone of about 6 m thickness in which the ETS sequence takes place.

The GPS data show some irregularities and offsets between the events, thus suggesting perturbations to the system due to seasonal or secondary transient effects. However, within the 20 years interval these perturbations are recovered by the system back to its fundamental mode, the stable multiphysical oscillator of fig. 7b. This in turn could suggest that there is small variation in the parameters and only one eigenmode is preferred. Thus, the system can absorb these perturbations due to the stable nature of the fundamental limit cycle and cannot switch to a different one.

In the case of Cascadia ETS sequence the loading conditions used ( $\tau_n$  and  $\sigma_n$ ) were constant in time. Therefore, as suggested above, the 20 years of GPS recordings were matched with a single limit cycle of the system (Fig. 7b). This result reveals that Cascadia is a self-sustained process equilibrating near the minimum dissipation capacity of the subduction system.

## 6.2 Alternating modes - Hikurangi ETS sequence

A question that naturally arises is whether the suggested formulation can also be used for less regular GPS signals. The application of the present model to an irregular case study was performed by [PVH<sup>+</sup>14]. The basic assumption is that, unlike the Cascadia

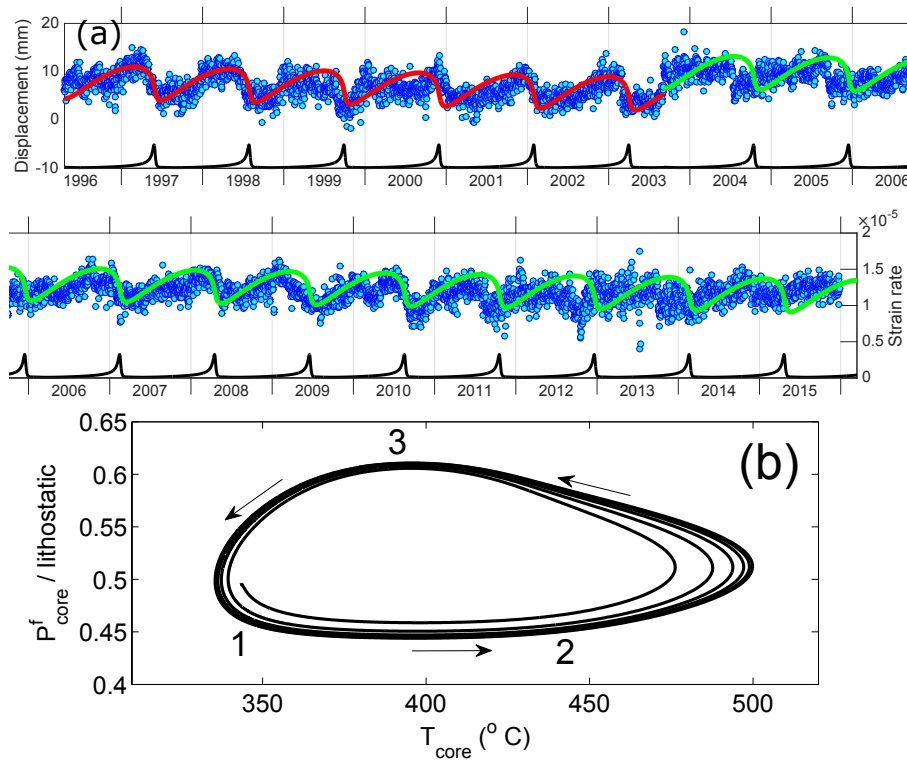


Figure 7: Regular ETS sequence in South Vancouver Island, Cascadia, station ALBH [NAS]. (a) The GPS data (blue dots) represent raw displacement data with its linear trend removed. The continuous sequence is shown split into the period from mid-1996 to mid-2006 (upper row) and beginning 2006 to end-2015 (lower row). The 20-year ETS sequence is matched (red and green lines) by a single stable limit cycle (b) and the strain rate curve (black line) incorporates the long slow creep periods (path 1-2) as well as the slow earthquake events due to the fluid release during the reaction (path 2-3). Any perturbations are recovered bringing the system back to the same cycle, as reflected in the GPS data of (a). The perturbation of mid-2000 was recovered by the system in 2001 and the perturbation, which affected the system in 2008, was recovered in 2011. Note that in October 2003 the sequence was interrupted due to a jump of the GPS sensor. The numerical fit is shifted (green line) to account for this jump.

case, the existence of irregular ETS sequences can be attributed to non constant parameter values which forces the system to switch between different material oscillators. Such a case could be obtained if, for instance, the dimensionless groups are allowed to evolve in time (as shown in [PVRLY14]) or in space, accounting for the different geologies and ambient conditions intersected by the fault. A natural consequence of the temporal and spatial variation of the parameters is that the system would turn into a multi-period, multi-scale chaotic attractor and the subduction system will depart from its minimum dissipation limit and driven towards the maximum dissipation.

The Grunfest and the Lewis numbers are bearing the information of the loading conditions, and are therefore the parameters that can vary in time. Having already pointed out the role of the critical Grunfest number  $Gr_B$  as a global attractor of the oscillator, we assume here that its evolution is the most probable cause for the presence of alternating oscillatory modes in the system. Following the discussion in section ?? the time variation of the Grunfest and associated Lewis number can be affected by short term seismic stress perturbations in the vicinity of the subduction zone. As pointed out in the case of Cascadia, the fast time scale of the process is approximately 2 weeks. This means that a seismic event happens on an even faster time scale, which will provoke an almost instantaneous jump in the stress applied on the shear zone boundaries. The latter can be equated to step-like perturbations on the Grunfest number in the framework of the present chemical oscillator model.

From the fitting process of the GPS sequence in New Zealand (Fig. 8) it was deduced that the oscillators comprise two modes. The first mode (mode 1 in Fig. 8) is exactly identical to the one derived from the Cascadia fit. The second mode is shown as mode 2 in Fig. 8 and has a significantly larger temperature variation of around  $270^\circ\text{C}$ , from  $330^\circ\text{C}$  to approximately  $600^\circ\text{C}$ . During both cycles the fluid pressure rises from hydrostatic values (40% of the lithostatic) to about 60% of the lithostatic when the forward reaction is the dominant mechanism. A major outcome of this fitting process is that, similar to Cascadia, the width of the shear zone where all the mechanisms presented operate, is calculated around 6 metres wide. In addition, as suggested in [PVH<sup>+</sup>14], the common oscillator is a fundamental mode (or eigenmode in a mathematical context) of serpentinite deformation.

As far as material constants are concerned, these were considered to be the same for Cascadia and Hikurangi suggesting the common serpentinite nature of the lubricating shear zones. The only difference between the two cases is the emergence of a second oscillator in New Zealand that was attributed to an overstress transient of the order of 60kPa in shear [PVH<sup>+</sup>14]. This derivation suggests that the elastodynamic transients of the surrounding environment cannot be neglected in the Hikurangi trench. Since mode 2 displays the higher amplitude oscillations it is identified as the one closer to the global attractor (the homoclinic point) and mode 1 is interpreted as a higher Grunfest number mode.

This means that in Hikurangi the dynamics of the serpentinite oscillator between the two modes depicted in (Fig. 8) are driven by evolving (in time) boundary conditions. Unlike Cascadia, where constant stress boundary conditions could reproduce

20 years of ETS activity, in New Zealand the loading stress exhibits time variations thus not placing the subduction environment in the minimum dissipation limit. However, since the system is not admitting damped oscillations, Hikurangi it is also not driven at its maximum dissipation limit. It is therefore in an intermediate loading regime, oscillating continuously between 2 different modes and driving both the slow earthquake activity and the fast seismic events in the vicinity of Gisborne [?, see also] Poulet 2014a.

## 7 Discussion

In this contribution we link the observed double localization patterns in fault zones with a discussion on their possible driving energetics and timescales of formation. We have shown that the thick fault zone is a result of a solid mechanical instability, acting as a vessel for the ultralocalized instability. In the case of brittle failure negligible additional energy is required as the system behaves in a near temperature-independent, close to criticality regime. In the case of ductile failure the shear zone is not necessarily at criticality through time but the fluid-like creep motions raise the local dissipation to eventually trigger an energy transformation in an ultralocalized PSZ. Under the assumption of microstructural steady state of the shear zone the latter instability is periodic.

We have presented in Figure 6 a direct comparison of brittle and ductile/creep fractures in shear zones. In the brittle case it is known from field and laboratory observations that the PSZ represents an ultralocalised process zone, consisting of ultrafine particles that have usually undergone mechano-chemical degradation (gelification, decarbonation and dehydration reactions, melting, as thoroughly discussed in [THH<sup>+</sup>11]). Therefore, although the mechanism of the fault zone formation is the material bifurcation from homogenous deformation [MV87], the formation of PSZ's should be considered the effect of the chemical-mechanical deformation following the onset of the initial structure.

The ductile shear zone in Figure 6 features a chemical transition from host rock to hanging rock and a strong grain size reduction towards the PSZ [HHp<sup>+</sup>08]. The mechanism of localisation, although different from the brittle case, has the same style of energetic transition where microstructural changes are captured by their latent heat effects inside the PSZ. The main difference in terms of energetics is the time-scale of deformation, which we have shown to be governed by the energy equation and lastly the thermal activation.

In the brittle zone thermal activation is not considered important. However, a similar energetic transition may be taking place. The activation process can equally be triggered by a lowering of the critical threshold to near ambient condition through the access of fluids interacting with the host rock. It can be argued that in the brittle case the thermal time scale control is replaced by the mechanism of fluid transfer during

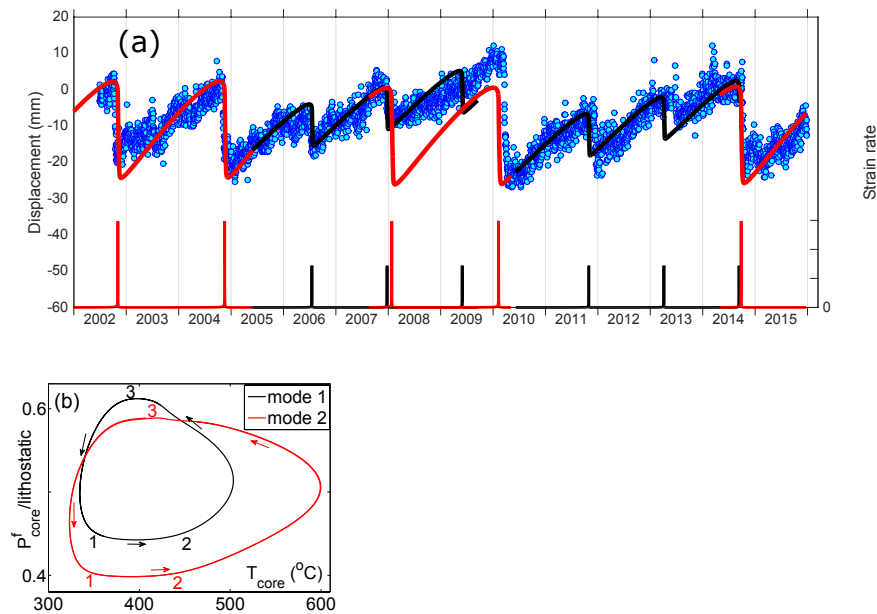


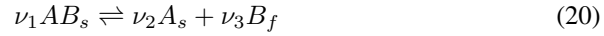
Figure 8: Irregular ETS sequence of Gisborne, New Zealand, station GISB [NAS]. (a) The GPS data (blue dots) represent raw displacement data with its linear trend removed. The signal is non-periodic and the suggested fit consists of 2 modes. The first mode (red line) has higher displacement and strain rates (shown at the bottom) per event and a period of 2 years, and the second one (black line) has a period of about 14 months. Figure until end of 2013 is as published in June 2014 [PVH<sup>+</sup>14]. (b) Limit cycles of the two modes identified. Note that this bi-modal chaotic oscillator is driven from the elastic surrounding, with the transition from mode 1 to mode 2 being the natural mode of the elastic loading. The reverse transition requires additional excitation that would relax the applied shear stress, e.g. from nearby seismic events in the vicinity of the system. Such an event was recorded at the end of 2007, causing the perturbation recorded by the GPS station, and shifting the sequence back to mode 1 of the oscillator.

fault slip. These mechanisms can be low temperature pressurisation effects [Sib73, Lac80, WS05, SJP05, Ric06] or high temperature chemical effects such as dehydration of minerals or decomposition of carbonates, theoretically studied recently [SF09, VAV10, BSCS10, BSS11] and reported to take place in real faults [Hea07, FNB<sup>+</sup>08] and experiments at laboratory conditions [HSH<sup>+</sup>07, FDHS10, BHS<sup>+</sup>11, PHM<sup>+</sup>11, CVTM13]. Additional mechanisms that include dry phase transitions such as breakage can be formulated in a similar thermodynamic framework [Ein07a, Ein07b, LBZ14b, LBZ14a]. Therefore the above described framework illustrates an energy based formulation for instabilities of solid matter with emergent length scales of localisation.

This fundamental outcome is illustrated in the present approach by two scales of localisation naturally emerging and corresponding to two different energy regimes. These are the traditional Solid Mechanical localization during failure leading to a finite width shear band that can be described by internal variables and the Fluid Dynamical post-failure localization related to a phase change that counterintuitively leads to ultra thin shear zones within the master Solid Mechanical containment. We identify these fundamental outcomes to be a plausible explanation for the two scale localization phenomena described in this work.

## A Poro-chemical model

At high temperatures the solid  $AB$  breaks down, producing excess  $B$  fluid, and increasing the fluid pore pressure through a general fluid-release reaction of the form:



We assume the following relations for the partial molar reaction rates for the species,

$$\begin{aligned} r_{AB} &= - \left[ \frac{\rho_{AB}}{M_{AB}} (1 - \phi)(1 - s) \right]^{\nu_1} k_F \exp(-Q_F/RT) \\ r_A &= \left[ \frac{\rho_A}{M_A} (1 - \phi)s \right]^{\nu_2} k_R \exp(-Q_R/RT) \\ r_B &= \left[ \Delta\phi_{chem} \frac{\rho_B}{M_B} \right]^{\nu_3} k_R \exp(-Q_R/RT) \end{aligned} \quad (21)$$

From the stoichiometry of the considered reaction, Eq.(20), it should hold that:

$$-\frac{r_{AB}}{\nu_1} = \frac{r_A}{\nu_2} = \frac{r_B}{\nu_3}. \quad (22)$$

From Eqs. (21-22), and for  $\nu_1 = \nu_2 = \nu_3 = 1$  we derive the poro-chemical model

$$\Delta\phi_{chem} = A_\phi \frac{1 - \phi_0}{1 + \frac{\rho_B}{\rho_A} \frac{M_A}{M_B} \frac{1}{s}}, \quad (23)$$

$$s = \frac{\omega_{rel}}{1 + \omega_{rel}}, \text{ and}$$

$$r_{rel} = \frac{\rho_{AB}}{\rho_A} \frac{M_A}{M_{AB}} K_c \exp\left(\frac{\Delta h}{RT}\right).$$

In Eqs. (23),  $K_c = k_F/k_R$  is the ratio of the pre-exponential factors of the Arrhenius reaction rates and  $\Delta h = Q_R - Q_F$  the difference of the forward and reverse activation energies. The parameter  $A_\phi$  is a coefficient that determines the amount of the interconnected pore-volume (porosity) created due to the reaction. We assume that all the fluid generated contributes to the interconnected pore volume, and thus set  $A_\phi = 1$ .

Following these considerations, the rates of the forward ( $\omega_F$ ) and reverse ( $\omega_R$ ) first order reactions can be calculated to be

$$r_F = r_{AB} = \frac{\rho_{AB}}{M_{AB}} (1 - \phi)(1 - s) k_F e^{-Q_F/RT} \quad (24)$$

$$r_R = r_A r_B = \frac{\rho_A \rho_B}{M_A M_B} (1 - \phi) s \Delta\phi_{chem} k_R e^{-Q_R/RT}. \quad (25)$$

Note that, for simplicity we have assumed in Eqs. (21) that the two products are produced with the same pre-exponential factor and activation energies. If this is not the case the above model should be modified accordingly. The net reaction rate would then be  $r = r_F - r_R \frac{M_{AB}}{\rho_{AB}}$  (the reverse reaction rate was normalized with the reference concentration  $\frac{\rho_{AB}}{M_{AB}}$  for dimensional purposes), which however would be essentially irreversible ( $r_F \gg r_R$ ) in the case  $K_c = k_F/k_R \gg 1$ .

## References

- [ABZ12] A. A. Allam and Y. Ben-Zion. Seismic velocity structures in the southern california plate-boundary environment from double-difference tomography. *Geophys. J. Int.*, (190):1181–1196, 2012.
- [APV14] S. Alevizos, T. Poulet, and E. Veveakis. Thermo-poro-mechanics of chemically active creeping faults. 1: Theory and steady state considerations. *Journal of Geophysical Research: Solid Earth*, 119(6):4558–4582, 2014.
- [BE08] F.V. De Blasio and A. Elverhøi. A model for frictional melt production beneath large rock avalanches. *J. Geophys. Res.*, 113:F02014, 2008.
- [BHS<sup>+</sup>11] N. Brantut, R. Han, T. Shimamoto, N. Findling, and A. Schubnel. Fast slip with inhibited temperature rise due to mineral dehydration: Evidence from experiments on gypsum. *Geology*, 39(1):59–62, 2011.

- [BSCS10] N. Brantut, A. Schubnel, J. Corvisier, and J. Sarout. Thermochemical pressurization of faults during coseismic slip. *J. Geophys Res.*, 115:B05314, 2010.
- [BSS11] N. Brantut, J. Sulem, and J. Schubnel. Effect of dehydration reactions on earthquake nucleation: Stable sliding, slow transients and unstable slip. *J. Geophys Res.*, 116:B05304, 2011.
- [BZS03] Y. Ben-Zion and C. G. Sammis. Characterization of fault zones. *Pure Appl. Geophys.*, (160):677–715, 2003.
- [CB92] A. Chrysochoos and F. Belmahjoub. Thermographic analysis of thermomechanical couplings. *Archives Mechanics*, 44(1):55–68, 1992.
- [CC98] F. Chester and J. Chester. Ultracataclasite structure and friction processes of the punchbowl fault, san andreas system, california. *Tectonophysics*, pages 199–221, 1998.
- [CDMB04] F. Cornet, M. Doan, I. Moretti, and G. Borm. Drilling through the active aigion fault: the aig10 well observatory. *Comptes Rendus Geosciences*, 336(4-5):395–406, 2004.
- [CEB93] Frederick M. Chester, James P. Evans, and Ronald L. Biegel. Internal structure and weakening mechanisms of the san andreas fault. *Journal of Geophysical Research: Solid Earth*, 98(B1):771–786, 1993.
- [CVTM13] C. Colletini, C. Viti, T. Tesei, and S. Mollo. Thermal decomposition along natural carbonate faults during earthquakes. *Geology*, page doi:10.1130/G34421.1, 2013.
- [CZV11] Francesco Cecinato, Antonis Zervos, and Emmanuil Veveakis. A thermo-mechanical model for the catastrophic collapse of large landslides. *International Journal for Numerical and Analytical Methods in Geomechanics*, 35(14):1507–1535, 2011.
- [Ein07a] I. Einav. Breakage mechanics—part i: Theory. *Journal of the Mechanics and Physics of Solids*, 55(6):1274 – 1297, 2007.
- [Ein07b] I. Einav. Breakage mechanics—part ii: Modelling granular materials. *Journal of the Mechanics and Physics of Solids*, 55(6):1298 – 1320, 2007.
- [FDHS10] F. Ferri, G. DiToro, T. Hirose, and T. Shimamoto. Evidence of thermal pressurization in high-velocity friction experiments on smectite-rich gouges. *Terra Nova*, 22(5):347–353, 2010.
- [FLR03] D. R. Faulkner, A. C. Lewis, and E. H. Rutter. On the internal structure and mechanics of large strike-slip fault zones: field observations of the carboneras fault in southeastern spain. *Tectonophysics*, (367):235–251, 2003.

- [FNB<sup>+</sup>08] V. Famin, S. Nakashima, A-M. Boullier, K. Fujimoto, and T. Hirono. Earthquakes produce carbon dioxide in crustal faults. *Earth. Plan. Sci. Lett.*, 265:487–497, 2008.
- [Fow97] A.C. Fowler, editor. *Mathematical Models in the Applied Sciences*. Cambridge University Press, 2 edition, 1997.
- [Fuj69] C. Fujita. On the non-linear equations  $du + e^u = 0$  and  $v_t = dv + e^v$ . *Bull. Am. Math. Soc.*, 75.:132 – 135., 1969.
- [GAA10] L. Goren, E. Aharonov, and M. H. Anders. The long runout of the heart mountain landslide: Heating, pressurization, and carbonate decomposition. *Journal of Geophysical Research: Solid Earth*, 115(B10):n/a–n/a, 2010.
- [Hea07] T. Hirono and et al. A chemical kinetic approach to estimate dynamic shear stress during the 1999 taiwan chi-chi earthquake. *Geophys. Res. Lett.*, 34:L19308, 2007.
- [HHp<sup>+</sup>08] M. Herwegh, J. Hurzeler, O. pfiffner, S. Schmid, R. Abart, and A. Ebert. The glarus thrust: excursion guide and report of a field trip of the swiss tectonic studies groups. *Swiss Journal of Geosciences*, 101(2):323–340, 2008.
- [Hil62] R. Hill. Acceleration waves in solids. *J. Mech. Phys. Solids*, 10:1–16, 1962.
- [HSH<sup>+</sup>07] R. Han, T. Shimamoto, T. Hirose, J.H. Ree, and J. Ando. Ultralow friction of carbonate faults caused by thermal decomposition. *Science*, 316:878–881, 2007.
- [HvDS<sup>+</sup>11] R.E. Holdsworth, E.W.E. van Diggelen, C.J. Spiers, J.H.P. de Bresser, R.J. Walker, and L. Bowen. Fault rocks from the {SAFOD} core samples: Implications for weakening at shallow depths along the san andreas fault, california. *Journal of Structural Geology*, 33(2):132 – 144, 2011.
- [KL97] L. Kennedy and J. Logan. The role of veining and dissolution in the evolution of fine -grained ylonites: the mcconnell thrust, alberta. *J. Struct. Geology*, 19(6):785–797, 1997.
- [LA07] Goren L. and E. Aharonov. Long runout landslides: The role of frictional heating and hydraulic diffusivity. *Geophys. Res. Lett.*, 34:L07301, 2007.
- [Lac80] A. Lachenbruch. Frictional heating, fluid pressure and the resistance to fault motion. *J. Geophys. Res.*, 85:6097–6112, 1980.
- [LBZ14a] V. Lyakhovsky and Y. Ben-Zion. A continuum damage-breakage faulting model accounting for solid-granular transitions. *Pure Appl. Geophys.*, page Submitted, 2014.

- [LBZ14b] V. Lyakhovsky and Y. Ben-Zion. Damage-breakage rheology model and solid-granular transition near brittle instability. *J. Mech. Phys. Solids*, (64):184–197, 2014.
- [Man66] J. Mandel. Conditions de stabilite et postulate de drucker. *Rheology and Soil Mechanics*, pages 58–67, 1966.
- [MV87] H. Muhlhaus and I. Vardoulakis. Thickness of shear bands in granular materials. *Geotechnique*, 37(3):271–283, 1987.
- [NAS] NASA. jet propulsion laboratory, caltech: <http://sideshow.jpl.nasa.gov/post/series.html>.
- [NS05] H. Noda and T. Shimamoto. Thermal pressurization and slip-weakening distance of a fault: An example of the hanaore fault, southwest japan. *Bull. Seism. Soc. Am.*, 95(4), 2005.
- [Per66] P. Perzyna. Fundamental problems in viscoplasticity. *Adv. Appl. Mech.*, 9:243–377, 1966.
- [PHM<sup>+</sup>11] N. De Paola, T. Hirose, T. Mitchell, G. Di Toro, T. Togo, and T. Shimamoto. Fault lubrication and earthquake propagation in thermally unstable rocks. *Geology*, 39(1):35–38, 2011.
- [PV11] S. Papanicolopoulos and E. Veveakis. Sliding and rolling dissipation in cosserat plasticity. *Granular Matter*, 13(3):197–204, 2011.
- [PVH<sup>+</sup>14] Thomas Poulet, Manolis Veveakis, Marco Herwegh, Thomas Buckingham, and Klaus Regenauer-Lieb. Modeling episodic fluid-release events in the ductile carbonates of the glarus thrust. *Geophysical Research Letters*, 41(20):7121–7128, 2014.
- [PVRLY14] T. Poulet, E. Veveakis, K. Regenauer-Lieb, and D. A. Yuen. Thermo-poro-mechanics of chemically active creeping faults: 3. the role of serpentinite in episodic tremor and slip sequences, and transition to chaos. *Journal of Geophysical Research: Solid Earth*, 119(6):4606–4625, 2014.
- [Rei64] M Reiner. The deborah number. *Physics Today*, pages 152–153, 1964.
- [RFMM12] C. Rowe, A. Fagereng, J. Miller, and B. Mapani. Signature of coseismic decarbonation in dolomitic fault rocks of the naukluft thrust, namibia. *Earth Plan. Sci. Let.*, 333-334:200–210, 2012.
- [Ric06] J. R. Rice. Heating and weakening of faults during earthquake slip. *J. Geophys. Res.*, 111:B05311, 2006.
- [RJ75] Rice JR. Rudnicki JW. Conditions for the localization of deformation in pressure sensitive dilatant materials. *J. Mech. Phys. Solids*, 23:371–394, 1975.

- [RLVP<sup>+</sup>13a] K. Regenauer-Lieb, M. Veveakis, T. Poulet, F. Wellmann, A. Karrech, J. Liu, J. Hauser, C. Schrank, O. Gaede, and M. Trefry. Multiscale coupling and multiphysics approaches in earth sciences: Applications. *Journal of Coupled Systems and Multiscale Dynamics*, 1(3):doi:10.1166/jcsmd.2013.1021, 2013.
- [RLVP<sup>+</sup>13b] K. Regenauer-Lieb, M. Veveakis, T. Poulet, F. Wellmann, A. Karrech, J. Liu, J. Hauser, C. Schrank, O. Gaede, and M. Trefry. Multiscale coupling and multiphysics approaches in earth sciences: Theory. *Journal of Coupled Systems and Multiscale Dynamics*, 1(1):49–73, 2013.
- [RLYF09] K. Regenauer-Lieb, D. Yuen, and F. Fousseis. Landslides, ice quakes, earthquakes: A thermodynamic approach to surface instabilities. *Pure. Appl. Geophys.*, 166(10-11):1885–1908, 2009.
- [RRRH00] P. Rosakis, A.J. Rosakis, G. Ravichandran, and J. Hodowany. A thermodynamic internal variable model for the partition of plastic work into heat and stored energy in metals. *J. Mech. Phys. Solids*, 48:581–607, 2000.
- [SF09] J. Sulem and V. Famin. Thermal decomposition of carbonates in fault zones: slip-weakening and temperature-limiting effects. *J. Geophys. Res.*, 114:B03309, 2009.
- [Sib73] R. Sibson. Interaction between temperature and pore-fluid pressure during earthquake faulting – a mechanism for partial or total stress relief. *Nature*, 243:66–68, 1973.
- [Sib03] R. Sibson. Thickness of the seismic slip zone. *Bull. Seism. Soc. Am.*, 93:1169–1178, 2003.
- [SJP05] Ouffroukh H. Sulem J., Vardoulakis I. and V. Perdikatsis. Thermo-poro-mechanical properties of the aigion fault clayey gouge - application to the analysis of shear heating and fluid pressurization. *Soils and Foundations*, 45:97–108, 2005.
- [SLV07] J. Sulem, P. Lazar, and I. Vardoulakis. Thermo-poro-mechanical properties of clayey gouge and application to rapid fault shearing. *Int. J. Num. Anal. Meth. Geomechanics*, 31(3):523–540., 2007.
- [SS14] Ioannis Stefanou and Jean Sulem. Chemically induced compaction bands: Triggering conditions and band thickness. *Journal of Geophysical Research: Solid Earth*, 119(2):880–899, 2014.
- [SSV11] J. Sulem, I. Stefanou, and E. Veveakis. Stability analysis of undrained adiabatic shearing of a rock layer with cosserat microstructure. *Granular Matter*, 13(3):261–268, 2011.
- [TA45] AV Tobolsky and RD Andrews. Systems manifesting superposed elastic and viscous behaviour. *J.Chem. Phys.*, 13(1):3–27, 1945.

- [THH<sup>+</sup>11] G. Di Toro, R. Han, T. Hirose, N. DePaola, S. Nielsen, K. Mizoguchi, F. Ferri, M. Cocco, and T. Shimamoto. Fault lubrication during earthquakes. *Nature*, 471:494–498, 2011.
- [Tow09] John Townend. Drilling, sampling, and monitoring the alpine fault: Deep fault drilling project—alpine fault, new zealand; franz josef, new zealand, 22–28 march 2009. *Eos, Transactions American Geophysical Union*, 90(36):312–312, 2009.
- [TQ34] G. Taylor and H. Quinney. The latent energy remaining in a metal after cold working. *Proc. R. Soc., Ser. A.*, 143:307 – 326., 1934.
- [Var2a] I. Vardoulakis. Dynamic thermo-poro-mechanical analysis of catastrophic landslides. *Geotechnique*, 52:157–171, 2002a.
- [VAV10] E. Veveakis, S. Alevizos, and I. Vardoulakis. Chemical reaction capping of thermal instabilities during shear of frictional faults. *J. Mech. Phys. Solids*, 58:1175 – 1194, 2010.
- [VPA14] E. Veveakis, T. Poulet, and S. Alevizos. Thermo-poro-mechanics of chemically active creeping faults: 2. transient considerations. *Journal of Geophysical Research: Solid Earth*, 119(6):4583–4605, 2014.
- [VRL14] E. Veveakis and K. Regenauer-Lieb. The fluid dynamics of solid mechanical shear zones. *Pure Appl. Geophys.*, 171:3159–3174, 2014.
- [VRL15] E Veveakis and Regenauer-Lieb. Cnoidal waves in solids. *Journal of Mechanics and Physics of Solids*, 78:231–248, 2015.
- [VRLW14] E. Veveakis, K. Regenauer-Lieb, and R.F. Weinberg. Ductile compaction of partially molten rocks: the effect of non-linear viscous rheology on instability and segregation. *Geophysical Journal International*, 200(1):519–523, 2014.
- [VS95] I. Vardoulakis and J. Sulem, editors. *Bifurcation Analysis in Geomechanics*. Blackie Acc. and Professional, 1995.
- [VSS12] E. Veveakis, J. Sulem, and I. Stefanou. Modeling of fault gouges with cosserat continuum mechanics: Influence of thermal pressurization and chemical decomposition as coseismic weakening mechanisms. *J. Struct. Geology*, 38:254–264, 2012.
- [VSS13] E. Veveakis, I. Stefanou, and J. Sulem. Failure in shear bands for granular materials: thermo-hydro-chemo-mechanical effects. *Geotechnique Let.*, 3(2):31–36, 2013.
- [VVD07] E. Veveakis, I. Vardoulakis, and G. DiToro. Thermoporomechanics of creeping landslides: The 1963 vaiont slide, northern italy. *J. Geophys. Res.*, 112:F03026, 2007.

- [WS03] C. A. J. Wibberley and T. Shimamoto. Internal structure and permeability of major strike-slip fault zones: The median tectonic line in mid prefecture, southwest japan. *J. Struct. Geol.*, 25:59–78, 2003.
- [WS05] C. Wibberley and T. Shimamoto. Earthquake slip weakening and asperities explained by thermal pressurization. *Nature*, 426(4):689–692, 2005.
- [YS77] D. Yuen and G. Schubert. Asthenospheric shear flow: thermally stable or unstable? *Geophys. Res. Lett.*, 4(11):503–506, 1977.

---

# Numerical modelling of Multiphysics couplings and strain localization

**F. Collin<sup>1</sup>, P. Kotronis<sup>2</sup>, B. Pardoën<sup>3</sup>**

<sup>1</sup>*Department ArGEnCo, University of Liège, Belgium ;*

<sup>2</sup>*GeM (Institut de Recherche en Génie Civil et Mécanique), Ecole Centrale de Nantes, France ;*

<sup>3</sup>*Department of Civil Engineering, Laval University, Canada.*

---

*Rupture in geomaterials is often preceded by a localization of the deformations within thin bands. The strain localization is therefore an important process, which has been studied both experimentally and theoretically. This paper summarizes the main observations on localized phenomena and proposes numerical tools to characterize localization processes. To deal with interactions occurring between the different phases of porous media, a regularization technique based on the second gradient model has been extended to multiphysic couplings.*

## 1 Introduction

Since the material behaviour and rupture are of importance regarding the design of geotechnical works for which the materials can be subjected to strong solicitations, failure has been widely investigated in geomechanics. Experimental observations on geomaterials clearly indicate the appearance of localised ruptures [Des84]. Theoretically, the concept of rupture surface is one of the oldest case of material localised failure and was already used in the design of works and structures few centuries ago [Cou73]. In some cases, a diffuse mode of failure can also be observed and it corresponds to homogeneous failure in laboratory tests [KGDL06]. Nowadays, it is commonly assumed that localised deformation and damage can appear in materials prior to the rupture in many situations. In rock material, a stress redistribution can engender damage that can firstly be diffused then localised. Once the damage threshold is reached, microcracks initiate, then grow, accumulate, and propagate within the material. If the microcracks coalesce, the distributed damage can further lead to strain

localisation and to the initiation of interconnected fractures by the onset of macrocracks, which provokes a sudden material rupture [Die03].

The fracturing process instigates discontinuities in the material that can be represented theoretically and numerically by various approaches. Two main categories exist: the continuous and discrete descriptions of fracture. The continuous description includes material damage and strain localisation, while the discrete description explicitly represents cracks. In fracture mechanics, the different fractures can be in tensile or opening mode (mode I), in sliding shear mode (mode II), in tearing shear mode (mode III), or in mixed-mode (mode I-II, [JS88]). The modelling of shear strain localisation is a continuous approach that does not explicitly reproduce fractures and their discontinuities. Nevertheless, it generally induces the appearance of shear bands and a non-uniform strain distribution that may engender a displacement discontinuity between the material located on the two sides of a shear band.

Furthermore, soils and rocks are porous materials, where the porous volume is filled with one or several fluids (water, gas, oil ...). The general behaviour of the medium depends not only on the skeleton response (solid phase) to a given loading path, but also on the interactions occurring between the different phases of the medium. Capillary effects, temperature variations, chemical reactions induce specific behaviours, which have to be modelled by multiphysical constitutive laws. The numerical tools for modelling strain localization problems have thus to be extended to this multiphysics context, to deal with applications related, for instance, to nuclear waste disposal and concrete behaviour under severe loading. Then, new questions arise concerning the interactions between localization process and physical process (like liquid diffusion for example). The answer to these new questions can only be given by experimental evidences. The section 2 of this paper summarizes the main observations on the localization phenomenon, coming from experimental results. Section 3 describes the regularization methods used to model properly the strain localization process. Section 4 is the description of the coupled second gradient model in saturated conditions. A biaxial compression test is modelled in order to show the ability of the second gradient model to represent correctly the post-peak behaviour. In section 5, the second gradient model is extended to unsaturated conditions. The example of a gallery excavation is proposed in section 6 to evidence the influence of hydro-mechanical couplings in saturated and unsaturated conditions on the strain localization process. Some conclusions end up the paper in section 7.

## 2 Experimental evidences of strain localisation

Strain localisation is frequently observed prior to material rupture. Starting from a homogeneous deformation state, strain localisation consists in a brutal accumulation of strain in a limited zone that can lead to cracks and failure (rupture lines). In geomaterials like soils and rocks it is often considered as a shear strain accumulation in band mode [Des05]. Nevertheless, the type of localisation may be of different nature

for other materials.

Geomaterials have low tensile strength, thus tensile rupture is arduous to characterise. On the other hand, plenty of small-scale compression laboratory tests are dedicated to strain localisation [VGG78, HD93, FHMV96, FHMV97, ABS03] and allow to characterise the compression material behaviour up to the rupture. They are generally realised on axisymmetric triaxial or plane-strain biaxial compression apparatus and involve special techniques, such as stereophotogrammetry [Des84, DV04], X-ray microtomography, and three dimensional digital image correlation [LBD<sup>+</sup>07], to study the evolution of the strain localisation process. The advantage of biaxial compression experiments is that the localisation process is clearly evidenced, whereas it can remain hidden inside the sample in triaxial compression tests.

Under compressive regime, rupture is governed essentially by shear failure and these experimental studies generally highlight shear strain localisation in band mode [Des05]. It is commonly accepted that the shear band establishment corresponds to a peak stress in the stress-strain global response curve of the specimen [MD99, Des05].

The experimental localisation studies mostly analyse the behaviour of sand and only a few are actually available on rocks [BDR00]. Analysing the formation of fractures and strain localisation bands in rocks is quite challenging due to their high resistance and brittle behaviour (quasi-brittle material), thence the development of appropriate apparatus designed to test this type of material is necessary [DV04].

### 3 Regularisation methods

The further step is to define an appropriate and robust method that allows to properly model strain localisation and shear banding with the finite element method, leading finally to rupture in localised mode. Local descriptions of failure with classical finite element methods are not efficient in the reproduction of strain localisation because they suffer a mesh dependency (to mesh size and orientation) as indicated by [PM81], [ZPV01b], [CLC09], and [WW10]. This pathological problem is due to the properties of the underlying mathematical problem.

The dependence to the finite element discretisation can be solved by employing a proper regularisation technique. Such method has to introduce an internal length scale in the problem to model correctly the post-localisation behaviour. Two principal categories of enhanced models exist: one consists in the enrichment of the constitutive law with for instance non-local [BBC84, PCB87, PdBB<sup>+</sup>96, GSH12] or gradient plasticity [Aif84, dBM92, PdBBdV96], the other approaches in the enrichment of the continuum kinematics with microstructure effects. For this second category the microkinematics are characterised at microscale in addition to the classical macrokinematics [CC09, Tou62, Min64, Ger73]. However, enhanced models restore mesh objectivity but not the uniqueness of the solution.

### 3.1 Enrichment of the constitutive law

In this approach, an internal length scale is introduced at the level of the constitutive model. Advanced analyses of localisation phenomena have indicated that constitutive equations with internal length are one solution to model strain localised pattern properly.

The internal length scale is introduced by developing non-local definition of internal variables involved in the material behaviour. The non-local variable  $\hat{v}$  at a material point  $x_i$  can be defined as an averaging value of the local variable  $v$  in a considered region  $\Omega$  near that point [PCB87, PGdBB01], as illustrated in Fig. 1.

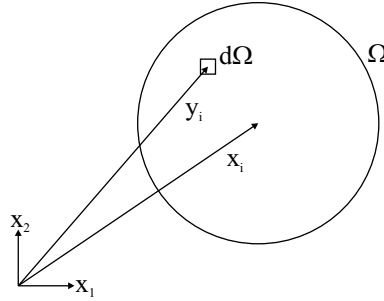


Figure 1: Non-local approach on a representative material volume.

The non-local integral method gives:

$$\hat{v}(x_i) = \frac{1}{V} \int_{\Omega} \Psi v(y_i) d\Omega \quad (1)$$

$$V = \int_{\Omega} \Psi d\Omega \quad (2)$$

where  $x_i$  is the coordinate vector of the material point where the non-local variable is considered,  $\Omega$  is a representative volume centred in  $x_i$ ,  $y_i$  is the coordinate vector of the infinitesimal volume  $d\Omega$ , and  $\Psi$  is a weight function scaling  $\hat{v}$  to  $\hat{v} = v$  for a homogeneous distribution of the variable. It is generally defined with a Gaussian distribution:

$$\Psi = \frac{1}{(2\pi)^{3/2} l_c^3} \exp\left(-\frac{\|x_i - y_i\|^2}{2 l_c^2}\right) \quad (3)$$

which depends on the distance  $\|x_i - y_i\|$  and on a characteristic length parameter  $l_c$ . This length parameter, or internal length scale, defines the material volume that significantly contributes to the non-local variable and is consequently related to the microstructure.

The regularised variable can also be defined explicitly from the local variable  $v(x_i)$  and its gradient. In his pioneering works, [Aif84] introduced such gradient in the constitutive equations. The explicit gradient formulation is:

$$\hat{v} = v + \bar{l} \frac{\partial^2 v}{\partial x_i \partial x_i} \quad (4)$$

where the dependence of  $v$  and  $\hat{v}$  on the coordinate vector  $x_i$  is dropped for simplicity and  $\bar{l}$  has the dimension of length squared so  $\sqrt{\bar{l}}$  can be related to the internal length scale  $l_c$  introduced to regularise the model. Because the gradient term is a local quantity, the spatial interaction of the material points located in the vicinity of  $\hat{v}$  is infinitesimal and the explicit gradient model is therefore local. This is a main difference with the non-local integral formulation of Eq. 1 where the interaction distance is finite and related to the weight function. Moreover, the explicit gradient formulation can be derived from the non-local integral formulation by introducing the gradient of the internal variable, expanding the local variable  $v(y_i)$  into a Taylor series [BBC84, LB88, PdBBdV96], using the weight function definition of Eq. 3, and neglecting the terms above the second order (approximation).

The definition of Eq. 4 is less suitable in the context of numerical analyses, such as the finite element method, because of the explicit dependence of  $\hat{v}$  with its local (second) gradient. This dependence leads to a continuity requirement for the internal variable which has to be a continuously differentiable function (class  $C^1$  function whose derivative is continuous). To avoid this drawback, an alternative implicit gradient formulation, introducing an approximation of Eq. 1 similar to Eq. 4, can be expressed as follows [PdBBdV96, PGdBB01]:

$$\hat{v} - \bar{l} \frac{\partial^2 \hat{v}}{\partial x_i \partial x_i} = v \quad (5)$$

and enables a continuous definition of  $v$  (class  $C^0$  function). For the implicit gradient model, the non-local internal variable is an additional unknown which is solution of the Helmholtz differential equation 5. Solution of this equation can only be found provided that additional boundary condition on  $\hat{v}$  is specified. The following condition is usually assumed [LB88]:

$$\frac{\partial \hat{v}}{\partial x_i} n_i = 0 \quad (6)$$

where  $n_i$  is the normal unit vector to the external boundary. This condition enables  $\hat{v} = v$  for homogeneous distribution. In contrast to the explicit formulation, the non-local variable  $\hat{v}$  is implicitly given as the solution of Eqs. 5 and 6, and the spatial interaction has a finite distance that implies a non-local character. The solution is of the same form of the non-local equation 1 with  $\Psi = Gr$  and  $V = 1$ ,  $Gr$  being the Green's function [Zau89]:

$$\hat{v}(x_i) = \int_{\Omega} Gr v(y_i) d\Omega \quad (7)$$

$$Gr = \frac{1}{4\pi \bar{l} \|x_i - y_i\|} \exp\left(-\frac{\|x_i - y_i\|}{\sqrt{\bar{l}}}\right) \quad (8)$$

The implicit gradient model is therefore a special case of the non-local model.

Non-local quantities as well as gradient of internal variables can finally be introduced in constitutive models. Among other authors, Bazant, Pijaudier-Cabot, and co-workers [BBC84, PCB87] proposed a family of constitutive models derived from the non-local damage theory in which a non-local internal variable is used instead of the local one. For instance, a non-local damage energy release rate obtained by Eq. 1 is introduced in the damage loading function. Other variables such as non-local equivalent strain are usually used in damage model [PGdBB01].

### 3.2 Enrichment of the kinematics

The previous approaches (enrichment of the constitutive law) introduce the effect of microstructure with non-local or gradient terms but the microstructure itself is not explicitly defined. To this end, the classical kinematics of a continuous medium can be enriched with additional description of the microstructure kinematics, leading to a microstructure continuum medium also called enriched medium.

For a classical continuous medium, a material particle of volume  $\Omega$  is defined at macroscopic scale by its (macro) displacement field  $u_i$ . The classical kinematic fields are the macro-deformation field:

$$F_{ij} = \frac{\partial u_i}{\partial x_j} \quad (9)$$

corresponding to the gradient of the displacement field, the macro-strain field:

$$\varepsilon_{ij} = \frac{1}{2} (F_{ij} + F_{ji}) \quad (10)$$

corresponding to the symmetric part of  $F_{ij}$ , and the macro-rotation field:

$$r_{ij} = \frac{1}{2} (F_{ij} - F_{ji}) \quad (11)$$

corresponding to the antisymmetric part of  $F_{ij}$ . Their rate forms are also commonly used; the velocity gradient field:

$$L_{ij} = \frac{\partial \dot{u}_i}{\partial x_j} \quad (12)$$

the strain rate field:

$$\dot{\varepsilon}_{ij} = \frac{1}{2} (L_{ij} + L_{ji}) \quad (13)$$

and the spin rate field:

$$\dot{\omega}_{ij} = \frac{1}{2} (L_{ij} - L_{ji}) \quad (14)$$

The first and most famous enhanced model was developed by the Cosserat brothers [CC09] who introduced local rotation degrees of freedom  $r_i^c$  in addition to the displacements of classical continua  $u_i$  (Fig. 2). The Cosserat (or micropolar) elastic continuum theory is mostly suitable for the kinematic description of granular materials. Accordingly, additional kinematic fields are introduced [VS95]. The deformation due to the particle rotation, also called micro-rotation (antisymmetric tensor) becomes:

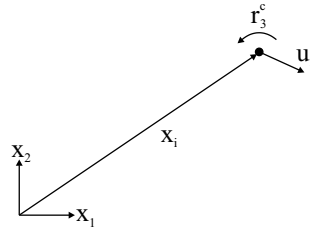


Figure 2: Kinematic degrees of freedom of the Cosserat elastic continuum theory.

$$r_{ij}^c = e_{ijk} r_k^c \quad (15)$$

where  $e_{ijk}$  is the alternating tensor, and the gradient of the particle rotation, also called curvature:

$$K_{ij}^c = \frac{\partial r_i^c}{\partial x_j} \quad (16)$$

A relative strain is deduced as the difference between macro-deformation and micro-rotation:

$$\bar{\epsilon}_{ij} = F_{ij} - r_{ij}^c \quad (17)$$

whose symmetric part coincides with the macro-strain  $\epsilon_{ij}$  and its antisymmetric part with the difference between the macro and micro-rotation  $r_{ij} - r_{ij}^c$ . The latter characterises the relative rotation of a material point with regard to the rotation of its neighbourhood. A couple stress (torques) tensor associated to the rotations is thus added introducing bending and torsion at the material point. This results in a moment equilibrium equation involving the couple stresses that comes in addition to the classical (local) momentum balance equation involving the stress field  $\sigma_{ij}$ . Moreover, supplementary elastic constants are considered in the constitutive equations which consist of internal length scale parameters related to the microstructure [VS95].

In the 1960's, [Tou62] and [Min64] defined materials with microstructure. A macro-volume  $\Omega$  is composed of smaller microscale particles that can be represented by a micro-volume  $\Omega^m$ , embedded in the material volume  $\Omega$  (Fig. 3). A micro-displacement field  $u_i^m$  is defined independently of the macro-displacement  $u_i$  and its gradient leads to a micro-deformation field:

$$v_{ij} = \frac{\partial u_i^m}{\partial x_j} \quad (18)$$

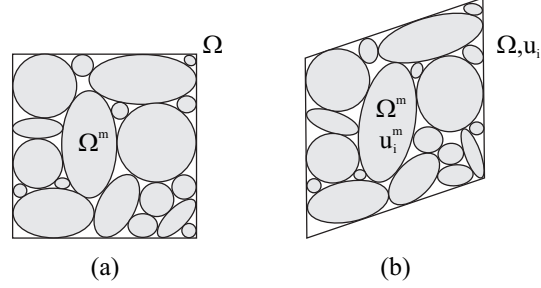


Figure 3: Kinematics of a microstructure continuum: (a) initial configuration and (b) configuration after external solicitation with relative displacement of the microstructure.

which is homogeneous in the micro-volume  $\Omega^m$  but non-homogeneous in the macro-volume  $\Omega$ .

The symmetric and antisymmetric parts of  $\mathbf{v}_{ij}$  correspond to the micro-strain and micro-rotation:

$$\boldsymbol{\varepsilon}_{ij}^m = \frac{1}{2} (\mathbf{v}_{ij} + \mathbf{v}_{ji}) \quad (19)$$

$$\mathbf{r}_{ij}^m = \frac{1}{2} (\mathbf{v}_{ij} - \mathbf{v}_{ji}) \quad (20)$$

with the micro-rotation corresponding to the rotation components of the Cosserat model  $r_{ij}^m = r_{ij}^c$  (Eq. 15). Cosserat model is in fact a particular case of a microstructure medium. Moreover, the micro second gradient is defined as:

$$h_{ijk} = \frac{\partial \mathbf{v}_{ij}}{\partial x_k} = \frac{\partial^2 \mathbf{u}_i^m}{\partial x_j \partial x_k} \quad (21)$$

The relative deformation of the microstructure is defined as the difference between the macro and the micro-deformation fields:

$$\bar{\boldsymbol{\varepsilon}}_{ij} = F_{ij} - \mathbf{v}_{ij} \quad (22)$$

whose symmetric part coincides with the difference between the macro and the micro-strain  $\boldsymbol{\varepsilon}_{ij} - \boldsymbol{\varepsilon}_{ij}^m$  and its antisymmetric part with the difference between the macro and micro-rotation  $r_{ij} - r_{ij}^m$ . Similar to the Cosserat's continuum description, additional stresses are introduced: the microstress, an additive stress field associated to the microstructure, and the double stress.

Later, [Ger73] introduced the virtual power principle to provide a global framework for the microstructure continuum formulation. This principle states that, by equilibrium, the virtual power of all forces acting on a mechanical system is null. In the following, materials with microstructure defined by [Min64] and [Ger73] will be considered.

A large panel of models are developed in the literature by adding mathematical constraints to microstructure media. Among them, the second gradient model developed in Grenoble [CCH98, CCM01] will be most particularly developed hereafter. Yet, the following conclusions can be generalised to other regularisation techniques.

#### 4 Coupled local second gradient model for microstructure saturated media

The coupled local second gradient model is developed for enriched continua including microstructure effects [CCM01]. This model was extended from monophasic to biphasic porous media (solid and fluid) by [CCC06] to highlight the possible interactions of the fluid (liquid water) with the strain localisation process and with the internal length introduced by the model. The developments proposed by [CCC06] are recalled in this section. They account for a medium with incompressible solid grains, under saturated and isothermal conditions. The solid and fluid phases are considered as immiscible and phase changes, like evaporation and dissolution, are therefore not taken into account.

As for a classical continuum, the material is considered as a porous medium and the balance equations are based on mixture theories. The unknowns of the coupled problem are the macro-displacement  $u_i$ , the micro-deformation field  $v_{ij}$  (or the micro-displacement field  $u_i^m$  by Eq. 18), and the pore water pressure  $p_w$ . An additional unknown field of Lagrange multipliers  $\lambda_{ij}$  will be added for the finite element method implementation.

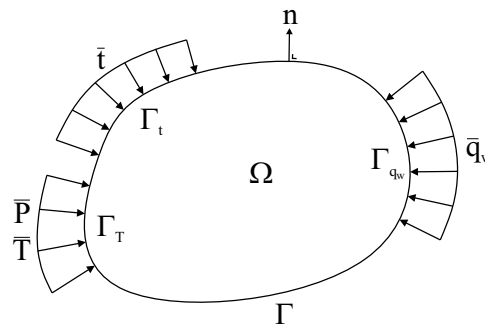


Figure 4: Material system with current configuration  $\Omega$  and boundary conditions for the second gradient model.

## 4.1 Balance equations for microstructure poromechanics

### 4.1.1 Local second gradient model for a monophasic medium

The class of virtual kinematics introduced in the virtual work principle for the classical kinematic theory can be extended in the framework of a microstructure continuum theory, by adding a description of the microstructure kinematics to the classical displacement field. According to Eq. 18, the kinematics at microscale are described by a microkinematic gradient field  $\mathbf{v}_{ij}$ . With respect to classical continuum mechanics, additional terms are added in the internal virtual work of a given body [Ger73]. The following expression holds for any virtual quantities:

$$W_{int}^* = \int_{\Omega} (\sigma_{ij} F_{ij}^* - \tau_{ij} \bar{\epsilon}_{ij}^* + \Sigma_{ijk} h_{ijk}^*) d\Omega \quad (23)$$

where  $\bar{\epsilon}_{ij}^*$  is the virtual relative deformation of the microstructure:

$$\bar{\epsilon}_{ij}^* = F_{ij}^* - \mathbf{v}_{ij}^* \quad (24)$$

$\tau_{ij}$  is an additional stress associated to the microstructure also called the microstress,  $h_{ijk}^* = \frac{\partial \mathbf{v}_{ij}^*}{\partial x_k}$  is the virtual micro second gradient, and  $\Sigma_{ijk}$  is the double stress dual of  $h_{ijk}^*$ , which needs an additional constitutive law introducing the internal length scale. The external virtual work can be defined as follows:

$$W_{ext}^* = \int_{\Omega} \rho g_i u_i^* d\Omega + \int_{\Gamma_{\sigma}} (\bar{t}_i u_i^* + \bar{P}_{ij} \mathbf{v}_{ij}^*) d\Gamma \quad (25)$$

where  $\bar{P}_{ij}$  is an additional external double surface traction acting on a part  $\Gamma_T$  of the boundary  $\Gamma$  (Fig. 4) and  $\Gamma_{\sigma} = \{\Gamma_I \cup \Gamma_T\}$  regroups the classical and additional external solicitations. The virtual work principle assumes the equality between internal and external virtual works and leads to the weak form of the momentum balance equation:

$$\int_{\Omega} (\sigma_{ij} F_{ij}^* - \tau_{ij} (F_{ij}^* - \mathbf{v}_{ij}^*) + \Sigma_{ijk} h_{ijk}^*) d\Omega = \int_{\Omega} \rho g_i u_i^* d\Omega + \int_{\Gamma_{\sigma}} (\bar{t}_i u_i^* + \bar{P}_{ij} \mathbf{v}_{ij}^*) d\Gamma \quad (26)$$

The local equilibrium equations are formulated for the macro and the micro quantities; the local momentum balance equations are:

$$\frac{\partial (\sigma_{ij} - \tau_{ij})}{\partial x_j} + \rho g_i = 0 \quad (27)$$

$$\frac{\partial \Sigma_{ijk}}{\partial x_k} - \tau_{ij} = 0 \quad (28)$$

and the boundary conditions are:

$$\bar{t}_i = (\sigma_{ij} - \tau_{ij}) n_j \quad (29)$$

$$\bar{P}_{ij} = \Sigma_{ijk} n_k \quad (30)$$

The boundary conditions for the mixture are also enriched with microstructure effects which leads to non-classical boundary conditions.

In the specific case of local second gradient model used in the following, a kinematic constraint is added in order to obtain a local second gradient continuum medium. No relative deformation of the microstructure is assumed  $\bar{\epsilon}_{ij} = 0$ , meaning that the microkinematic gradient is equal to the macro-deformation:

$$v_{ij} = F_{ij} \quad (31)$$

As a consequence:

$$v_{ij}^* = F_{ij}^* \quad (32)$$

for the virtual fields. Therefore, the principle of virtual work can be rewritten as follows:

$$\int_{\Omega} \left( \sigma_{ij} \frac{\partial u_i^*}{\partial x_j} + \Sigma_{ijk} \frac{\partial^2 u_i^*}{\partial x_j \partial x_k} \right) d\Omega = \int_{\Omega} \rho g_i u_i^* d\Omega + \int_{\Gamma_{\sigma}} (\bar{t}_i u_i^* + \bar{T}_i Du_i^*) d\Gamma \quad (33)$$

where  $\bar{T}_i$  is the additional external double force per unit area on  $\Gamma_T$  (Fig. 4) and the notation  $Da$  denotes the normal derivative of any quantity  $a$ :

$$Da = \frac{\partial a}{\partial x_i} n_i \quad (34)$$

with:

$$Du_i^* = \frac{\partial u_i^*}{\partial x_j} n_j = F_{ij}^* n_j = v_{ij}^* n_j \quad (35)$$

The local momentum balance equation reads:

$$\frac{\partial \sigma_{ij}}{\partial x_j} - \frac{\partial^2 \Sigma_{ijk}}{\partial x_j \partial x_k} + \rho g_i = 0 \quad (36)$$

and the boundary conditions are:

$$\bar{t}_i = \sigma_{ij} n_j - n_k n_j D\Sigma_{ijk} - \frac{D\Sigma_{ijk}}{Dx_k} n_j - \frac{D\Sigma_{ijk}}{Dx_j} n_k + \frac{Dn_l}{Dx_l} \Sigma_{ijk} n_j n_k - \frac{Dn_j}{Dx_k} \Sigma_{ijk} \quad (37)$$

$$\bar{T}_i = \bar{P}_{ij} n_j = \Sigma_{ijk} n_j n_k \quad (38)$$

where  $\frac{Da}{Dx_i}$  is the tangential derivative of any quantity  $a$ :

$$\frac{Da}{Dx_i} = \frac{\partial a}{\partial x_i} - \frac{\partial a}{\partial x_j} n_j n_i \quad (39)$$

The local second gradient possesses the advantage that the constitutive equations remain local, with the stress fields  $\sigma_{ij}$  and  $\Sigma_{ijk}$  being local quantities. A second gradient extension can thenceforward be formulated for any classical continuum mechanics constitutive law.

#### 4.1.2 Second gradient constitutive equation

Similarly to classical media for which a constitutive equation links the stress to the kinematic history, an additional constitutive law has to be defined between the double stress and the microkinematics. The latter is assumed to be decoupled of the classical first gradient part. However, only a little information is available on the relation existing between the double stress and the micro-deformation. A linear elastic mechanical law is chosen for simplicity reasons with the purpose of introducing as few additional parameters as possible. It consists in an isotropic linear relationship involving five independent parameters derived by [Min65]:

$$\tilde{\Sigma}_{ijk} = D_{ijklmn} \frac{\partial \dot{v}_{lm}}{\partial x_n} \quad (40)$$

giving the Jaumann double stress rate:

$$\dot{\tilde{\Sigma}}_{ijk} = \dot{\Sigma}_{ijk} + \Sigma_{ljk} \omega_{li} + \Sigma_{imk} \omega_{mj} + \Sigma_{ijp} \omega_{pk} \quad (41)$$

as a function of the micro second gradient rate  $\dot{h}_{ijk}$ . Because the physical meaning of the material parameters composing  $D_{ijklmn}$  is not well established, a simplified version introducing only one parameter has been proposed [MCC02]. For two-dimensional problems, it reads:

$$\begin{bmatrix} \tilde{\Sigma}_{111} \\ \tilde{\Sigma}_{112} \\ \tilde{\Sigma}_{121} \\ \tilde{\Sigma}_{122} \\ \tilde{\Sigma}_{211} \\ \tilde{\Sigma}_{212} \\ \tilde{\Sigma}_{221} \\ \tilde{\Sigma}_{222} \end{bmatrix} = D \begin{bmatrix} 1 & 0 & 0 & 0 & 0 & \frac{1}{2} & \frac{1}{2} & 0 \\ 0 & \frac{1}{2} & \frac{1}{2} & 0 & -\frac{1}{2} & 0 & 0 & \frac{1}{2} \\ 0 & \frac{1}{2} & \frac{1}{2} & 0 & -\frac{1}{2} & 0 & 0 & \frac{1}{2} \\ 0 & 0 & 0 & 1 & 0 & -\frac{1}{2} & -\frac{1}{2} & 0 \\ 0 & -\frac{1}{2} & -\frac{1}{2} & 0 & 1 & 0 & 0 & 0 \\ \frac{1}{2} & 0 & 0 & -\frac{1}{2} & 0 & \frac{1}{2} & \frac{1}{2} & 0 \\ \frac{1}{2} & 0 & 0 & -\frac{1}{2} & 0 & \frac{1}{2} & \frac{1}{2} & 0 \\ 0 & \frac{1}{2} & \frac{1}{2} & 0 & 0 & 0 & 0 & 1 \end{bmatrix} \begin{bmatrix} \frac{\partial \dot{v}_{11}}{\partial x_1} \\ \frac{\partial \dot{v}_{11}}{\partial x_2} \\ \frac{\partial \dot{v}_{12}}{\partial x_1} \\ \frac{\partial \dot{v}_{12}}{\partial x_2} \\ \frac{\partial \dot{v}_{21}}{\partial x_1} \\ \frac{\partial \dot{v}_{21}}{\partial x_2} \\ \frac{\partial \dot{v}_{22}}{\partial x_1} \\ \frac{\partial \dot{v}_{22}}{\partial x_2} \end{bmatrix} \quad (42)$$

The constitutive elastic parameter  $D$  represents the physical microstructure and the internal length scale relevant for the shear band width is related to this parameter [CCH98, KCB<sup>+</sup>07, CCC09].

### 4.1.3 Coupled local second gradient model

The second gradient theory was extended from monophasic to biphasic medium by [CCC06]. As for a monophasic medium, microstructure effects have to be introduced in the balance equations of classical poromechanics.

The linear momentum balance equation is identical to Eq. 33:

$$\int_{\Omega} \left( \sigma_{ij} \frac{\partial u_i^*}{\partial x_j} + \Sigma_{ijk} \frac{\partial^2 u_i^*}{\partial x_j \partial x_k} \right) d\Omega = \int_{\Omega} \rho g_i u_i^* d\Omega + \int_{\Gamma_{\sigma}} (\bar{t}_i u_i^* + \bar{T}_i D u_i^*) d\Gamma \quad (43)$$

The water mass balance equation is written, in a weak form, in a similar way as the momentum balance equation. A kinematically admissible virtual pore water pressure field  $p_w^*$  is considered and is involved, as well as its first derivative, in the internal and external virtual quantities. The water mass balance equation reads:

$$\int_{\Omega} \left( \dot{M}_w p_w^* - f_{w,i} \frac{\partial p_w^*}{\partial x_i} \right) d\Omega = \int_{\Omega} Q_w p_w^* d\Omega - \int_{\Gamma_{q_w}} \bar{q}_w p_w^* d\Gamma \quad (44)$$

where  $M_w$  is the water mass inside  $\Omega$ ,  $f_{w,i}$  is the water mass flow,  $Q_w$  is a sink term of water mass, and  $\bar{q}_w$  is the input water mass (positive for inflow) per unit area on a part  $\Gamma_{q_w}$  of  $\Gamma$  (Fig. 4).

According to the previous assumptions, the momentum balance equation Eq. 33 remains valid provided  $\rho$  and  $\sigma_{ij}$  are defined, knowing that the medium is a mixture of a solid phase and one fluid.

The mixture homogenised mass density is given by:

$$\rho = \rho_s (1 - \Phi) + \rho_w \Phi \quad (45)$$

and the effective stress is defined according to the Terzaghi's postulate:

$$\sigma_{ij} = \sigma'_{ij} + p_w \delta_{ij} \quad (46)$$

Furthermore, it is assumed that the pore fluid does not have an influence at microscale; therefore, pore water pressure variations do not generate microkinematic gradients. Such additional hypothesis was formulated by Ehlers [EV98] on a Cosserat model for a biphasic medium. Second gradient effects are only assumed for the solid phase and the water mass balance equation Eq. 44 of classical poromechanics is conserved. The governing equations of the coupled problem are therefore Eqs. 33 and 44.

As already mentioned for the classical poromechanics, the effect of water on the total stress is defined according to the effective stress postulate (Eq. 46) while on the

contrary the double stress  $\Sigma_{ijk}$  is independent of the pore water pressure. The double stress is only related to the solid phase.

The water mass  $M_w$  inside  $\Omega$  and the water mass flow  $f_{w,i}$  are defined in the following equations:

$$M_w = \rho_w \bar{\Phi} \Omega \quad (47)$$

$$f_{w,i} = -\rho_w \frac{k_w}{\mu_w} \left( \frac{\partial p_w}{\partial x_i} + \rho_w g_i \right) \quad (48)$$

The definitions of the phase density variations and of the porosity evolution are:

$$\frac{\dot{\rho}_w}{\rho_w} = \frac{\dot{p}_w}{\chi_w} \quad (49)$$

$$\dot{\rho}_s = 0 \quad (50)$$

$$\dot{\Phi} = (1 - \Phi) \frac{\dot{\Omega}}{\Omega} \quad (51)$$

The latter lead to the time derivative of the water mass per unit mixture volume:

$$\dot{M}_w = \rho_w \left( \frac{\dot{p}_w}{\chi_w} \bar{\Phi} + \frac{\dot{\Omega}}{\Omega} \right) \quad (52)$$

## 4.2 Coupled finite element formulation

### 4.2.1 Numerical implementation

The virtual work formulation of second gradient models can be implemented in a finite element code. To implement the momentum balance equation of Eq. 33, the displacement field has to be a continuously differentiable function because second order derivatives of the displacement field are involved [ZPV01b]. To avoid the use of C1 function, the kinematic restrictions  $v_{ij} = F_{ij}$  and  $v_{ij}^* = F_{ij}^*$  are introduced in the momentum balance equation through a field of Lagrange multipliers  $\lambda_{ij}$  related to a weak form of the constraint [CCH98]. The field equations of the numerical coupled problem are:

$$\int_{\Omega'} \left( \sigma_{ij}^t \frac{\partial u_i^*}{\partial x_j^t} + \Sigma_{ijk}^t \frac{\partial v_{ij}^*}{\partial x_k^t} \right) d\Omega' - \int_{\Omega'} \lambda_{ij}^t \left( \frac{\partial u_i^*}{\partial x_j^t} - v_{ij}^* \right) d\Omega' = \int_{\Omega'} \rho^t g_i u_i^* d\Omega' + \int_{\Gamma_\sigma} \left( \bar{t}_i^t u_i^* + \bar{T}_i^t v_{ik}^* n_k^t \right) d\Gamma' \quad (53)$$

$$\int_{\Omega^t} \lambda_{ij}^* \left( \frac{\partial u_i^t}{\partial x_j^t} - v_{ij}^t \right) d\Omega^t = 0 \quad (54)$$

$$\int_{\Omega^t} \left( \dot{M}_w^t p_w^* - f_{w,i}^t \frac{\partial p_w^*}{\partial x_i^t} \right) d\Omega^t = \int_{\Omega^t} Q_w^t p_w^* d\Omega^t - \int_{\Gamma_{q_w}^t} \bar{q}_w^t p_w^* d\Gamma^t \quad (55)$$

where the notation  $a^t$  corresponds to the current value of any quantity  $a$  for a given time  $t$ . For boundary conditions problems, the virtual quantities included in the above equations depend on the boundary conditions history. Thus, the governing equations and the constitutive equations have to hold at any time  $t$ .

#### 4.2.2 Linearisation of the field equations

Solving the loading process of a boundary conditions problem consists in determining the unknown fields  $u_i$ ,  $v_{ij}$ ,  $\lambda_{ij}$ , and  $p_w$  for which the equilibrium equations 53, 54, and 55 are valid. Since this system of non-linear equations is *a priori* not verified for any instant  $t$ , the problem is numerically solved by iterative procedure. It involves a time discretisation over finite time steps  $\Delta t$ :

$$\tau = t + \Delta t \quad (56)$$

and an implicit scheme of finite differences for the rate of any quantity  $a$ :

$$\dot{a}^\tau = \frac{a^\tau - a^t}{\Delta t} \quad (57)$$

A full Newton-Raphson method is used to find a solution for the new fields  $u_i$ ,  $v_{ij}$ ,  $\lambda_{ij}$ , and  $p_w$  at the end of each time step which is in equilibrium with the boundary conditions.

Following the approach of [BA95], the method aims to define a linear auxiliary problem deriving from the continuum one. A first configuration  $\Omega^t$  in equilibrium with the boundary conditions at a given time  $t$  is assumed to be known and another  $\Omega^\tau$  in equilibrium at the end of the time step  $\tau = t + \Delta t$  has to be found. The aim of the iterative numerical procedure is to determine this new configuration at the end of the time step. Firstly, a configuration which is close to the solution but not at equilibrium is guessed and denoted as  $\Omega^{\tau 1}$ . Both configurations at time  $t$  and  $\tau 1$  are assumed to be known and non-equilibrium forces for the three considered equations, i.e. the residuals  $\Delta_1^{\tau 1}$ ,  $\Delta_2^{\tau 1}$ , and  $\Delta_3^{\tau 1}$ , are defined. The objective is to find another configuration  $\Omega^{\tau 2}$  close to  $\Omega^{\tau 1}$  for which the non-equilibrium forces vanish. To obtain the linear auxiliary problem, the field equations for  $\Omega^{\tau 2}$  are subtracted from the field equations in configuration  $\Omega^{\tau 1}$ , after being rewritten in configuration  $\Omega^{\tau 1}$  by using the Jacobian matrix of the transformation between the two configurations:

$$\bar{F}_{ij} = \frac{\partial x_i^{\tau 2}}{\partial x_j^{\tau 1}} \quad (58)$$

and its Jacobian determinant:

$$\det(F) = \left| \frac{\partial x_i^{\tau_2}}{\partial x_j^{\tau_1}} \right| \quad (59)$$

Assuming that  $g_i$ ,  $\bar{t}_i$ ,  $\bar{q}_w$ , and  $Q_w$  are independent of the different unknown fields (displacement and pore water pressure), and that  $\bar{T}_i$  vanishes give:

$$\begin{aligned} & \int_{\Omega^{\tau_1}} \frac{\partial u_i^*}{\partial x_l^{\tau_1}} \left( \sigma_{ij}^{\tau_2} \frac{\partial x_l^{\tau_1}}{\partial x_j^{\tau_2}} \det(F) - \sigma_{il}^{\tau_1} \right) + \frac{\partial v_{ij}^*}{\partial x_l^{\tau_1}} \left( \Sigma_{ijk}^{\tau_2} \frac{\partial x_l^{\tau_1}}{\partial x_k^{\tau_2}} \det(F) - \Sigma_{ijl}^{\tau_1} \right) d\Omega^{\tau_1} \\ & - \int_{\Omega^{\tau_1}} \frac{\partial u_i^*}{\partial x_l^{\tau_1}} \left( \lambda_{ij}^{\tau_2} \frac{\partial x_l^{\tau_1}}{\partial x_j^{\tau_2}} \det(F) - \lambda_{il}^{\tau_1} \right) - v_{ij}^* (\lambda_{ij}^{\tau_2} \det(F) - \lambda_{ij}^{\tau_1}) d\Omega^{\tau_1} \quad (60) \\ & - \int_{\Omega^{\tau_1}} u_i^* (\rho^{\tau_2} \det(F) - \rho^{\tau_1}) g_i d\Omega^{\tau_1} = -\Delta_1^{\tau_1} \end{aligned}$$

$$\int_{\Omega^{\tau_1}} \lambda_{ij}^* \left( \left( \frac{\partial u_i^{\tau_2}}{\partial x_k^{\tau_1}} \frac{\partial x_k^{\tau_1}}{\partial x_j^{\tau_2}} \det(F) - \frac{\partial u_i^{\tau_1}}{\partial x_j^{\tau_1}} \right) - (v_{ij}^{\tau_2} \det(F) - v_{ij}^{\tau_1}) \right) d\Omega^{\tau_1} = -\Delta_2^{\tau_1} \quad (61)$$

$$\int_{\Omega^{\tau_1}} p_w^* (\dot{M}_w^{\tau_2} \det(F) - \dot{M}_w^{\tau_1}) - \frac{\partial p_w^*}{\partial x_l^{\tau_1}} \left( f_{w,i}^{\tau_2} \frac{\partial x_l^{\tau_1}}{\partial x_i^{\tau_2}} \det(F) - f_{w,l}^{\tau_1} \right) d\Omega^{\tau_1} = -\Delta_3^{\tau_1} \quad (62)$$

By making the two configurations tend towards each other, the variations between them can be defined for any quantity  $a$  as:

$$da^{\tau_1} = a^{\tau_2} - a^{\tau_1} \quad (63)$$

The balance equations can be rewritten by taking into account these variations. The complete development of the linearisation of the field equation system and of the resulting linear auxiliary problem is exposed by [CCC06].

### 4.2.3 Spatial discretisation

In finite element methods, each continuum body is discretised by finite elements and the above field equations are spatially discretised. For the second gradient model, the discretisation is realised by two-dimensional plane-strain isoparametric finite elements. These elements are composed of eight nodes for the displacement field  $u_i$  and

the pore water pressure  $p_w$ , four nodes for the microkinematic gradient field  $v_{ij}$ , and one node for the Lagrange multiplier field  $\lambda_{ij}$  (Fig. 5). Quadratic serendipity shape functions [ZT00] are used for the  $u_i$  and  $p_w$  interpolations, linear shape functions are used for  $v_{ij}$ , whereas  $\lambda_{ij}$  is assumed constant.

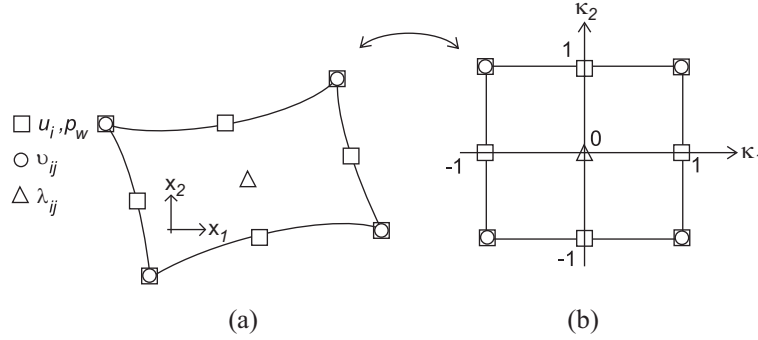


Figure 5: Finite element used for the spatial discretisation of the coupled local second gradient model: (a) current quadrilateral element and (b) parent element [CCC06].

The balance equations of the coupled finite element problem (linear auxiliary problem) have to be rewritten in matricial form to define the local stiffness matrix of an element:

$$\int_{\Omega^{\tau 1}} \left[ U_{(x_1, x_2)}^{*, \tau 1} \right]^T [E^{\tau 1}] \left[ dU_{(x_1, x_2)}^{\tau 1} \right] d\Omega^{\tau 1} = -\Delta_1^{\tau 1} - \Delta_2^{\tau 1} - \Delta_3^{\tau 1} \quad (64)$$

where  $\left[ dU_{(x_1, x_2)}^{\tau 1} \right]$  is the vector of the unknown increments of nodal variables in the current element configuration:

$$\left[ dU_{(x_1, x_2)}^{\tau 1} \right]_{25 \times 1} = \left[ \frac{\partial du_1^{\tau 1}}{\partial x_1^{\tau 1}} \quad \frac{\partial du_1^{\tau 1}}{\partial x_2^{\tau 1}} \quad \frac{\partial du_2^{\tau 1}}{\partial x_1^{\tau 1}} \quad \frac{\partial du_2^{\tau 1}}{\partial x_2^{\tau 1}} \quad du_1^{\tau 1} \quad du_2^{\tau 1} \quad \frac{\partial dp_w^{\tau 1}}{\partial x_1^{\tau 1}} \quad \frac{\partial dp_w^{\tau 1}}{\partial x_2^{\tau 1}} \quad dp_w^{\tau 1} \quad \frac{\partial dv_{11}^{\tau 1}}{\partial x_1^{\tau 1}} \quad \frac{\partial dv_{11}^{\tau 1}}{\partial x_2^{\tau 1}} \quad \frac{\partial dv_{12}^{\tau 1}}{\partial x_1^{\tau 1}} \quad \dots \quad \frac{\partial dv_{22}^{\tau 1}}{\partial x_2^{\tau 1}} \quad dv_{11}^{\tau 1} \quad dv_{12}^{\tau 1} \quad dv_{21}^{\tau 1} \quad dv_{22}^{\tau 1} \quad d\lambda_{11}^{\tau 1} \quad d\lambda_{12}^{\tau 1} \quad d\lambda_{21}^{\tau 1} \quad d\lambda_{22}^{\tau 1} \right]^T \quad (65)$$

$\left[ U_{(x_1, x_2)}^{*, \tau 1} \right]$  is a vector having the same structure with the corresponding virtual quantities:

$$\left[ U_{(x_1, x_2)}^{*, \tau 1} \right]_{1 \times 25} = \left[ \frac{\partial u_1^*}{\partial x_1^{\tau 1}} \quad \frac{\partial u_1^*}{\partial x_2^{\tau 1}} \quad \frac{\partial u_2^*}{\partial x_1^{\tau 1}} \quad \frac{\partial u_2^*}{\partial x_2^{\tau 1}} \quad u_1^* \quad u_2^* \quad \frac{\partial p_w^*}{\partial x_1^{\tau 1}} \quad \frac{\partial p_w^*}{\partial x_2^{\tau 1}} \quad p_w^* \quad \frac{\partial v_{11}^*}{\partial x_1^{\tau 1}} \quad \frac{\partial v_{11}^*}{\partial x_2^{\tau 1}} \quad \frac{\partial v_{12}^*}{\partial x_1^{\tau 1}} \quad \dots \quad \frac{\partial v_{22}^*}{\partial x_2^{\tau 1}} \quad v_{11}^* \quad v_{12}^* \quad v_{21}^* \quad v_{22}^* \quad \lambda_{11}^* \quad \lambda_{12}^* \quad \lambda_{21}^* \quad \lambda_{22}^* \right] \quad (66)$$

and  $[E^{\tau 1}]$  is the current element stiffness (tangent) matrix defined as follows:

$$[E^{\tau 1}]_{25 \times 25} = \begin{bmatrix} E_{1_{4 \times 4}}^{\tau 1} & 0_{4 \times 2} & K_{WM_{4 \times 3}}^{\tau 1} & 0_{4 \times 8} & 0_{4 \times 4} & -I_{4 \times 4} \\ G_{1_{2 \times 4}}^{\tau 1} & 0_{2 \times 2} & G_{2_{2 \times 3}}^{\tau 1} & 0_{2 \times 8} & 0_{2 \times 4} & 0_{2 \times 4} \\ K_{MW_{3 \times 4}}^{\tau 1} & 0_{3 \times 2} & K_{WW_{3 \times 3}}^{\tau 1} & 0_{3 \times 8} & 0_{3 \times 4} & 0_{3 \times 4} \\ E_{2_{8 \times 4}}^{\tau 1} & 0_{8 \times 2} & 0_{8 \times 3} & D_{8_{8 \times 8}}^{\tau 1} & 0_{8 \times 4} & 0_{8 \times 4} \\ E_{3_{4 \times 4}}^{\tau 1} & 0_{4 \times 2} & 0_{4 \times 3} & 0_{4 \times 8} & 0_{4 \times 4} & I_{4 \times 4} \\ E_{4_{4 \times 4}}^{\tau 1} & 0_{4 \times 2} & 0_{4 \times 3} & 0_{4 \times 8} & -I_{4 \times 4} & 0_{4 \times 4} \end{bmatrix} \quad (67)$$

The matrices  $[E_1^{\tau 1}]$ ,  $[E_2^{\tau 1}]$ ,  $[E_3^{\tau 1}]$ ,  $[E_4^{\tau 1}]$ , and  $[D^{\tau 1}]$  are the same as the ones used in the local second gradient model for monophasic medium by [CM04] ( $[D^{\tau 1}] = D_{ijklmn}$  in Eqs. 40 and 42).  $[K_{WW}^{\tau 1}]$  is the classical stiffness matrix of a flow problem,  $[K_{MW}^{\tau 1}]$  and  $[K_{WM}^{\tau 1}]$  are matrices of the coupling between the flow and the mechanical problems detailed by [CCC06]. Moreover,  $[G_1^{\tau 1}]$  and  $[G_2^{\tau 1}]$  are related to the contribution of gravity volume force.

The finite element spatial discretisation of the linear auxiliary problem is introduced in Eq. 64 by using transformation matrices  $[T^{\tau 1}]$  and  $[B]$  that connect the current element vector  $[dU_{(x_1, x_2)}^{\tau 1}]$  to the parent element vector  $[dU_{(\kappa_1, \kappa_2)}^{\tau 1}]$  and to the nodal variables  $[dU_{Node}^{\tau 1}]$ :

$$[dU_{(x_1, x_2)}^{\tau 1}] = [T^{\tau 1}] [dU_{(\kappa_1, \kappa_2)}^{\tau 1}] = [T^{\tau 1}] [B] [dU_{Node}^{\tau 1}] \quad (68)$$

The matrices  $[B]$  and  $[T^{\tau 1}]$  contain the interpolation functions and their derivatives. Moreover, the vector  $[U_{(x_1, x_2)}^{*, \tau 1}]$  is related to  $[U_{Node}^{*, \tau 1}]$  in the same manner.

The integration in Eq. 64 can be expressed for each parent element as follows:

$$\int_{\Omega^{\tau 1}} [U_{(x_1, x_2)}^{*, \tau 1}]^T [E^{\tau 1}] [dU_{(x_1, x_2)}^{\tau 1}] d\Omega^{\tau 1} = [U_{Node}^{*, \tau 1}]^T [k^{\tau 1}] [dU_{Node}^{\tau 1}] \quad (69)$$

where  $[k^{\tau 1}]$  is the local element stiffness matrix:

$$[k^{\tau 1}] = \int_{-1}^1 \int_{-1}^1 [B]^T [T^{\tau 1}]^T [E^{\tau 1}] [T^{\tau 1}] [B] \det(J^{\tau 1}) d\kappa_1 d\kappa_2 \quad (70)$$

with  $\det(J^{\tau 1})$  the determinant of the Jacobian matrix of the transformation between the parent  $(\kappa_1, \kappa_2)$  and the current  $(x_1, x_2)$  elements:

$$\det(J^{\tau 1}) = \left| \frac{\partial x_i^{\tau 1}}{\partial \kappa_j} \right| \quad (71)$$

The residual terms are also computed locally for each element and define the elementary out of balance force vector  $[f_{OB}^{\tau 1}]$ :

$$-\Delta_1^{\tau 1} - \Delta_2^{\tau 1} - \Delta_3^{\tau 1} = [U_{Node}^{*,\tau 1}]^T [f_{OB}^{\tau 1}] \quad (72)$$

#### 4.2.4 Global solution

Once the elementary stiffness matrices and out of balance force vectors are computed, they are assembled to obtain the global stiffness matrix  $[K^{\tau 1}]$  and the global out of balance force vector  $[F_{OB}^{\tau 1}]$  of the whole continuum. The linear auxiliary system is solved by computing:

$$[K^{\tau 1}] [\delta U_{Node}^{\tau 1}] = - [F_{OB}^{\tau 1}] \quad (73)$$

where  $[\delta U_{Node}^{\tau 1}]$  is the global correction vector of the nodal degrees of freedom. The current configuration is actualised by adding the corrections to their respective current values. The new current configuration is closer to the well-balanced configuration and its equilibrium is checked, leading to a new iteration or to the end of the loading step of the iterative procedure.

### 4.3 Two-dimensional specimen under compression

A finite element modelling of two-dimensional plane-strain compression tests is first considered. These tests have been widely reproduced on small-scale specimens to emphasise the strain localisation effects.

Among various authors, the results obtained by [CLC09] for a uniaxial compression are principally developed hereafter. A sketch of the boundary value problem in plane-strain state is illustrated in Fig. 6. The vertical displacement  $u_a$  of the sample upper surface (smooth and rigid boundary) is progressively increased during the test with a constant loading strain rate to model the vertical compression. The vertical displacement of the bottom surface is blocked (rigid boundary) and the displacement of the central node is blocked in both directions to avoid rigid body displacement.

#### 4.3.1 Classical medium

A mechanical modelling is presented hereafter for a classical medium (without a regularization method). The (first gradient) constitutive law is an elastoplastic strain-softening model in an associated softening plasticity framework ( $\varphi = \psi$ ,  $F^p = G^p$ ): a Drucker-Prager yield criterion is considered with no hardening of the friction angle, and a cohesion softening function [CLC09].

A homogeneous response of the specimen is first studied. The global response is detailed in Fig. 7 (a) where one can observe a linear elastic behaviour, then a non-linear

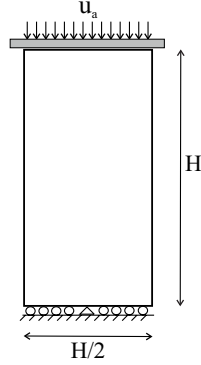


Figure 6: Sketch of the plane-strain compression test.

plastic behaviour before the peak stress including cohesion softening, and finally a plastic behaviour with decrease of the global load response. Concerning the orientation of the shear band, the Rice criterion gives the orientation of the first possible shear band occurrence [RR75],[Ric76]. This criterion can be used for a single-mechanism elastoplastic model such as the studied problem. The Rice criterion  $det(\Lambda_{jk})$  evolution is presented during the increasing loading history in Fig. 7 (b) as a function of  $\tan\Theta$ ,  $\Lambda_{jk}$  is the Acoustic tensor and  $\Theta$  is the orientation of the shear band normal to the loading vertical axis, i.e. the shear band orientation with the horizontal direction. The criterion is positive ( $det(\Lambda_{jk}) > 0$ ) as long as the behaviour is elastic and even for an elastoplastic loading until the first bifurcation is predicted ( $det(\Lambda_{jk}) = 0$ ). For a certain load, the bifurcation criterion is met at every material point and two symmetric (conjugate) bifurcation directions are predicted with an orientation of  $\Theta = \pm 60^\circ$ . This bifurcation point corresponds to the peak stress on the global response curve and to the start of the load response reduction in associated plasticity. A range of possible orientations is predicted for an increasing load corresponding to a multitude of possible solutions ( $det(\Lambda_{jk}) \leq 0$ ).

For a perfect sample, although softening plasticity is considered, the strain localisation is not automatically triggered and the numerical solution may remain homogeneous even after the bifurcation criterion is met. In reality, the localisation process is generated because geomaterials exhibit heterogeneities. Different numerical procedures are available to force the occurrence of strain localisation. The most used one is the introduction of an imperfection, such as disturbing force, material imperfection, or geometrical defect [CRB97, MCC02, ZSS01]. The modification of numerical parameters, such as time step size and sequences can also be performed [MSC14, SaHC09]. A third method that will be discussed later is a random initialisation of variables [CCC01].

Among these procedures, [CLC09] introduced a material imperfection in the bottom left finite element of the sample under compression. Initially the strain field in the

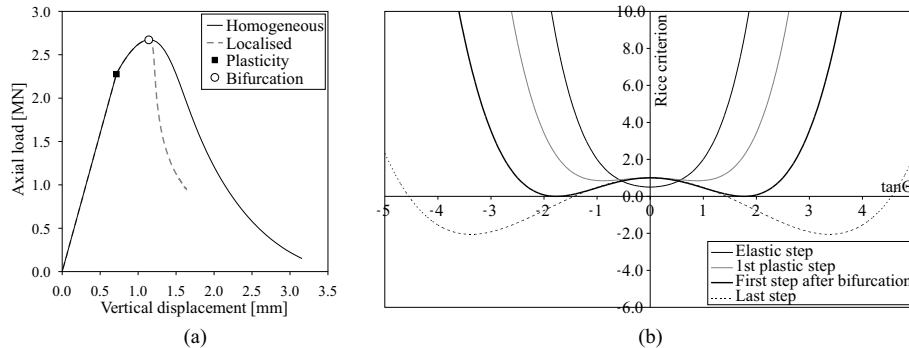


Figure 7: Uniaxial compression: (a) global specimen response curves and (b) Rice criterion at several loading steps for the homogeneous solution [CLC09].

sample is homogeneous, and once the bifurcation criterion is met, the imperfection instigates the development of a shear band across the specimen. The strain localisation as well as its dependency to the mesh size is illustrated in Fig. 8 for a classical medium. The localised solution is therefore non-homogeneous, with the shear band under plastic loading and the outer material under elastic unloading. The global sample response is detailed in Fig. 7 (a) where a rapid decrease of the global reaction is observed once the shear band establishes. The shear band appearance corresponds therefore to the curve peak load (or peak stress) as concluded from laboratory evidences in section 2. The latter also indicate that a material inclusion can act as a strain localisation attractor, which is confirmed by the numerical results. The non-uniqueness issue of the problem after the bifurcation point has consequently been addressed by the imperfection inclusion which leads to one post-bifurcation solution.

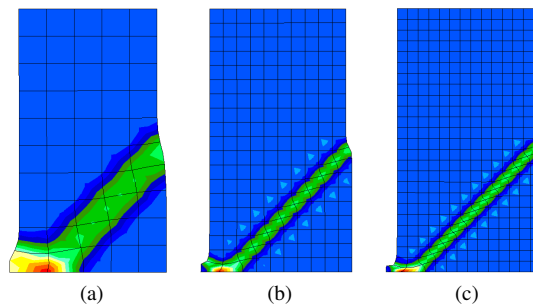


Figure 8: Localised patterns represented by the deviatoric deformation for classical medium: finite element meshes of (a) 50, (b) 190, and (c) 325 elements.

### 4.3.2 Microstructure enhanced medium

To fix the pathological mesh sensitivity, an enhanced microstructure medium is used. More specifically, the local second gradient medium is adopted, with the second gradient constitutive law given by Eq. 42. The strain localisation pattern induced by the imperfection is illustrated in Fig. 9 with the Gauss integration points under softening plastic loading shown as red squares. This representation permits to measure the shear band width and to notice that it stays constant no matter the element size, implying that the shear strain localisation is mesh-independent. Thus, the strain localisation is correctly regularised thanks to the internal length scale introduced by the second grade model. This is also the case for unstructured mesh [BCC06] and for a biphasic porous medium under saturated conditions, using the coupled local second gradient model [CCC06].

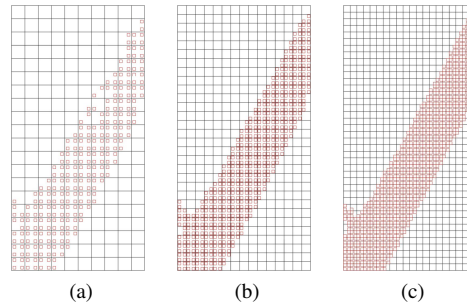


Figure 9: Localised patterns represented by the plastic zone for a second gradient medium: finite element meshes of (a) 200, (b) 450, and (c) 800 elements.

However, the regularisation of the strain localisation process is satisfactory, provided that the second gradient elastic modulus  $D$  is calibrated properly to represent the shear bands properly. As already mentioned, the internal length scale inherent to the second gradient mechanical law is related to this constitutive parameter. The value of  $D$  should be therefore evaluated based on experimental measurements of shear band thickness for the considered material. From a modelling point of view, a better numerical prediction of the post-localisation plastic behaviour within the bands is obtained if at least three elements compose the shear band width [BCC06]. This remark is valid for any regularisation technique including the second gradient model but also gradient plasticity and non-local models.

### 4.3.3 Non-uniqueness of the solution

The non-uniqueness of the post-peak solution of an initial boundary value problem can be studied using special numerical techniques. In fact, instead of using a material

imperfection, localised solutions can be found for a homogeneous material using a random initialisation of the strain rate field (nodal velocities) or of material characteristics at the beginning of the iterative procedure. This technique has been mainly proposed by Chambon and co-workers [CCC01] who developed an algorithm to search several possible localised solutions by random initialisation. This algorithm has been adapted to the second-gradient models by [CM04].

Numerical modelling of compression tests performed with the second gradient model illustrates the non-uniqueness of localised solutions of the same initial boundary value problem [BCC06]. The random initialisation is adopted for the increment of nodal quantities  $[dU_{Node}^{\tau 1}]$  (Eq. 68) related to the values obtained at the end of the preceding time step. The obtained non-homogeneous solutions are detailed in Fig. 10 (a) where the different solutions exhibit one to three bands with a possible reflection on the top and bottom faces of the sample because of the imposed vertical displacement. The results indicate that the band thickness is reproducible even if the localisation pattern is different in terms of bands position and number.

As before, the strain localisation occurring at the bifurcation point is due to the strain softening behaviour and possible elastic unloading. Fig. 10 (b) illustrates the global response curves that are different of those in Fig. 7 because a different first gradient law is used. These curves are grouped in packages characterised by the number of deformation bands. It is evident that the higher the band number, the closer the curves are to the homogeneous plastic case. A similar conclusion was drawn from the bar in traction studied by [CCH98], [JKC14].

#### 4.3.4 Bifurcation criterion for the second gradient model

A bifurcation analysis applied to the second gradient model is proposed by [BCC06]. The authors indicate that the bifurcation criterion of the second gradient model is, as for a classical medium, a necessary but not sufficient condition for the localisation onset and that it is met after the bifurcation criterion of the classical medium is verified. Thus, the bifurcation analysis reduces to an analysis on the classical part of the constitutive model.

## 5 Coupled local second gradient model for an unsaturated medium

The procedure to extend the local second gradient model in saturated conditions to other multiphysical contexts is more or less the same: additional balance equations have to be considered to model the other processes. The main issue is not a numerical one but rather a physical one. What are the possible interactions between the second gradient model and the thermal diffusion, the suction or the chemical reaction? These

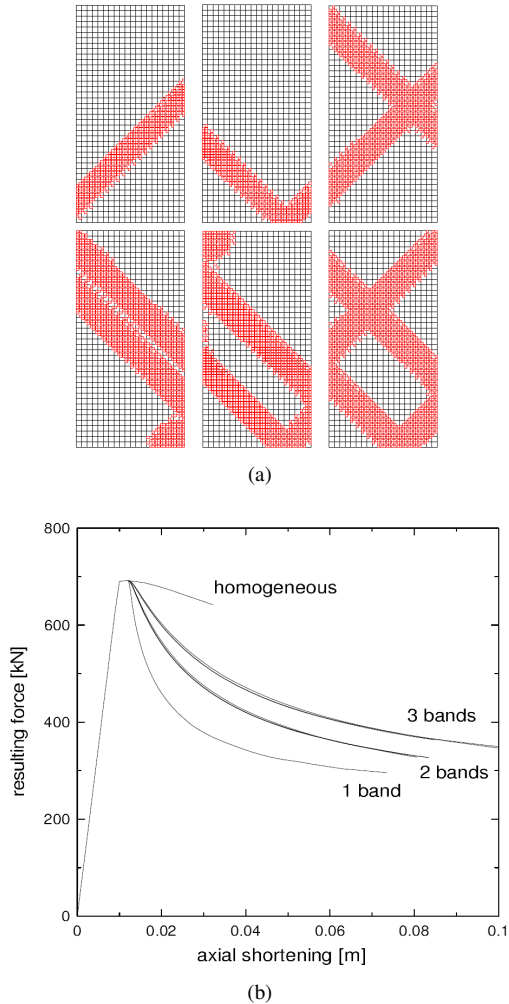


Figure 10: Example of localised solutions for a compression test obtained after a random initialisation: (a) plastic zone and (b) global response curve [BCC06].

questions should be first addressed by experimental campaigns. Concerning the internal length introduced by the second gradient model, it comes as the ratio of two constitutive moduli: the one related to the second gradient constitutive law and the one related to the classical law [CCH98]. Considering that the classical constitutive moduli are influenced by the different processes (chemical, thermal, suction . . .), the conclusions should be that the internal length scale should be modified by these latter processes (under the condition that second gradient law is not influenced by the processes). This should be again confirmed by some experimental evidences!

The coupled local second gradient model developed by [CCC06] for a biphasic porous medium can be extended to unsaturated materials with compressible solid grains. Hereafter, the unsaturated conditions are taken into account and the compressibility of the solid grains is introduced through the Biot's coefficient. Additionally, the permeability anisotropy is incorporated in the model to better represent the water flows, even if the mechanical behaviour remains isotropic.

## 5.1 Partial saturation conditions

For unsaturated conditions the water mass inside a porous material volume  $\Omega$  corresponds to:

$$M_w = \rho_w \Phi S_{r,w} \Omega \quad (74)$$

and its time derivative corresponds to:

$$\dot{M}_w = \dot{\rho}_w \Phi S_{r,w} \Omega + \rho_w \dot{\Phi} S_{r,w} \Omega + \rho_w \Phi \dot{S}_{r,w} \Omega + \rho_w \Phi S_{r,w} \dot{\Omega} \quad (75)$$

This amount of water, which depends on the degree of water saturation  $S_{r,w}$ , leads to the following mixture homogenised mass density:

$$\rho = \rho_s (1 - \Phi) + S_{r,w} \rho_w \Phi \quad (76)$$

and the water advective flow for anisotropic hydraulic permeability is given by Darcy's law:

$$f_{w,i} = -\rho_w \frac{k_{w,ij} k_{r,w}}{\mu_w} \left( \frac{\partial p_w}{\partial x_j} + \rho_w g_j \right) \quad (77)$$

where  $k_{r,w}$  is the water relative permeability.

The fluid mass and fluid flows are mostly governed by the water retention property of the material and by its hydraulic permeability. Both of them are related to the partial water saturation and a relative permeability coefficient is introduced in the generalised Darcy's law. Among various possible analytical expressions, the water retention and relative permeability curves are given by van Genuchten's and Mualem's models [Mua76, vG80]:

$$S_{r,w} = S_{res} + (S_{max} - S_{res}) \left( 1 + \left( \frac{p_c}{P_r} \right)^{\frac{1}{1-\mathcal{M}}} \right)^{-\mathcal{M}} \quad (78)$$

$$k_{r,w} = \sqrt{S_{r,w}} \left( 1 - \left( 1 - S_{r,w} \frac{1}{\mathcal{M}} \right)^{\mathcal{M}} \right)^2 \quad (79)$$

where  $P_r$  is the air entry pressure,  $S_{max}$  and  $S_{res}$  are the maximum and residual water degrees of saturation,  $\mathcal{M}$  is a model coefficient, and  $p_c$  is the capillary pressure.

## 5.2 Anisotropy of the intrinsic permeability

The advective flow of water (Eq. 77) depends on the anisotropic characteristics of the material through the anisotropic intrinsic permeability. For anisotropic materials and by symmetry of the tensor, the intrinsic permeability tensor  $k_{w,ij}$  requires six components to describe the flow characteristics. However, materials commonly exhibit limited forms of anisotropy and stratified geomaterials require only two parameters for the description of the water flow. For horizontal layering in the plane  $(x_1, x_3)$ , the intrinsic hydraulic permeability tensor is defined with the horizontal and vertical permeabilities,  $k_{w,h}$  and  $k_{w,v}$ , as follows:

$$k_{w,ij} = \begin{bmatrix} k_{w,h} & 0 & 0 \\ 0 & k_{w,v} & 0 \\ 0 & 0 & k_{w,h} \end{bmatrix} \quad (80)$$

## 5.3 Compressibility of the solid grains

The material compressibility is defined within the scope of poroelasticity [DC93] and is based on the different compressibilities of a porous material. Those are: the compressibility of the bulk material  $C$  (solid skeleton), the compressibility of the pores  $C_p$ , and the compressibility of the solid phase  $C_s$  (rock matrix) with  $C_s < C$ . The different types of compressibility induce different behaviours of the rock matrix and of the porous material. They can deform differently and the porous material may enter plastic state while the solid grains remain elastic. In the general Biot framework [Bio41], the Biot's coefficient is expressed by:

$$b = \frac{\Phi C_p}{C} = 1 - \frac{K}{K_s} \quad (81)$$

as a function of the drained bulk modulus of the material  $K$  and the bulk modulus of the solid phase  $K_s$ . This coefficient represents the relative deformability of the solid grains with regard to the solid skeleton [Bio41, BW57, Ske60]. Biot proposed for the effective stress definition to use  $b$  as a scaling factor that reduces the effect of  $p_w$  on  $\sigma_{ij}$  due to a reduction of pore compressibility. The Biot's stress definition can be formulated under unsaturated conditions presuming that the assumptions on compressibility hold under these conditions [NL08]:

$$\sigma_{ij} = \sigma'_{ij} - b S_{r,w} p_w \delta_{ij} \quad (82)$$

The latter expression includes the effect of partial saturation on the effective stress field (tensile stress is positive).

For the solid phase behaviour, the isotropic solid density variation is linked to the variations of pore water pressure and mean effective stress by [DC93, Cou04]:

$$\frac{\dot{\rho}_s}{\rho_s} = \frac{(b - \Phi) S_{r,w} \dot{p}_w - \dot{\sigma}'}{(1 - \Phi) K_s} \quad (83)$$

The time derivative of the porosity is obtained by solid mass conservation  $\dot{M}_s = 0$  and reads:

$$\dot{\Phi} = (1 - \Phi) \left( \frac{\dot{\rho}_s}{\rho_s} + \frac{\dot{\Omega}}{\Omega} \right) = (1 - \Phi) \left( \frac{(b - \Phi) S_{r,w} \dot{p}_w - \dot{\sigma}'}{(1 - \Phi) K_s} + \frac{\dot{\Omega}}{\Omega} \right) \quad (84)$$

Furthermore, the time derivative of the water mass in Eq. 75 becomes by including the fluid compressibility, the porosity variation, and by considering a unit mixture volume:

$$\dot{M}_w = \rho_w \left( \frac{\dot{p}_w}{\chi_w} \Phi S_{r,w} + \frac{\dot{p}_w}{K_s} (b - \Phi) S_{r,w}^2 + \left( \frac{\dot{\Omega}}{\Omega} - \frac{\dot{\sigma}'}{K_s} \right) S_{r,w} + \Phi \dot{S}_{r,w} \right) \quad (85)$$

The above expressions can be rewritten under poroelastic assumption:

$$\dot{\sigma}' = K \dot{\epsilon}_v = K \frac{\dot{\Omega}}{\Omega} \quad (86)$$

and using the Biot's coefficient expression of Eq. 81. The equations become:

$$\frac{\dot{\rho}_s}{\rho_s} = \frac{(b - \Phi) S_{r,w} \dot{p}_w - K \frac{\dot{\Omega}}{\Omega}}{(1 - \Phi) K_s} \quad (87)$$

$$\dot{\Phi} = (b - \Phi) \left( \frac{S_{r,w}}{K_s} \dot{p}_w + \frac{\dot{\Omega}}{\Omega} \right) \quad (88)$$

$$\dot{M}_w = \rho_w \left( \frac{\dot{p}_w}{\chi_w} \Phi S_{r,w} + \frac{\dot{p}_w}{K_s} (b - \Phi) S_{r,w}^2 + b \frac{\dot{\Omega}}{\Omega} S_{r,w} + \Phi \dot{S}_{r,w} \right) \quad (89)$$

Biot's theory and the equations of poroelasticity are valid only for an elastic behaviour. Extending these equations to poroplasticity [Cou95] with permanent changes in fluid mass content and in porosity requires to include the plastic material behaviour, which is complex to implement and is not included in this chapter.

According to the previous assumptions, the momentum balance equation Eq. 33 and the water mass balance equation Eq.44 remain valid provided that the different variables included in these two equations are adapted to unsaturated conditions ( $\rho$ ,  $\sigma_{ij}$ ,  $\dot{M}_w$  ...).

## 6 Modelling of a gallery excavation

The processes of underground drilling and induced shear strain localisation are investigated at large scale. [PV92] were the first to present a numerical analysis of progressive localisation around an excavated cavity in rock with a Cosserat microstructure. In

the following, a gallery excavation is considered in a clayey rock. In the rock mass, the fractured structure around the galleries develops preferentially in the horizontal or vertical direction depending on the anisotropy of both stress state and material properties [ALN<sup>+</sup>14]. As a first large-scale approach including strain localisation, an isotropic mechanical model is used with the objective of analysing if the appearance of fractures during the drilling of galleries is governed by the anisotropy of the *in situ* stress state [PLC15]. So far, the numerical modelling of gallery drilling with the second gradient model has highlighted strain localisation but was essentially limited to mechanical analyses with isotropic initial stress state [Fer09, SaHC09].

Moreover, during the operational phases of underground openings, an air ventilation is performed inside the galleries to control the air relative humidity and temperature. This ventilation induces fluid transfers and a desaturation of the rock that must be taken into account in the coupled second gradient model.

Many studies have been performed with two-dimensional isotropic mechanical models. Our purpose is to investigate if this type of model can reproduce the *in situ* observations and measurements by incorporating the fracture modelling with strain localisation. The zone that develops around the gallery is called excavation fractured zone, and it is related to the irreversible hydro-mechanical property changes.

It should be pointed out that regularisation techniques have already been used for this type of problem. They generate results that are mesh-independent but these theories do not restore the uniqueness of the solution for the gallery excavation problem [Fer09, SaHC09]. These remarks are valid for all regularisation methods.

## 6.1 Numerical model

A hydro-mechanical modelling of a gallery excavation is performed in two-dimensional plane strain state. The modelled gallery corresponds to the GED gallery of the Andra's URL oriented parallel to the minor horizontal principal total stress  $\sigma_h$  and having a radius of 2.3 m. The initial pore water pressure and anisotropic stress state are:

$$\sigma_{x,0} = \sigma_H = 1.3 \sigma_h = 15.6 \text{ MPa}$$

$$\sigma_{y,0} = \sigma_v = 12 \text{ MPa}$$

$$\sigma_{z,0} = \sigma_h = 12 \text{ MPa}$$

$$p_{w,0} = 4.5 \text{ MPa}$$

A schematic representation of the models, the meshes, and the boundary conditions is detailed in Fig. 11. Two meshes are used: a full gallery and a quarter of a gallery. The mesh extension of the full gallery is 120 m, both horizontally and vertically, and the spatial discretisation is performed with a total of 29040 nodes and 7440 elements. Assuming symmetry along the x and y-axes, only one quarter of the gallery can be discretised. In this case, the mesh extension is 60 m, both horizontally and vertically,

and the discretisation is performed with a total of 9801 nodes and 2480 elements. For both meshes, the initial stresses and pore water pressure are imposed at the mesh external boundary (drained boundary) and the meshes have a more refined discretisation close to the gallery. To establish the symmetry, the normal displacements and the normal water flows are blocked to a value of zero along the symmetry axes, which are therefore impervious. Nonetheless, as mentioned by [ZPV01a], a special care must be brought to the kinematic boundary conditions required to establish the symmetry. Due to the existence of gradient terms in the equilibrium equations, higher order constraints have to be characterised in addition to the classical boundary condition on the normal displacements. This second kinematic condition requires that the radial displacement  $u_r$  must be symmetric on both sides of the symmetry axes. This implies that the normal derivative of  $u_r$ , with respect to the tangential (orthoradial) direction  $\theta$ , has to cancel:

$$\frac{\partial u_r}{\partial \theta} = 0 \quad (90)$$

which is equivalent to:

$$x - axis : \quad \frac{\partial u_x}{\partial y} = 0 \quad (91)$$

$$y - axis : \quad \frac{\partial u_y}{\partial x} = 0 \quad (92)$$

Furthermore, natural boundary conditions for the double forces,  $\bar{T}_i = 0$ , are assumed on the different boundaries and gravity is not taken into account.

The gallery excavation can now be considered. It is modelled by decreasing during 5 days the total stresses and the pore water pressure at the gallery wall from their initial values to the atmospheric pressure of 100 kPa. After the excavation, the calculation is extended to 1000 days under constant total radial stress, to highlight possible long-term effects (Fig. 12). This stress imposition is representative of unsupported galleries.

To model the air ventilation inside the gallery, a classical flow boundary condition is assumed and imposes the suction corresponding to the relative humidity of the cavity air at the tunnel wall. Two cases are considered for the air inside the gallery (Fig. 12). In the first case, there is no ventilation inside the gallery; thus, the air is saturated with water vapour and this maximum concentration corresponds to  $RH = 100\%$ . According to Kelvin's law, the corresponding pore water pressure at the gallery wall is the atmospheric pressure  $p_w = 100$  kPa. The pore water pressure is then maintained constant after the end of the excavation and the rock mass remains almost saturated. In the second case, air ventilation is taken into account, since ventilation is usually realised in the galleries composing underground structures. It may drain the water from the rock, desaturate it, and modify the structure, the fracturing pattern, as well as the size of the fractured zone. Air ventilation can thus be modelled in order to observe its effects on the rock material. A theoretical ventilation, with constant air relative humidity, is envisaged to obtain a first outlook of the ventilation effect on shear banding. The air which is injected in the gallery is dryer than previously and a lower relative

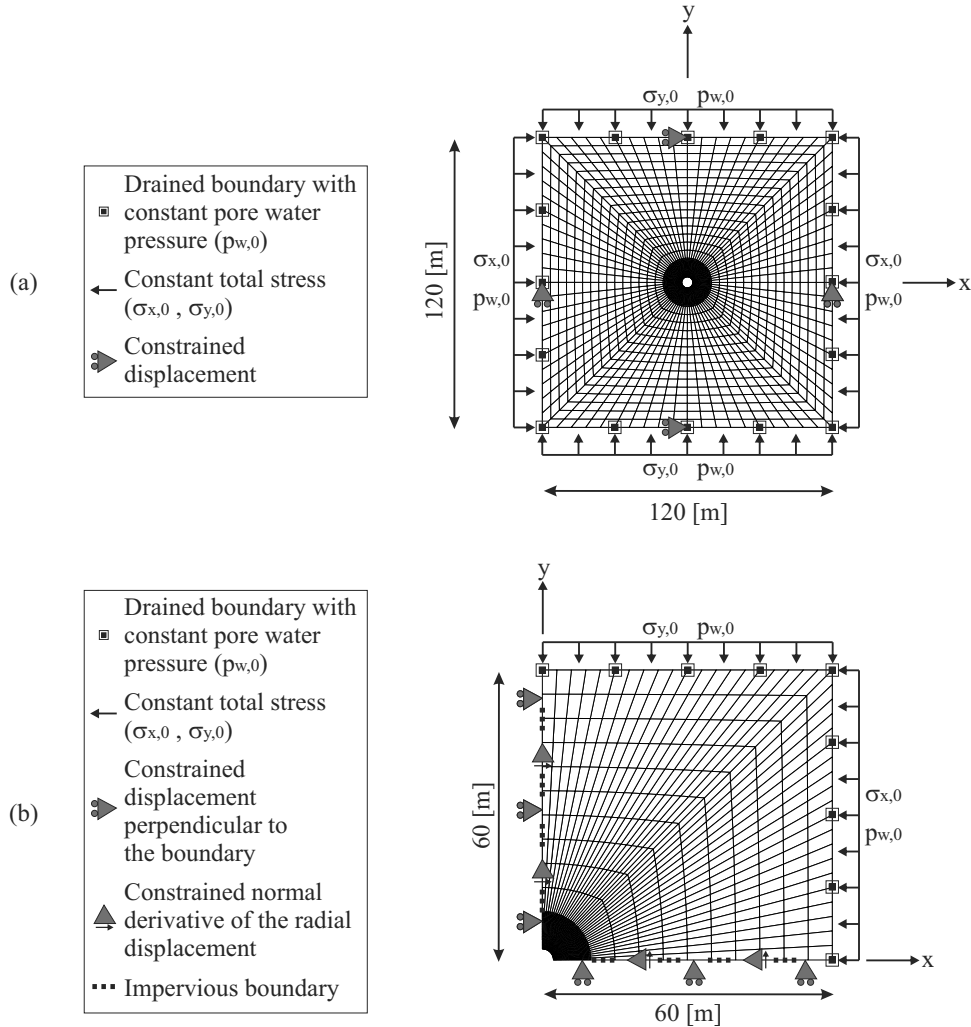


Figure 11: Schematic representation of the models used for the modelling of a gallery excavation: (a) full gallery and (b) quarter of a gallery.

humidity of 80 % with a temperature of 25 °C ( $T = 298.15$  K) are considered. Following Kelvin’s law, this humidity corresponds to a pore water pressure at gallery wall of  $p_w = -30.7$  MPa. To reach this value, the decrease of  $p_w$  is performed in two steps: firstly, it decreases from its initial value to the atmospheric pressure during the excavation (5 days), and then an initiation phase of ventilation is considered (5 days) to reach the final value. After this initiation phase, a constant ventilation is maintained.

The imposed boundary conditions at gallery wall, for total stresses and pore water

pressure evolutions, are presented in Fig. 12 for the two considered cases. It is worth mentioning that the ventilation effect on the shear banding is therefore represented by the hydro-mechanical model. In fact, the ventilation influences the pore water pressures and the effective stresses, which then influence the shear strain localisation structure and behaviour.

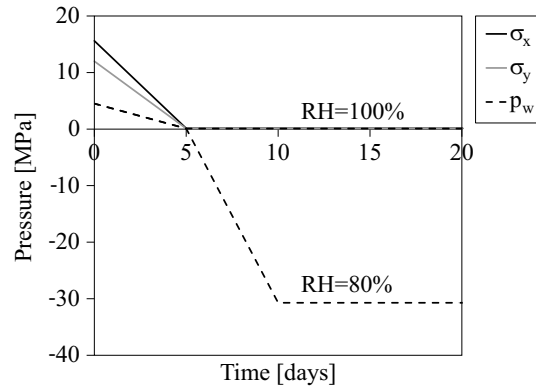


Figure 12: Imposed total stresses and pore water pressure at the gallery wall for the modelling of a gallery excavation with and without air ventilation.

The main purpose of this numerical modelling is to represent the fractures with shear strain localisation and to reproduce, as well as possible, the *in situ* measurements and observations with an isotropic mechanical model.

## 6.2 Influence of *in situ* stress and permeability anisotropies

Creation and evolution of the fractured zone can be observed through the evolution of shear strain localisation. The latter is not *a priori* assured to be symmetric around the gallery and many solutions could emerge [SaHC09]. To avoid any early symmetry assumption, the excavation of a full gallery is firstly modelled with incompressible solid grains  $b = 1$  and no ventilation. With a circular gallery and an isotropic state, it is not possible to trigger the shear strain localisation and the deformation remains diffuse. Strain localisation can be triggered through the introduction of an imperfection in the material.

However, in case of anisotropic stress state of the rock with  $\sigma_{x,0} = 15.6 \text{ MPa}$  and  $\sigma_{y,0} = \sigma_{z,0} = 12 \text{ MPa}$ , the shear strain localisation appears without adding an imperfection in the rock. Fig. 13 illustrates the evolution of the strain localisation around the gallery, during and after drilling. The numerical results presented are the total deviatoric strain, the plastic zone, and the deviatoric strain increment which represents the band activity:

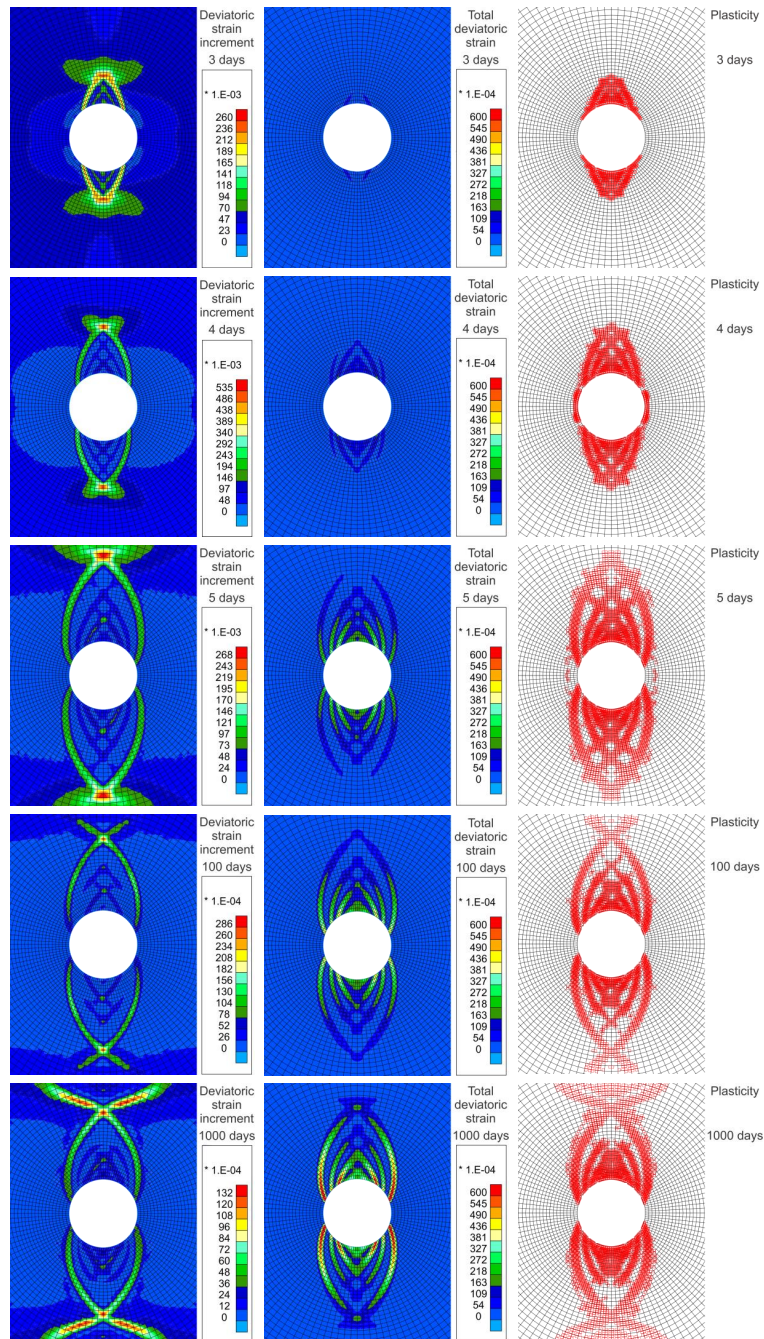


Figure 13: Evolution of strain localisation during and after the gallery excavation (5 days of excavation), for a full gallery and for a rock having anisotropic hydraulic permeability and anisotropic stress state.

$$\hat{\epsilon}_{eq} = \sqrt{\frac{2}{3}} \hat{\epsilon}_{ij} \hat{\epsilon}_{ij} \quad (93)$$

where  $\hat{\epsilon}_{ij}$  is the deviatoric total strain field calculated from the total strain tensor  $\epsilon_{ij}$ :

$$\hat{\epsilon}_{ij} = \epsilon_{ij} - \frac{\epsilon_{kk}}{3} \delta_{ij} \quad (94)$$

$$\kappa_{eq} = \frac{\dot{\hat{\epsilon}}_{eq} dt}{\int \dot{\hat{\epsilon}}_{eq} dt} \quad (95)$$

The modelling exhibits a symmetric chevron fracture pattern around the gallery similar to *in situ* observations for galleries parallel to  $\sigma_h$ . The chevron fractures appear during the excavation and are mainly concentrated above the gallery because of the material anisotropic stress state. On the contrary, introducing only the anisotropy of the intrinsic water permeability with  $k_{w,h} = 4 \times 10^{-20} m^2$  and  $k_{w,v} = 1.33 \times 10^{-20} m^2$  does not lead to strain localisation unless an imperfection is introduced. It means that the appearance and shape of the strain localisation are mainly due to mechanical effects linked to the anisotropic stress state. The shear banding zone develops preferentially in the direction of the minor principal stress in the gallery section.

### 6.3 Influence of second gradient boundary condition

The previous modelling highlights that the anisotropic stress state is at the origin of a symmetry in the localisation pattern around the gallery. Then, it would be convenient, in the following, to consider only a quarter of a gallery. However, in the context of second gradient theory, a boundary condition of higher order should be considered in addition to the classical boundary condition of constrained displacement perpendicular to the boundary [ZPV01a]. This second kinematic condition specifies that the normal derivative of the radial displacement has to cancel on the symmetry axes.

To illustrate the necessity of this second gradient boundary condition, the strain localisation pattern of Fig. 13 is compared to the pattern obtained on a quarter of a gallery. The modelling on a quarter of a gallery is computed with the specific second gradient boundary condition, and with  $b = 1$  and no ventilation as previously. In Fig. 14, one can observe that using the second gradient boundary condition produces a shear strain localisation pattern that is similar to the full-gallery results. Thus, it is confirmed that, for calculation simplicity and symmetry reasons, a quarter of a gallery can be adopted for future modelling, provided that the specific second gradient boundary condition is used.

### 6.4 Influence of Biot's coefficient

Even if strain localisation seems to be mainly controlled by mechanical effects, hydraulic conditions can also impact the shear banding pattern. Here, the focus is on the

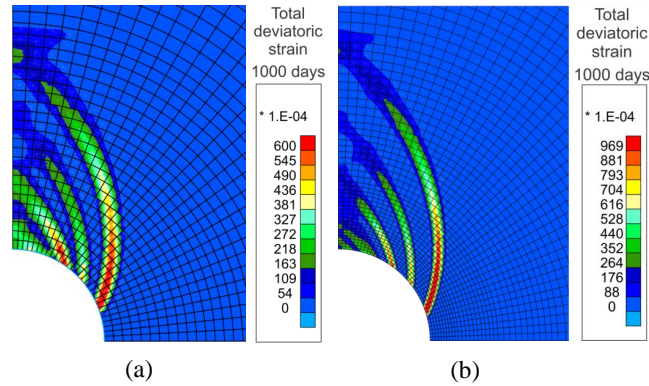


Figure 14: Comparison of the strain localisation pattern at the end of the calculation for the modelling of: (a) a full gallery and (b) a quarter of a gallery with the second gradient boundary condition.

influence of Biot's coefficient for the case without ventilation. In the first calculation, it is assumed that the solid grains are incompressible, which implies  $b = 1$  (Fig. 15). In the second calculation, a value of  $b = 0.6$  is used (Fig. 16). Comparison of Figs. 15 and 16 indicates that the Biot's coefficient significantly influences the shear band pattern. With a value of 0.6, less bands appear and the shear strain localisation is delayed. In fact, the strain remains diffuse until the fourth day of the excavation; nonetheless, the localisation appears before the end of the excavation. This can be explained by examining the stresses close to the gallery. At the gallery wall, the total stresses and the pore water pressure are imposed. Consequently, following the Biot's effective stress definition for unsaturated materials of Eq. 82, the lower the Biot's coefficient, the higher the effective compressive stress at the gallery wall. This implies that the rock close to the gallery wall is more resistant and that the shear strain localisation appears later.

## 6.5 Influence of gallery ventilation

The modelling presented hereafter includes the initial anisotropies, a Biot's coefficient value of 0.6, and the gallery ventilation. The drilling phase is not influenced by the ventilation, and the same results as in Fig. 16 are obtained until 5 days of computation. The results obtained after the excavation, displayed in Fig. 17, indicate that the suction imposed at the wall strongly influences the results. Following the effective stress definition, the higher the suction, the higher the effective stress (Fig. 20). As noted before, this involves that the material is more resistant, and in this case, becomes elastic again close to the gallery. This inhibits the shear strain localisation around the gallery.

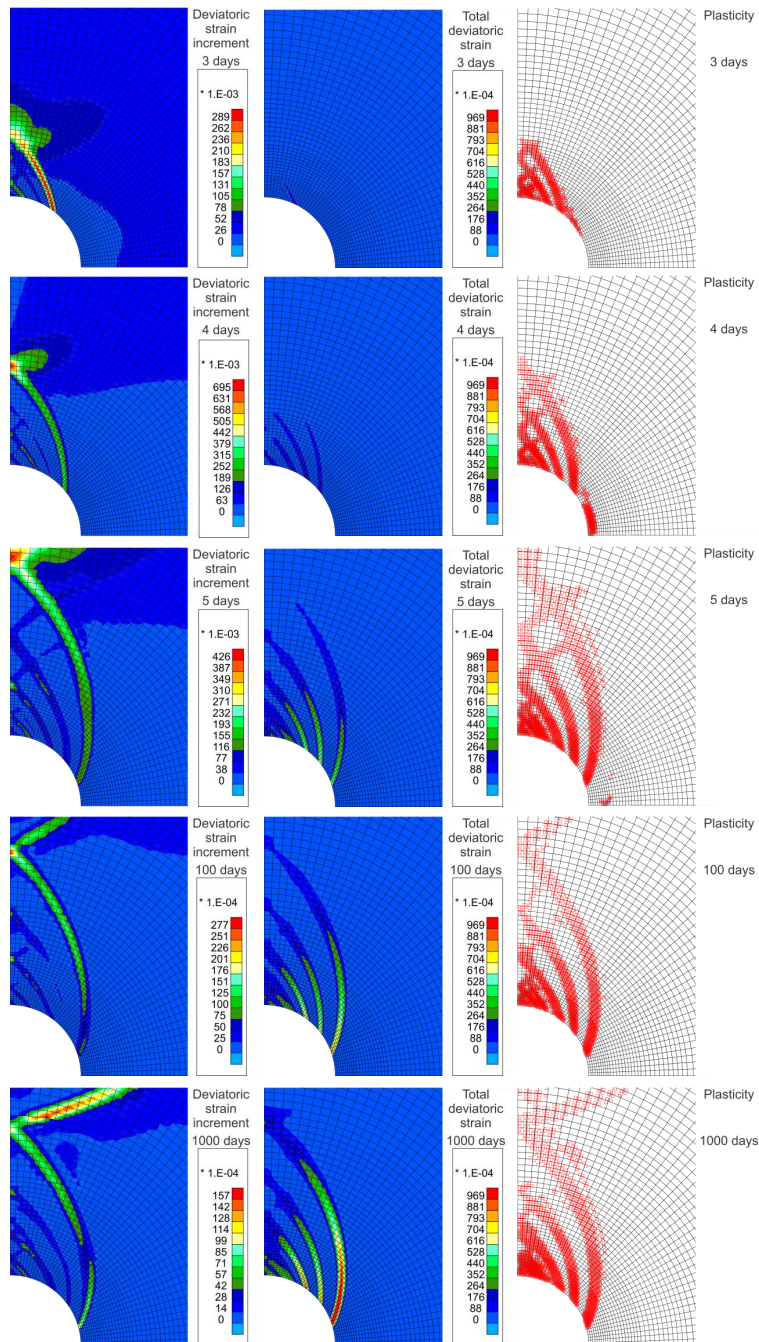


Figure 15: Evolution of strain localisation during and after gallery excavation (5 days of excavation), without gallery ventilation and for a Biot's coefficient value of 1.

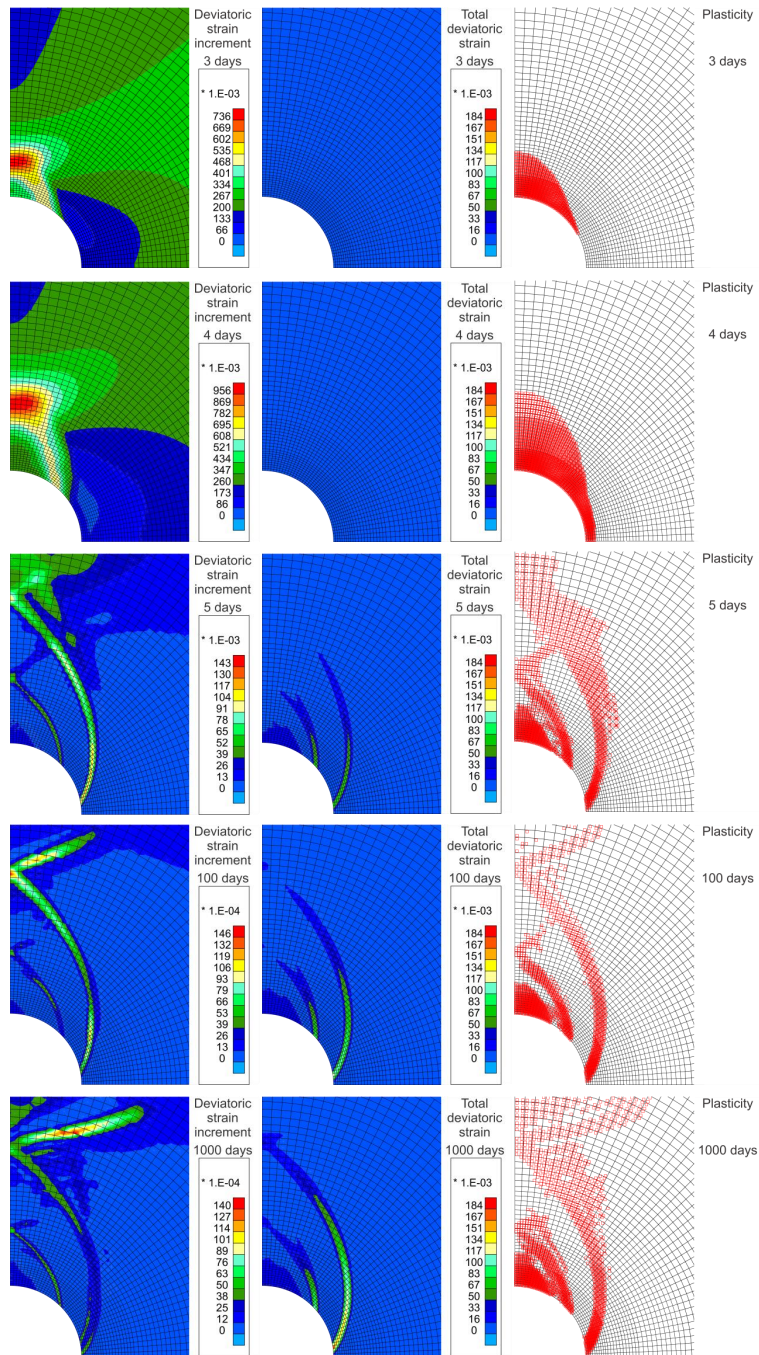


Figure 16: Evolution of strain localisation during and after gallery excavation (5 days of excavation), without gallery ventilation and for a Biot's coefficient value of 0.6.

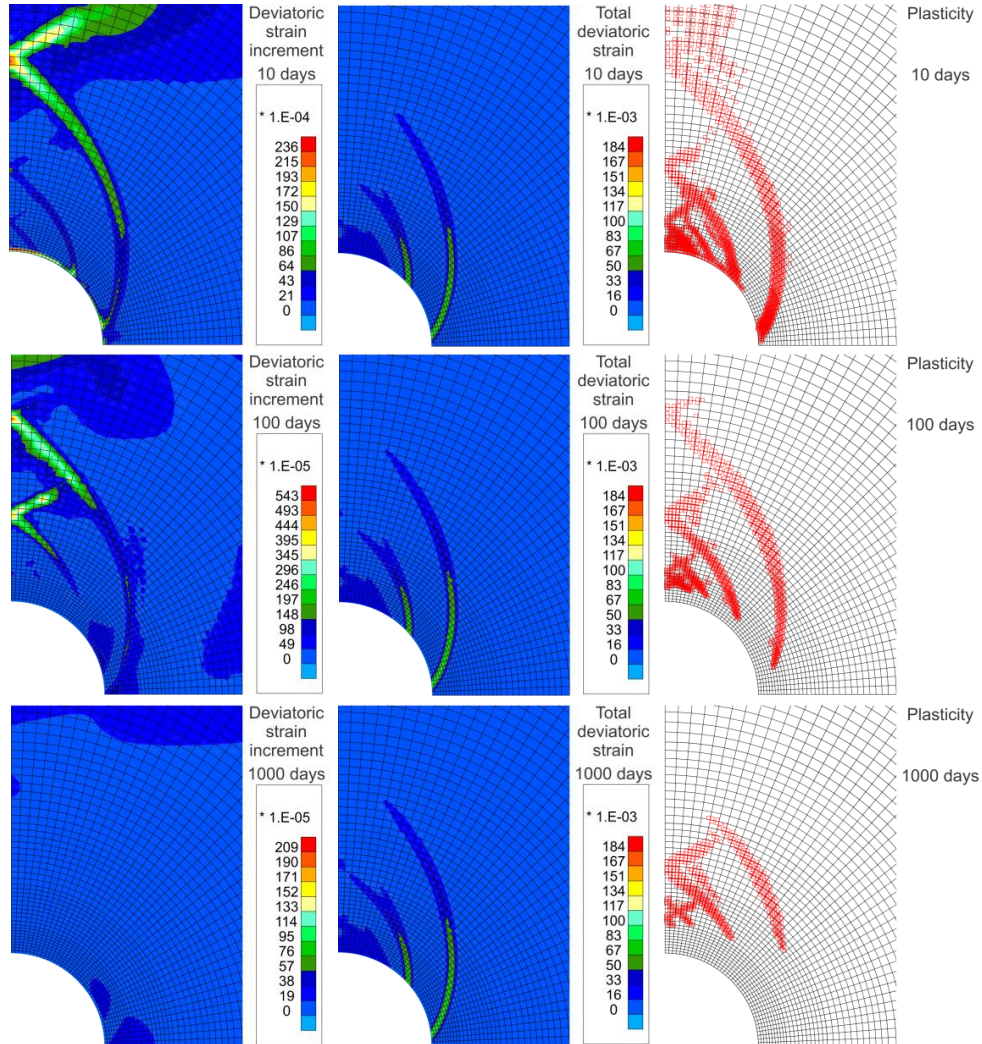


Figure 17: Evolution of strain localisation after gallery excavation, with gallery ventilation and for a Biot's coefficient value of 0.6.

Various numerical results, coming from the gallery wall and the rock mass, are interpreted hereafter in order to emphasize the influence of the gallery air ventilation. The results come from the selected cross-sections and observation points on gallery wall that are presented in Fig. 18. The vertical cross-section goes through the shear bands and the results along it highlights the effects of strain localisation, which is not the case for the horizontal cross-section. Furthermore, the results are compared for the cases considering ( $RH = 80\%$ ) or not ( $RH = 100\%$ ) the ventilation.

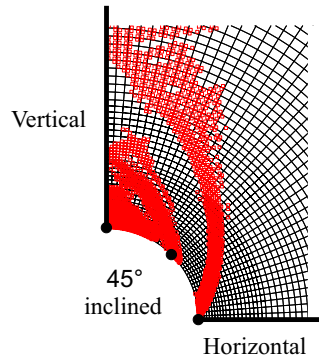


Figure 18: Positions of cross-sections and gallery wall observation points.

The evolution of pore water pressure for the vertical and horizontal cross-sections is detailed in Fig. 19. In the rock mass, an increase of pressure is observed in the vertical direction and a decrease in the horizontal direction up to a radial distance of about 30 m. These overpressures are related to the hydro-mechanical coupling induced by the anisotropy of the initial stress state. The influence of the strain localisation bands is visible vertically but not horizontally. It is illustrated by the fluctuations of the pore water pressure in limited zones, with a decrease in the shear band. The influence of the shear band can be mostly observed during the first 50 days of calculation then it tends to vanish. This is due to the strain increment inside the bands (band activity) and the hydro-mechanical coupling. As expected, the influence of the ventilation is marked close to the gallery wall, but tends to disappear deeper in the rock.

The stress paths at the gallery wall are detailed in Fig. 20 where  $q$  is the deviatoric stress:

$$q = \sqrt{3} II_{\delta'} \quad (96)$$

and  $p'$  is the mean effective stress. As mentioned before, in the case of ventilation, the effective stresses are much higher due to suction. This explains the difference between the stress paths of the modelling with and without ventilation, after the end of the drilling phase.

All these results are evidences that noticeable differences exist whether ventilation is applied or not. For the modelling with ventilation,  $p_w$  remains negative close to the gallery (Fig. 19), the effective stresses increase after the excavation (Fig. 20) and the material becomes elastic again. Consequently, the desaturation of the rock close to the gallery inhibits the shear strain localisation (Fig. 17), which has the effect of restricting further deformation. On the contrary, without ventilation,  $p_w$  close to the gallery wall increases after the excavation (Fig. 19), the effective stresses reduce (Fig. 20) and the material remains partly plastic close to the gallery (Fig. 16). This increases the deformation and the gallery convergence.

If the problem is studied with an isotropic model, without considering strain locali-

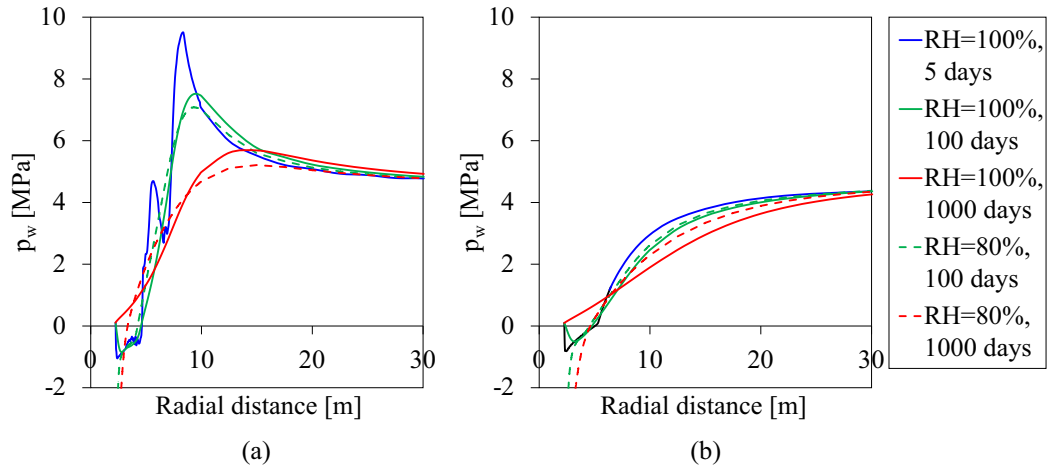


Figure 19: Evolution of pore water pressure along (a) vertical and (b) horizontal cross-sections, after gallery excavation.

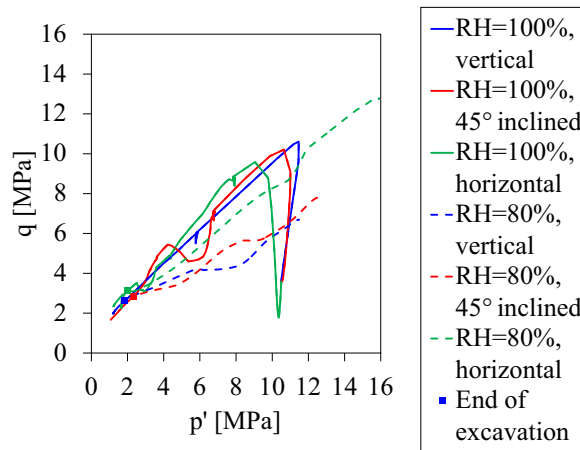


Figure 20: Stress paths at the gallery wall, during and after gallery excavation.

sation but modelling the gallery ventilation, then the horizontal and vertical convergences are more or less equal. Only the fracturing and strain localisation processes permit to produce the convergence anisotropy. In fact, neither the fracturing pattern nor the gallery convergence can be well reproduced with classical approach [PC16]. The creation of fractures, globally above the gallery due to the material anisotropic stress state, increases both the vertical and the horizontal convergences. In that latter direction, the proximity of the shear bands induces excessive deformations. In the

long term, the delayed deformations that are observed in saturated conditions are explained by consolidation. In contrast to this, when gallery ventilation is reproduced, the material close to the gallery wall becomes elastic again which restricts the plastic deformation and convergence in the long term. The performed numerical modelling highlights the effect of gallery ventilation on the hydraulic transfer and progressive drainage of the surrounding rock. However, the considered air ventilation is theoretical and a real ventilation could be considered [CCP<sup>+</sup>13], [PTC16]. Moreover, the water transfer and its kinetics close to the gallery are mainly conditioned by the hydro-mechanical property changes inside the excavation damaged zone. In fact, the damaged zone developing around galleries due to the drilling process is composed of fractures having a significant irreversible impact on flow and transport characteristics [TBD05]. For a shear banding approach, the impact of fracturing on the transport properties can be addressed by associating the intrinsic permeability increase with mechanical deformation [PTC16], which is amplified in the strain localisation discontinuities. Such dependence permits to reproduce a significant permeability increase of several orders of magnitude in the excavation damaged zone [PTC16], in agreement with available experimental measurements [ALN<sup>+</sup>14].

## 7 Conclusions

Rupture in geomaterials is often preceded by a localization of the deformations within thin bands. The strain localization is thus an important process, which has been studied both experimentally and theoretically. The developments of geomechanics in the field of coupled multiphysic processes impose the study of strain localization to these new conditions. Interactions between the different processes can indeed occur. Furthermore, the numerical modelling of shear bands with classical finite element suffers of a mesh dependency problem. An internal length scale has to be introduced in the model. Among the different regularization techniques, we propose a second gradient coupled model for an application to gallery excavation. It has been shown that the model regularizes the solution but does not restore its uniqueness. The extension of such theories to other multiphysic context is more an experimental problem than a numerical one. Experiments still have to exhibit the influence of temperature, suction or chemical concentration on the occurrence and the thickness of the strain localization!

## References

- [ABS03] K Alshibli, S Batiste, and S Sture. Strain Localization in Sand: Plane Strain versus Triaxial Compression. *J Geotech Geoenviron Eng*, 129(6):483–494, 2003.
- [Aif84] E C Aifantis. On the microstructural origin of certain inelastic models. *J Eng Mater Technol*, 106(4):326–330, 1984.

- [ALN<sup>+</sup>14] G Armand, F Leveau, C Nussbaum, R de La Vaissiere, A Noiret, D Jaeggi, P Landrein, and C Righini. Geometry and properties of the excavation-induced fractures at the Meuse/Haute-Marne URL drifts. *Rock Mech Rock Eng*, 47(1):21–41, 2014.
- [BA95] R I Borja and E Alarcon. A mathematical framework for finite strain elastoplastic consolidation part 1: Balance laws, variational formulation, and linearization. *Comput Methods Appl Mech Engrg*, 122(1-2):145–171, 1995.
- [BBC84] Z P Bazant, T B Belytschko, and T P Chang. Continuum Theory for Strain Softening. *J Eng Mech*, 110(12):1666–1692, 1984.
- [BCC06] P Bésuelle, R Chambon, and F Collin. Switching deformation modes in post-localization solutions with a quasibrittle material. *J Mech Mater Struct*, 1(7):1115–1134, 2006.
- [BDR00] P Bésuelle, J Desrues, and S Raynaud. Experimental characterisation of the localisation phenomenon inside a vosges sandstone in a triaxial cell. *Int J Rock Mech Min Sci*, 37(8):1223–1237, 2000.
- [Bio41] M A Biot. General theory for three-dimensional consolidation. *J Appl Phys*, 12(2):155–164, 1941.
- [BW57] M A Biot and D G Willis. The Elastic Coefficients of the Theory of Consolidation. *J Appl Mech*, 24:594–601, 1957.
- [CC09] E Cosserat and F Cosserat. *Théorie des Corps Déformables*. Hermann, Paris, 1909.
- [CCC01] R Chambon, S Crochepeyre, and R Charlier. An algorithm and a method to search bifurcation points in non-linear problems. *Int J Numer Meth Engng*, 51(3):315–332, 2001.
- [CCC06] F Collin, R Chambon, and R Charlier. A finite element method for poro mechanical modelling of geotechnical problems using local second gradient models. *Int J Numer Meth Engng*, 65(11):1749–1772, 2006.
- [CCC09] F Collin, D Caillerie, and R Chambon. Analytical solutions for the thick-walled cylinder problem modeled with an isotropic elastic second gradient constitutive equation. *Int J Solids Struct*, 46(22-23):3927–3937, 2009.
- [CCH98] R Chambon, D Caillerie, and N El Hassan. One-dimensional localisation studied with a second grade model. *Eur J Mech A-Solid*, 17(4):637–656, 1998.
- [CCM01] R Chambon, D Caillerie, and T Matsushima. Plastic continuum with microstructure, local second gradient theories for geomaterials : localization studies. *Int J Solids Struct*, 38(46-47):8503–8527, 2001.

- [CCP<sup>+</sup>13] R Charlier, F Collin, B Pardoën, J Talandier, J P Radu, and P Gerard. An unsaturated hydro-mechanical modelling of two in-situ experiments in Callovo-Oxfordian argillite. *Eng Geol*, 165:46–63, 2013.
- [CLC09] F Collin, S Levasseur, and R Chambon. Numerical post failure methods in multiphysical problems. *Eur J Environ Civ Eng*, 13(7-8):983–1004, 2009.
- [CM04] R Chambon and J C Moullet. Uniqueness studies in boundary value problems involving some second gradient models. *Comput Methods Appl Mech Engrg*, 193(27-29):2771–2796, 2004.
- [Cou73] C A Coulomb. Essai sur une application des règles de maximis et minimis à quelques problèmes de statique, relatifs à l’architecture. *Académie Royale des Sciences*, 7:343–382, 1773.
- [Cou95] O Coussy. *Mechanics of Porous Continua*. John Wiley & Sons, Chichester, 1995.
- [Cou04] O Coussy. *Poromechanics*. John Wiley & Sons, Chichester, 2004.
- [CRB97] R Charlier, J P Radu, and J D Barnichon. Water movement effect on the strain localisation during a biaxial compression. In G Pande and S Pietruszczak, editors, *Numerical Models in Geomechanics, NUMOG VI*, pages 219–224, Rotterdam, 1997. Balkema.
- [dBM92] R de Borst and H B Mühlhaus. Gradient-dependent plasticity: Formulation and algorithm aspects. *Int J Numer Meth Engng*, 35(3):521–539, 1992.
- [DC93] E Detournay and A H D Cheng. *Comprehensive Rock Engineering: Principles, Practice and Projects*, volume 2 Analysis and Design Method, chapter 5 Fundamentals of Poroelasticity, pages 113–171. Pergamon Press, Oxford, 1993.
- [Des84] J Desrues. *La localisation de la déformation dans les matériaux granulaires*. PhD thesis, Université Joseph Fourier, Institut National Polytechnique, Grenoble, 1984.
- [Des05] J Desrues. Hydro-mechanical coupling and strain localization in saturated porous media. *Rev Eur Génie Civ*, 9(5-6):619–634, 2005.
- [Die03] M S Diederichs. Rock Fracture and Collapse Under Low Confinement Conditions. *Rock Mech Rock Eng*, 36(5):339–381, 2003.
- [DV04] J Desrues and G Viggiani. Strain localization in sand: an overview of the experimental results obtained in Grenoble using stereophotogrammetry. *Int J Numer Anal Meth Geomech*, 28(4):279–321, 2004.

- [EV98] W Ehlers and W Volk. On theoretical and numerical methods in the theory of porous media based on polar and non-polar elasto-plastic solid materials. *Int J Solids Struct*, 35(34-35):4597–4617, 1998.
- [Fer09] R Fernandes. *Modélisation numérique objective des problèmes hydromécaniques couplés dans le cas des géomatériaux*. PhD thesis, Université Joseph Fourier, Grenoble, 2009.
- [FHMV96] R Finno, W Harris, M Mooney, and G Viggiani. Strain localization and undrained steady state of sands. *J Geotech Engrg*, 122(6):462–473, 1996.
- [FHMV97] R Finno, W Harris, M Mooney, and G Viggiani. Shear bands in plane strain compression of loose sand. *Géotechnique*, 47(1):149–165, 1997.
- [Ger73] P Germain. The method of virtual power in continuum mechanics. Part 2 Microstructure. *SIAM J Appl Math*, 25(3):556–575, 1973.
- [GSH12] N Guy, D M Seyed, and F Hild. A probabilistic nonlocal model for crack initiation and propagation in heterogeneous brittle materials. *Int J Numer Meth Engng*, 90(8):1053–1072, 2012.
- [HD93] C Han and A Drescher. Shear bands in biaxial tests on dry coarse sand. *Soils Found*, 33(1):118–132, 1993.
- [JKC14] Gwendal Jouan, Panagiotis Kotronis, and Frédéric Collin. Using a second gradient model to simulate the behaviour of concrete structural elements. *Finite Elements in Analysis and Design*, 90:50 – 60, 2014.
- [JS88] Y S Jenq and S P Shah. Mixed-mode fracture of concrete. *Int J Fracture*, 38(2):123–142, 1988.
- [KCB<sup>+</sup>07] P Kotronis, F Collin, P Bésuelle, R Chambon, and J Mazars. Local Second Gradient Models and Damage Mechanics: 1D Post-Localization Studies in Concrete Specimens. In G Exadaktylos and I Vardoulakis, editors, *Bifurcation, Instabilities and Degradation in Geomechanics*, pages 127–142. Springer, 2007.
- [KGDLO6] H D V Khoa, I O Georgopoulos, F Darve, and F Laouafa. Diffuse failure in geomaterials: Experiments and modelling. *Comput Geotech*, 33(1):1–14, 2006.
- [LB88] D Lasry and T Belytschko. Localization limiters in transient problems. *Int J Solids Struct*, 24(6):581–597, 1988.
- [LBD<sup>+</sup>07] N Lenoir, M Bornert, J Desrues, P Bésuelle, and G Viggiani. Volumetric digital image correlation applied to X-ray microtomography images from triaxial compression tests on argillaceous rock. *Strain*, 43(3):193–205, 2007.

- [MCC02] T Matsushima, R Chambon, and D Caillerie. Large strain finite element analysis of a local second gradient model: application to localization. *Int J Numer Meth Engng*, 54(4):499–521, 2002.
- [MD99] M Mokni and J Desrues. Strain localisation measurements in undrained plane-strain biaxial test on Hostun RF sand. *Mech Cohes-Frict Mat*, 4(4):419–441, 1999.
- [Min64] R D Mindlin. Micro-structure in linear elasticity. *Arch Ration Mech An*, 16(1):51–78, 1964.
- [Min65] R D Mindlin. Second gradient of strain and surface-tension in linear elasticity. *Int J Solids Struct*, 1:417–438, 1965.
- [MSC14] F Marinelli, Y Sieffert, and R Chambon. Hydromechanical modelling of an initial boundary value problem: Studies of non-uniqueness with a second gradient continuum. *Int J Solids Struct*, 2014.
- [Mua76] Y Mualem. A new model for predicting the hydraulic conductivity of unsaturated porous media. *Water Resour Res*, 12(3):513–522, 1976.
- [NL08] M Nuth and L Laloui. Effective stress concept in unsaturated soils: Clarification and validation of a unified framework. *Int J Numer Anal Meth Geomech*, 32(7):771–801, 2008.
- [PC16] B Pardoen and F Collin. Modelling the influence of strain localisation and viscosity on the behaviour of underground drifts drilled in claystone. *Comput Geotech*, 2016. in press.
- [PCB87] G Pijaudier-Cabot and Z P Bazant. Nonlocal damage theory. *J Eng Mech*, 113(10):1512–1533, 1987.
- [PdBB<sup>+</sup>96] R H J Peerlings, R de Borst, W A M Brekelmans, J H P de Vree, and I Spee. Some observations on localisation in non-local and gradient damage models. *Eur J Mech A/Solids*, 15(6):937–953, 1996.
- [PdBBdV96] R H J Peerlings, R de Borst, W A M Brekelmans, and J H P de Vree. Gradient enhanced damage for quasi-brittle materials. *Int J Numer Meth Engng*, 39(19):3391–3403, 1996.
- [PGdBB01] R H J Peerlings, M G D Geers, R de Borst, and W A M Brekelmans. A critical comparison of nonlocal and gradient-enhanced softening continua. *Int J Solids Struct*, 38(44-45):7723–7746, 2001.
- [PLC15] B Pardoen, S Levasseur, and F Collin. Using Local Second Gradient Model and Shear Strain Localisation to Model the Excavation Damaged Zone in Unsaturated Claystone. *Rock Mech Rock Eng*, 48(2):691–714, 2015. doi: 10.1007/s00603-014-0580-2.

- [PM81] S T Pietruszczak and Z Mróz. Finite element analysis of deformation of strain-softening materials. *Int J Numer Meth Engng*, 17(3):327–334, 1981.
- [PTC16] B Pardoën, J Talandier, and F Collin. Permeability evolution and water transfer in the excavation damaged zone of a ventilated gallery. *Int J Rock Mech Min Sci*, 85:192–208, 2016. 10.1016/j.ijrmms.2016.03.007.
- [PV92] P C Papanastasiou and I G Vardoulakis. Numerical treatment of progressive localization in relation to borehole stability. *Int J Numer Anal Meth Geomech*, 16(6):389–424, 1992.
- [Ric76] J R Rice. The localization of plastic deformation. In W T Koiter, editor, *Theoretical and Applied Mechanics*, volume 1, pages 207–220. North-Holland Publishing Company, 1976.
- [RR75] J W Rudnicki and J R Rice. Conditions for the localisation of deformation in pressure sensitive dilatant materials. *J Mech Phys Solids*, 23:371–394, 1975.
- [SaHC09] Y Sieffert, S al Holo, and R Chambon. Loss of uniqueness of numerical solutions of the borehole problem modelled with enhanced media. *Int J Solids Struct*, 46(17):3173–3197, 2009.
- [Ske60] A W Skempton. Effective stress in soils, concrete and rocks. In *Pore Pressure and Suction in Soils*, pages 4–16, London, 1960. Butterworths.
- [TBD05] C F Tsang, F Bernier, and C Davies. Geohydromechanical processes in the Excavation Damaged Zone in crystalline rock, rock salt, and indurated and plastic clays - in the context of radioactive waste disposal. *Int J Rock Mech Min Sci*, 42(1):109–125, 2005.
- [Tou62] R Toupin. Elastic materials with couple-stresses. *Arch Ration Mech An*, 11(1):385–414, 1962.
- [vG80] M T van Genuchten. A closed-form equation for predicting the hydraulic conductivity of unsaturated soils. *Soil Sci Soc Am J*, 44(5):892–898, 1980.
- [VGG78] I Vardoulakis, M Goldscheider, and Q Gudehus. Formation of shear bands in sand bodies as a bifurcation problem. *Int J Numer Anal Meth Geomech*, 2(2):99–128, 1978.
- [VS95] I Vardoulakis and J Sulem. *Bifurcation Analysis in Geomechanics*. Blackie Academic and Professional, 1995.
- [WW10] S Wu and X Wang. Mesh Dependence and Nonlocal Regularization of One-Dimensional Strain Softening Plasticity. *J Eng Mech*, 136(11):1354–1365, 2010.

- [Zau89] E Zauderer. *Partial Differential Equations of Applied Mathematics*. Wiley, Chichester,UK, second ed. edition, 1989.
- [ZPV01a] A Zervos, P Papanastasiou, and I Vardoulakis. Modelling of localisation and scale effect in thick-walled cylinders with gradient elastoplasticity. *Int J Solids Struct*, 38(30-31):5081–5095, 2001.
- [ZPV01b] A Zervos, P Papanastasiou, and I Vardoulakis. A finite element displacement formulation for gradient elastoplasticity. *Int J Numer Meth Engng*, 50(6):1369–1388, 2001.
- [ZSS01] H W Zhang, L Sanavia, and B A Schrefler. Numerical analysis of dynamic strain localisation in initially water saturated dense sand with a modified generalised plasticity model. *Comput Struct*, 79(4):441–459, 2001.
- [ZT00] O C Zienkiewicz and R L Taylor. *The Finite Element Method*. Butterworth-Heinemann, Stonchem, MA, fifth edition edition, 2000.



©ALERT Geomaterials  
INPG – 3SR  
46 avenue Félix Viallet  
BP 53  
38041 GRENOBLE CEDEX 9  
FRANCE

ISBN 978-2-9542517-8-3

Fon: +33 (0) 456 528 621  
Fax: +33 (0) 476 827 043  
president@alertgeomaterials.eu  
<http://alertgeomaterials.eu>

---

All rights reserved. No part of this book may be reproduced in any form or by any electronic or mechanical means, including information storage and retrieval systems, without written permission from the publisher or author, except in the case of a reviewer, who may quote brief passages embodied in critical articles or in a review.



## **ALERT Doctoral School 2016**

### *Modelling of instabilities and bifurcation in Geomechanics*

---

Editors: J. Sulem, I. Stefanou, E. Papamichos, M. Veveakis

T. Hueckel

Instability Phenomena in Geomechanics- A Review from a Multi-Physics Point of View

I. Stefanou, S. Alevizos

Fundamentals of bifurcation theory and stability analysis

J. Sulem

Material instability and strain localization analysis

P. Bésuelle, P. Lanatà

Experimental investigation of the emergence of strain localization in geomaterials

P. Papanastasiou, A. Zervos

Numerical modelling of strain localization

E. Papamichos

Numerical modeling of bifurcation: Applications to borehole stability, multilayer buckling, and rock bursting

J. Sulem, I. Stefanou

Multiphysics couplings and strain localization in geomaterials

M. Veveakis

Thermo-poro-mechanics of chemically active faults

F. Collin, P. Kotronis, B. Pardoen

Numerical modelling of multiphysics couplings and strain localization

ISBN 978-2-9542517-8-3